

Frequency Conversion of Optical Signals Using Coherently Prepared Media

by

Ryan S. Bennink

Submitted in Partial Fulfillment of
the Requirements for the Degree
Doctor of Philosophy

Supervised by
Robert W. Boyd

The Institute of Optics
The College
School of Engineering and Applied Sciences

University of Rochester
Rochester, NY

2004

to my parents, who have always supported me

CURRICULUM VITAE

Ryan Bennink was born in Champaign-Urbana, Illinois in 1972 and grew up on the outskirts of East Lansing, Michigan. He attended Hope College from 1991 to 1995, maintaining a 4.0 GPA and graduating with a B.S. degree in physics and mathematics. As a Marshall Scholar, he spent two years studying physics at King's College, University of London, where he earned an M.Sci degree and was awarded both college and university prizes. In 1997 he began the Ph.D program in Optics at the University of Rochester with the support of a Sproull fellowship. Under the supervision of Dr. Robert Boyd, he has been researching quantum optics and quantum electronics.

PUBLICATIONS

- “Influence of coherent Raman scattering on electromagnetically induced transparency in atomic sodium vapor.” Vincent Wong, Ryan S. Bennink, Alberto M. Marino, Robert W. Boyd, C. R. Stroud, Jr., and F. A. Narducci. (*submitted to Phys. Rev. A*)
- “Realization of the Einstein-Podolsky-Rosen paradox using momentum- and position- entangled photons.” John C. Howell, Ryan S. Bennink, Sean J. Bentley, and Robert W. Boyd. (*to appear in Phys. Rev. Lett., 2004*).
- “Quantum and classical coincidence imaging.” Ryan S. Bennink, Sean J. Bentley, Robert W. Boyd, and John C. Howell. *Phys. Rev. Lett.* **92**, 033601 (2004).
- “Thirteen pump-probe resonances of the sodium D1 lines.” Vincent Wong, Robert W. Boyd, C. R. Stroud, Ryan S. Bennink, and Alberto M. Marino. *Phys. Rev. A* **68**, 012502 (2003).
- “Improved measurement of multimode squeezed light via an eigenmode approach.” Ryan S. Bennink and Robert W. Boyd. *Phys. Rev. A* **66**, 053815 (2002).
- “‘Two-Photon’ Coincidence Imaging with a Classical Source.” Ryan S. Bennink, Sean J. Bentley, and Robert W. Boyd. *Phys. Rev. Lett.* **89**, 113601 (2002).
- “Comment on ‘Resonance-fluorescence and absorption spectra of a two-level atom driven by a strong bichromatic field.’” David L. Aronstein, Ryan S. Bennink, Robert W. Boyd, and C. R. Stroud, Jr. *Phys. Rev. A* **65**, 067401 (2002).
- “Honeycomb pattern formation by laser-beam filamentation in atomic sodium vapor.” Ryan S. Bennink, Vincent Wong, Alberto M. Marino, David L. Aronstein, Robert W. Boyd, and Daniel J. Gauthier. *Phys. Rev. Lett.* **88**, 113901 (2002).
- “Absorptionless self-phase-modulation via dark-state electromagnetically induced transparency.” Vincent Wong, Robert W. Boyd, C. R. Stroud, Ryan S. Bennink, David L. Aronstein and Q-Han Park. *Phys. Rev. A* **65**, 013810 (2001).
- “Enhanced self-action effects by electromagnetically induced transparency in the two-level atom.” Ryan S. Bennink, Robert W. Boyd, C. R. Stroud, Jr., and Vincent Wong. *Phys. Rev. A* **63**, 033804 (2001).

“Intrinsic optical bistability in a thin layer of nonlinear optical material by means of local field effects.” Young-Kwon Yoon, Ryan S. Bennink, Robert W. Boyd, and J. E. Sipe. *Opt. Comm.* **179**, 577 (2000).

“Conversion of unpolarized light to polarized light with greater than 50% efficiency by photorefractive two-beam coupling.” John E. Heebner, Ryan S. Bennink, Robert W. Boyd, and R. A. Fisher. *Opt. Lett.* **25**, 257 (2000).

“Accessing the optical nonlinearity of metals with metal-dielectric photonic bandgap structures.” Ryan S. Bennink, Young-Kwon Yoon, Robert W. Boyd, and J. E. Sipe. *Opt. Lett.* **24**, 1416 (1999).

“An efficient method of implementing near-field diffraction in computer-generated hologram design.” R. S. Bennink, A. K. Powell, and D. A. Fish. *Opt. Comm.* **141**, 194 (1997).

CONFERENCE PRESENTATIONS

- “Quantum Imaging and EPR: Violation of the continuous-variable EPR bound by a factor of 100.” Ryan S. Bennink, Sean J. Bentley, Robert W. Boyd, and John C. Howell. *Physics of Quantum Electronics* (2004).
- “Graphical solution of coherent Raman systems using the Bloch Sphere.” Ryan S. Bennink, C. R. Stroud, Jr., and Robert W. Boyd. *Quantum Electronics and Laser Science* (2003).
- “Electromagnetically induced absorption and transparency in a single Raman spectrum.” Ryan S. Bennink, Alberto M. Marino, Vincent Wong, C. R. Stroud, Jr., and Robert W. Boyd. *Quantum Electronics and Laser Science* (2003).
- “Quantum and classical aspects of coincidence imaging.” Ryan S. Bennink, Sean J. Bentley and Robert W. Boyd. *Quantum Electronics and Laser Science* (2003).
- “Improved measurement of multimode squeezed light via eigenmode decomposition.” Ryan S. Bennink and Robert W. Boyd. *Quantum Electronics and Laser Science* (2002).
- “Honeycomb pattern formation by laser-beam filamentation in atomic sodium vapor.” Ryan S. Bennink, Vincent W. Wong, David L. Aronstein, Robert W. Boyd, Svetlana G. Lukishova, Alberto M. Marino, and Carlos R. Stroud, Jr. *Quantum Electronics and Laser Science* (2001).
- “Metal-dielectric photonic bandgap structures: highly nonlinear, transmissive composite optical materials.” Ryan S. Bennink, Young-Kwon Yoon, Robert W. Boyd, and John E. Sipe. *Quantum Electronics and Laser Science* (2000).

ACKNOWLEDGEMENTS

There is no doubt that who and where I am today is in large part due to the support and influence of others. From family and friends to teachers and professors, many people have played a role in my completion of this degree. I now want to thank those who have had such a significant impact on my life and work at Rochester.

First and foremost, I want to thank my family. Mom, Dad, Jill—I love you. Your advice and encouragement have meant more to me than you know. In years of wandering, you have been to me compass, mirror, and friend. Much of who I am, I am because of who you are.

For my development from student to scientist, I am most indebted to Professor Boyd. Not only has he shaped how I think about light and directed me into worthwhile projects, he has taught me by example many things about being a scientist, which as an incoming student I never imagined would be part of my education: about running a group, forming collaborations, convincing others your research is important, and the art of diplomacy. If that weren't enough, he also taught me how to ski. I am fortunate to have spent these years working under someone so knowledgeable, pleasant, and (let's admit it) entertaining. I am fortunate, too, to have benefitted from the knowledge and insights of Professor Stroud on a regular basis. I am very grateful to Dr. Frank Narducci and Dr. Dan Gauthier, whose laboratory skills and experimental wisdom were indispensable; I believe our research took a significant step forward every time they visited our laboratory. Finally, I would like to thank Professor Howell. Though we met and starting working together only a year ago, it has been a very good year. He has been a great help to me in my research and in my transition to a career. Of all the people I have worked with while at Rochester, I can think of few who are nicer or whose company I enjoy more.

I have also benefited tremendously from other students. John Heebner initiated me to the Boyd laboratory and provided me with many insights over the years. It was my pleasure to have as a friend and sounding board David Aronstein, who enthusiastically received my reports of my forays into the nether regions of physics, and on many occasions helped me develop my nascent ideas. I only regret that we did not manage to hang out more often. Regarding my thesis work, it is not an exaggeration

to say that I would not have accomplished it without Vincent Wong and Alberto Marino. Not only has my thinking been sharpened through many discussions of atomic physics with them, but they have been my teammates in the laboratory, together with me maintaining the dye lasers and taking data. My advice to you both is to decide exactly what you need to do to graduate, then pursue it with focus. I also want to thank Sean Bentley for working with me on several quantum imaging experiments. Finally, I want to express my appreciation to all those who have been part of the Boyd group these past six years. It has been my joy to work with you all, and I am proud to have you as my colleagues.

I would also like to thank Betsy, Gayle, Joan, and Noelene for their assistance over the years. No matter how many times you had to remind me how to fill out the same form, you never made me feel bad about it.

In my research I have learned that the properties of an atom are significantly affected by its environment. I too have been strongly affected by “external influences”—those who have been a part of my life outside the university. To Pastor Wally, the Pathseekers, and the Edgewood Free Methodist Church: it took me a few years, but I finally found you; and I am so glad that I did. You have been my community, and have enriched my life greatly. To Mike Hernberg and those in the former GCF Bible study: I thank you for several years of friendship and challenging, intellectual Christian fellowship. Most important of all, I wish to say a very fond “thank-you” and “farewell” to Dave Fischer, with whom I have shared an apartment for the past six years. From pizza nights, to the countless episodes of our favorite reruns we watched together, to the computer games you got me addicted to, to our discussions of life, technology, politics and faith—in all ways you have been a great apartmentmate. Parting makes me say Grrr... Arrgh.

There are others of course, too many to mention by name, who have played some role in my completion of this degree. Rest assured, I remember you and appreciate all you have done for me. But an acknowledgement must end somewhere. So, to everyone I say...

Thank you.

Abstract

In the past decade, researchers have found that the optical properties of a medium can be dramatically altered by optically driving the medium into a coherent superposition of its quantum states. Optical transitions from these states can interfere, leading to optically induced absorption or transparency. Such “coherently prepared media” (CPM) typically have large wave-mixing susceptibilities without the resonant absorption that usually accompanies large nonlinear susceptibilities. In certain schemes, a large material coherence can act as an oscillator which scatters optical waves into modes of different frequency with high efficiency. Technologies based on this process could find uses ranging from telecommunications to X-ray pulse characterization. The present work investigates the ability to coherently prepare an atomic vapor and to use that coherence to shift optical signals from one frequency to another with high efficiency, bandwidth, and fidelity.

My theoretical studies of coherent preparation include both simple and many-state systems. While two-state systems can display some coherent effects, coherent effects are much more clearly displayed in three- and four-state systems. A Bloch-sphere representation of Raman systems is developed, which yields simple, easy-to-interpret graphical solutions and illustrates basic physical principles of coherent preparation through simple formulas. The complications of coherently preparing a real vapor are also considered and discussed in detail. Experimentally, a pair of laser fields were used to create coherence between the $3S_{1/2}$ hyperfine levels of sodium vapor. Coherence-based optical effects including transparency, four-wave mixing, and Raman scattering were observed. Finally, coherence-induced Raman scattering was used to perform fast (> 20 MHz), high-fidelity ($> 99\%$) conversion of AM and FM optical signals from one carrier frequency to another. In spite of these successes, the degree of coherence produced and the conversion efficiency were not as large as one would hope. My work concludes with a discussion of the obstacles encountered in achieving large coherent effects in vapors and how they might be overcome.

Contents

List of Tables	xiii
List of Figures	xiv
List of Symbols and Acronyms	xvii
1 Introduction	1
1.1 Background	2
1.2 Applications	7
1.3 Outline	8
2 A Bloch-Vector Model of Raman Systems	11
2.1 The Vector Representation of Raman Systems	12
2.2 The Vector Equation of Motion	16
2.3 The Steady-State Equation and General Solution	19
2.4 Steady-State Solutions for Special Cases	23
2.5 The Equation of Motion for $\vec{\rho}$ in a General Raman System	24
2.6 Summary	25
3 Coherent Nonlinear Optics in Λ and $\Lambda\Lambda$ Systems	26
3.1 The Ground State Coherence	26
3.2 Absorption and Electromagnetically Induced Transparency	30
3.3 Coherent Raman Scattering	35

3.4	Summary	40
4	What About Coherence in Two-State Systems?	42
4.1	Two States Driven by One Field	42
4.2	Two States Driven by More than One Field	43
4.3	Summary	45
5	Coherent Preparation of Many-State Atoms	46
5.1	Notation and Conventions	46
5.2	Generalization of the Dark/Bright Basis	50
5.3	Multi-state Effects	52
5.4	Dark States in the Sodium D1 Line	55
5.5	Numerical Studies	64
5.6	Summary	71
6	Coherent Preparation of Atomic Vapors	73
6.1	Effects Resulting from Atomic Motion	74
6.2	Interactions Between Atoms	82
6.3	Considerations Associated with Propagation	85
6.4	Technical Considerations	88
6.5	Simulation of Coherent Preparation of Sodium Vapor	93
6.6	Summary	97
7	Experimental Studies of Coherence in Sodium Vapor	99
7.1	The Experimental Setup	99
7.2	Coherence Relaxation Studies	104
7.3	Coherence-Induced Transparency, Absorption, and Raman Scattering	110
7.4	Frequency Conversion of an Optical Signal Using Hyperfine Coherence	116
7.5	Summary	121

8 Summary and Perspective	122
8.1 Summary	122
8.2 Perspective	125
References	129
A Effective Matrix Elements for Multiplets	141
B Matrix Elements of the Electric and Magnetic Dipole Operators	145
B.1 Derivation of the Matrix Elements	145
B.2 Computed Matrix Elements	151
C Relaxation in Quantum Systems	157
C.1 Derivation of the Relaxation Terms	158
C.2 Examples	164
D Theory for Numerical Solution of a Two-Manifold System	168
D.1 The Physical Model	168
D.2 Derivation of the Master Equation	171
D.3 Solving the Master Equation in the Steady-State	175
D.4 Calculating Optical Properties	177

List of Tables

5.1	Schmidt states of the sodium D1 $\Lambda_{1y,2x}^1$ system	59
5.2	Schmidt states of the sodium D1 $\Lambda_{1y,2x}^2$ system	61
5.3	Dark states of the sodium D1 line in the presence of a magnetic field	62
A.1	Effective parameters for sodium D1 hyperfine transitions	144
A.2	Effective parameters for sodium D2 hyperfine transitions	144
B.1	Electric dipole matrix elements for sodium D1 states	152
B.2	Electric dipole matrix elements for sodium D2 states	153
B.3	Magnetic dipole matrix elements for sodium $S_{1/2}$ states	155
B.4	Magnetic dipole matrix elements for sodium $P_{1/2}$ states	156

List of Figures

1.1	Coherent population trapping (concept)	3
1.2	Electromagnetically induced transparency (concept)	5
1.3	Other systems involving quantum coherence	6
1.4	Application of coherent preparation to X-ray SPIDER	9
2.1	Example Raman systems	13
2.2	The Bloch sphere	14
2.3	The two-field vector	15
2.4	The 3-state Λ system	16
2.5	Contributions to the steady-state Bloch vector	21
2.6	Bloch vector solutions for the pump-pump configuration	22
2.7	Bloch vector solutions for the pump-probe configuration	22
3.1	Ground state coherence vs. frequency in a Λ system	28
3.2	Ground-state coherence vs. saturation in a Λ system	29
3.3	Absorption saturation due to CPT in a Λ system	32
3.4	EIT in a Λ system	33
3.5	Stimulated Raman scattering via coherent population trapping.	35
3.6	Spatial evolution of the fields in coherent Raman scattering	37
4.1	“Dressing” of states by a strong field	44
4.2	Transparency in a driven 2-state system	45

5.1	Relaxation bias (concept)	53
5.2	Extraneous trap states (concept)	54
5.3	Zeeman structure of the sodium D1 states	55
5.4	The scheme for coherent preparation of sodium.	56
5.5	The scheme for coherent Raman scattering in sodium.	57
5.6	Population trapping vs. intensity in a sodium atom	65
5.7	Absorption saturation vs. intensity in a sodium atom	66
5.8	Hyperfine coherences in a sodium atom without a magnetic field	67
5.9	EIT in a sodium atom	67
5.10	The absorption spectra of sodium atoms with and without hyperfine coherence	68
5.11	Raman scattering susceptibility vs. frequency	69
5.12	Hyperfine coherences in a sodium atom with a magnetic field	70
5.13	Occupancy of “the” sodium dark state vs. frequency	71
6.1	Diffusion in a cylinder	77
6.2	Comparison of the spectra of Doppler shifts, Raman coherence, and an optical resonance	82
6.3	Time-dependent EIT in the presence of unwanted phase modulation	91
6.4	Calculated sodium vapor absorption spectra with and without CPT	95
6.5	Calculated EIT and hyperfine coherence in sodium vapor	95
6.6	Calculated spatial evolution of the control fields and Raman scattered fields in sodium vapor	96
7.1	Experimental setup (schematic)	101
7.2	Experimental apparatus (photos)	102
7.3	Measuring the hyperfine relaxation rate (concept)	105
7.4	Measuring the ground hyperfine coherence relaxation rate (concept)	105
7.5	Typical hyperfine relaxation curves	108
7.6	Hyperfine relaxation rates vs. helium pressure	109

7.7	Net trapping ability vs. buffer gas pressure	109
7.8	Sodium single-field transmission spectra	111
7.9	Sodium two-field transmission spectra	112
7.10	Sodium two-field transmission spectra vs. helium pressure	113
7.11	Sodium Raman spectra showing EIT and CRS	114
7.12	CPT and four-wave mixing of the control fields (concept)	115
7.13	Frequency conversion of an AM optical signal	119
7.14	Frequency conversion of an FM optical signal	120
D.1	Screenshot of the user interface for numerical modelling	169
D.2	The “two-manifold” model	170

List of Symbols and Acronyms

α	absorption coefficient, 34
$ b\rangle$	bright state, 3
b_{eg}	branching ratio, 143
CPM	coherently prepared medium, 1
CPT	coherent population trapping, 2
CRS	coherent Raman scattering, 7
CW	continuous-wave (not pulsed or modulated), 6
χ	optical susceptibility, 33
$\tilde{\chi}$	atomic susceptibility, 48
$\tilde{\chi}_{12}$	Raman scattering susceptibility, 58
$ d\rangle$	dark state, 2
D	diffusion constant, 75
Δ	detuning of control fields from excited state(s), 2
$\bar{\Delta}$	normalized control field detuning, 19
Δ_{rms}	width of the distribution of optical Doppler shifts, 78

Δ_v	optical Doppler shift (change in Δ for velocity v), 78
Δ'	detuning of probe and signal fields from excited state(s), 36
δ	Raman detuning, 2
$\bar{\delta}$	normalized Raman detuning, 19
δ_{rms}	width of the distribution of Raman Doppler shifts, 80
E	excited level (multiplet), 46
\mathbf{E}, E	optical (electric) field amplitude, 17
EIA	electromagnetically induced absorption, 5
EIT	electromagnetically induced transparency, 4
η	total ground state population, 13
F	quantum number for total angular momentum, 54
$F, F' F''$	angular momentum numbers for states in $3S_{1/2}, 3P_{1/2}, 3P_{3/2}$ manifolds, 55
\vec{F}	“force” vector, points $\vec{\rho}$ toward the dark state, 19
$f(\tau)$	fraction of atoms that take longer than τ to leave the interaction region, 75
G	ground level (multiplet), 46
Γ_E	excited level population decay rate, 16
Γ_G	ground level (Raman) population relaxation rate, 16
Γ_{trans}	rate of transit of atoms in and out of interaction region, 74
$g(v)$	Maxwell velocity distribution, 78
γ_E	excited level coherence (or optical polarization) decay rate, 16
γ_G	ground level (Raman) coherence decay rate, 16

k	wavenumber, 33
Λ	“Lambda” system (2 ground states, 1 excited state, 2 fields), 2
$\Lambda\Lambda$	double- Λ system (two Λ systems with common ground states), 6
$\Lambda_{1y,2x}^{F'}$	sodium Lambda system formed by y - and x - polarized fields coupling the $F = 1$ and $F = 2$ ground levels, respectively, to excited level F' , 56, 60
l	mean free path, 74
λ	wavelength, 76
m	magnetic quantum number, 54
μ_{eg}	electric dipole matrix element, 17
$\check{\mu}_{eg}$	relative dipole matrix element, 48
\mathcal{N}	atom number density, 33
$\check{\mathcal{N}}$	number of atoms per cubic wavelength, 49
ν	frequency, 76
Ω	nominal Rabi frequency, 47
Ω_1, Ω_2	Rabi frequency of control fields in a Λ system, 17
Ω_{eg}	Rabi frequency (strength of coupling between a field and a pair of states), 17
Ω_x, Ω_y	nominal Rabi frequencies of x, y polarized fields in sodium experiments and simulations, 55
Ω_{2x}, Ω_{1y}	same as Ω_x, Ω_y , with emphasis that Ω_x (Ω_y) couples the $F = 2$ (1) level, 56
ω	angular frequency, 76
P	buffer gas pressure, 75

Φ	phase of ρ_{21} relative to the dark state phase, 30
\mathbf{p}, p	atomic dipole moment, 33
$\check{\mathbf{p}}$	normalized atomic dipole, 48
R	optical pumping rate coefficient, 16
\vec{R}	optical pumping vector (characterizes control fields), 15
ρ_{21}	ground state coherence (in a Raman system), 13
ρ	density matrix, 13
$\vec{\rho}$	Bloch's state vector, 13
s	Raman saturation parameter, 27
s	saturation parameter, 65
s_0	line-center value of s , 78
σ	cross section, 49, 74
\vec{T}	“torque” vector, turns $\vec{\rho}$ away from the dark state, 19
θ_R	polar angle of \vec{R} , 27
t_{trans}	transit time (time an atom spends in the interaction region), 74
u, v, w	Cartesian coordinates of $\vec{\rho}$, 13
\bar{v}	average speed of an atom, 74
v_{rms}	root-mean-square atomic velocity in one dimension, 78

Chapter 1

Introduction

It has long been known that light can alter the optical properties of a medium. That is, the coefficient which relates the electromagnetic field to the material response can depend on the electromagnetic field itself. In this sense the material is optically nonlinear. Generally, intense optical fields are needed to see nonlinear effects. Since the invention of the laser in the late 1950's, the subject of nonlinear optics has grown tremendously. There is an incredible variety of nonlinear phenomena ranging from self-action effects to light-by-light interactions. Many mechanisms of nonlinearity fall into one of two broad categories. There are processes in which light incoherently redistributes the material's electron population. These processes can be relatively strong. They lead to effects which include absorption saturation and the intensity-dependent refractive index. On the other hand, there are processes which induce virtual transitions in the material. These processes create small coherent oscillations in the material and are responsible for many wave mixing phenomena, including harmonic generation and sum/difference frequency mixing. These processes can be extremely fast (fs response times).

Over the past 10-15 years, however, it has been found that the multiple laser fields can interact in ways which put a medium into a strong superposition of quantum states. That is, the electrons are distributed coherently over two or more quantum states. In these *coherently prepared media*¹ (CPM), different optical transitions involving the mutually coherent states can interfere quantum

¹M. O. Scully and co-workers refer to such media as "phaseonium." While this term has some technical merit, and the advantage of conciseness, it sounds to me like something from a bad episode of *Star Trek*.

mechanically, resulting in dramatic changes to the optical response. Such changes are said to be “electromagnetically induced.” Since they often occur even with weak optical fields, very large nonlinear susceptibilities can be ascribed to CPM. Indeed, many nonlinear phenomena of interest (such as wave mixing) are greatly enhanced by quantum coherence. Electromagnetically induced nonlinearities can be either fast or slow; when they involve metastable states, the resulting spectral features can be extremely narrow (as small as 10’s of Hz or 10^{-11} nm). CPM have also been used to demonstrate novel phenomena such as propagation of light at a velocity of a few meters per second. A full overview of the applications of CPM will be given later in this chapter. But first it will be helpful to look more closely at the concept of coherent preparation and the context in which it developed.

1.1 Background

The first reported observation of coherent preparation of a medium was by Alzetta *et al.* [1]. They observed that the resonant fluorescence of a sodium vapor in the presence of two laser fields vanished when the frequency difference of the two lasers was exactly equal to the frequency difference of the ground hyperfine levels. The mechanism responsible for this effect was termed *coherent population trapping* (CPT) by Gray, Whitley, and Stroud [2]. They considered an excited state coupled by two fields to two ground states (a “ Λ ” system, Fig. 1.1a). Apart from relaxation processes, the probability amplitude of the excited state obeys the equation

$$\dot{c}_3 = \frac{i}{2}(\Omega_1 c_1 + \Omega_2 e^{i\delta t} c_2) e^{i\Delta t} \quad (1.1)$$

where c_1, c_2 are the probability amplitudes of the ground states, $\Omega_{1,2}$ are proportional to the amplitudes of the optical fields, Δ is the detuning of the first field from its transition, and δ is the difference between the ground state frequency separation and the beat frequency of the two lasers. When $\delta = 0$, there is a particular superposition of the ground states, namely the one with $c_2/c_1 = -\Omega_1/\Omega_2$, such that $\dot{c}_3 = 0$. This “dark state” $|d\rangle$, so named because it produces no fluorescence, is completely decoupled from the excited state and is transparent to the applied fields. The orthogonal

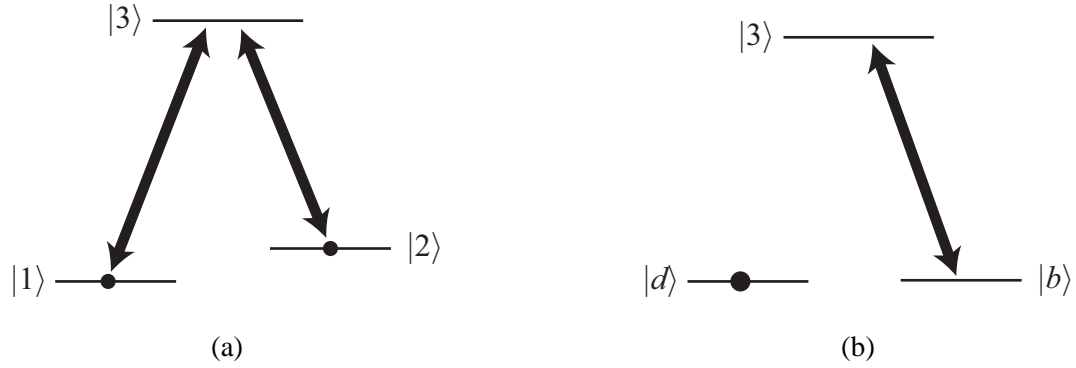


Figure 1.1: Coherent population trapping (CPT). (a) A Λ system. (b) The population is pumped into a superposition of the ground states, denoted $|d\rangle$ for “dark state”, that is uncoupled to the excited state. The atom becomes completely transparent to both fields.

superposition is coupled to the excited state and is called the “bright state” $|b\rangle$, Fig. (1.1b). The system always evolves into the dark state within a few radiative lifetimes, since any population which decays from the excited state into the dark state is not removed by optical excitation. The population is trapped in a coherent superposition of the ground states. The coherence between states $|1\rangle$ and $|2\rangle$ is $c_1 c_2^*$. The coherence is maximal in the sense that it is as large as possible for the given distribution of population (mathematically, its magnitude cannot exceed $\sqrt{|c_1|^2 |c_2|^2}$). In the case of balanced fields ($|\Omega_1| = |\Omega_2|$) the magnitude of the coherence reaches the ultimate maximum of $1/2$.

It is important to note that the vanishing absorption is not simply a result of saturation or optical Stark shifts of the transitions; it results from quantum interference between the two pathways for absorption. Quantum interference between multiple transitions is a very general phenomenon and has been studied for many years. Fano [3] found that the rate of ionization of an atom by an ultraviolet field exhibits interference effects when the ionization can occur both by direct excitation and by non-radiative transfer from an auto-ionizing state. Conversely, when two coherently excited states decay to a common lower state, the fluorescence exhibits a beat note at the frequency difference of the excited states, a phenomenon known as “quantum beats” [4, 5]. Cardimona, Raymer and Stroud [6] showed that if two transitions have the same dipole matrix element, they interact via spontaneous emission in such a way as to end up making equal but opposite contributions to the

atom's total dipole moment. This may be understood as coherent population trapping in the *excited* states: Although the field initially excites the symmetric superposition state, spontaneous emission moves the system to the antisymmetric superposition state which is decoupled from the total field consisting of the driving field and the radiation reaction field. As with coherent trapping in ground states, this dark state is stable and transparent to the field. Malcuit, Gauthier, and Boyd [7] observed suppression of amplified spontaneous emission due to four-wave mixing in sodium. In this case, the fields evolved upon propagation to the point where the probability amplitude of excitation by the pump field was exactly cancelled by the probability amplitude of excitation by the parametrically amplified fields.

The field of quantum coherent optics truly gained its identity and began to develop following a publication of Harris in 1990 [8]. Harris proposed a scheme² in which a strong “control” field drives a pair of unpopulated states (Fig. 1.2a), one of which ($|2\rangle$) is metastable. The surprising result is that if a probe field couples a populated state $|0\rangle$ to state $|1\rangle$, then no population appears in state $|1\rangle$; rather it appears in $|2\rangle$, where the probability amplitude of state $|2\rangle$ is directly proportional to the probe field. That is, the linear (1-photon) susceptibility of the probe vanishes, but the nonlinear (2-photon) susceptibility does not³. In fact, the probe absorption profile shows a narrow dip in the middle of the resonant absorption feature, while the coherence ρ_{20} shows a corresponding peak. The vanishing of the probe susceptibility prompted Harris to call this phenomenon *electromagnetically induced transparency* (EIT).

This transparency can be explained in much the same way as the transparency which occurs in the coherent population trapping scheme: the coherence between states $|0\rangle$ and $|2\rangle$ results in destructive interference between the probability amplitudes of transitions to the intermediate state $|1\rangle$. However, it is also possible to explain EIT using a rather different picture involving “dressed” states. One may say that the control field combines with the bare states $|1\rangle$ and $|2\rangle$ to form a pair of dressed states $|+\rangle$, $|-\rangle$ (Fig. 1.2b). The probe field then excites both of these states simultaneously.

²The scheme originally proposed by Harris was actually slightly more complicated; in Harris's scheme, state $|1\rangle$ is excited by two-photon absorption through a virtual intermediate state. I have chosen the simpler scheme shown in Fig. 1.2a in order to draw out the essence of the phenomenon.

³Note that in a real atom, the parity of states $|0\rangle$ and $|2\rangle$ would be such that a superposition of these states would have no dipole moment; but here it does no harm to pretend otherwise.

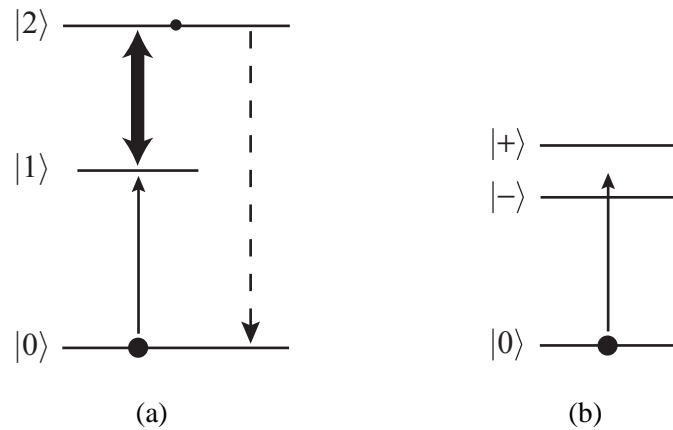


Figure 1.2: Electromagnetically induced transparency (EIT). (a) A strong field couples two unpopulated states, one of which is driven by a weak field. Remarkably, the system is coherently excited to state $|2\rangle$ rather than state $|1\rangle$, so that the medium becomes transparent to the probe beam while generating a new frequency component. (b) The transparency of the probe can be understood as a consequence of interference between dressed states created by the strong field.

As it happens, the dressed states couple to $|0\rangle$ with identical dipole matrix elements. Hence coherent population trapping in the dressed states occurs via the Cardimona-Raymer-Stroud mechanism, and the response at the probe frequency vanishes.

Electromagnetically induced transparency has now been studied both theoretically [8–13] and experimentally [11, 14–17] in systems with various numbers of levels and various coupling schemes. One should not get the impression that all quantum interference is destructive, however. Electromagnetically induced absorption (EIA) can occur in two-level systems when both levels are Zeeman multiplets and the upper level has a larger degeneracy than the lower level [18–21]. This occurs as a result of spontaneous transfer of coherence from the excited states to the ground states [22]. Coherent wave mixing can also produce a kind of EIA as photons are removed from one field and emitted into another (cf. §7.3). Electromagnetically induced features can also occur in two-state systems driven by strong polychromatic fields [23–27].

So far, the discussion has considered steady-state coherence in systems driven by continuous-wave (“CW”) fields. The dynamics of coherently prepared atomic systems (and associated optical

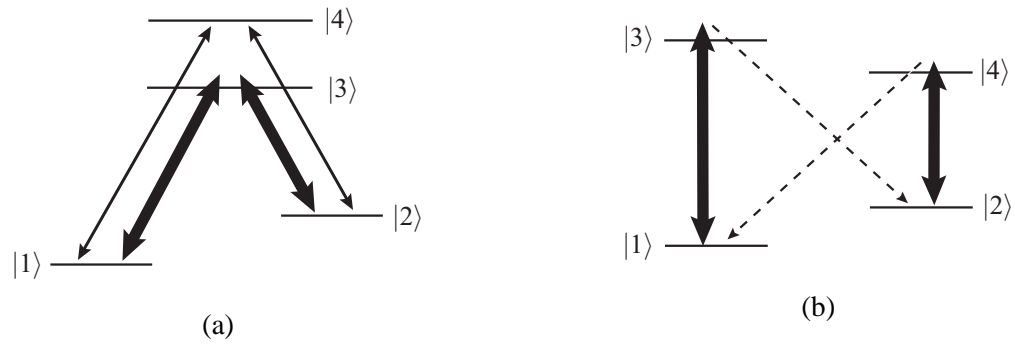


Figure 1.3: Other simple systems which exhibit quantum coherent effects. (a) The $\Lambda\Lambda$ system. (b) The “bow-tie” system. The applied control fields and spontaneously emitted signal and idler fields undergo strong four-wave mixing enhanced by EIT.

effects) have been studied as well. Λ , $\Lambda\Lambda$ (Fig. 1.3a) and “bow tie” systems (Fig. 1.3b) in particular have received much attention. Sudden turn-off or turn-on of the fields produces absorption transients which decay on a timescale of the spontaneous emission lifetime as the system fluoresces or is optically pumped into a new dark state [28–31]. The dark state can be prepared more quickly [on the time of the inverse Rabi frequency⁴ of the control field(s)], however, by adiabatically varying the fields [32, 33]. In Λ media, absorption of the bright state component of initially unmatched pulses leads, upon propagation, to matched pulses [34] whose fluctuations are correlated [35]. When one of the fields is much stronger than the other, phase squeezing [36] and extremely large dispersion [37] of the weak field results. CW beams propagating in bow-tie systems undergo four-wave mixing [38] and in counter-propagating geometries can experience mirrorless parametric oscillation [39, 40]. In phase conjugation geometries, the signal and conjugate fields are predicted to be strongly squeezed [41].

This brief review presents only a fraction the work which has been done in coherent atomic systems. The interested reader may consult [42–44] for a more extensive review of CPT, EIT, and related effects.

⁴See eqn. 2.7 for the definition of the Rabi frequency.

1.2 Applications

From the start, coherent preparation was seen as a way to greatly enhance the strength of nonlinear processes [8]. In the context of wave mixing it has led to efficient infrared upconversion [45, 46], efficient phase conjugation [47], coherent Raman scattering (CRS) [48–52], and control of phase-matching [53]. In certain schemes the dispersive and absorptive nonlinearities are greatly enhanced [54, 55] to the extent that measurable nonlinear effects occur with optical energies at the level of only a few photons per atomic cross section [56]. Such schemes are at the heart of recent proposals for photon-number-resolving detectors with extremely high quantum efficiency [57, 58]. Another application which spurred the development of coherent preparation was amplification (or lasing) without inversion [59–62]: by using quantum interference to eliminate absorption without disabling stimulated emission, EIT makes possible lasers that have extremely low thresholds. As coherent preparation and associated phenomena have become more widely recognized and understood over the past decade, many new applications have been proposed and/or developed. For example, coherent Raman features tend to be extremely narrowband, and some researchers are exploring the uses of such features in atomic clocks [63, 64] and for highly sensitive magnetometry [65–68]. Because these features are very narrow, they exhibit very steep dispersion; thus coherent preparation is seen by some as a mechanism for achieving and controlling extremely large changes in group velocity. Ultra-slow light [37, 69] is a promising technology for devices such as optical buffers and adjustable optical delays [70]. From a slightly different perspective, atomic coherence may be viewed as a degree of freedom capable of storing information, resulting in a number of schemes for “atomic memories” [71–75]. Still others see the ability to induce transparency or absorption as a mechanism for all-optical switching [76–80], which is of interest in optical communications and computing.

Although many workers have studied the use of coherent preparation in sum/difference frequency generation, the main concern in these studies has been efficiency—the total amount of power converted from one frequency to another. To my knowledge, the use of material coherence generated in this way to transfer *information* from one frequency band to another remains virtually unexplored (although similar ideas have recently been explored using traditional Raman scattering, e.g. [81]).

Recently, coherent Raman scattering was used to shift the center frequency of an incoherent light field, preserving the spectral power distribution in the process [82]. However, the light which is scattered by a material coherence can be expected to preserve both the amplitude and phase of each frequency component of the input field. If the scattering process has a flat, dispersionless frequency response, then a signal contained in the input field will appear in the scattered field. This technique has obvious application to telecommunications. Data expressed as phase or amplitude modulation at one wavelength could be transferred to a different wavelength.

Efficient, phase- and amplitude-preserving scattering could also be applied toward the characterization of supershort (sub-fs) X-ray pulses. While methods for characterizing ultrashort radiation in the visible regime are well-established, methods for characterizing ultrashort radiation in the ultraviolet or X-ray regime are still being developed. One visible-regime technique which could potentially be applied to X-rays is called SPIDER [83]. In this technique the complex amplitude of the pulse is extracted from a spectral shear interferogram, which is formed by interfering the pulse with a frequency-shifted copy of itself. Since nonlinear interactions involving X-rays are extremely weak, traditional wave-mixing schemes (such as sum frequency generation) are not capable of creating the needed frequency-shifted copy. But an X-ray could scatter off the coherence in a prepared medium with relatively high efficiency⁵, producing a copy of the pulse shifted by a visible or RF frequency and enabling the SPIDER technique (Fig. 1.4). As I will show in §3.3.2, the bandwidth of coherent scattering is as large as the bandwidth of the excited state or band. Thus coherent scattering into the continuum has the extremely large bandwidth needed for supershort pulse characterization.

1.3 Outline

The aim of my research over the past several years has been to understand coherent preparation of atomic vapors and to demonstrate the usefulness of coherent preparation for frequency shifting. In particular, a major goal was to demonstrate the transfer of phase and amplitude information from one frequency band to another with high efficiency, fidelity, and bandwidth. In the chapters which

⁵Since the material coherence can be as large as the population of electrons available for excitation, the scattering of the X-ray to a different frequency can occur with the efficiency of a linear process.

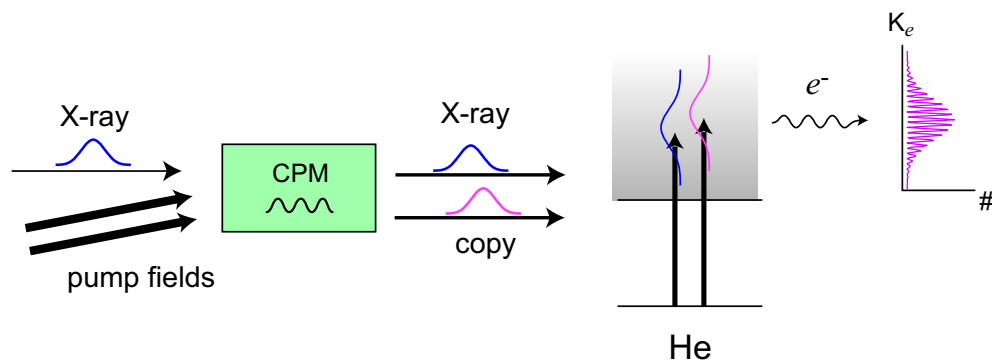


Figure 1.4: A proposal for ultrashort X-ray pulse characterization using coherent preparation, based on the SPIDER technique. An X-ray scatters off the coherence of a prepared medium, generating a frequency-shifted copy of itself. The two pulses interfere in the spectral domain, and the interferogram is reproduced in the kinetic energies of ionized helium. The complex amplitude of the original pulse may then be reconstructed from the interferogram.

follow, I report on my theoretical and experimental studies of coherent preparation.

In this work, the ideal coherent medium is modelled as a collection of Λ systems. Chapter 2 begins the discussion with a theoretical analysis of the Λ system. Solutions are obtained using a novel geometrical approach involving Bloch's vector and a Stokes-like vector. In Chapter 3, the model is used to understand optical phenomena that result from ground state coherence. Before turning to more complicated and realistic models, Chapter 4 briefly addresses the question of why a simple 2-state system does not make for a satisfactory coherent medium. The lessons learned in these chapters lay the foundation for Chapters 5 and 6, in which the phenomena of real atomic vapors are considered. Chapter 7 describes my experimental studies of hyperfine (spin) coherence in sodium vapor, including characterization of coherence, observation of quantum coherent optical effects, and a demonstration of frequency conversion of both phase and amplitude signals. The main text concludes in Chapter 8 with a summary and commentary on the findings of my research. There are also several appendices containing additional material which may be of interest to some readers. Appendices A, B, and C present formulas and results which are "known" but not frequently explained. As they were crucial to the development of my understanding of atom-light interactions,

I have included them here. Finally, Appendix D details the physical and mathematical theory behind the computer software I wrote to solve for the behavior of illuminated atomic systems.

Chapter 2

A Bloch-Vector Model of Raman Systems

Large coherences can be produced in systems with two or more ground states via the process of coherent population trapping. The simplest system of this type is the Λ system (see Fig. 1.1a). As we will see, maximal coherence builds up between the ground states when the beat note of the fields matches the frequency difference of the ground states. This phenomenon is often explained by viewing the system in a special basis: the population is optically pumped out of one superposition of the ground states (the “bright” state) into the orthogonal superposition (the “dark state”), which is uncoupled from the fields. However, this basis provides little conceptual or computational advantage if the fields are not exactly tuned to the ground state difference frequency or if the ground states are connected by more than one absorption-emission transition (for example, if there are multiple pairs of fields coupling to multiple excited states). It would be useful, then, to find another representation which facilitates analysis of such systems by transcending the issue of which basis to use.

In this chapter, I develop a vector model of Raman systems and use it to obtain general solutions for the 3-state (Λ) system. This model uses a Bloch vector to describe the ground states and a Stokes-like vector to describe each pair of fields. Because this model is geometrical, it allows one to visualize Raman systems and their solutions more readily. Algebraically, it leads to concise equations of motion and solutions. It is especially useful when a system cannot be simplified by

expressing it in terms of a dark/bright basis.

I note that other authors have described 3-state systems using 2-state Bloch equations [84–87]. However, to my knowledge the solutions given here and in Chapter 3 are novel in their form and/or the method by which they are obtained.

2.1 The Vector Representation of Raman Systems

Raman scattering refers to scattering of a field by a low-frequency mode of a medium, typically a rotational or vibrational mode of a molecule. In the quantum view of scattering, the molecule makes a transition from one rovibrational state to another by absorbing an incident photon and then emitting a photon whose frequency is shifted from that of the incident photon by the frequency difference of the initial and final states. This frequency is the *Raman frequency*. A similar process can occur in atoms. For example, a two-photon process may take an atom from one hyperfine level to another within a given electronic orbital, resulting in oscillations of the nuclear and electronic spins. These ground hyperfine states are typically very long-lived, with the consequence that very large spin oscillations (i.e. very large hyperfine coherences) can build up if the atom is driven by two fields separated by the Raman frequency.

For what follows, a Raman system may be generally defined as a system consisting of two low-energy states coupled to a pair (or pairs) of fields, where the beat frequency of each field pair is close to the Raman frequency (Fig. 2.1). The difference δ between the beat frequency and the Raman frequency will be called the *Raman detuning*. The simplest Raman system is a Λ system, in which two ground states are coupled by two optical transitions to a common excited state. The next simplest Raman system is the double-lambda ($\Lambda\Lambda$) system, which has two excited states and four optical transitions. One could also imagine Raman systems in which the ground states are excited by pairs of ultraviolet (UV) fields or X-rays to a continuum of excited states.

The optical properties of a Raman system are determined primarily by the distribution of popu-

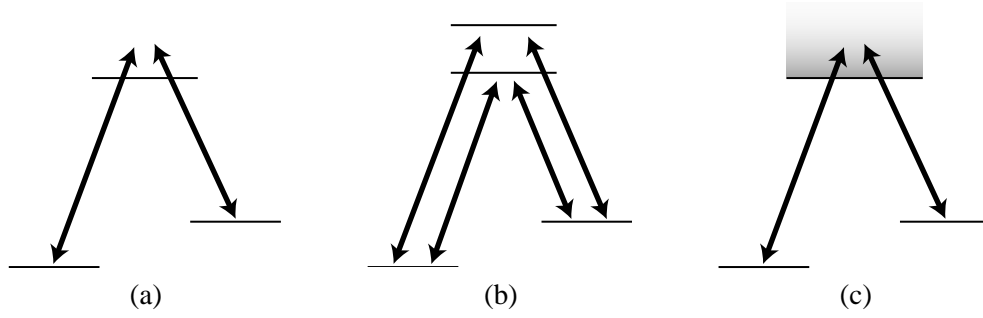


Figure 2.1: Example Raman systems. (a) The Λ system. (b) The $\Lambda\Lambda$ system. (c) Joint excitation to the continuum.

lation in the two ground states, which may be characterized by the 2×2 density matrix

$$\rho = \begin{pmatrix} \rho_{11} & \rho_{12} \\ \rho_{21} & \rho_{22} \end{pmatrix}. \quad (2.1)$$

Alternatively, the ground states may be characterized by the vector

$$\vec{\rho} \equiv \begin{pmatrix} u \\ v \\ w \end{pmatrix} = \begin{pmatrix} 2 \operatorname{Re} \rho_{21} \\ 2 \operatorname{Im} \rho_{21} \\ \rho_{22} - \rho_{11} \end{pmatrix} \quad (2.2)$$

and an additional quantity $\eta \equiv 1 - \rho_{33}$ which gives the total population of the ground states. The unit vectors associated with the coordinates u, v, w will be denoted $\hat{u}, \hat{v}, \hat{w}$. The vector $\vec{\rho}$, originally developed to describe spin- $\frac{1}{2}$ systems, is widely known as Bloch's vector. Under conditions of weak optical excitation, $\eta \approx 1$ and $\vec{\rho}$ alone is sufficient to characterize the ground states.

Several facts concerning the Bloch vector are noteworthy:

- All possible states are contained within a sphere of unit radius.
- Points directly opposite one another on the surface of the sphere correspond to orthogonal states. That is, each diameter defines a basis.

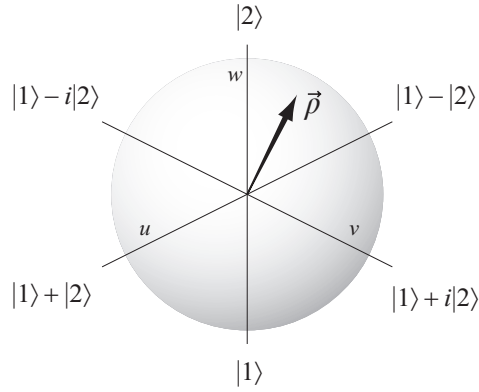


Figure 2.2: The Bloch sphere. Each point in the sphere represents a possible density matrix for the two ground states. Points on the surface of the sphere describe pure states, a few of which are labelled. The ground state inversion is given by the projection of $\vec{\rho}$ onto the north-south axis. The ground state coherence is given by the projection of $\vec{\rho}$ onto the equatorial plane.

- Points along a diameter correspond to incoherent mixtures of the two states connected by the diameter. The “inversion” (population difference of the two states) is given by the projection of $\vec{\rho}$ on the diameter.
- The origin corresponds to an equal (half and half) incoherent mixture of any pair of orthogonal states.

Fig. 2.2 shows the Bloch sphere and its relation to various combinations of the ground states. The points $\langle u, v, w \rangle = \langle 0, 0, 1 \rangle$ and $\langle 0, 0, -1 \rangle$ correspond to the bare states $|1\rangle$ and $|2\rangle$ respectively. Hence the w (north-south) axis defines the bare state basis. Two other notable bases are defined by the u and v axes. The u axis intersects the unit sphere at $\langle \pm 1, 0, 0 \rangle$ which correspond to the states $(|1\rangle \pm |2\rangle)/\sqrt{2}$. Similarly, the v axis intersects the unit sphere at $\langle 0, \pm 1, 0 \rangle$ which correspond to the states $(|1\rangle \pm i|2\rangle)/\sqrt{2}$. Therefore the physical meaning of $\vec{\rho}$ is as follows:

- The inversion $\rho_{22} - \rho_{11}$ is given by the projection of $\vec{\rho}$ onto the north-south axis.
- The coherence ρ_{21} is given by (half) the projection of $\vec{\rho}$ onto the equatorial plane.

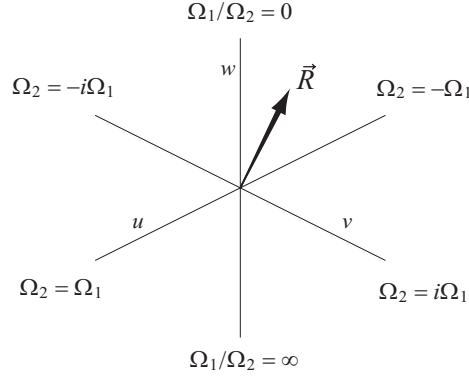


Figure 2.3: The optical pumping vector \vec{R} , which represents the pair of fields. Different directions describe different relative intensities or phases of the fields. The length of the vector is the maximum rate at which the fields can pump population to the excited state.

Just as a 3-vector and a scalar characterize the ground states, a 3-vector and scalar can characterize each pair of optical fields¹ (Fig. 2.3). Suppose that a pair of fields couples states $|1\rangle$ and $|2\rangle$ respectively to an excited state e . Let Ω_1, Ω_2 be the coupling amplitude of each field. I define the *optical pumping vector* as

$$\vec{R} \equiv \begin{pmatrix} R_u \\ R_v \\ R_w \end{pmatrix} \equiv \frac{1}{4} \frac{\gamma_E}{\Delta^2 + \gamma_E^2} \begin{pmatrix} 2 \operatorname{Re} \langle \Omega_2^* \Omega_1 \rangle \\ 2 \operatorname{Im} \langle \Omega_2^* \Omega_1 \rangle \\ |\Omega_2|^2 - |\Omega_1|^2 \end{pmatrix} \quad (2.3)$$

where $\langle \dots \rangle$ denotes an ensemble average (allowing for mutually incoherent fields), Δ is the detuning of the fields from the excited state, and γ_E is the decoherence rate of the excited state. (More generally γ_E is the decoherence rate of the atomic dipole moment, or the half-width of the spectral

¹Alternatively we could combine the 3-vector components and the scalar into a 4-vector. This 4-vector would essentially be the Stokes vector, except that in this case the field components refer to two different frequency modes rather than two different polarizations of the same spatial mode. However, in using 4-vectors we would lose the ability to visualize the problem easily, which is a primary motivation of this approach. Furthermore, we will find that the problem can be expressed very naturally in terms of 3 vectors.

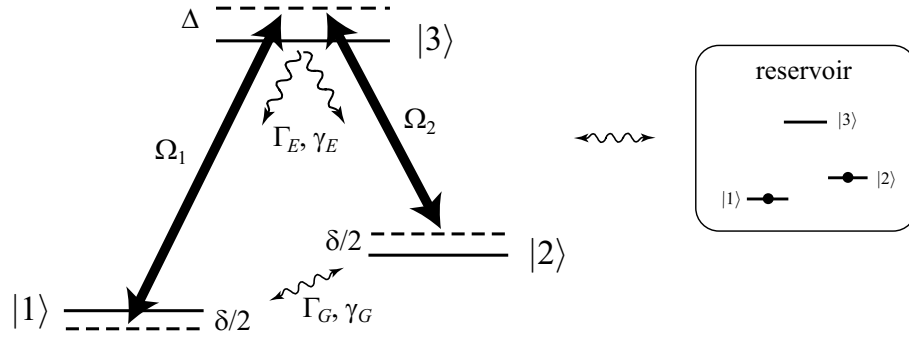


Figure 2.4: Schematic of the 3-state Raman system analyzed in this chapter. *Notation:* Ω_1, Ω_2 , the Rabi frequencies of the fields; Δ , the optical (single-field) detuning; δ , the Raman detuning; Γ_E, γ_E , the excited state population and coherence decay rates; Γ_G, γ_G the population and coherence decay rates for the ground states. The relaxation rates are phenomenological parameters representing a variety of contributions, including interaction or exchange with a thermalized reservoir (ensemble relaxation).

line.) This vector has units of a rate, and is closely related to the *optical pumping rate*

$$R \equiv \frac{1}{4} \frac{\gamma_E}{\Delta^2 + \gamma_E^2} \left(|\Omega_1|^2 + |\Omega_2|^2 \right). \quad (2.4)$$

If the two fields are mutually coherent, then the length of \vec{R} is R ; otherwise, $|\vec{R}| < R$. Physically, $2R$ is the rate at which the atom would be excited in the absence of coherence and saturation.

2.2 The Vector Equation of Motion

The important physics of coherent (and incoherent) population trapping is demonstrated in a simple 3-state Λ system (Fig. 2.4). In the absence of relaxation mechanisms, the equation of motion for the density matrix of this system is

$$\frac{d}{dt} \rho = -\frac{i}{\hbar} [\mathbf{H}, \rho] \quad (2.5)$$

where, in a suitably chosen rotating frame,

$$\mathbf{H} = \hbar \begin{pmatrix} \frac{1}{2}\delta & 0 & \frac{1}{2}\Omega_1^* \\ 0 & -\frac{1}{2}\delta & \frac{1}{2}\Omega_2^* \\ \frac{1}{2}\Omega_1 & \frac{1}{2}\Omega_2 & -\Delta \end{pmatrix}. \quad (2.6)$$

The coupling constants Ω_1, Ω_2 are known as the *Rabi frequencies* of the fields. In general, the Rabi frequency of a field \mathbf{E} that couples a state $|g\rangle$ to a higher state $|e\rangle$ is

$$\Omega_{eg} \equiv \frac{2\langle e|(-e\mathbf{r})|g\rangle \cdot \mathbf{E}}{\hbar}. \quad (2.7)$$

The quantity $\boldsymbol{\mu}_{eg} \equiv \langle e|(-e\mathbf{r})|g\rangle$ is the *electric dipole matrix element*. For the Λ system we write $\Omega_j = (2\boldsymbol{\mu}_{3j} \cdot \mathbf{E}_j)/\hbar$ for $j = 1, 2$.

Relaxation processes contribute additional terms to eqn. (2.5). Formal methods exist for obtaining such terms (see Appendix C), but here they may be regarded as phenomenological terms. With such terms included, the elements of ρ are governed by

$$\dot{\rho}_{11} = \frac{1}{2}\Gamma_E \rho_{33} - \Gamma_G (\rho_{11} - \rho_{11}^{\text{fsv}}) - \text{Im}(\Omega_1^* \rho_{31}) \quad (2.8)$$

$$\dot{\rho}_{22} = \frac{1}{2}\Gamma_E \rho_{33} - \Gamma_G (\rho_{22} - \rho_{22}^{\text{fsv}}) - \text{Im}(\Omega_2^* \rho_{32}) \quad (2.9)$$

$$\dot{\rho}_{21} = (i\delta - \gamma_G) \rho_{21} + \frac{i}{2}\Omega_2^* \rho_{31} - \frac{i}{2}\Omega_1 \rho_{32}^* \quad (2.10)$$

$$\dot{\rho}_{33} = -\Gamma_E \rho_{33} + \text{Im}(\Omega_1^* \rho_{31}) + \text{Im}(\Omega_2^* \rho_{32}) \quad (2.11)$$

$$\dot{\rho}_{31} = (i(\Delta + \delta/2) - \gamma_E) \rho_{31} + \frac{i}{2}\Omega_1(\rho_{11} - \rho_{33}) + \frac{i}{2}\Omega_2 \rho_{21} \quad (2.12)$$

$$\dot{\rho}_{32} = (i(\Delta - \delta/2) - \gamma_E) \rho_{32} + \frac{i}{2}\Omega_2(\rho_{22} - \rho_{33}) + \frac{i}{2}\Omega_1 \rho_{21}^*. \quad (2.13)$$

The decay rates represent multiple contributions. For example, the excited state population decay rate Γ_E includes spontaneous emission as well as exchange of the atom with an unexcited atom from a reservoir. γ_E is as defined before. (For these quantities I denote the excited state with an “E” instead of a “3”, so that the final results will appear in a more general and physically meaningful form.) Γ_G and γ_G are the population relaxation rate and mutual decoherence rate of the ground

states.

ρ_{11}^{rsv} and ρ_{22}^{rsv} are the ground state occupancies of atoms in the reservoir. Assuming that the reservoir is in thermal equilibrium, the reservoir atoms are in an incoherent mixture of states, where the occupancy ρ_{jj} of state j is proportional to the Boltzmann factor $\exp(-\hbar\omega_j/k_B T)$. In a hot medium (room temperature qualifies as “hot”), $k_B T/\hbar$ is much larger than a typical Raman frequency and much smaller than a typical optical frequency; thus in a thermalized atom, the population is equally distributed among the ground states: $\rho_{11}^{\text{rsv}} = \rho_{22}^{\text{rsv}} = 1/2$.

The strategy for realizing the vector model is to eliminate the matrix elements involving the excited state $|3\rangle$ and express the remaining equations in terms of $\vec{\rho}$ and \vec{R} . If $|\Delta| \gg \Omega_1, \Omega_2$ so that ρ_{31} and ρ_{32} reach equilibrium rapidly, or if we restrict ourselves to steady state analysis, we may take $\dot{\rho}_{31} = \dot{\rho}_{32} \approx 0$ and obtain

$$\rho_{31} \approx \frac{\frac{i}{2}\Omega_1(\rho_{11} - \rho_{33}) + \frac{i}{2}\Omega_2\rho_{21}}{D} \quad (2.14)$$

$$\rho_{32} \approx \frac{\frac{i}{2}\Omega_2(\rho_{22} - \rho_{33}) + \frac{i}{2}\Omega_1\rho_{21}^*}{D'} \quad (2.15)$$

where $D \equiv \gamma_E - i(\Delta + \delta/2)$ and $D' \equiv \gamma_E - i(\Delta - \delta/2)$. At this point we assume that the Raman detuning δ is small compared to the characteristic rate of the optical transitions, that is $|\delta| \ll |\gamma_E - i\Delta|$. This allows us to make the approximation $D' \approx D \approx \gamma_E - i\Delta$, which simplifies the subsequent algebra considerably. This is not a restrictive assumption, since coherent effects (which are the subject of interest) only occur when δ is small; when δ is large, the ground state coherence will be small and the system can be analyzed with rate equations. If we make the additional assumptions $\gamma_G = \Gamma_G$ (i.e. the ground states decohere via depopulation alone) then eqns. (2.8)–(2.13) can be rewritten as

$$\frac{d}{dt}\vec{\rho} = \left(\delta\hat{w} - \frac{\Delta}{\gamma_E}\vec{R} \right) \times \vec{\rho} - (R + \gamma_G)\vec{\rho} - (1 - 3\rho_{33})\vec{R} \quad (2.16)$$

$$\frac{d}{dt}\rho_{33} = -\Gamma_E\rho_{33} + \left(\vec{\rho} \cdot \vec{R} + (1 - 3\rho_{33})R \right). \quad (2.17)$$

Each term above describes a different physical process that influences the ground states:

- $-\gamma_G \vec{\rho}$ describes the relaxation of the system to the thermal state.
- $\delta \hat{w} \times \vec{\rho}$ accounts for detuning from the Raman frequency. Its effect is to rotate $\vec{\rho}$ about the w axis. It is the only term which breaks the rotational symmetry of the model.
- $-\frac{\Delta}{\gamma_E} \vec{R} \times \vec{\rho}$ accounts for detuning from the optical (single photon) transition frequency. Its effect is to rotate $\vec{\rho}$ about \vec{R} .
- The terms $-R\vec{\rho} - (1 - 3\rho_{33})\vec{R}$ and $\vec{\rho} \cdot \vec{R} + (1 - 3\rho_{33})R$ describe optical pumping. Since these terms are largest when $\vec{\rho} \approx \vec{R}/R$ and smallest when $\vec{\rho} \approx -\vec{R}/R$, these two states are interpreted as the bright state and dark states, respectively.
- $\Gamma_E \rho_{33}$ describes population transfer from the excited state to the ground states via spontaneous emission and by ensemble relaxation.

2.3 The Steady-State Equation and General Solution

The steady-state equation for $\vec{\rho}$ can be written in the extremely simple form

$$\vec{\rho} - \vec{T} \times \vec{\rho} = (1 - 3\rho_{33})\vec{F} \quad (2.18)$$

where

$$\vec{F} \equiv -\frac{\vec{R}}{R + \gamma_G}, \quad (2.19)$$

$$\vec{T} \equiv \delta \hat{w} - \bar{\Delta} \frac{\vec{R}}{R + \gamma_G}, \quad (2.20)$$

and

$$\bar{\delta} \equiv \frac{\delta}{R + \gamma_G}, \quad \bar{\Delta} \equiv \frac{\Delta}{\gamma_E}. \quad (2.21)$$

\vec{F} is a “force” vector which determines the primary direction and magnitude of $\vec{\rho}$. \vec{F} is antialigned with \vec{R} , and therefore its orientation is determined entirely by the amplitudes of the two fields. It reaches unit length as R becomes much greater than γ_G . For vanishing δ and Δ , $\vec{\rho}$ is

aligned with \vec{F} . \vec{T} is a “torque” vector which rotates $\vec{\rho}$ away from \vec{F} when $\delta \neq 0$. Its first term, $\bar{\delta}\hat{w}$, is the only term which breaks the rotational symmetry of the model. It expresses the fact that the Raman detuning is defined in the bare basis.

Eqn. (2.18) and the steady-state scalar equation for ρ_{33} can be solved independently. This is so because $\vec{\rho}$ scales directly with $1 - 3\rho_{33}$; that is, $\vec{\rho} = (1 - 3\rho_{33}) \vec{\rho}|_{\eta=1}$. The steady-state solution of eqn. (2.17) may then be written as

$$0 = \Gamma_E \rho_{33} - (1 - 3\rho_{33}) \left(R + \vec{R} \cdot \vec{\rho}|_{\eta=1} \right). \quad (2.22)$$

Rearranging (2.22) gives

$$\rho_{33} = \frac{R + \vec{R} \cdot \vec{\rho}|_{\eta=1}}{\Gamma_E + 3 \left(R + \vec{R} \cdot \vec{\rho}|_{\eta=1} \right)}. \quad (2.23)$$

The solution of (2.18) can be obtained readily by simple vector manipulations, yielding

$$\vec{\rho} = (1 - 3\rho_{33}) \left(\vec{F} + \frac{\vec{T} \times \vec{F} + \vec{T} \times (\vec{T} \times \vec{F})}{1 + |\vec{T}|^2} \right). \quad (2.24)$$

The three vector contributions to $\vec{\rho}$ are shown in Figure 2.5. The first contribution, $\vec{F} = -\vec{R}/(R + \gamma_G)$, places $\vec{\rho}$ near the dark state $-\vec{R}/R$. The second contribution, $\vec{T} \times \vec{F}$, is proportional to δ and shifts the phase of ρ_{21} . The third contribution, $\vec{T} \times (\vec{T} \times \vec{F})$, shifts the inversion by an amount proportional to $\delta\Delta$. Eqn. (2.24) can be written more explicitly as

$$\vec{\rho} = (1 - 3\rho_{33}) \left[\vec{F} + \frac{\bar{\delta} (\hat{w} \times \vec{F}) + \bar{\delta}^2 (\hat{w} \times (\hat{w} \times \vec{F})) + \bar{\delta}\bar{\Delta} (\vec{F} \times (\hat{w} \times \vec{F}))}{1 + \bar{\delta}^2 + \bar{\Delta}^2 F^2 + 2\bar{\delta}\bar{\Delta} (\hat{w} \cdot \vec{F})} \right]. \quad (2.25)$$

I note that dotting (2.18) with $\vec{\rho}/\rho$ yields $\rho = (1 - 3\rho_{33})F \cos \phi$, where ϕ is the angle between $\vec{\rho}$ and \vec{F} . This is the equation of a sphere whose surface touches the origin. That is, *all solutions for a given value of $(1 - 3\rho_{33})\vec{F}$ lie on a sphere whose diameter is the vector $(1 - 3\rho_{33})\vec{F}$* . By dotting eqn. (2.18) with $\hat{w} - \bar{\Delta}\hat{w} \times \vec{F}$, it can be shown that the solutions are constrained to a plane which is independent of δ . Therefore, as δ is varied, $\vec{\rho}$ must trace out the intersection of a plane with a sphere: a circle. Some solution families are shown in Figs. 2.6, 2.7. At Raman resonance

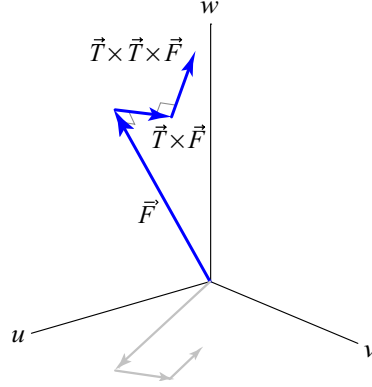


Figure 2.5: The contributions to the steady-state value of $\vec{\rho}$ (eqn. 2.24).

($\delta = 0$), $\vec{\rho} = (1 - 3\rho_{33})\vec{F}$. For $R \gg \gamma_G$, this state coincides with the dark state $-\vec{R}/R$; $|\vec{\rho}|$ is close to 1, and the ground state coherence (the length of $\vec{\rho}$ in the equatorial plane) is maximal. For symmetric excitation ($|\Omega_1| = |\Omega_2|$, Fig. 2.6), the population is evenly split between the two ground states and $\vec{\rho}$ lies in the equatorial plane. For highly asymmetric excitation ($|\Omega_1| \gg |\Omega_2|$, Fig. 2.7), $\vec{\rho}$ lies near the north or south pole. As δ varies from 0, the magnitude of the coherence decreases and the phase of the coherence (the angle of $\vec{\rho}$ in the equatorial plane) deviates from the dark state phase, i.e. the phase which leads to destructive interference of absorption. If $\Delta = 0$, and the fields are not too strong, then varying the Raman detuning does not alter the ground state inversion. However, if $\Delta \neq 0$, the circles are tilted from horizontal: as δ changes, one field tunes closer to the excited state than the other and the population shifts toward the ground state which is less resonantly coupled.

The solutions for strong fields are not circular, but elliptical. This can be understood as follows: As δ moves away from zero, the ground state coherence decreases and the two absorption pathways interfere less destructively. Because the fields are strong, a significant amount of optical excitation occurs. Depletion the ground state population forces the state vector to shrink, effectively stretching the circles toward the origin.

I now examine the solutions in some specific cases.

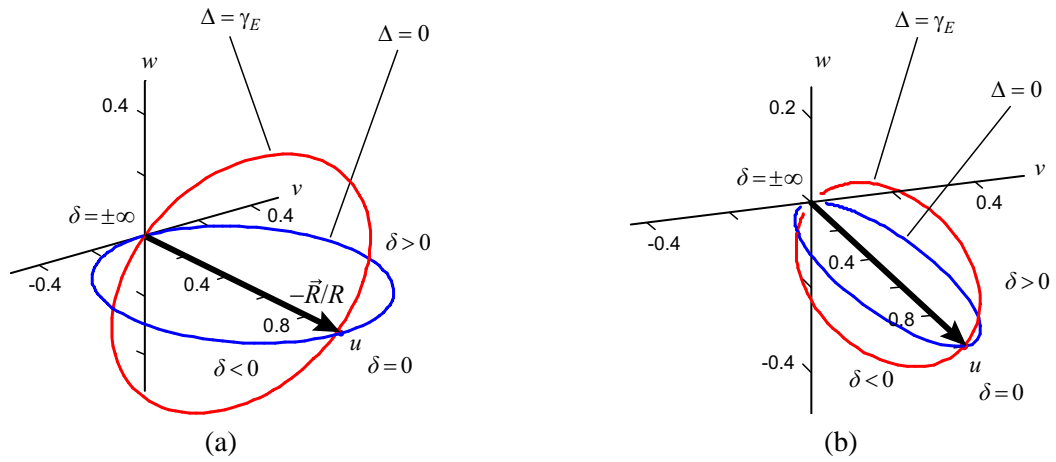


Figure 2.6: Representative steady-state solutions of the Bloch vector equation as a function of Raman detuning δ , in the case of balanced fields ($\Omega_1 = -\Omega_2$). The black arrow points to the dark state. (a) Weak field solutions. (b) Strong field solutions.

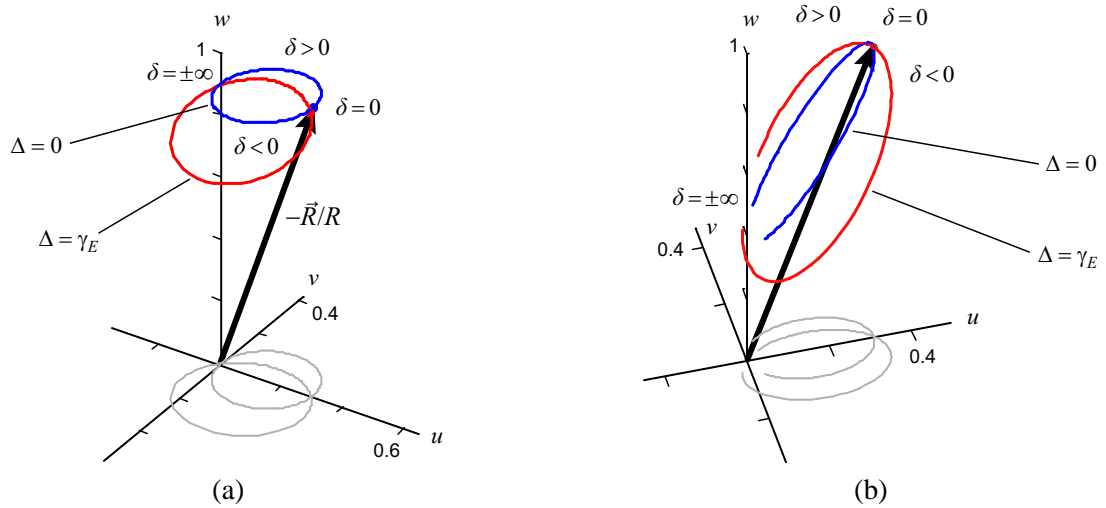


Figure 2.7: Representative steady-state solutions of the Bloch vector equation as a function of Raman detuning δ , in the case of imbalanced fields ($\Omega_1 = -5\Omega_2$). (a) Weak field solutions. (b) Strong field solutions.

2.4 Steady-State Solutions for Special Cases

2.4.1 Raman resonance

With $\delta = 0$, eqn. (2.18) reduces to $\vec{\rho} = (1 - 3\rho_{33})\vec{F}$. Now, a desirable operating condition is that $\gamma_G, \Gamma_G \ll \Gamma_E$. Under such conditions, it can be shown that

$$\vec{\rho} \simeq -\frac{\vec{R}}{R + \gamma_G} \quad (2.26)$$

$$\rho_{33} \simeq \frac{\gamma_G}{\Gamma_E} \frac{R}{R + \gamma_G}. \quad (2.27)$$

For $R \ll \gamma_G$, $\vec{\rho} \approx 0$; the system remains in its thermalized condition (incoherent mixture of ground states). For $R \gg \gamma_G$, $\vec{\rho}$ approaches the dark state $-\vec{R}/R$. The excited state population saturates at the small value γ_G/Γ_E . This is to be contrasted with the value of $1/3$ that is obtained with two mutually incoherent fields.

2.4.2 Incoherent fields

For mutually incoherent fields, $R_u = R_v = 0$. Then \vec{T} , \vec{F} , and $\vec{\rho}$ all lie along the w axis, and we again have the simple solution $\vec{\rho} = (1 - 3\rho_{33})\vec{F}$, regardless of δ and Δ . The new algebraic feature is that R is not equal to $|\vec{R}|$ ($= |R_w|$). We find

$$\vec{\rho}\Big|_{\eta=1} = -\frac{R_w}{R + \gamma_G} \hat{w}, \quad (2.28)$$

$$R + \vec{R} \cdot \vec{\rho}\Big|_{\eta=1} = R - \frac{R_w^2}{R + \gamma_G}. \quad (2.29)$$

Again taking $\gamma_G, \Gamma_G \ll \Gamma_E$, the solutions are

$$\vec{\rho} = -\frac{\Gamma_E (R_2 - R_1)}{(\gamma_G + R_1 + R_2)\Gamma_E + 12R_1R_2} \hat{w} \quad (2.30)$$

$$\rho_{33} = \frac{(R_1 + R_2)\gamma_G + 4R_1R_2}{(\gamma_G + R_1 + R_2)\Gamma_E + 12R_1R_2} \quad (2.31)$$

where R_j is defined according to eqn. (2.4) with Ω_j in place of $|\Omega_1|^2 + |\Omega_2|^2$. At small R_1, R_2 , eqns. (2.30) and (2.31) reduce to eqns. (2.26) and (2.27). As $R_1, R_2 \rightarrow \infty$, $\vec{\rho} \rightarrow 0$ and $\rho_{33} \rightarrow \frac{1}{3}$. These results are the same as what is obtained from a rate treatment of a 3-level system.

2.4.3 Raman-Detuned Fields

Consider again coherent fields, but suppose now that $\bar{\delta}$ is very large². Then

$$\vec{\rho}\Big|_{\eta=1} \approx \vec{F} + \hat{w} \times (\hat{w} \times \vec{F}) = \hat{w}(\hat{w} \cdot \vec{F}) = -\frac{R_w}{R + \gamma_G} \hat{w}, \quad (2.32)$$

$$R + \vec{R} \cdot \vec{\rho}\Big|_{\eta=1} = R - \frac{R_w^2}{R + \gamma_G}. \quad (2.33)$$

These expressions are the same as those we just obtained for incoherent fields, eqns. (2.28) and (2.29). It follows that solutions $\vec{\rho}$ and ρ_{33} will also be the same. We conclude that *at large Raman detuning, mutually coherent fields produce the same effect as mutually incoherent fields.*

2.5 The Equation of Motion for $\vec{\rho}$ in a General Raman System

We have derived the equations of motion for a three-level system with two fields. Provided that the excitation remains small ($\eta \simeq 1$), we can generalize (2.16) and (2.17) to describe a system with multiple excited states and multiple pairs of fields. Let n index the Raman transitions, with corresponding quantities \vec{R}_n , R_n , and Δ_n . (The Raman detuning δ must be the same for all pairs of fields.) Then eqns. (2.16) and (2.17) generalize to

$$\frac{d}{dt} \vec{\rho} \simeq \left(\delta \hat{w} - \sum_n \frac{\Delta_n}{\gamma_E} \vec{R}_n \right) \times \vec{\rho} - \left(\sum_n R_n + \Gamma \right) \vec{\rho} - \sum_n \vec{R}_n + \Gamma \vec{\rho}^{\text{sv}}. \quad (2.34)$$

$$\frac{d}{dt} \rho_{ee} \simeq \Gamma_E \rho_{ee} - \left(\vec{\rho} \cdot \sum_n \vec{R}_n + \sum_n R_n \right) \quad (2.35)$$

for each excited state e . Eqns. (2.24) and (2.23) remain valid if one replaces $\Delta \vec{R}$ in eqn. (2.20) with $\sum_n \Delta_n \vec{R}_n$ and then replaces all remaining occurrences of R and \vec{R} with $\sum_n R_n$ and $\sum_n \vec{R}_n$.

²With this supposition, we are in danger of violating the condition $|\delta| \ll |\gamma_E + i\Delta|$ that justifies the approximation leading to (2.16). Nevertheless the model makes a useful prediction in this regime.

respectively.

2.6 Summary

A novel geometric model was developed for simple Raman systems involving two ground states. Under the conditions of adiabaticity and near-Raman-resonance, the dynamics of a 3-state Raman system can be described by an ordinary vector differential equation involving Bloch's vector to represent the ground states of the system and a Stokes-like vector that represents the fields. The steady-state solutions form circles or ellipses as functions of the Raman detuning, showing how the ground state population and coherence vary in the vicinity of the Raman resonance. It was also shown how the model may be extended to describe Raman systems with multiple excited states.

Chapter 3

Coherent Nonlinear Optics in Λ and $\Lambda\Lambda$ Systems

Raman systems, such as the Λ and $\Lambda\Lambda$ system, can develop a large ground state coherence when the beat frequency of the driving fields matches the Raman frequency. This coherence produces a quantum interference between the two absorption pathways which generally leads to cancellation of the absorption. Electromagnetically induced transparency is just one example of how quantum coherence can mediate strong interactions between optical fields. Other nonlinear optical processes, such as four-wave mixing and Raman scattering, can occur with high efficiency (approaching that of a linear process) as a result of large quantum coherence in a medium. Though simple, 3- and 4-state systems exhibit a rich variety of coherent effects and can be used to explain a great deal of the behavior of more complicated media such as alkali vapors. Studying these simple systems will reveal a number of basic physical phenomena and scaling laws that will serve as a foundation for the analysis of coherence in sodium vapor, which is taken up in later chapters.

3.1 The Ground State Coherence

In a study of effects arising from quantum coherence, the first questions to ask are, How much coherence can be achieved? What parameters determine its phase and magnitude? According to

eqn. (2.2), the coherence is determined by the u and v components of $\vec{\rho}$:

$$\rho_{21} = \frac{1}{2}(\hat{u} + i\hat{v}) \cdot \vec{\rho}. \quad (3.1)$$

Without loss of generality we may take the relative phase the two fields to be such that $\Omega_2^*\Omega_1$ is real. Then the optical pumping vector \vec{R} lies in the plane $v = 0$ and we may write $\vec{F} = -F(\hat{u} \sin \theta_R + \hat{v} \cos \theta_R)$ where $F = |\vec{F}|$ and

$$\theta_R = 2 \tan^{-1} \frac{|\Omega_1|^2}{|\Omega_2|^2} \quad (3.2)$$

is the polar angle of \vec{R} . ($\theta_R = 0$ for $\Omega_1 = 0$, $\theta_R = \pi$ for $\Omega_2 = 0$, and $\theta_R = \pi/2$ for $|\Omega_1| = |\Omega_2|$.)

Using the result (2.25), we have

$$\hat{u} \cdot \vec{\rho} = -F \sin \theta_R \left[\frac{1 + \bar{\Delta}^2 F^2 - \bar{\delta} \bar{\Delta} F \cos \theta_R}{1 + \bar{\delta}^2 + \bar{\Delta}^2 F^2 - 2\bar{\delta} \bar{\Delta} F \cos \theta_R} \right] \quad (3.3)$$

$$\hat{v} \cdot \vec{\rho} = -F \sin \theta_R \left[\frac{\bar{\delta}}{1 + \bar{\delta}^2 + \bar{\Delta}^2 F^2 - 2\bar{\delta} \bar{\Delta} F \cos \theta_R} \right] \quad (3.4)$$

or

$$\rho_{21} = -\frac{F}{2} \sin \theta_R \left[\frac{1 + \bar{\Delta}^2 F^2 - \bar{\delta} \bar{\Delta} F \cos \theta_R + i\bar{\delta}}{1 + \bar{\Delta}^2 F^2 - 2\bar{\delta} \bar{\Delta} F \cos \theta_R + \bar{\delta}^2} \right]. \quad (3.5)$$

[In these equations and all that follow, I suppress the factor $(1 - 3\rho_{33})$ which accounts for population depletion.] Fig. 3.1 shows the behavior of ρ_{21} for various values of the parameters. When $\bar{\Delta} \cos \theta_R = 0$, ρ_{21} behaves like an optical (single-field) coherence: its real and imaginary parts are given by the standard absorptive and dispersive line shapes. When $\bar{\Delta} \cos \theta_R \neq 0$, the features are asymmetric.

At the Raman resonance ($\delta = 0$), ρ_{21} reaches its peak value of $-\frac{1}{2}F \sin \theta_R$, that is

$$\rho_{21}|_{\text{peak}} = -\frac{\langle \Omega_2^* \Omega_1 \rangle}{|\Omega_1|^2 + |\Omega_2|^2} \frac{s}{s+1} \quad (3.6)$$

where

$$s \equiv \frac{R}{\gamma_G} \quad (3.7)$$

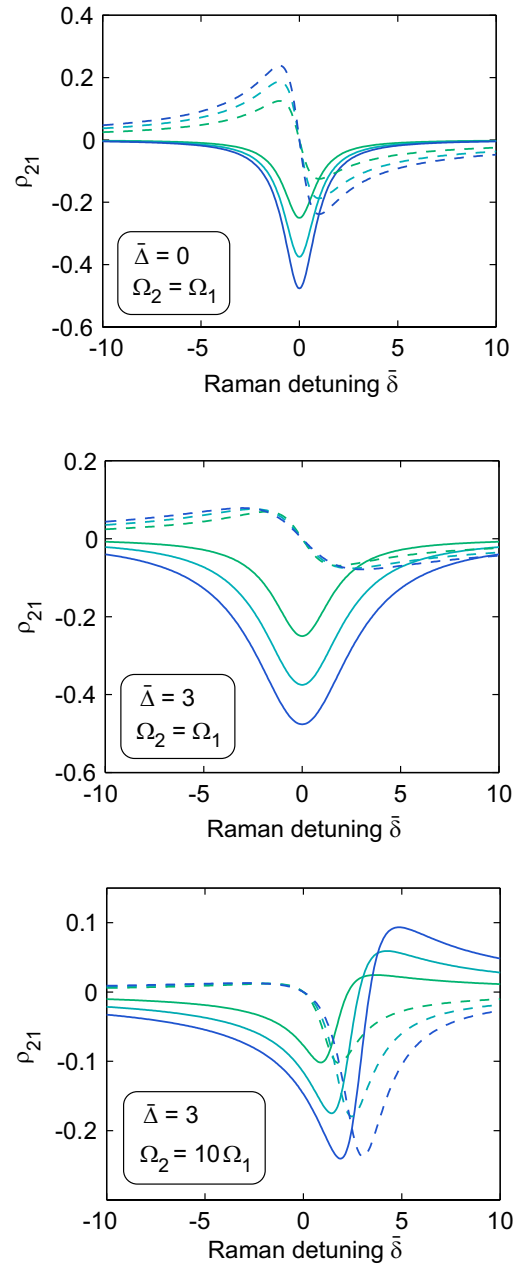


Figure 3.1: The real (solid) and imaginary (dashed) parts of the ground state coherence ρ_{21} , eqn. (3.5), for varying degrees of Raman saturation. In order of increasing size of the curves, the values of R/γ_G are 1, 3, and 20. Note that the scale of the horizontal axis also depends on R and γ_G [see eqn. (2.21)].

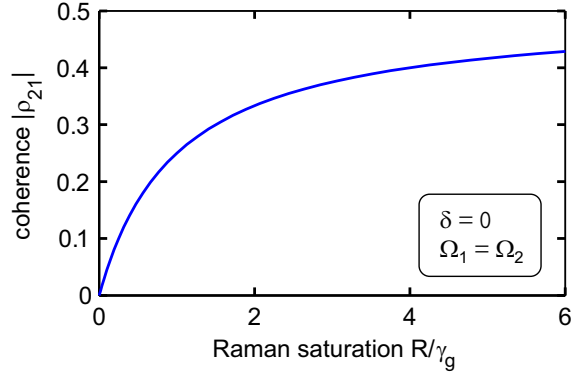


Figure 3.2: Dependence of the ground state coherence on the saturation of the Raman transition.

is the *Raman saturation parameter*. We will see that this dimensionless parameter determines the degree of all coherent effects. The ground state coherence is small when $s \ll 1$ and approaches its maximal value for $s \gg 1$ (Fig. 3.2). (As might be expected, the ground state coherence is also proportional to the relative coherence of the fields.) We thus arrive at the condition for coherence

$$\frac{1}{4} \frac{\gamma_E}{\Delta^2 + \gamma_E^2} (|\Omega_1|^2 + |\Omega_2|^2) \gg \gamma_G. \quad (3.8)$$

In physical terms, *the optical pumping rate must greatly exceed the ground state relaxation rate in order to achieve large coherence*. This is the first important lesson to learn from the Λ system.

From eqn. (3.6) we see that the peak coherence is maximized by using balanced fields ($|\Omega_1| = |\Omega_2|$). In this situation one has

$$\rho_{21} = -\frac{F}{2} \left[\frac{1 + \bar{\Delta}^2 F^2 + i\bar{\delta}}{1 + \bar{\Delta}^2 F^2 + \bar{\delta}^2} \right]. \quad (3.9)$$

The dispersive and absorptive components of ρ_{21} each have a characteristic width of $\sqrt{1 + \bar{\Delta}^2 F^2}$.

In terms of the dimensional experimental parameters, this yields the coherence half-width

$$\delta_{\text{coh}} = (R + \gamma_G) \sqrt{1 + \frac{\Delta^2}{\gamma_E^2} \frac{1}{(1 + \gamma_G/R)^2}}. \quad (3.10)$$

The intrinsic linewidth of the resonance is (to within a small factor) the ground state relaxation rate γ_G ; however, it broadens with the optical pumping rate R as well as with the optical detuning Δ . Note that R also depends on Δ .

The phase of ρ_{21} may generally be written as $\arg \rho_{21} = \pi + \phi_R + \Phi$ where ϕ_R is the azimuthal angle of \vec{R} and Φ is the difference between $\arg \rho_{21}$ and the phase of the dark state. In the present context, we find

$$\tan \Phi \equiv \frac{\text{Im } \rho_{21}}{\text{Re } \rho_{21}} \quad (3.11)$$

$$= \frac{\bar{\delta}}{1 + \bar{\Delta}^2 F^2 - \bar{\delta} \bar{\Delta} F \cos \theta_R}. \quad (3.12)$$

At $\delta = 0$, ρ_{21} has the opposite phase of $\Omega_2^* \Omega_1$. The destructive interference responsible for transparency is directly attributable to this 180° phase shift. For the case $\Delta = 0$, $\tan \Phi = \delta / (R + \gamma_G)$. Again, we find that *the characteristic width of the Raman coherence resonance is $R + \gamma_G$* . This is the second significant insight to be gained from the Λ system.

Having attained a grasp of the coherent phenomenology of a Λ medium, we turn now to the phenomenology of optical effects due to the quantum coherence of the medium.

3.2 Absorption and Electromagnetically Induced Transparency

One of the characteristic signatures of quantum coherence is a very narrow feature in the absorption spectrum of a medium. Typically, an absorption dip of sub-natural width¹ is the experimentalist's simplest indicator of coherent preparation. Hence it is important to understand how these absorption features are related to the ground state coherence.

3.2.1 The Photon Absorption Rate

The rate at which an atom (such as a Λ system) removes photons from a field is the net rate at which the atom is excited. In the steady state, this is equal to the rate at which the atom de-excites. Thus

¹Sub-natural, meaning that the width of the feature as a function of the Raman detuning is less than the inverse of the lifetime of the excited state(s).

the total rate of absorption (in photons per unit time, including both fields) in a Λ system is $\Gamma_E \rho_{33}$.

From eqn. (2.23) we have

$$\text{absorption rate} = \Gamma_E \rho_{EE} = \frac{\Gamma_E R \left(1 - \hat{F} \cdot \vec{\rho}\Big|_{\eta=1}\right)}{\Gamma_E + 3R \left(1 - \hat{F} \cdot \vec{\rho}\Big|_{\eta=1}\right)} \quad (3.13)$$

where I have used the fact that $\vec{R}/R = -\vec{F}/F$. In the case that the excitation rate is small compared to the spontaneous emission rate², the absorption rate is just $R \left(1 - \hat{F} \cdot \vec{\rho}\Big|_{\eta=1}\right)$. Now,

$$1 - \hat{F} \cdot \vec{\rho}\Big|_{\eta=1} = 1 - F \left(\frac{1 - 2\bar{\delta}\bar{\Delta}F \cos \theta_R + \bar{\Delta}^2 F^2 + \bar{\delta}^2 \cos^2 \theta_R}{1 - 2\bar{\delta}\bar{\Delta}F \cos \theta_R + \bar{\Delta}^2 F^2 + \bar{\delta}^2} \right). \quad (3.14)$$

At Raman resonance the absorption rate is $R(1 - F)$. Far from Raman resonance, the absorption rate is $R(1 - F \cos^2 \theta_R)$. Since $\cos^2 \theta_R \leq 1$, the absorption is less at Raman resonance. The reduction of absorption at resonance may be quantified as follows:

$$\text{resonant absorption factor} = \frac{\text{absorption at Raman resonance}}{\text{absorption away from Raman resonance}} \quad (3.15)$$

$$= \frac{1 - F}{1 - F \cos^2 \theta_R} \quad (3.16)$$

$$= \frac{1}{1 + s \sin^2 \theta_R}. \quad (3.17)$$

We see that *the amount of induced transparency at the Raman resonance is directly related to the Raman saturation s* (Fig. 3.3). If only one field is applied ($\Omega_1 = 0$ or $\Omega_2 = 0$), then $\sin \theta_R = 0$ and the absorption becomes independent of the Raman detuning (as one would expect). Conversely, the maximum contrast in absorption occurs with balanced fields, in which case

$$\text{absorption rate} = R \left[1 - F \left(\frac{1 + \bar{\Delta}^2 F^2}{1 + \bar{\Delta}^2 F^2 + \bar{\delta}^2} \right) \right]. \quad (3.18)$$

²The degree of excitation will be small either if the fields are weak or if the system is in a dark state. Given that $\gamma_G \ll \Gamma_E$, a sufficient condition for weak excitation is $|\delta \sin \theta_R| \ll \sqrt{\Gamma_E \gamma_G} (s^{1/2} + s^{-1/2})$.

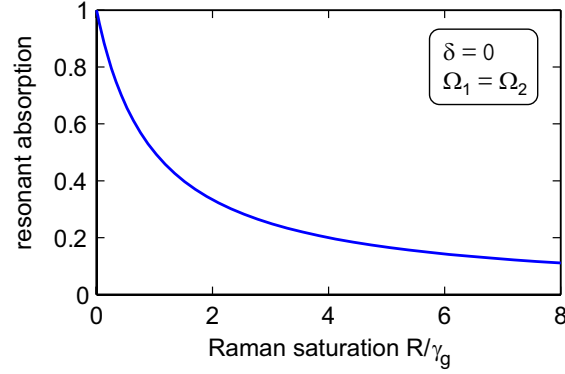


Figure 3.3: Induced transparency at the Raman resonance may be understood as a saturation of the Raman transition. “1” denotes the value of the absorption coefficient in the absence of ground state coherence.

In this case, the shape of the absorption dip is Lorentzian (Fig. 3.4) with depth $F = s/(s + 1)$ and half-width

$$\delta_{\text{abs}} = (R + \gamma_G) \sqrt{1 + \frac{\Delta^2}{\gamma_E^2} \frac{1}{(1 + \gamma_G/R)^2}}. \quad (3.19)$$

Note that this is the same as the coherence width δ_{coh} .

The analysis of the absorption in the most general case is less simple. However, a few general comments can be made. Firstly, as R becomes larger, the absorption becomes less sensitive to δ [cf. eqn. (3.13)]. This is because saturation of the optical transitions will reduce the absorption even when quantum interference does not. Secondly, the absorption dip becomes asymmetric when both $\Delta \neq 0$ and $|\Omega_1| \neq |\Omega_2| \neq 0$.

Finally, it should be remembered that the Bloch vector model (on which the results of this section depend) is valid only for $|\delta| \ll |\Delta + i\gamma_E|$. If $R \gg \gamma_E$, then the width of the Raman resonance is larger than the range of validity of δ and the widths given by eqns. (3.10) and (3.19) should not be taken too seriously.

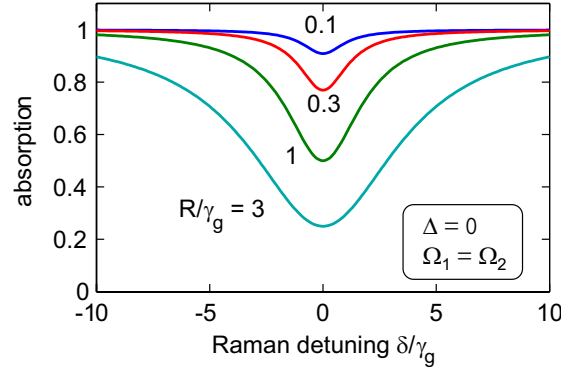


Figure 3.4: The electromagnetically induced transparency feature which occurs at Raman resonance.

3.2.2 Absorption Constants of Propagation

So far, we have considered only the total absorption. In many cases one would like to know the absorption coefficients for the fields separately. Under the slowly-varying amplitude approximation, the evolution of the electric field E is described by the differential equation

$$\frac{d}{dz}E = \frac{ik}{2}\chi E \quad (3.20)$$

where $k = 2\pi/\lambda$ is the free space wavenumber of the field and χ is the optical susceptibility. In dilute media, or whenever local field effects may be ignored,

$$\chi = \frac{\mathcal{N}}{\varepsilon_0 E} \quad (3.21)$$

where \mathcal{N} is the number density of atoms and p is the local dipole moment per atom. In general, the dipole moment is a vector given by

$$\mathbf{p}(t) = \sum_{a,b} \boldsymbol{\mu}_{ab}^* \rho_{jk}(t). \quad (3.22)$$

The evolution of the j th control field ($j = 1, 2$) obeys

$$\frac{d}{dz} E_j = \frac{ik_j}{2\varepsilon_0} \mathcal{N} \mu_{3j}^* \rho_{3j}. \quad (3.23)$$

In terms of the Rabi frequency,

$$\Omega_j^* \frac{d}{dz} \Omega_j = \mathcal{N} \frac{ik_j}{\varepsilon_0 \hbar} \Omega_j^* |\mu_{3j}|^2 \rho_{3j} \quad (3.24)$$

giving

$$\frac{d}{dz} |\Omega_j|^2 = -\frac{2\mathcal{N}k_j |\mu_{3j}|^2}{\varepsilon_0 \hbar} \text{Im}(\Omega_j^* \rho_{3j}) \quad (3.25)$$

$$\equiv -\alpha_j |\Omega_j|^2. \quad (3.26)$$

Now, it can be shown that

$$\text{Im}(\Omega_1^* \rho_{31}) = \frac{1}{2} [\Gamma_E \rho_{33} + \gamma_G w] \quad (3.27)$$

$$\text{Im}(\Omega_2^* \rho_{32}) = \frac{1}{2} [\Gamma_E \rho_{33} - \gamma_G w]. \quad (3.28)$$

(Note that the sum is proportional to ρ_{33} , confirming the argument made at the beginning of section §3.2.1.) A very simple result is obtained in the case $\delta = 0$:

$$\text{Im}(\Omega_j^* \rho_{3j}) = \frac{1}{2} \Gamma_E \rho_{33} \frac{|\Omega_j|^2}{|\Omega_1|^2 + |\Omega_2|^2} \quad (3.29)$$

which, by use of (3.25) and (2.27), leads to the absorption coefficients

$$\alpha_j = \frac{\mathcal{N}k_j |\mu_{3j}|^2}{\varepsilon_0 \hbar} \frac{\gamma_E}{\Delta^2 + \gamma_E^2} \frac{1}{1+s}. \quad (3.30)$$

This expression is identical to that of a two-state atom whose saturation parameter is R/γ_G instead of R/γ_E . In other words, the transparency of the dark state can be attributed to saturation of the Raman transition, which is γ_E/γ_G times easier to saturate than an optical transition.

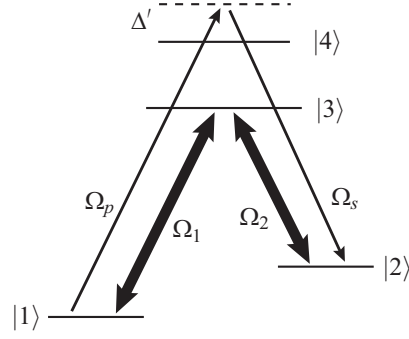


Figure 3.5: Stimulated Raman scattering via coherent population trapping. The control fields Ω_1, Ω_2 create quantum coherence between the ground states. A weak probe field Ω_p scatters off this coherence, generating a signal field Ω_s .

3.3 Coherent Raman Scattering

Besides inducing transparency, ground state coherence in a Raman system can also induce Raman scattering. This process may be more generally viewed as four-wave mixing enhanced by coherent population trapping. In this section we consider the evolution of two weak fields (a “probe” and a “signal”, denoted p and s respectively) in a medium coherently prepared by a pair of strong fields (Fig. 3.5). For simplicity, I will suppose that both pairs of fields are exactly resonant with the Raman transition ($\delta = 0$) and that the probe and signal fields do not disturb the ground state coherence created by the strong fields. (See [38] for a more general treatment.)

3.3.1 Spatial Evolution of the Input and Scattered Fields

In the slowly-varying amplitude approximation, the probe and signal fields evolve according to

$$\frac{d}{dz} E_p = \frac{i}{2} k_p \mathcal{N} \mu_{41}^* \rho_{41} \quad (3.31)$$

$$\frac{d}{dz} E_s = \frac{i}{2} k_s \mathcal{N} \mu_{42}^* \rho_{42} \quad (3.32)$$

where “4” refers to a real or effective excited state. To first order in the weak fields we have

$$\rho_{41} = \frac{i}{2(\gamma_{E'} - i\Delta')} (\rho_{11}\Omega_p + \rho_{21}\Omega_s), \quad (3.33)$$

$$\rho_{42} = \frac{i}{2(\gamma_{E'} - i\Delta')} (\rho_{12}\Omega_p + \rho_{22}\Omega_s), \quad (3.34)$$

where $\gamma_{E'}$ and Δ' are the detuning from and decay rate of state $|4\rangle$. The values of ρ_{11} , ρ_{22} , and ρ_{21} can be obtained from (2.26). It will be sufficient for the present derivation to take $\Delta = 0$, $\delta = 0$, and $R/(R + \gamma_G) \simeq 1$. One obtains

$$\rho_{21} \simeq -\frac{\Omega_2^*\Omega_1}{|\Omega_1|^2 + |\Omega_2|^2}, \quad \rho_{11} \simeq \frac{|\Omega_2|^2}{|\Omega_1|^2 + |\Omega_2|^2}, \quad \rho_{22} \simeq \frac{|\Omega_1|^2}{|\Omega_1|^2 + |\Omega_2|^2}. \quad (3.35)$$

The resulting propagation equations may be written as

$$\frac{d}{dz} \begin{pmatrix} \Omega_p \\ \Omega_s \end{pmatrix} = \begin{pmatrix} -\kappa_p & \kappa_p \frac{\Omega_1}{\Omega_2} \\ \kappa_s \frac{\Omega_2}{\Omega_1} & -\kappa_s \end{pmatrix} \begin{pmatrix} \Omega_p \\ \Omega_s \end{pmatrix} \quad (3.36)$$

where

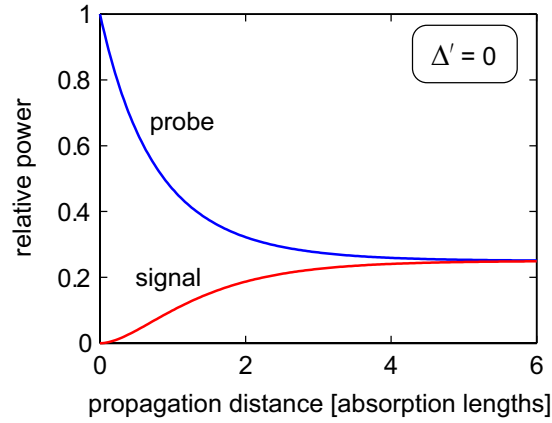
$$\kappa_p = \frac{k_p N |\mu_{41}|^2}{2\hbar\epsilon_0(\gamma_{E'} - i\Delta')} \frac{|\Omega_2|^2}{|\Omega_1|^2 + |\Omega_2|^2}, \quad \kappa_s = \frac{k_s N |\mu_{42}|^2}{2\hbar\epsilon_0(\gamma_{E'} - i\Delta')} \frac{|\Omega_1|^2}{|\Omega_1|^2 + |\Omega_2|^2}. \quad (3.37)$$

The eigenvalues of this system are 0 and $-(\kappa_p + \kappa_s)$. Supposing that there is no signal field incident on the medium, the fields are given by

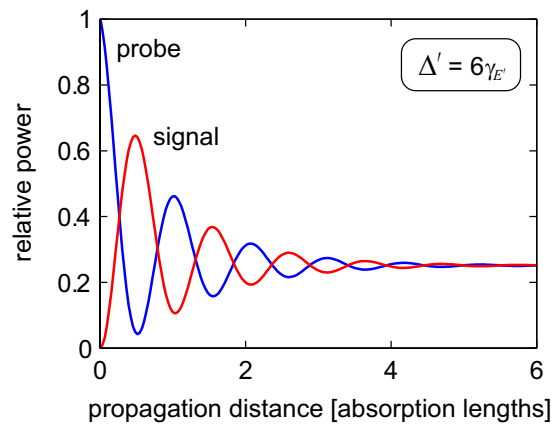
$$\Omega_p(z) = \frac{\kappa_s + \kappa_p e^{-(\kappa_p + \kappa_s)z}}{\kappa_p + \kappa_s} \Omega_p(0), \quad (3.38)$$

$$\Omega_s(z) = \frac{\Omega_2 \kappa_s (1 - e^{-(\kappa_p + \kappa_s)z})}{\Omega_1 (\kappa_p + \kappa_s)} \Omega_p(0). \quad (3.39)$$

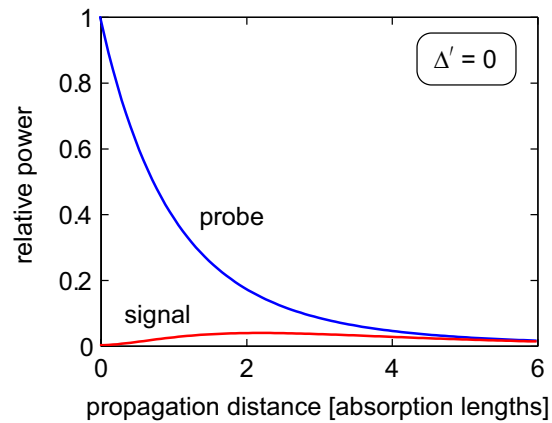
For $\Delta' = 0$ (Fig. 3.6a), κ_p and κ_s are real and energy is transferred from the probe to the signal in a distance on the order of $(\kappa_p + \kappa_s)^{-1}$, which is roughly equal to the absorption length for either field ($(2\kappa_p)^{-1}$ and $(2\kappa_s)^{-1}$ respectively). For $|\Delta'| \gg \gamma_{E'}$ (Fig. 3.6b), κ_p and κ_s are mostly imaginary; energy oscillates between the probe and the signal with a spatial period of $2\pi/\text{Im}(\kappa_p + \kappa_s)$, which



(a)



(b)



(c)

Figure 3.6: Spatial evolution of the fields in coherent Raman scattering. (a) Resonant scattering. (b) Non-resonant scattering. (c) Resonant scattering with 50% of maximal coherence. Note, the absorption length is larger in (b) than in (a) and (c).

will be much shorter than either of the absorption lengths $(2 \operatorname{Re} \kappa_p)^{-1}$ or $(2 \operatorname{Re} \kappa_s)^{-1}$. In both cases, the fields eventually reach a configuration which is transparent to the medium, $\Omega_p(\infty)/\Omega_s(\infty) = \Omega_1/\Omega_2$. In the initial stages of conversion, $(\kappa_p + \kappa_s)z \ll 1$ and

$$\Omega_s(z) \simeq \frac{k_s N |\mu_{42}|^2 z}{2\hbar\varepsilon_0(\gamma_{E'} - i\Delta')} \frac{\Omega_2 \Omega_1^*}{|\Omega_1|^2 + |\Omega_2|^2} \Omega_p(0). \quad (3.40)$$

In both of these cases, for which maximal coherence was assumed, half the power is lost before the fields reach a steady state in which the pump and probe each have 25% of the input power. When the coherence is less than maximal, a steady state does not exist; the Raman scattering is eventually dominated by linear absorption. In the case of resonant scattering with 50% of the maximal coherence (in which case the scattering susceptibility is half the linear susceptibility), the signal power peaks after about 2 absorption lengths at about 4% of the input probe power (Fig. 3.6c). In order to get higher efficiencies, one must detune the probe and propagate further (or use a denser medium).

Compared to most nonlinear processes, coherent Raman scattering is highly efficient: a significant fraction of the probe power is transferred to the signal in a distance characteristic of a linear process. But more than just power is transferred. Since the complex amplitude of the output signal is directly proportional to the complex amplitude of the input probe, the complete phase and amplitude information of the probe is preserved in the output. Thus, coherent Raman scattering may be used to shift the spatio-temporal content of a field at one frequency to another frequency. In case of non-dissipative scattering ($\Delta' \gg \gamma'_{E'}$), even the quantum state of the input field is transferred. The quantum operators \hat{a}_p and \hat{a}_s for the probe and signal fields obey a propagation equation which is identical to eqn. (3.36), apart from a few constants of scale. The solution is

$$\begin{pmatrix} \hat{a}_p(z) \\ \hat{a}_s(z) \end{pmatrix} = \begin{pmatrix} \frac{\kappa_s + \kappa_p e^{-(\kappa_p + \kappa_s)z}}{\kappa_p + \kappa_s} & \frac{\sqrt{\kappa_p \kappa_s} (1 - e^{-(\kappa_p + \kappa_s)z})}{\kappa_p + \kappa_s} \\ \frac{\sqrt{\kappa_p \kappa_s} (1 - e^{-(\kappa_p + \kappa_s)z})}{\kappa_p + \kappa_s} & \frac{\kappa_p + \kappa_s e^{-(\kappa_p + \kappa_s)z}}{\kappa_p + \kappa_s} \end{pmatrix} \begin{pmatrix} \hat{a}_p(0) \\ \hat{a}_s(0) \end{pmatrix} \quad (3.41)$$

which describes a unitary transformation (κ_p and κ_s are imaginary). In the special case $\kappa_p = \kappa_s$ and $(\kappa_p + \kappa_s)z = \pi i$, one obtains $\hat{a}_s(z) = \hat{a}_p(0)$ and $\hat{a}_p(z) = \hat{a}_s(0)$. That is, the quantum states of

the signal and probe field modes are exchanged.

3.3.2 The Scattering Bandwidth

A noteworthy feature of the system discussed in this section is that the ground state coherence is constant—it is prepared by CW pump fields. Thus the scattering bandwidth is not limited by the time it takes to achieve coherent population trapping. As I show below, the bandwidth is not limited to the spontaneous emission rate. Coherent Raman scattering can in fact have a very large bandwidth, making it of interest for telecommunications as well as novel applications including characterization of ultrashort X-ray pulses.

Suppose that instead of a single excited state, the probe and signal fields interact with a manifold of states. Or, suppose that the medium is inhomogeneously broadened. In either case the quantity $\mu_{4g}^* \rho_{4g}$ in eqns. (3.31) and (3.32) should be replaced by $\sum_e \mu_{eg}^* \rho_{eg}$ where $g = 1, 2$ and e denotes either a particular excited state in a manifold or a particular atom within an inhomogeneous distribution. Now, for the purposes of this argument it is sufficient to consider either field in isolation, in which case, for example,

$$\dot{\rho}_{e1} = -(i\omega_e - \gamma_e)\rho_{e1} + \frac{i}{\hbar} \mu_{e1} E_p(t) \rho_{11}. \quad (3.42)$$

Assuming ρ_{e1} is zero before the probe pulse arrives,

$$\rho_{e1}(t) = \frac{i}{\hbar} \mu_{e1} \int_{-\infty}^t e^{(i\omega_e + \gamma_e)(t'-t)} E_p(t') \rho_{11} dt'. \quad (3.43)$$

Then the polarization is

$$p(t) = \frac{i}{\hbar} \sum_e \int_{-\infty}^t e^{(i\omega_e + \gamma_e)(t'-t)} |\mu_{e1}|^2 E_p(t') \rho_{11} dt'. \quad (3.44)$$

In the limit of a continuous (or at least dense) distribution of excited states, $\sum_e |\mu_{e1}|^2$ may be replaced by $\int d\omega |\mu_\omega|^2 D(\omega)$, where μ_ω is the effective matrix element for the states with frequency ω , and $D(\omega)$ is the density of states. For simplicity I will also suppose that each excited state has

the same decay rate γ . Then

$$p(t) = \frac{i}{\hbar} \int_{t_0}^t M(t-t') e^{\gamma(t'-t)} E_p(t') \rho_{11} dt' \quad (3.45)$$

where

$$M(\tau) = \int e^{-i\omega\tau} D(\omega) |\mu_\omega|^2 d\omega \quad (3.46)$$

is the temporal response or “memory” of the manifold. If the manifold is broad and smooth (i.e. $|\mu_\omega|^2 D(\omega)$ does not vary significantly over a bandwidth γ), then $M(\tau) e^{-\gamma\tau} \approx M(\tau)$ and

$$p(t) \approx \frac{i}{\hbar} \int M(t-t') E_p(t') \rho_{11} dt'. \quad (3.47)$$

or, in the spectral domain,

$$p(\omega) \approx \frac{2\pi i}{\hbar} D(\omega) |\mu_\omega|^2 E_p(\omega) \rho_{11}. \quad (3.48)$$

This polarization and others of similar form enter directly into the equations governing coherent Raman scattering, namely eqn. (3.36). From eqn. (3.48) it is apparent that *the bandwidth of coherent Raman scattering is the width of the band of states excited by the probe (the inhomogeneous line width)*. The linewidth γ of the individual states plays no role. In the case that $D(\omega) |\mu_\omega|^2$ is broader and more slowly varying than $E_p(\omega)$, $M(t-t') \approx \delta(t-t')$ and the scattering polarization is directly proportional to the probe.

3.4 Summary

In this chapter, the Bloch vector model was used to make several predictions concerning coherence and coherent nonlinear optics in Raman systems. We found that the three most important parameters are the optical pumping rate R , the ground state relaxation rate γ_G , and the Raman detuning δ . We found that near Raman resonance, a large coherence builds up in the ground states, resulting in quantum interference which reduces the absorption. The magnitude of the coherence and the reduction in absorption are both determined by the value of the Raman saturation parameter $s =$

R/γ_G ; the larger s , the larger the coherence and the greater the reduction in absorption. The width of this Raman resonance is $R + \gamma_G$ for fields tuned near the excited state; however, the width increases for $|\Delta| \gtrsim R$. We learned that at Raman resonance, the absorption coefficients for the fields have the same form as that of a saturable 2-state system, but with a saturation intensity that is γ_E/γ_G times smaller. Finally, we saw that the ground state coherence can act as an oscillator which scatters a probe field, effectively shifting its amplitude and phase content to a different frequency band. Because the coherence is large, the scattering susceptibility is comparable in magnitude to a linear susceptibility, allowing for very high conversion efficiencies. The bandwidth is equal to the width of the inhomogeneously broadened line, or in the case of a continuum of states, to the bandwidth of the coupling to the continuum. In either case, large bandwidths are available for frequency conversion of signals.

Chapter 4

What About Coherence in Two-State Systems?

In the previous chapters we have considered coherent preparation of a 3-state system by the mechanism of coherent population trapping. Why bother with three states? Why not simply drive a 2-state system with a strong laser to produce quantum coherence? “Coherent preparation” would then seem to be a trivial subject. In this chapter I indicate why such an approach is not really advantageous, either conceptually or practically.

4.1 Two States Driven by One Field

Let us review the behavior of the simplest possible system: two states driven by a monochromatic optical field. If the system is closed, a steady state is reached which is characterized by the density matrix elements

$$\rho_{ee} = \frac{1}{2} \frac{s}{1+s} \quad (4.1)$$

$$\rho_{gg} = 1 - \frac{1}{2} \frac{s}{1+s} \quad (4.2)$$

$$\rho_{eg} = \sqrt{\frac{\Gamma_e}{4\gamma_e}} \frac{\sqrt{s}}{1+s} \quad (4.3)$$

where e and g denote excited and ground states, Ω is the Rabi frequency of the fields, and

$$s \equiv \frac{\gamma_e}{\Gamma_e} \left| \frac{\Omega}{-\Delta - i\gamma} \right|^2 \quad (4.4)$$

is the (optical) saturation parameter, not to be confused with the Raman saturation parameter s used in other chapters. At low intensities nearly all the population is in the ground state and there is little coherence. As the intensity increases, the excited state population grows to the asymptotic limit of half the population in each state. Unlike in a 3-state system, the coherence does not grow monotonically with intensity. Since the coherence goes as $\sqrt{s}/(1+s)$ instead of $s/(1+s)$, it peaks (with a value of $\sqrt{\Gamma_e/\gamma_e}/4$) at $s = 1$. But the most important difference is that in the 2-state system, increasing coherence corresponds to increasing interaction with the field. This is because the coherence is directly related to the dipole moment. Thus coherence is achieved at the cost of strong absorption, thereby limiting the thickness of the medium that can be coherently prepared. One possible work-around is to tune the laser away from resonance, so that the material response is mostly dispersive. But in this case a much higher intensity is required to achieve the same level of saturation. Note that the saturation intensity of a 2-state system is already generally much higher than that of a well-chosen 3-state system¹. In terms of the amount of coherence that can be achieved, the amount of absorption, and the intensity required, the 2-state system with one field is inferior to the 3-state system with two fields.

4.2 Two States Driven by More than One Field

It would appear that a 2-state system with a single field is too simple to possess the desirable characteristics (in regard to coherent preparation) of 3-state systems. Perhaps the problem is not the number of states, but rather the number of fields? It is well-known that a strong field splits the excited and ground states by putting significant amounts of population in energy levels defined by the fields (Fig. 4.1). One may therefore expect that such a system could show many if not all of the

¹If a two-state transition is optically allowed, the excited state must relax to the ground state, resulting in decoherence and a larger saturation intensity. In a well-chosen 3-state system, the coherence is produced between two metastable states.

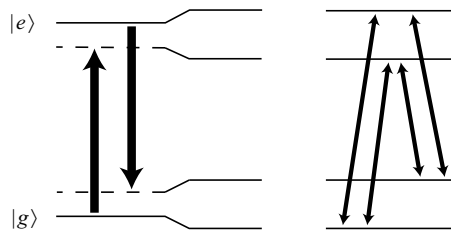


Figure 4.1: “Dressing” of states by a strong field. The field splits states $|e\rangle$ and $|g\rangle$, creating a system with three resonance frequencies. When probed by weak fields, the driven system acts in many ways like a system with more than two levels.

phenomena associated with quantum coherence: EIT, large wave-mixing susceptibilities (coherent scattering), lasing without inversion, slow light, etc. Indeed, after the concept of EIT was introduced, a number of workers re-examined the two-state system driven by multiple fields, looking for effects similar to those attributed to EIT. There is now a vast literature on the subject [88]. At the risk of oversimplification, this field may be summarized as follows: The weak-field susceptibility of a 2-state system is drastically modified when the system is driven by one or more strong fields. Many effects occur which are reminiscent of quantum coherent effects; but they are not always the result of similar physics. For example, a vanishing weak-field absorption (Fig. 4.2) is sometimes due to a balance between absorption and emission (optical interference) rather than destructive interference of two absorption processes (quantum interference). Analysis of these systems is actually rather complicated, and distinguishing quantum interference from “ordinary” optical interference is not always easy. It appears that multiple driving fields at different frequencies are required to produce situations which are truly analogous to coherent preparation in 3- or 4-state systems [27]. Such systems are just as complicated, if not more so, than the Λ system.

Thus one need not look past the 3-state system for direct and effective demonstrations of quantum coherence and its associated affects. There are other reasons one might choose to work with systems involving more than two states. For instance, large coherences at frequencies ranging from RF to the visible can be generated with all-optical technology (just two low-power lasers). Coherence can be produced between states for which direct transitions are forbidden by selection rules.

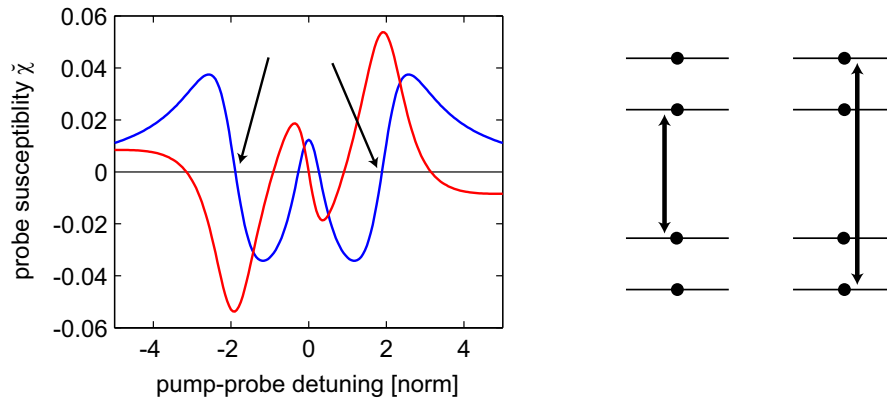


Figure 4.2: Transparency in a driven 2-state system. The absorption of a weak field in the driven system vanishes at the points indicated by arrows (*left*). However, the vanishing of absorption does not correspond to a true dark state, since the dispersive component of the susceptibility does not also vanish. This kind of transparency can be understood in the dressed-state basis as a balancing of absorption and gain at either frequency (*right*). Parameters for the control field: $\Omega = 2\gamma_e$, $\Delta_e = 0$.

Furthermore, the superposition states can be chosen to be metastable, resulting in very narrow spectral features and low saturation intensities.

Regardless of the relative merits of 2- and 3-state systems, all the experiments reported in this work involve coherent preparation of the sodium D1 system, which most closely resembles a 3-state Λ system. Hence, I will not discuss 2-state systems any further. The interested reader may consult the references indicated above for more information.

4.3 Summary

I have argued that the 3-state, 2-field system is the simplest system that illustrates coherent preparation and its benefits. While one can create quantum coherence by driving a 2-state system with a single field, the coherence is accompanied by strong absorption and hindered by relaxation due to spontaneous emission. These problems can be overcome by driving the system with a strong polychromatic field; however, the resulting system is at least as complicated, both conceptually and experimentally, as a 3-state system.

Chapter 5

Coherent Preparation of Many-State

Atoms

In the previous chapters, 3- and 4-state systems were studied as the simplest examples of coherent Raman systems. But the materials provided by nature are far more complex. Even alkali vapors, which consist of relatively isolated, single-valence-electron atoms, possess numerous states and are graced¹ with many complicating effects. In this chapter, I explore some of the ways in which a multiplicity of ground states affects coherent population trapping and complicates quantum coherent optical processes.

5.1 Notation and Conventions

5.1.1 Nominal Rabi Frequencies

A spectroscopic line of an atom generally contains contributions from transitions involving many different pairs of states. Each pair of states $|e\rangle$ and $|g\rangle$ (where e denotes a state in excited level E and g denotes a state in ground level G) couples to the electric field with a strength that is characterized by the electric dipole matrix element μ_{eg} . While it is generally necessary to know the values of the matrix elements for all pairs of states in order to accurately model coherent phenomena, it can still

¹If it weren't for these complications, people like myself would be out of work.

be useful to assign a nominal dipole matrix element to the spectral line as a whole. As explained in Appendix A, there are two different effective matrix elements associated with spontaneous and stimulated transitions.² Of the two, the effective matrix element which characterizes spontaneous emission is more fundamental. It is also the quantity reported by experimentalists who measure “the” matrix element associated with a given spectral line.³ For these reasons, I define the *nominal electric dipole matrix element* of a spectral line as

$$\mu \equiv \sqrt{\Gamma_E \frac{3\pi\hbar\epsilon_0 c^3}{\omega_{EG}^3}} \quad (5.1)$$

where ω_{EG} is the angular frequency of the transition and Γ_E is the spontaneous emission rate of the states in level E .⁴ μ is the dipole matrix element that a two-state atom would have if its spontaneous emission rate were Γ_E . For the sodium D lines, $\mu = 2.51ea_0$ where a_0 is the Rydberg constant. More generally, the nominal matrix element for a whole system (whether it encompasses one or more spectroscopic lines) may be defined as

$$\mu \equiv \sqrt{\frac{1}{N_E} \sum_{e,g} |\mu_{eg}|^2} \quad (5.2)$$

where N_E is the number of excited states.

Having chosen a characteristic dipole moment, it makes sense to define the *nominal Rabi frequency* of a field component \mathbf{E} in analogy with eqn. (2.7):

$$\Omega = \frac{2\mu\mathbf{E}}{\hbar}. \quad (5.3)$$

The nominal Rabi frequency is convenient in that it is unique (independent of atomic structure) for

²The quick explanation is that spontaneous processes involve all polarizations while stimulated processes involve a particular polarization.

³A common alternative to the effective matrix element $\mu_{EG,\text{spont}}$ is the *oscillator strength*

$$f_{GE} \equiv \frac{2}{3} \frac{m_e \omega_{EG}}{e^2 \hbar} \frac{N_E}{N_G} \mu_{EG,\text{spont}}^2$$

where N_E and N_G are the number of states in the excited and ground levels, respectively [89].

⁴In an atom, the spontaneous emission rate is the same for all excited states in the same level. This fact can be inferred from the principle of isotropy.

each field component, yet is expressed in the same units as the rates and frequencies which appear in the dynamical equations for the state of the atom. The actual Rabi frequency of \mathbf{E} on each separate transition is related to the nominal Rabi frequency by

$$\Omega_{eg} = \boldsymbol{\Omega} \cdot \check{\boldsymbol{\mu}}_{eg} \quad (5.4)$$

where

$$\check{\boldsymbol{\mu}}_{eg} \equiv \frac{\boldsymbol{\mu}_{eg}}{\mu} \quad (5.5)$$

is the *relative matrix element* associated with states $|e\rangle$ and $|g\rangle$. The relative matrix elements have the property $\sum_g |\check{\boldsymbol{\mu}}_{eg}|^2 = 1$.

5.1.2 The atomic response

The parameters that determine the behavior an atomic medium—the state energy levels, rates of relaxation processes, and Rabi frequencies of the electric and magnetic fields—can all be measured in units of frequency. The use of a common scale simplifies analytical results, makes it easier to determine the dominant influences, and provides some degree of normalization. It is likewise convenient to express the atomic response (i.e. the induced dipole moment) on this same scale. I define the *normalized dipole moment* as

$$\check{\mathbf{p}} \equiv \frac{\Gamma_E}{\mu} \mathbf{p} = \Gamma_E \sum_{e,g} (\check{\boldsymbol{\mu}}_{eg})^* \rho_{eg}. \quad (5.6)$$

$\check{\mathbf{p}}$ has units of frequency and is on the scale of the nominal Rabi frequency of the applied field; in fact $\check{\mathbf{p}} = i\boldsymbol{\Omega}$ in the case of weak, resonant excitation of a two-state atom. The atomic susceptibility (a.k.a. polarizability) tensor $\check{\boldsymbol{\chi}}$ can be defined by the relation

$$\check{\mathbf{p}} = \check{\boldsymbol{\chi}} \boldsymbol{\Omega}. \quad (5.7)$$

As a notational shorthand, I will write $\check{\boldsymbol{\chi}} = \check{\mathbf{p}}/\boldsymbol{\Omega}$ and use the scalar $\check{\chi}$ to denote a generic element of $\check{\boldsymbol{\chi}}$. $\check{\chi}$ is typically on the order of unity. More accurately, it is roughly equal to the square of the

effective relative matrix element for the states involved⁵.

The atomic susceptibility is also very simply related to the optical susceptibility. Upon combining eqns. (3.21), (5.1), (5.3), (5.6), and (5.7) one obtains⁶

$$\chi = \frac{3}{4\pi^2} \tilde{\mathcal{N}} \frac{\tilde{\mathbf{p}}}{\Omega} \simeq 0.076 \tilde{\mathcal{N}} \tilde{\chi}. \quad (5.9)$$

where $\tilde{\mathcal{N}} \equiv \mathcal{N}\lambda^3$ is the number of atoms per cubic wavelength; a moderately dense vapor has $\tilde{\mathcal{N}} \sim 1$. Sometimes it is useful to think of the optical interaction as a collision between a photon and an atom with an effective area or *cross section* σ . The cross section may be written as

$$\sigma = \frac{3\lambda^2}{2\pi} \tilde{\chi} \simeq 0.48\lambda^2 \tilde{\chi}. \quad (5.10)$$

Finally, I note that the spatial evolution of the fields can be expressed in terms of these normalized quantities as

$$\frac{d\Omega}{dz} = ik \frac{3}{8\pi^2} \tilde{\mathcal{N}} \tilde{\mathbf{p}}. \quad (5.11)$$

Remarkably, these last three equations are valid regardless of the number of states or the values of the matrix elements.

Thus we find that a system consisting of a multistate medium and optical field(s) can be characterized by four sets of quantities which are either dimensionless or have units of frequency: (1) the relative dipole matrix elements; (2) the spontaneous emission rate; (3) the nominal Rabi frequency of the applied field; and (4) the nominal Rabi frequency of the induced dipole moment.

⁵If $\tilde{\mu}$ is the effective relative matrix element for a transition, the weak-field susceptibility is

$$\tilde{\chi} = \frac{i}{2} \frac{\Gamma}{\gamma - i\Delta} \tilde{\mu}^2 \rho \quad (5.8)$$

where ρ is the population of the initial state and Γ, γ, Δ are the decay and detuning parameters of the transition. At resonance, and in the absence of pressure broadening, this formula reduces to $\tilde{\chi} = i\tilde{\mu}^2 \rho$.

⁶This result ignores inhomogeneous broadening. As rule-of-thumb, inhomogeneous broadening reduces the resonant susceptibility by the ratio of the inhomogeneous to homogeneous line widths.

5.2 Generalization of the Dark/Bright Basis

Coherent population trapping in a Λ system is easy to understand in terms of the dark and bright states. It takes little more than inspection of eqn. (1.1) to determine that a particular combination of the two ground states is decoupled from the excited field. However, when there are multiple ground states coupled to multiple excited states by multiple fields, it is harder to see whether or not a dark state exists. A more formal procedure for identifying dark states is needed.

The interaction between the atom and the optical field is characterized by the following part of the Hamiltonian⁷:

$$\hat{H}_{EG} = \frac{\hbar}{2} \sum_{e,g} \Omega_{eg} |e\rangle \langle g|. \quad (5.12)$$

In a certain basis for the ground states, this operator will be “diagonal.” That is, it is possible to write

$$\hat{H}_{EG} = \frac{\hbar}{2} \sum_n \Omega_n |E_n\rangle \langle G_n| \quad (5.13)$$

for some set of ground states $|G_n\rangle$, excited states $|E_n\rangle$, and scalars Ω_n . This kind of diagonalization is analogous to eigenmode decomposition and is known variously as Schmidt decomposition or singular value decomposition⁸. The scalars Ω_n are called the singular values. Each Schmidt state $|G_n\rangle$ is a distinct superposition of bare ground states which is excited with effective Rabi frequency Ω_n . A vanishing singular value indicates a state which is not excited by the fields at all, i.e. a dark state. Since there can only be as many (non-zero) singular values as there are excited states, we can know that there is always a dark state if the number of ground states N_G exceeds the number of excited states N_E . In fact, the number of dark states is always at least $N_G - N_E$.

The Schmidt basis, then, is the generalization of the dark-bright basis which is so helpful in Λ systems. In this basis the multiple excitation pathways are separate and do not interfere. The distribution of population among these states is therefore a study in optical pumping, for which (incoherent) rate equations are sufficient. In general, the atom will be optically pumped from the bright

⁷I will refer to the part of the Hamiltonian that describes photoexcitation as the interaction Hamiltonian, although this term is usually applied to the Hermitian operator that describes both photoexcitation and photoemission.

⁸Any matrix M (whether square or not) can be diagonalized by a dual unitary transformation: $U^\dagger M V = D$ where D is a diagonal matrix and U and V are unitary matrices. Singular value decomposition of M amounts to a determination of U , V , and the diagonal of D (the singular values).

states to the dark states; the larger Ω_n , the smaller the steady probability of $|G_n\rangle$. It should be noted, however, that states with intermediate coupling constants will act like dark states at low intensities and like bright states at high intensities: At low intensities, such a state will be excited more slowly and will end up with more population than the strongly coupled states; at high intensities, it will be excited rapidly enough to overcome relaxation and will be depopulated in favor of true dark states.

The Schmidt-basis approach can be very helpful, but one must use it with care since it ignores the frequency distribution of the states and the fields. First of all, it is blind to the fact that off-resonant transitions are less important than resonant transitions. Secondly, the frequency distribution of states and fields may be such that it is impossible to choose a set of energy origins for the states (a so-called “rotating frame”) which simultaneously eliminates the rotation of the coupling constants Ω_{eg} and of the ground states. In this case the Schmidt states will be time-dependent, and coherent population trapping will be hindered because the trap state(s) will be continually changing. In such situations the Schmidt basis is of little use. For example, it has already been noted (Chapter 2) that the dark-bright basis is not helpful for analyzing the 3-state Λ system if the fields are not Raman resonant.

For simplicity, in the following section I will consider only those systems in which every near-resonant coupling between field and atom has the same detuning. Then it is possible to choose a rotating frame in which all resonantly coupled states have the same energy and all the coupling constants are time-independent. Generally, this occurs when an atom has well-separated levels in the absence of DC electric and magnetic fields and the frequency differences between the various field components equal the intervals between ground levels. In such cases, the behavior may be understood in terms of optical pumping between Schmidt states. The rate equations for the Schmidt states are then

$$\dot{\rho}_{e_j} = -(\Gamma_E + \Gamma_G)\rho_{e_j} + 2R_j(\rho_{g_j} - \rho_{e_j}) \quad (5.14)$$

$$\dot{\rho}_{g_j} = \sum_k b_{jk}\Gamma_E\rho_{e_k} - \Gamma_G\rho_{g_j} + \frac{1}{N}\Gamma_G + 2R_j(\rho_{e_j} - \rho_{g_j}) \quad (5.15)$$

where Γ_E is the spontaneous emission rate of the excited states, b_{eg} is the spontaneous emission

branching ratio, Γ_G is the population relaxation rate between the ground Schmidt states, N is the number of ground states, ρ_{e_j} (ρ_{g_j}) is the population of the j th excited (ground) Schmidt state, and

$$R_j = \frac{1}{4} \frac{\gamma_E}{\Delta_E^2 + \gamma_E^2} \Omega_j^2 \quad (5.16)$$

is (half) the optical pumping rate associated with the j th singular value.

5.3 Multi-state Effects

5.3.1 Relaxation Bias

In a Λ system, there are only two Schmidt states: the dark state and the bright state. An atom which is in a thermal mixture of bare states has an equal probability of being found in the bright state or the dark state. Hence, whenever a coherently prepared atom relaxes to the thermal state, it has a 50% chance of remaining in the dark state. Consider now a multistate system in which there are N Schmidt states, one of which is dark and the remainder of which are bright. Then every time the atom relaxes, the probability of remaining in the dark state is only $1/N$. That is, it has a much higher chance of relaxing to a bright state than the dark state (Fig. 5.1). I call this effect *relaxation bias*. For the same intrinsic relaxation rate, it is harder to maintain the dark state population when there are fractionally few dark states than when there are many.

This principle can be seen in the steady-state solution of eqns. (5.14) and (5.15) for the case of N_D dark states ($R_1 = R_2 = \dots = R_{N_D} = 0$), $N - N_D$ equal bright states ($R_{N_D+1} = \dots = R_N = R$), and uniform decay ratios ($b_{jk} = 1/N$). For $2\Gamma_G/\Gamma_E \ll N_D/N$, one finds that the total population in the dark states is

$$\text{trapped population} = \sum_{j=1}^M \rho_{g_1} \approx \frac{N_D}{N} + \frac{N - N_D}{N} \frac{2R}{2R + (N/N_D)\Gamma_G}. \quad (5.17)$$

The population in the dark state(s) goes from its equilibrium value of N_D/N at $R = 0$ to its saturating value of 1 as $R \rightarrow \infty$. The saturation parameter is $2R/(N\Gamma_G/N_D) = (2N_D/N)s$ where s is the saturation parameter defined for the Λ system [eqn. (3.7)]. Although the branching ratios

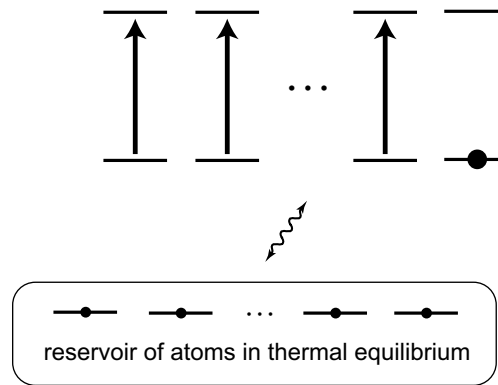


Figure 5.1: Relaxation bias in many-state systems. The more bright states there are, the more likely relaxation is to move the system from the desired dark state to a bright (undesired) state.

to different Schmidt states are generally not equal as supposed, and the bright states generally have different coupling constants, we may take as a rule-of-thumb that *the smaller the fraction of states that act as traps, the higher the optical intensity needed to achieve trapping.*

5.3.2 Extraneous Trap States

As suggested previously, a given system may have more than one dark state. (Recall that if there are N_G ground states and N_E excited states, then there are at least $N_G - N_E$ dark states.) Even if a system has only one dark state, it may have yet have multiple “dim” states, states with relatively small coupling constants. Dim states will trap population almost as effectively as dark states for weak or modest intensities, and will contribute little to the total absorption (since they have small coupling constants). If the point of population trapping is simply to reduce absorption, then the more trap states, the better (for the reasons discussed in the previous section). However, if the point is to create coherence in the medium, then a multiplicity of trap states may not be desirable. Suppose, for example, that there are N_T trap states, only one of which involves the desired coherence. Then even for large optical intensities the population will be roughly evenly distributed among the trap states, and the coherence will be roughly N_T times smaller than if the remaining trap states did not exist (Fig. 5.2). These *extraneous trap states* keep some population from being pumped into the

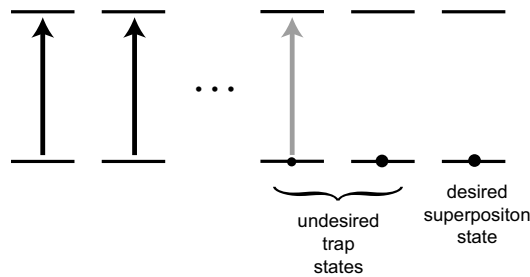


Figure 5.2: Extraneous trap states in many-state systems. Not all uncoupled or weakly coupled Schmidt states may possess a desired property (e.g. hyperfine coherence). Undesired trap states compete for population with the desired dark state.

desired dark state. An even worse situation occurs when some of the trap states involve coherences of opposite sign. In this case, little or no net coherence may be created even when all the population is pumped into the dark states.

5.3.3 Zeeman Splitting and Magnetic Broadening

The eigenstates of a free atom are eigenstates of the total angular momentum (characterized by the quantum number F) and its projection onto some quantization axis (characterized by the “magnetic” quantum number m). In the absence of a magnetic field, states of the same F (*Zeeman states*) have the same energy. When a weak magnetic field is applied along the quantization axis, the energies of the Zeeman states shift in proportion to their magnetic number m (Fig. 5.3). The Schmidt decomposition is no longer helpful as the bare states attempt to rotate at different rates, thereby mixing the Schmidt states. However, if the energy shifts are large enough, the off-resonant bare states will have essentially no coherence with each other and may be treated using rate equations. As I will show below, splitting the sodium Zeeman energies causes some of the dark states to shift their Raman frequencies and causes others to become bright [90].

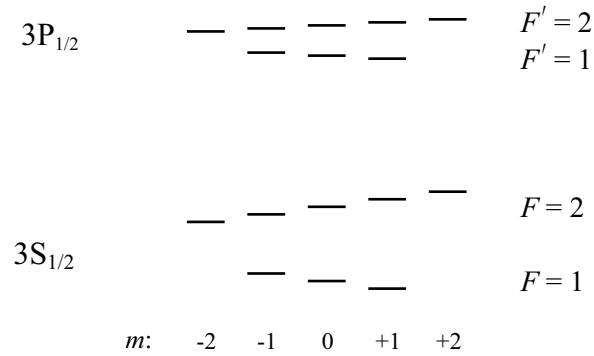


Figure 5.3: Zeeman shifts of the sodium D1 states in the presence of a DC magnetic field along the quantization axis. (Not to scale.)

5.4 Dark States in the Sodium D1 Line

In the absence of a magnetic field, the sodium D1 line ($3S_{1/2} \leftrightarrow 3P_{1/2}$ transitions, Fig. 5.4) contains 4 hyperfine levels: 2 ground levels (with $F = 1, 2$) and 2 excited levels (with angular momentum $F' = 1, 2$). The ground levels are split by 1772 MHz; the excited levels are split by 189 MHz. At low vapor densities⁹ these splittings are much larger than the optical linewidth (10 MHz). A field which resonantly couples one of the ground levels to one of the excited levels will be far from resonance with any other pair of levels. Therefore, a pair of fields with a frequency difference of 1772 MHz can form a resonant Λ system involving either excited level. These two Λ systems may be regarded separately since the fields can be resonant with only one excited level at a time.

5.4.1 Schmidt States for the Sodium D1 $\Lambda_{1y,2x}^1$ Subsystem

Consider two “control” fields, polarized in the x and y directions, with nominal Rabi frequencies Ω_x and Ω_y , respectively. Suppose that the y -polarized field is resonant with the $F = 1 \leftrightarrow F' = 1$ transition and that the x -polarized field is resonant with the $F = 2 \leftrightarrow F' = 1$ transition. Because the ground levels are far apart, the coupling of the x field to the $F = 1$ level and of the y field to the $F = 2$ level can be ignored. As a reminder of which field is meant to couple to which ground level,

⁹With excessive pressure broadening, the excited hyperfine levels might not be well-separated.

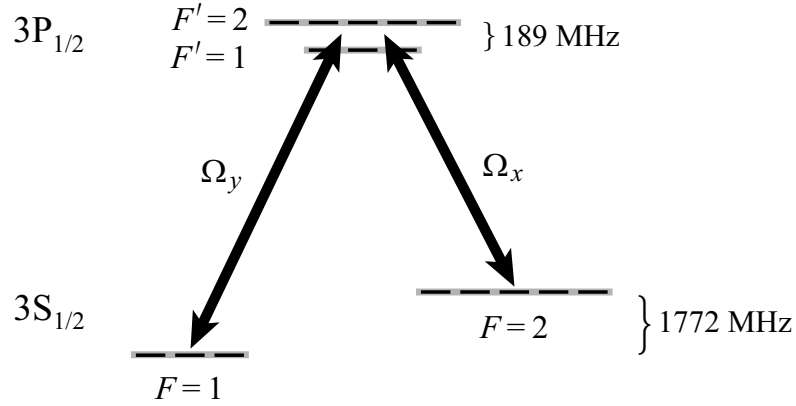


Figure 5.4: The scheme for coherent preparation of sodium. The sodium D1 line contains four hyperfine levels, each of which is a Zeeman multiplet. Through the process of coherent population trapping, a pair of fields pumps the sodium into a superposition of the ground hyperfine levels.

I will sometimes use the subscripts $_{1y}$ and $_{2x}$ for quantities associated with the x and y fields. In this fashion the subsystem formed by the fields, the $F = 1, 2$ ground states, and the $F' = 1$ states will be denoted $\Lambda_{1y,2x}^1$.

The interaction between the atom and fields is characterized by matrix elements of the form $\frac{\hbar}{2} \langle F' = 1, m' | \tilde{\mu} | F, m \rangle \cdot \Omega_{x \text{ or } y}$. These matrix elements can be evaluated using the first three rows of Table B.1, yielding the interaction Hamiltonian

$$H_{1y,2x}^1 = \frac{\hbar}{2} \begin{pmatrix} & \frac{-i\Omega_y}{\sqrt{24}} & & \frac{\Omega_x}{\sqrt{4}} & & \frac{-\Omega_x}{\sqrt{24}} \\ \frac{i\Omega_y}{\sqrt{24}} & & \frac{-i\Omega_y}{\sqrt{24}} & & \frac{\Omega_x}{\sqrt{8}} & \frac{-\Omega_x}{\sqrt{8}} \\ & \frac{i\Omega_y}{\sqrt{24}} & & & \frac{\Omega_x}{\sqrt{24}} & \frac{-\Omega_x}{\sqrt{4}} \end{pmatrix}. \quad (5.18)$$

The arrangement of states is the same as that of Table B.1. Vanishing elements are not shown. The Schmidt states and singular values for this system are given in Table 5.1. With eight ground states but only three (relevant) excited states, there are five dark states and three bright states. Out of the five dark states, three do not involve any hyperfine coherence¹⁰. These three states therefore qualify

¹⁰The dark states are degenerate, so of course they are somewhat arbitrary. The states given in Table 5.1 were chosen for their symmetry. As I will discuss in §5.4.3, a different set of dark states is convenient when a magnetic field is applied.

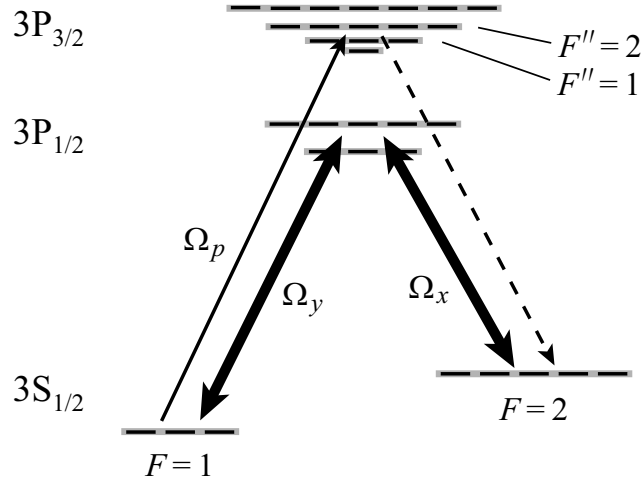


Figure 5.5: The scheme for coherent Raman scattering in sodium. A probe field Ω_p scatters off the ground hyperfine coherence created by the control fields. Selection rules allow scattering via states with $F'' = 1$ or $F'' = 2$ only.

as extraneous traps. They limit coherent preparation because they leave only 40% of the population to be coherently trapped. Furthermore, these states will still act as traps when the fields are not tuned to the Raman resonance, making the EIT effect less dramatic.

The Schmidt states which possess hyperfine coherence have coherences between several different pairs of states. While one could simply sum up these coherences to obtain a measure of the total hyperfine coherence, a more relevant quantity is the effective hyperfine coherence which contributes to a desired wave mixing process, such as Raman scattering. Table 5.1 gives the Raman scattering susceptibility for each Schmidt state when the two pump fields are balanced ($\Omega_x = \Omega_y$). The susceptibilities are calculated in the following way: Suppose that a weak probe beam of nominal Rabi frequency Ω_p is tuned to the $F'' = 1$ or $F'' = 2$ hyperfine level in the $3P_{3/2}$ level (Fig. 5.5). If the atom is in the n th Schmidt ground state, then the first-order polarization induced by the probe beam is

$$\mathbf{p} = \frac{i}{\hbar} \frac{\langle G_n | \hat{\boldsymbol{\mu}} \hat{H}_{\text{probe}} | G_n \rangle}{\gamma_E - i\Delta_E} \quad (5.19)$$

where \hat{H}_{probe} is the interaction Hamiltonian involving the probe beam and Δ_E is the detuning

from the nearest excited hyperfine level. Taking $\Delta_E = 0$ and assuming that there is no pressure broadening, we have

$$\check{\mathbf{p}} = i \sum_{g,g'} \sum_e \langle G_n | g' \rangle \langle g' | \check{\boldsymbol{\mu}} | e \rangle \langle e | (\check{\boldsymbol{\mu}} \cdot \boldsymbol{\Omega}_p) | g \rangle \langle g | G_n \rangle \quad (5.20)$$

which gives the (tensor) polarizability

$$\check{\chi} = \frac{\check{\mathbf{p}}}{\boldsymbol{\Omega}_p} = i \sum_{g,g'} \sum_e \langle g | G_n \rangle \langle G_n | g' \rangle \check{\boldsymbol{\mu}}_{g'e} \check{\boldsymbol{\mu}}_{eg}. \quad (5.21)$$

If one wanted to obtain the linear susceptibility $\check{\chi}_{11}$ or $\check{\chi}_{22}$, g and g' would be restricted to just the $F = 1$ or $F = 2$ states, respectively. The Raman susceptibility $\check{\chi}_{12}$ is obtained by summing g over the $F = 1$ states and g' over the the $F = 2$ states¹¹. Noting that the polarization associated with Raman scattering is always perpendicular to the probe whenever the pump fields are cross polarized, the Raman susceptibility is reported as a scalar.

The Raman susceptibilities are smaller than those of a symmetric 3-state system (namely $1/4$, since $|\rho_{12}| = 1/2$ and $\check{\mu}_{2e}\check{\mu}_{e1} = 1/2$). However, they are on the same order as the linear susceptibilities for the D2 line (i.e., about as large as the matrix elements in Table B.2), a feature in keeping with the properties of 3-state Λ systems. Note that dark and bright states have equal and opposite Raman susceptibilities. This too, is like the behavior of a 3-state Λ system. In the case of complete trapping in the dark states, such that each dark state has population $1/5$, the net Raman susceptibility is $0.026i$ for scattering via the $F'' = 1$ level and $0.0125i$ for scattering via the $F'' = 2$ level.

5.4.2 Schmidt States for the D1 $\Lambda_{1y,2x}^2$ Subsystem

Suppose now that the y -polarized field is resonant with the $1 \leftrightarrow 2'$ transition ($\omega_y = \omega_{2'} - \omega_1$) and that the x -polarized field is resonant with the $2 \leftrightarrow 2'$ transition ($\omega_x = \omega_{2'} - \omega_2$). This system will

¹¹The Raman scattering susceptibility is the same for Stokes and anti-Stokes scattering because the polarizability is completely symmetric [cf. eqn. (5.21)]: the polarization in mode 2 due to a field E in mode 1 is the same as the polarization in mode 1 due to the field E in mode 2.

Schmidt States of the $\Lambda_{1y,2x}^1$ System

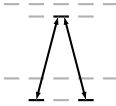
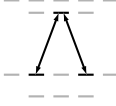
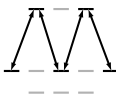
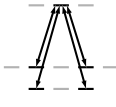
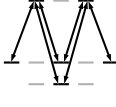
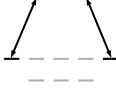
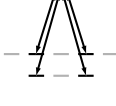
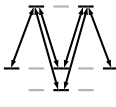
Coupling constant Ω_n	Schmidt state $ G_n\rangle$	$\check{\chi}_{12}$		Coupling Scheme
		$1''$	$2''$	
0	$\frac{ 1,-1\rangle+ 1,1\rangle}{\sqrt{2}}$	0	0	
0	$\frac{ 2,-1\rangle+ 2,1\rangle}{\sqrt{2}}$	0	0	
0	$\frac{ 2,-2\rangle+\sqrt{6} 2,0\rangle+ 2,2\rangle}{\sqrt{8}}$	0	0	
0	$\frac{\sqrt{3}\Omega_x(1,-1\rangle- 1,1\rangle)-i\Omega_y(2,-1\rangle- 2,1\rangle)}{\sqrt{6 \Omega_x ^2+2 \Omega_y ^2}}$	$\frac{i}{16}$	$\frac{i}{16}$	
0	$\frac{\sqrt{32}\Omega_x 1,0\rangle+i\Omega_y(\sqrt{3} 2,-2\rangle-\sqrt{2} 2,0\rangle+\sqrt{3} 2,2\rangle)}{\sqrt{32 \Omega_x ^2+8 \Omega_y ^2}}$	$\frac{i}{15}$	0	
$\frac{1}{2}\Omega_x$ or 0.5Ω	$\frac{ 2,-2\rangle- 2,2\rangle}{\sqrt{2}}$	0	0	
$\sqrt{\frac{1}{12} \Omega_y ^2+\frac{1}{4} \Omega_x ^2}$ or 0.58Ω	$\frac{\Omega_y^*(1,-1\rangle- 1,1\rangle)+i\sqrt{3}\Omega_x^*(2,-1\rangle- 2,1\rangle)}{\sqrt{6 \Omega_x ^2+2 \Omega_y ^2}}$	$\frac{-i}{16}$	$\frac{-i}{16}$	
$\sqrt{\frac{1}{12} \Omega_y ^2+\frac{1}{3} \Omega_x ^2}$ or 0.64Ω	$\frac{\sqrt{2}\Omega_y^* 1,0\rangle-i\Omega_x^*(\sqrt{3} 2,-2\rangle-\sqrt{2} 2,0\rangle+\sqrt{3} 2,2\rangle)}{\sqrt{8 \Omega_x ^2+2 \Omega_y ^2}}$	$\frac{-i}{15}$	0	

Table 5.1: One possible Schmidt decomposition of the sodium D1 $\Lambda_{1y,2x}^1$ subsystem. Numerical values of the coupling constants are given for the case $\Omega_x = \Omega_y \equiv \Omega$. $\check{\chi}_{12}$ is the atomic susceptibility for coherent Raman scattering. $1''$ and $2''$ refer to scattering via the $F'' = 1$ and $F'' = 2$ levels, respectively, of $3P_{3/2}$.

be denoted $\Lambda_{1y,2x}^2$. The interaction Hamiltonian that describes this subsystem is

$$H_{1y,2x}^2 = \frac{\hbar}{2} \begin{pmatrix} \frac{i\Omega_y}{\sqrt{4}} & & & & & & & & \frac{\Omega_x}{\sqrt{12}} \\ & \frac{i\Omega_y}{\sqrt{8}} & & & & & & & \frac{\Omega_x}{\sqrt{8}} \\ \frac{i\Omega_y}{\sqrt{24}} & & \frac{i\Omega_y}{\sqrt{24}} & & & & & & \frac{\Omega_x}{\sqrt{8}} \\ & \frac{i\Omega_y}{\sqrt{8}} & & & & & & & \frac{\Omega_x}{\sqrt{8}} \\ & & & \frac{i\Omega_y}{\sqrt{4}} & & & & & \frac{\Omega_x}{\sqrt{12}} \\ & & & & & & & & \frac{\Omega_x}{\sqrt{8}} \\ & & & & & & & & \frac{\Omega_x}{\sqrt{12}} \\ & & & & & & & & \frac{\Omega_x}{\sqrt{8}} \\ & & & & & & & & \frac{\Omega_x}{\sqrt{12}} \end{pmatrix} \quad (5.22)$$

which can be obtained using the last five rows of Table B.1. The Schmidt states and singular values for this system are given in Table 5.2. With five excited states, there are five bright states and three dark states. One of the dark states does not possess any hyperfine coherence. Again, the bright and dark states have equal and opposite Raman susceptibilities. In the case of complete trapping in the dark states, such that each dark state has population $1/3$, the net Raman susceptibility is $0.021i$ for scattering via the $F'' = 1$ level and $0.069i$ for scattering via the $F'' = 2$ level.

5.4.3 Magnetic Fields and “The” Sodium D1 Dark State

The Schmidt states for the $\Lambda_{1,2}^1$ and $\Lambda_{1,2}^2$ subsystems appear to be very similar; indeed, many of them have the same configuration. However, even those which have the same configuration have different coefficients. Therefore, if frequent velocity-changing collisions cause the atom to be Doppler shifted from one subsystem to the other on a time scale shorter than the optical pumping time, then little coherent population trapping will occur. Furthermore, all the Schmidt states of Tables 5.1 and 5.2 are unstable in the presence of a magnetic field. However, the dark states of the $\Lambda_{1,2}^1$ system may be recombined to yield a different set of dark states which include the three states given in Table 5.3. These three states remain dark when a z magnetic field is applied, although the Raman frequencies of the latter two states shift with the Zeeman levels. Three similar states can be constructed for the $\Lambda_{1y,2x}^2$ subsystem, although the two which involve the $m = 1$ or $m = -1$ ground states are not very dark; they are coupled to the $|2, -2\rangle$ and $|2, 2\rangle$ excited states. Nevertheless, for either subsystem, three separate trap states can be observed as a function of Raman frequency: the one involving the $m = 0$ states at 1772 MHz, the one involving the $m = 1$ states at the upshifted (or downshifted)

Schmidt States of the $\Lambda_{1y,2x}^2$ System

Coupling constant Ω_n	Schmidt state $ G_n\rangle$	$\check{\chi}_{12}$		Coupling Scheme
		1''	2''	
0	$\frac{\sqrt{3} 2,-2\rangle - \sqrt{2} 2,0\rangle + \sqrt{3} 2,2\rangle}{\sqrt{8}}$	0	0	
0	$\frac{i\Omega_x\sqrt{32} 1,0\rangle + \Omega_y(\sqrt{3} 2,-2\rangle + \sqrt{18} 2,0\rangle + \sqrt{3} 2,2\rangle)}{\sqrt{32 \Omega_x ^2 + 24 \Omega_y ^2}}$	0	$\frac{1}{7}$	
0	$\frac{i\Omega_x(1,-1\rangle - 1,1\rangle) + \sqrt{3}\Omega_y(2,-1\rangle - 2,1\rangle)}{\sqrt{2 \Omega_x ^2 + 6 \Omega_y ^2}}$	$\frac{i}{16}$	$\frac{i}{16}$	
$\frac{1}{\sqrt{12}}\Omega_x$ or 0.29Ω	$\frac{ 2,-2\rangle - 2,2\rangle}{\sqrt{2}}$	0	0	
$\sqrt{\frac{1}{4} \Omega_y ^2 + \frac{1}{12} \Omega_x ^2}$ or 0.58Ω	$\frac{i\sqrt{3}\Omega_y^*(1,-1\rangle - 1,1\rangle) + \Omega_x^*(- 2,-1\rangle + 2,1\rangle)}{\sqrt{2 \Omega_x ^2 + 6 \Omega_y ^2}}$	$-\frac{i}{16}$	$-\frac{i}{16}$	
$\sqrt{\frac{1}{4} \Omega_y ^2 + \frac{1}{3} \Omega_x ^2}$ or 0.76Ω	$\frac{i\sqrt{6}\Omega_y^* 1,0\rangle - \Omega_x^*(\sqrt{6} 2,0\rangle + 2,-2\rangle + 2,2\rangle)}{\sqrt{8 \Omega_x ^2 + 6 \Omega_y ^2}}$	0	$-\frac{i}{7}$	
$\simeq \sqrt{\frac{2-\sqrt{3}}{3} \frac{ \Omega_x\Omega_y ^2}{ \Omega_x ^2 + \Omega_y ^2}}$ or 0.21Ω	$\simeq \frac{\Omega_x(1,-1\rangle + 1,1\rangle) - i\Omega_y(2,-1\rangle + 2,1\rangle)}{\sqrt{2 \Omega_x ^2 + 2 \Omega_y ^2}}$	0	$\frac{i}{4\sqrt{3}}$	
$\simeq \sqrt{\frac{1}{3} \frac{ \Omega_x ^4 + \Omega_y ^4 + \sqrt{3} \Omega_x\Omega_y ^2}{ \Omega_x ^2 + \Omega_y ^2}}$ or 0.79Ω	$\simeq \frac{\Omega_y^*(1,-1\rangle + 1,1\rangle) + i\Omega_x^*(2,-1\rangle + 2,1\rangle)}{\sqrt{2 \Omega_x ^2 + 2 \Omega_y ^2}}$	0	$\frac{-i}{4\sqrt{3}}$	

Table 5.2: The Schmidt decomposition of the sodium D1 $\Lambda_{1y,2x}^2$ subsystem. Numerical values of the coupling constants are given for the case $\Omega_x = \Omega_y \equiv \Omega$. $\check{\chi}_{12}$ is the atomic susceptibility for coherent Raman scattering 1'' and 2'' refer to scattering via the $F'' = 1$ and $F'' = 2$ levels, respectively, of $3P_{3/2}$.

Trap States in the Presence of Magnetic Field

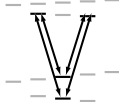
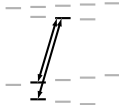
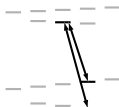
Coupling constant Ω_n	Schmidt state $ G_n\rangle$	$\check{\chi}_{12}$		Coupling Scheme
		1''	2''	
0	$\frac{i\Omega_x 1,0\rangle + \Omega_y 2,0\rangle}{\sqrt{ \Omega_x ^2 + \Omega_y ^2}}$	$\frac{-i}{24}$	$\frac{i}{8}$	
0	$\frac{i\sqrt{3}\Omega_x 1,-1\rangle + \Omega_y 2,-1\rangle}{\sqrt{3 \Omega_x ^2 + \Omega_y ^2}}$	$\frac{i}{32}$	$\frac{3i}{32}$	
0	$\frac{i\sqrt{3}\Omega_x 1,1\rangle + \Omega_y 2,1\rangle}{\sqrt{3 \Omega_x ^2 + \Omega_y ^2}}$	$\frac{i}{32}$	$\frac{3i}{32}$	

Table 5.3: Three alternative dark states in the sodium D1 $\Lambda_{1y,2x}^1$ subsystem, which remain stable in the presence of a DC magnetic field.

frequency, and the one involving the $m = -1$ states at the downshifted (upshifted) frequency.

The first state in Table 5.3 is special: It is common to both systems, is essentially insensitive to DC magnetic fields¹², and involves hyperfine coherence. Because of its robustness and desirable properties, it is in principle the best dark state for coherent preparation. Hence I designate it “the” dark state of the D1 Λ system:

$$|d_0\rangle = \frac{i\Omega_{2x}|1,0\rangle + \Omega_{1y}|2,0\rangle}{\sqrt{|\Omega_{2x}|^2 + |\Omega_{1y}|^2}}. \quad (5.23)$$

What is the physical nature of the state (5.23)? The $m = 0$ states are superpositions of nuclear

¹²Although the $m = 0$ states are not shifted by a z magnetic field, the field induces a coupling between them (note the off-diagonal elements in Table B.3). However, a static field is so far out of resonance with this transition (1772 MHz) that the characteristic transition rate, $\sim L^2/1772$ MHz (where L is the magnetic Rabi frequency), is usually negligible.

and electronic spin states:

$$|1, 0\rangle = \frac{|\frac{1}{2}\rangle|\downarrow\rangle - |-\frac{1}{2}\rangle|\uparrow\rangle}{\sqrt{2}} \quad (5.24)$$

$$|2, 0\rangle = \frac{|\frac{1}{2}\rangle|\downarrow\rangle + |-\frac{1}{2}\rangle|\uparrow\rangle}{\sqrt{2}} \quad (5.25)$$

where, e.g., $|\frac{1}{2}\rangle|\downarrow\rangle$ denotes the state with nuclear spin projection $1/2$ and electron spin projection $-1/2$. For the sake of discussion let us take $\Omega_{2x} = \Omega_{1y}$. In a physical reference frame where the energy difference between hyperfine levels has not been mathematically removed, the dark state evolves as

$$|d_0(t)\rangle = \frac{|1, 0\rangle + e^{-i\omega_{21}t}|2, 0\rangle}{\sqrt{2}} \quad (5.26)$$

$$= e^{-i\omega_{21}t/2} \left(\cos \frac{\omega_{21}t}{2} |\frac{1}{2}\rangle|\downarrow\rangle - i \sin \frac{\omega_{21}t}{2} |-\frac{1}{2}\rangle|\uparrow\rangle \right) \quad (5.27)$$

Thus the hyperfine coherence between $m = 0$ states represents a simultaneous oscillation of the electronic and nuclear spin projections. Similar interpretations can be given to other types of ground state coherences. For this reason, ground state coherences in alkali vapors are sometimes referred to as spin coherences or spin oscillations.

5.4.4 Schmidt States with Parallel Polarized Fields

For historical reasons, my work has always involved cross polarized control fields. One may ask whether parallel polarized fields (say, both x polarized) could also be used for coherent population trapping. I find that the Schmidt states for parallel polarized fields are superficially similar to those for cross polarized fields, but at the level of detail there are important differences. Firstly, the dark states of the Λ_{1x2x}^1 and the dark states of Λ_{1x2x}^2 span orthogonal spaces. That is, there is no dark state common to both subsystems. Secondly, there is no linear combination of dark states that is insensitive to magnetic fields. Finally, the signs of the hyperfine coherences are such that the Doppler-averaged Raman susceptibility vanishes for every Schmidt state. Thus coherent Raman scattering should not occur with parallel polarized fields. Experimentally, I have found elec-

tromagnetically induced transparency to be extremely weak and coherent Raman scattering to be nonexistent with parallel fields. Henceforth, I will consider only cross polarized control fields.

5.5 Numerical Studies

Having developed some physical intuition, we are now in a position to appreciate the results of numerical studies of coherent population trapping in the D1 transitions of sodium. The results which follow were obtained by numerically solving the steady-state equations for the density matrix of a system comprised of the sixteen states in the sodium $3S_{1/2}$ and $3P_{1/2}$ levels and two linearly polarized fields of equal intensity with a frequency difference close to the Raman frequency. (See Appendix D for details of the master equation and method of solution.) The ground state relaxation rate was taken to be 0.1 MHz for all calculations.

5.5.1 Without a Magnetic Field

The populations of the $\Lambda_{1y,2x}^1$ and $\Lambda_{1y,2x}^2$ Schmidt states as a function of optical intensity are shown in Fig. 5.6. For $\Lambda_{1y,2x}^1$ the fields were tuned to the $F' = 1$ level ($\Delta = 0$ MHz), while for $\Lambda_{1y,2x}^1$ the fields were tuned to the $F' = 2$ level ($\Delta = 189$ MHz). Consider first the $\Lambda_{1y,2x}^1$ subsystem: At very low intensities, the population is evenly distributed among all 8 Schmidt states. As the intensity increases, the populations of the 5 dark states increase to approximately 1/5 each, while the populations of the bright states decrease to approximately zero. The pumping from bright to dark states saturates when the nominal Rabi frequencies are approximately 5 MHz. Similar behavior occurs in the $\Lambda_{1y,2x}^2$ subsystem: starting from an even distribution, the populations of the 3 dark states increase to approximately 1/3 each, while the populations of the bright states decrease to approximately zero. Note that one of the states (the 7th Schmidt state, a weakly coupled state), acts as a trap state at low intensities (population initially increasing with intensity) and as a bright state at high intensities (population decreasing with intensity). For the $\Lambda_{1y,2x}^2$ subsystem, the trapping threshold occurs at approximately 10 MHz. For both subsystems, trapping is essentially complete when the fields have nominal Rabi frequencies of 25 MHz.

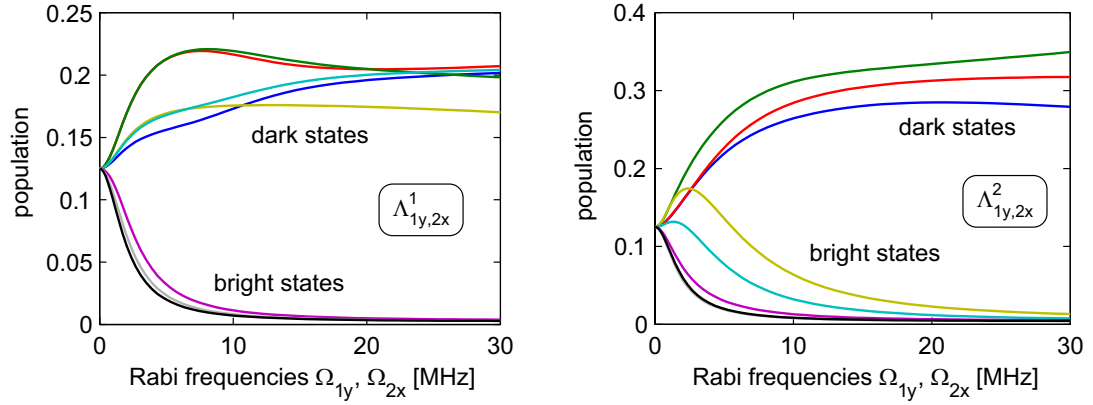


Figure 5.6: Population trapping in the $\Lambda_{1y,2x}^1$ and $\Lambda_{1y,2x}^2$ subsystems. As the Rabi frequencies of the control fields increase, more population is pumped into the dark states. *Conditions:* $\delta = 0$, $\Gamma_G = 0.1$ MHz.

The pumping of population into dark states causes a reduction of the absorption. The amount of reduction may be characterized by the saturation parameter s , defined here by $\alpha = \alpha_{\text{weak field}}/(1+s)$. In §3.2.2 we saw that the saturation parameter of a 3-state Λ system at Raman resonance is the same for both fields and is proportional to the total intensity, in fact proportional to Ω^2/Γ_g . In a system with many ground states, the saturation also depends on this ratio. But as shown in Fig. 5.7, the saturation parameter has a sub-linear dependence on this ratio. The reason is that as the intensity increases, optical pumping moves population from Schmidt states with large coupling constants to states with smaller coupling constants, and the fields become less effective at optical pumping. One may say that the Rabi frequency of the interaction becomes much smaller than the nominal Rabi frequencies of the fields, or that the saturation intensity increases as the optical intensity increases. The net result is that the actual saturation is much less than the nominal saturation parameter $(\Omega_x^2 + \Omega_y^2)/(4\gamma_G\gamma_E)$.

According to Tables 5.1 and 5.2, there are two dark superpositions for each subsystem involving coherences between $F = 1$ and $F = 2$ ground states. Several of these coherences are shown as a function of the Raman detuning in Fig. 5.8. The nominal Rabi frequencies of the fields are 25 MHz each so that trapping is essentially complete. For the $\Lambda_{1y,2x}^1$ subsystem, the two dark states which

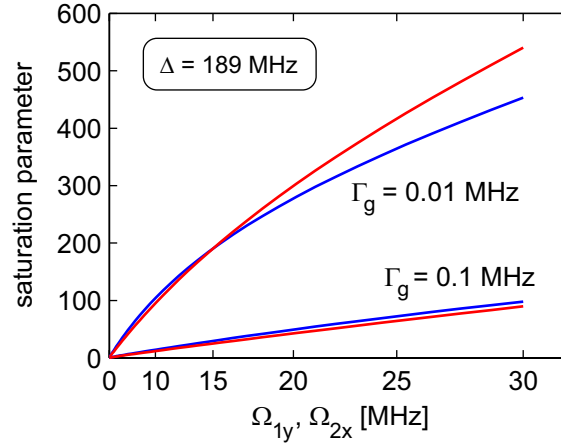


Figure 5.7: Saturation of absorption. At the Raman resonance, saturation results from population trapping. The saturation parameter increases sub-linearly with intensity (the horizontal scale is linear in intensity) because optical pumping gets more difficult as more population becomes trapped in dark states.

involve hyperfine coherence are approximately equally populated and contain approximately 40% of the total population, resulting in coherences between the pairs of states with $m = 0$, $m = 1$, and $m = -1$ of approximately 0.05. For the $\Lambda_{1y,2x}^2$ subsystem, the two hyperfine coherent dark states account for over 70% of the population, resulting in somewhat larger coherences.

Associated with the trapping of population in dark states is a decrease in the susceptibility. A pronounced dip in the susceptibilities¹³ occurs at the Raman resonance (Fig. 5.9, left) at both $\Delta = 0$ ($\Lambda_{1y,2x}^1$ dominant) and $\Delta = 189$ MHz ($\Lambda_{1y,2x}^2$ dominant). The reduction of absorption at Raman resonance can also be seen by comparing the left and right plots of Fig. 5.10 (note the different vertical scales). In these two plots, the peaks correspond to the $F' = 1$ and $F' = 2$ hyperfine levels. Together, Figs. 5.9 and 5.10 show that coherent population trapping reduces the absorption only by a factor of 2-4, even though the nominal pumping rate ($R = \frac{1}{4} \frac{(25 \text{ MHz})^2}{(10 \text{ MHz})/2} = 30$ MHz at optical resonance) is much larger than the relaxation rate, 0.1 MHz. This result supports the idea that coherent effects are harder to achieve and less pronounced in many-state systems.

¹³Both imaginary (absorptive) and real (dispersive) parts of the susceptibility are reduced at the Raman resonance. However, the absorptive component is more easily measured and reveals the effect more clearly (at resonance the dispersive part is already at or near a zero crossing).

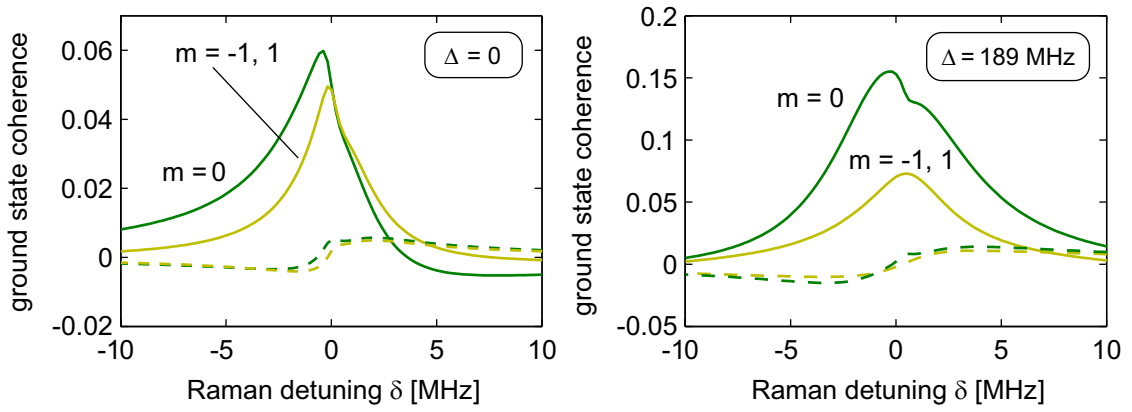


Figure 5.8: Real (dashed) and imaginary (solid) parts of hyperfine coherences involving states of particular magnetic number m . Large coherences (as a fraction of the population in each pair of states) develop in the vicinity of Raman resonance. *Conditions:* $\Omega_{1y} = \Omega_{2x} = 25$ MHz, $\Gamma_G = 0.1$ MHz.

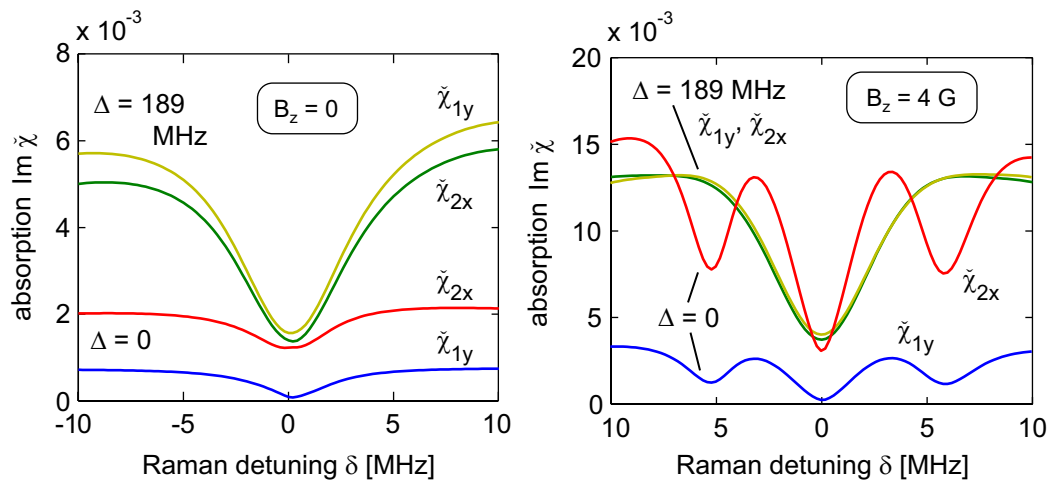


Figure 5.9: The susceptibilities for absorption of the control fields (imaginary parts of the susceptibility). Both fields show induced transparency in the vicinity of Raman resonance. In the presence of a magnetic field (*right*), the Raman resonance splits into three features. *Conditions:* $\Omega_{1y} = \Omega_{2x} = 25$ MHz, $\Gamma_G = 0.1$ MHz.

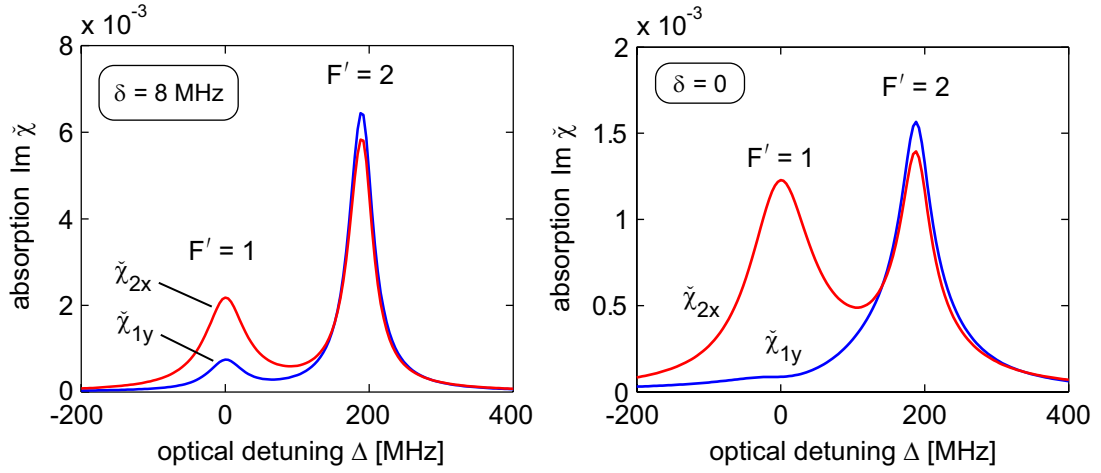


Figure 5.10: The absorption spectra for the control fields when resonant (*right*) or detuned (*left*) from the Raman frequency. Absorption is reduced across the entire D1 line at Raman resonance (note different vertical scales). *Conditions:* $\Omega_{1y} = \Omega_{2x} = 25$ MHz, $\Gamma_G = 0.1$ MHz.

Also associated with coherent population trapping is a large Raman scattering susceptibility. If the pump fields prepare the atom with density matrix $\hat{\rho}$, then the susceptibility of the prepared atom to a weak probe field is

$$\tilde{\chi} = i \sum_{g,g'} \sum_e \frac{\Gamma_E/2}{\gamma_E - i\Delta'_e} \langle g | \hat{\rho} | g' \rangle \tilde{\mu}_{g'e} \tilde{\mu}_{eg}, \quad (5.28)$$

where Δ'_e is the detuning of the probe field from excited state e . Fig. 5.11 shows the dependence of the Raman susceptibility $\tilde{\chi}_{12}$ on the detunings Δ and Δ' of the pump and probe fields from the $3P_{1/2}$ and $3P_{3/2}$ levels, respectively. (Just as $\Delta = 0$ means that the pump fields are tuned to the lowest hyperfine level of $3P_{1/2}$, $\Delta' = 0$ means that the probe field is tuned to the lowest hyperfine level of $3P_{3/2}$.) In this plot the pump and probe frequencies differ by a fixed amount, as is the case when the frequency shifts are caused by the Doppler effect.¹⁴ The pump-probe frequency difference was chosen so that $\Delta' = 50$ ($F'' = 2$) when $\Delta = 189$ ($F' = 2$), which maximizes both the peak and Doppler-averaged Raman susceptibility. The Raman susceptibility peaks at a value of about

¹⁴The Doppler effect is described in §6.1.3. If the pump and probe fields are copropagating, the ratio of their Doppler shifts is just the ratio of their wavelengths. The wavelengths of the D1 and D2 lines differ by only 0.1%; thus the pump and probe frequencies are shifted by essentially the same amount.

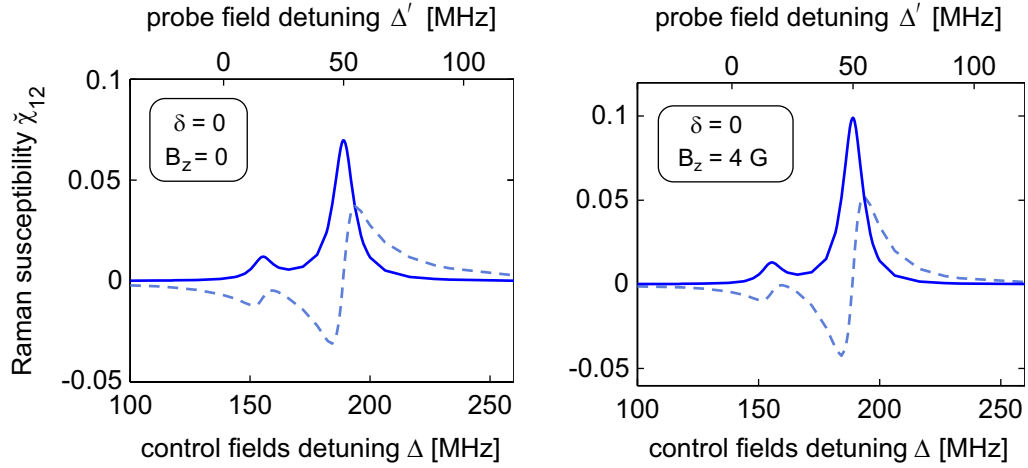


Figure 5.11: The real (dashed) and imaginary (solid) parts of the Raman scattering susceptibility for a probe which scatters off the hyperfine coherence created by the control fields. Although the distribution of ground state population is different in the presence of a magnetic field, the Raman scattering susceptibility is not significantly affected. *Conditions:* $\Omega_{1y} = \Omega_{2x} = 25$ MHz, $\Gamma_G = 0.1$ MHz.

$0.07i$, in agreement with the prediction of §5.4.2.

5.5.2 With a Magnetic Field

The calculations of the previous section were repeated, this time assuming a magnetic field of 4 Gauss in the z direction. As discussed in §5.4.3 the Schmidt basis is no longer meaningful in this case, but nevertheless there exist three trap states which possess hyperfine coherence between pairs of states with $m = 0$, $m = 1$, and $m = -1$. As shown in Fig. 5.12, these three coherences peak at different Raman detunings. As mentioned previously, the $m = 0$ trap is a true dark state in both $\Lambda_{1,2}^1$ and $\Lambda_{1,2}^2$ subsystems. In contrast, the $m = 1, -1$ states are weakly coupled (i.e., poor traps) in the $\Lambda_{1,2}^2$ subsystem; hence the rather weak coherence features when $\Delta = 189$ MHz (Fig. 5.12, right). In the presence of a magnetic field, a majority of the population can be trapped in one of these three states, as opposed to being distributed over multiple trap states in the case of no magnetic field (see Fig. 5.6). However, the total amount of trapped population is slightly less with a magnetic field than

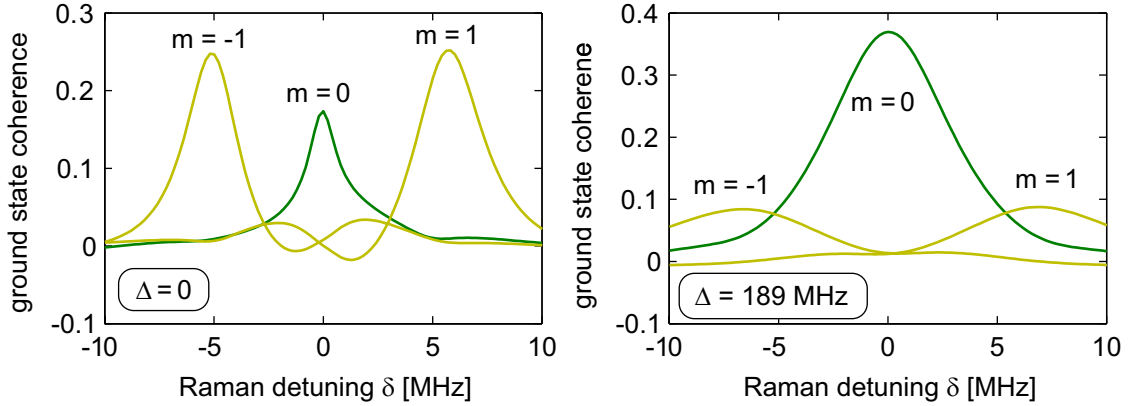


Figure 5.12: Imaginary parts of hyperfine coherences involving states of particular same magnetic number m . A magnetic field lifts the Zeeman degeneracy and leads to different Raman frequencies for the hyperfine coherences. *Conditions:* $\Omega_{1y} = \Omega_{2x} = 25$ MHz, $\Gamma_G = 0.1$ MHz.

without. This is probably due in part to relaxation bias and, depending on the size of the Zeeman shift, in part due to the decrease in the optical pumping rates out of the bright states as the Zeeman states are shifted out of resonance with the pump fields.

Associated with each trap state is a separate absorption dip (Fig. 5.9, right). Three dips are clearly visible in the Raman spectrum when $\Delta = 0$ MHz. Note that the absorption outside the Raman resonances is higher than the off-resonant absorption in the case of no magnetic field (Fig. 5.9, left). This occurs because, in the absence of a magnetic field, two out of five dark states do not involve hyperfine coherence and can trap population regardless of the Raman detuning. When a magnetic field is applied, these two trap states no longer exist; therefore the off-resonant absorption is higher. For $\Delta = 189$ MHz, only one absorption dip is visible; because the trapping in $m = 1, -1$ states is very poor, the absorption dips are too small to be seen.

As suggested previously, the $m = 0$ superposition state is the most robust trap state in the presence of a magnetic field. Nearly 80% of the population is pumped into this state when the pump fields are tuned to $F' = 2$ (Fig. 5.13). Although this is slightly less than the amount of coherently trapped population when no magnetic field is present (90%), the Raman susceptibility in this case is slightly larger (Fig. 5.11, right).

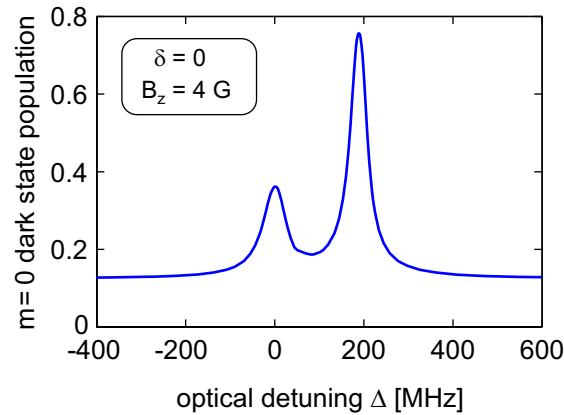


Figure 5.13: Population of “the” sodium D1 dark state [eqn. (5.23)] in the presence of a magnetic field. *Conditions:* $\Omega_{1y} = \Omega_{2x} = 25$ MHz, $\Gamma_G = 0.1$ MHz.

5.6 Summary

To understand coherent population trapping in systems with many states, the concept of dark states and bright states (which helps explain the physics of coherent population trapping in 3-state systems) was generalized to the concept of Schmidt states, which may be thought of as eigenstates of the optical excitation. Schmidt states may be either dark (uncoupled), bright (strongly coupled), or “dim” (weakly coupled). Under certain conditions, the action of multiple coherent fields in a many-state system can be understood in terms of optical pumping among Schmidt states. When there are relatively few trap states, relaxation tends to depopulate the trap states (relaxation bias). On the other hand, if there are multiple trap states, some of them (extraneous trap states) may have undesirable properties and compete with the desired states in trapping population. The behavior of many-state systems is further complicated by the fact that magnetic fields lift the degeneracy of state energies, causing different pairs of states to have different resonant frequencies. Generally speaking, the complications of many-state systems make coherent population trapping more difficult than in few-state systems, and correspondingly make coherent optical effects less pronounced.

The problem of a sodium atom interacting with two cross-linearly polarized fields to form a 3-level Λ system was analyzed in detail. Two such Λ systems exist in the D1 line of sodium, and

their Schmidt ground states were presented and discussed. It was found that both systems have multiple dark states, although only one state (a superposition of the two $m = 0$ ground states) is dark for both systems in the presence or absence of a magnetic field, and that some of the dark states do not involve any hyperfine coherence. Numerical studies showed that moderately large hyperfine coherences, as well as coherent optical phenomena such as electromagnetically induced absorption and coherent Raman scattering, can be induced via coherent population trapping; however, such effects are less pronounced than what one would find for a comparable Λ system composed of only three states.

Chapter 6

Coherent Preparation of Atomic Vapors

So far I have pretended that the atoms being coherently prepared are stationary and isolated, the only concession to the contrary being a phenomenological decay term which thermalizes the density matrix. Of course, atoms exist within an environment, and they are usually not at rest on the optical table just waiting to be experimented upon. In a typical atomic vapor experiment, the atoms are moving at speeds of kilometers per second, colliding with each other and with their container. Furthermore, the atoms act back on the electromagnetic field, producing an illumination different than what was applied. Technical issues, which always come into play in an experiment, can complicate or mask the desired phenomena. In this chapter I explore a variety of considerations which apply to experiments in atomic vapors, with a particular view toward implications for coherent preparation. Much of the relevant physics was developed in the 1950's and 1960's in studies of optical alignment of spin in atomic vapors. Many of the lessons learned from these studies apply to the present research because hyperfine coherences in alkalis are in fact coherences between different spin states. For a definitive guide to the foundational work in atomic vapors, the reader should consult Happer's review on optical pumping [91].

6.1 Effects Resulting from Atomic Motion

6.1.1 Exodus from the Interaction Region

In a typical vapor cell experiment, the control fields used to coherently prepare the atoms illuminate only a portion of the cross section of the vapor. Since the atoms in a hot vapor have a thermal velocity distribution, atoms which have been coherently prepared eventually leave the interaction region; meanwhile, atoms outside the interaction region, which generally have little or no coherence¹, enter the interaction region. This process leads to decay of the average coherence of the vapor in the interaction region. More generally, if we characterize the illuminated atoms by an average density matrix $\bar{\rho}$, atomic motion contributes the term $-\Gamma_{\text{trans}}(\bar{\rho} - \rho^{\text{rsv}})$ to $d\bar{\rho}/dt$, where ρ^{rsv} is the density matrix of an (unprepared) atom from the reservoir of unilluminated atoms and Γ_{trans} is the inverse of the characteristic transit time t_{trans} (the length of time an atom spends in the interaction region).

The interaction time depends on the size of the interaction region, the mean speed of the atoms, and the type of movement (ballistic or diffusive). The average speed is

$$\bar{v} = \sqrt{\frac{8k_B T}{\pi m}}. \quad (6.1)$$

where T is the vapor temperature in Kelvin, m is the atomic mass, and $k_B = 1.38 \times 10^{-23}$ J/K is Boltzmann's constant. For sodium vapor, a typical operating temperature is 150 °C. At this temperature $\bar{v} = 622$ m/s. The mean free path is

$$l = \frac{1}{\sigma \mathcal{N}} \quad (6.2)$$

where σ is the collisional cross section of atoms in a vapor and \mathcal{N} is the number density of atoms. Kinematic cross sections for gases are on the order of 5×10^{-15} cm² [93]. For a sodium density $\mathcal{N} = 1.4 \times 10^{11}$ cm⁻³, the mean free path is $l \sim 1500$ cm, which is much larger than the interaction

¹Atoms outside the interaction region are subject to processes which decrease coherence and thermalize the population distribution. In particular, collisions with the wall of the container cause spin flips which destroy hyperfine and Zeeman coherences. However, it is experimental lore that decoherence due to wall collisions can be drastically reduced by coating the container walls with paraffin wax [92]. (This technique would not seem to be applicable to sodium vapor, which requires a moderately high operating temperature.) In such cases coherence is built up nearly uniformly throughout the cell volume.

region. Hence, at typical operating temperatures, a pure sodium vapor operates in the ballistic regime. This means that the interaction time between an atom and beam of radius $r = 1$ mm is $t_{\text{trans}} \lesssim 2r/\bar{v} = 3 \mu\text{s}$.

The interaction time can be increased by adding a buffer gas. When the mean free path becomes small compared to the interaction region, the movement of atoms is diffusive with a diffusion constant [89]

$$D \approx \frac{\bar{v}l}{3}. \quad (6.3)$$

For helium, $\mathcal{N} = 3.3 \times 10^{16} \text{ cm}^{-3} \times P$ where P is the pressure in torr. The total cross section for velocity-changing collisions between helium and sodium has been measured to be $0.16 \times 10^{-17} \text{ cm}^2$ [94]. The mean free path is then $l = (20P)^{-1} \text{ cm}$, which is 0.5 mm at $P = 1$ torr. This gives an estimated diffusion coefficient of $1040 \text{ cm}^2/\text{s} \cdot \text{torr}$, which agrees with the results of more direct measurements [95] to within experimental error. The interaction time is on the order of the time it takes an atom to diffuse a distance r . Since the average distance an atom travels in a time t is $\sim \sqrt{Dt}$, we find $t_{\text{trans}} \sim r^2/D = 10 \mu\text{s}$.

The decay constant Γ_{trans} can be related to the diffusion constant by a simple argument: If a group of atoms initially covers an area A_0 , then after a time t the atoms are distributed over an area of approximately $A_0 + Dt$. Then the fraction of atoms in the original area² is $A_0/(A_0 + Dt)$ or

$$f = \frac{1}{1 + \Gamma_{\text{trans}}t} \quad (6.4)$$

where $\Gamma_{\text{trans}} = D/A_0$. (Rigorous analysis of the diffusive spreading of an initial Gaussian distribution validates eqn. (6.4) and yields $\Gamma_{\text{trans}} = D/r^2 = 1/t_{\text{trans}}$.)

Since the density of the vapor is uniform at all times, every atom which leaves the interaction region is replaced by an atom from outside the interaction region. The atoms outside the interaction region will have varying amounts of coherence, since some have just come from the interaction region while others have been outside the interaction region long enough to completely lose their coher-

²In the early studies of vapor relaxation (in the 1950's and 60's), experimenters tended to illuminate the entire cell. In such cases, the relaxation curves were close to exponential, corresponding to the decay of the lowest-order eigensolution of the diffusion equation. In the present work only the central portion of the cell is illuminated, and the eigenmode decomposition is less useful.

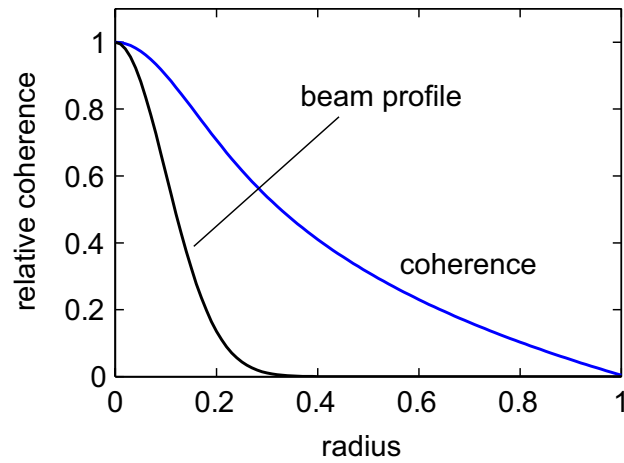
ence. Thus the rate at which the total coherence in the interaction region decays is related to, but somewhat less than, D/r^2 . However, the decay is still described reasonably well by a function of the form (6.4), as shown in Fig. 6.1. In the mathematical model which serves as the basis for the numerical studies in this work (see Appendix D), the effect of diffusion is approximated by exponential decay of the density matrix along with a compensating infusion of population in a thermal distribution.

6.1.2 Grating Washout

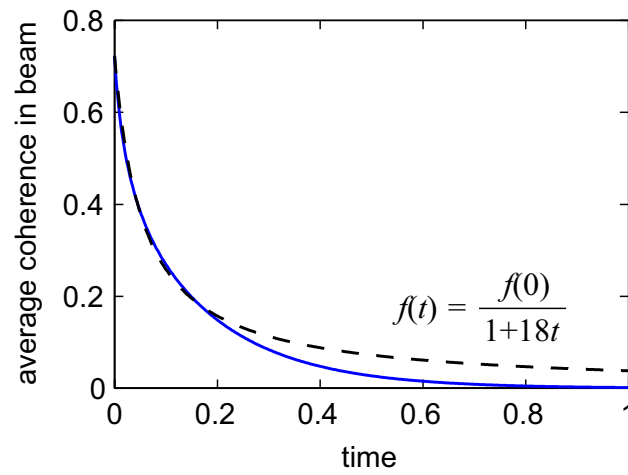
The coherence that exists throughout a coherently prepared vapor may be thought of as a type of grating. Such gratings can be associated with most wave mixing phenomena. A phenomenon which affects gratings in atomic vapors is “grating washout.” Since the grating is formed by atoms which are free to move, travel of atoms causes the grating to dissipate. In the case of a hyperfine coherence grating, the washout occurs as atoms with opposite phases migrate to the same region. How fast the grating decays depends directly on the rate of travel and inversely on the period of the grating. For the hyperfine coherence grating formed by two copropagating fields, the period is

$$\Lambda = \frac{2\pi}{k_1 - k_2}. \quad (6.5)$$

For a first analysis, we may take k_1 and k_2 to be the free-space wavenumbers, in which case $\Lambda = c/(\nu_1 - \nu_2)$, where $\nu = \omega/(2\pi) = c/\lambda$. At the Raman resonance of sodium, $\nu_1 - \nu_2 = 1772$ MHz which gives $\Lambda = 17$ cm. In a typical vapor cell of 8 cm or less, the grating goes through at most half a period over the length of the cell. Thus the majority of atoms have similar phases, and complete washout is not even possible. However, even if many periods are contained within the length of the cell, the period of the grating will certainly be much larger than the transverse extent of the beam. Most atoms will leave the beam region before travelling half a grating period in the longitudinal direction. Thus, grating washout with copropagating beams should be negligible compared to decoherence due to exodus.



(a)



(b)

Figure 6.1: Diffusion in a cylindrical volume of unit radius. The diffusant density represents the local degree of coherent preparation. The boundary condition is that coherence is destroyed at the outer boundary (radius = 1). (a) The intensity profile of the control fields and the equilibrium distribution of coherence as a function of radius. (b) The decay of the coherence in the illumination region (solid line), along with a function of the form (6.4). The decay constant is $\Gamma_{\text{trans}} = 18$, whereas a simple argument gives $\Gamma_{\text{trans}} = D/r^2 = 100$.

6.1.3 Doppler Shifts

An atom sees a slightly different laser frequency when it is moving than when it is at rest. The shift in frequency (the *Doppler shift*) is $\Delta_v = \mathbf{k} \cdot \mathbf{v}$ where \mathbf{k} is the wavevector of the laser and \mathbf{v} is the velocity of the atom. The distribution of velocities in any Cartesian dimension is $g(v) = \exp[-\frac{1}{2}(v/v_{\text{rms}})^2]/\sqrt{2\pi(v_{\text{rms}})^2}$ where

$$v_{\text{rms}} = \sqrt{\frac{k_B T}{m}}. \quad (6.6)$$

For sodium atoms at 150 °C, $v_{\text{rms}} = 390$ m/s. This corresponds to a root-mean-square frequency shift $\Delta_{\text{rms}} = (2\pi/\lambda)v_{\text{rms}} = 2\pi \times 662$ MHz for 589 nm wavelength light. The full width at half maximum of $g(v)$ is 1600 MHz, which is much larger than the splitting of the excited hyperfine levels (189 MHz for $3P_{1/2}$) but comparable to the frequency difference of the ground hyperfine levels (1772 MHz).

If the frequency difference of the ground states in a Raman system is small compared to the frequencies of the two driving fields, then the Raman transition is “Doppler free”: both fields experience nearly equal Doppler shifts, so that the Doppler shift of the Raman frequency is negligible. (This point will be examined further at the end of this section.) To good approximation, then, the Doppler shift simply changes the value of the excited state detuning Δ . Let us consider the effect this has on the induced absorption. At Raman resonance, the weak-field absorption rate is

$$\text{absorption rate} \propto \frac{1}{\Delta^2 + \gamma_E^2} \frac{1}{1 + s}. \quad (6.7)$$

We may write s in terms of the line center saturation s_0 as $s = s_0/(1 + \bar{\Delta}^2)$. The Doppler-broadened absorption rate is then

$$\text{absorption rate} \propto \int_{-\infty}^{\infty} \frac{1}{(\bar{\Delta}_0 - \bar{\Delta}_v)^2 + 1 + s_0} g(\bar{\Delta}_v) d\bar{\Delta}_v \quad (6.8)$$

where $\bar{\Delta}_0$ is the normalized detuning for a stationary atom. This expression, the convolution of a Lorentzian with a Gaussian, is known as the Voigt profile. Unfortunately it does not have a

simple representation. However, if the width of the Lorentzian is much less than the width of $g(\bar{\Delta}_v)$, then $g(\bar{\Delta}_v)$ can be approximated by its value at the peak of the Lorentzian. That is, if $\sqrt{1+s_0} \ll \Delta_{\text{rms}}/\gamma_E$ ($= 132$ for sodium in the absence of collisional broadening), then $g(\bar{\Delta}_v) \approx \exp[-\frac{1}{2}(\bar{\Delta}_0/\bar{\Delta}_{\text{rms}})^2]/\sqrt{2\pi\bar{\Delta}_{\text{rms}}^2}$ and

$$\text{Doppler-broadened absorption rate} \propto \frac{\pi g(\bar{\Delta}_0)}{\sqrt{1+s_0}}. \quad (6.9)$$

The factor $\pi g(\bar{\Delta}_0)$, which is approximately equal to $\gamma_E/\Delta_{\text{rms}}$ when $\Delta_0 = 0$, is the usual factor associated with the broadening of a line; if the fields were mutually incoherent or tuned outside the Raman line, the right-hand side of this expression would be just $\pi g(\bar{\Delta}_0)$. The factor $\sqrt{1+s_0}$ describes the effect of Raman saturation. We see that, in the limit of weak to moderate Raman saturation, *the factor which reduces the absorption at Raman resonance is only the square root of what it would be in the absence of Doppler broadening*. Thus Doppler broadening can significantly reduce the size of the transparency feature associated with coherent population trapping. If coherent population trapping would reduce the absorption by a factor of 100 without Doppler broadening, the reduction factor will be close to 10 when Doppler broadening is included. If the Raman saturation is very large, $s_0 \sim (\Delta_{\text{rms}}/\gamma_E)^2$, Doppler broadening does not reduce the transparency quite so much. Others [28, 96] have calculated the height and width of EIT features in a Doppler-broadened medium under various approximations.

The average coherence $\int_{-\infty}^{\infty} \rho_{21} g(\bar{\Delta}_v) d\bar{\Delta}_v$ may be calculated in a similar manner. However, this is often *not* the relevant measure of coherence in an experiment. For example, coherent Raman scattering may be used to measure the coherence. In such cases, the coherence is weighted by an additional factor which accounts for the resonance of the probe. Based on the discussion in §3.3, the amplitude of the scattered field is

$$\text{CRS efficiency} \propto \frac{\rho_{21}}{\Delta_4 + i\gamma_4} \propto \frac{1}{\bar{\Delta}_v + i\bar{\Delta}_v^2 + 1 + s_0}. \quad (6.10)$$

Here we have taken $\gamma_4 = \gamma_E$ and supposed that the probe field and control fields are nominally

resonant with their respective transitions in order to maximize the scattered field. Then

$$\text{CRS efficiency} \propto \int_{-\infty}^{\infty} \frac{\bar{\Delta}_v - i}{\bar{\Delta}_v^2 + 1} \frac{s_0}{\bar{\Delta}_v^2 + 1 + s_0} g(\bar{\Delta}_v) d\bar{\Delta}_v. \quad (6.11)$$

Again, we consider the typical situation in which the Doppler distribution is much wider than the other resonant responses, replacing $g(\bar{\Delta}_v)$ with $g(0)$. The term antisymmetric in $\bar{\Delta}_v$ vanishes, leaving

$$\text{CRS efficiency} \propto g(0) \int_{-\infty}^{\infty} \frac{s_0}{(\bar{\Delta}_v^2 + 1)(\bar{\Delta}_v^2 + 1 + s_0)} d\bar{\Delta}_v \quad (6.12)$$

$$\approx \frac{\gamma_E}{\Delta_{\text{rms}}} \sqrt{\frac{\pi}{2}} \frac{s_0}{1 + s_0} \quad (6.13)$$

where the approximation is accurate for $\sqrt{1 + s_0} \gg 1$. In this case the factor $s_0/(1 + s_0)$ which accounts for Raman coherence is the same as what it would be at line center in the absence of Doppler broadening. Thus the Raman scattering susceptibility is not proportional to the Doppler-averaged coherence; but *in a Doppler-broadened medium, the Raman scattering susceptibility is proportional to the peak coherence and is reduced by the same line-broadening factor as the linear absorption*. This can be understood by arguing that the dominant contribution to the Raman scattering comes from those atoms that are resonant with the probe; with the laser frequencies tuned as described above, those atoms are also resonant with the control fields.

Above it was argued that the residual Doppler shift of the Raman detuning δ is negligible. This point will now be considered more closely. The Raman Doppler shift is

$$\delta_v = (\mathbf{k}_1 - \mathbf{k}_2) \cdot \mathbf{v} \quad (6.14)$$

$$\approx \Delta_v \sqrt{\left(\frac{\nu_1 - \nu_2}{\nu}\right)^2 + \theta_{12}^2}. \quad (6.15)$$

where θ_{12} is the angle between \mathbf{k}_1 and \mathbf{k}_2 . In general we may write $\delta_v = \Delta_v(\delta_{\text{rms}}/\Delta_{\text{rms}})$ where $\delta_{\text{rms}} = \Delta_{\text{rms}}(\nu_1 - \nu_2)/\nu_1 \simeq \Delta_{\text{rms}}(\nu_1 - \nu_2)/\nu_2$ is the width of the Raman Doppler distribution.

Now, the coherence at Raman resonance is proportional to $s/(1 + s)$ [eqn. (3.6)]. Using the

relation $s = s_0/[1 + (\Delta_v/\gamma_e)^2]$, one finds that the value of Δ_v at which the coherence drops to 1/2 of its peak value (simply due to the reduced pumping rate) is

$$\Delta_v = \gamma_E \sqrt{1 + s_0}. \quad (6.16)$$

At this value of optical detuning, the Raman linewidth [eqn. (3.10)] is $\delta_{\text{coh}} = \gamma_G \sqrt{1 + s_0}$. Meanwhile, the residual Doppler shift which accompanies the optical shift Δ_v is

$$\delta_v = \left(\frac{\delta_{\text{rms}}}{\Delta_{\text{rms}}} \right) \gamma_E \sqrt{1 + s_0}. \quad (6.17)$$

Provided $(\delta_{\text{rms}}/\Delta_{\text{rms}})(\gamma_E/\gamma_G) \ll 1$,³ δ_v is much smaller than δ_{coh} . That is, the Raman coherence disappears entirely due to the reduction in the optical pumping rate before the residual Doppler shift exceeds the Raman line width.

Residual Doppler shifts, then, do not significantly diminish the height of a Doppler-weighted Raman feature. Yet one might expect them to contribute noticeably to widths of such features. The “transverse” component of the residual Doppler width is $\Delta_{\text{rms}}\theta_{12}$, which works out to 662 kHz per milliradian. This contribution can be eliminated by very careful alignment of the control fields or by use of a spatial filter to ensure that the control fields occupy the same spatial mode. But even if the fields are planar⁴ and copropagating, the broadening associated with the “longitudinal” component is $\Delta_{\text{rms}}(\nu_1 - \nu_2)/\nu = 2.3$ kHz. Thus Doppler broadening would seem to rule out sub-kHz line widths. Yet the data I will report in §7.2 describes Raman line widths of only a few hundred Hz. Features as narrow as 42 Hz have been observed by others [97].

This paradox can be resolved by arguing that the total coherence is dominated by atoms in a narrow velocity subclass. As discussed above, the coherence begins to fall off at $\Delta_v = \gamma_E \sqrt{1 + s_0}$. If this Δ_v is smaller than Δ_{rms} , then the bandwidth of the coherence (i.e. the bandwidth of the material oscillation) will be narrower than the residual Doppler distribution (Fig. 6.2). Furthermore,

³For the sodium D1 Λ system $\Delta_{\text{rms}}/\delta_{\text{rms}} = 2.8 \times 10^5$, while γ_E/γ_G is typically between 10 and 10^5 depending on the experimental conditions.

⁴A focused beam has an angular bandwidth $\theta \sim \lambda/d$ where d is the beam diameter. The present framework would then suggest that the Doppler-broadened width of the Raman line is $\delta_{\text{rms}} \sim v_{\text{rms}}\theta/\lambda = v_{\text{rms}}/d$. In the regime of ballistic atomic motion, this is just the linewidth associated with the transit time through the illumination region. But if the field is planar, the angular bandwidth vanishes along with the associated contribution to the residual Doppler shift.

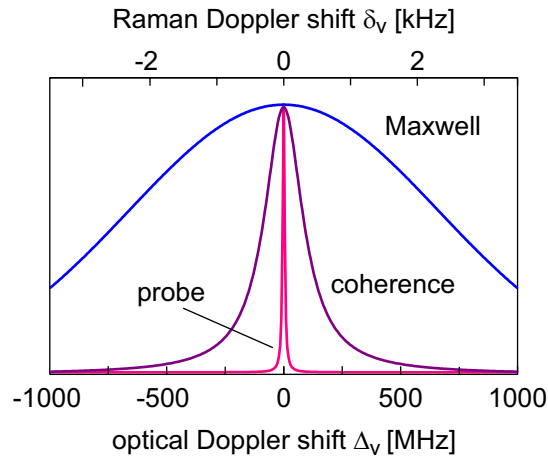


Figure 6.2: The Doppler (Maxwell) distribution, the frequency dependence of the coherence, and the resonant response to a probe field, shown as functions of the optical and Raman Doppler shifts. The spectral distribution of an experimental coherence signal is typically the product of all three functions. Hence the bandwidth of the coherence can be much less than the width of the Raman Doppler distribution.

if the coherence is measured via an optically resonant interaction (e.g. coherent Raman scattering), then the signal is dominated by those atoms which are resonant with the probe, i.e. by atoms whose velocities yield Doppler shifts $|\Delta_v| \lesssim \gamma_E$. Therefore the effective width of the Doppler distribution is γ_E , and the effective width of the Raman Doppler distribution is $\gamma_E(\delta_{\text{rms}}/\Delta_{\text{rms}}) = 17 \text{ Hz}$. In most experiments, this value is much smaller than the dominant contribution to the Raman line width. Thus we again find that residual Doppler broadening of the Raman line can be ignored (if the experiment is properly designed).

6.2 Interactions Between Atoms

The atoms in a vapor are not isolated; they interact via collisions and longer-range forces (e.g. van der Waals forces) to a degree that increases with number density. They also interact with the walls of their container. These interactions are responsible for a great variety of effects. Broadly speaking, these effects can be categorized as either elastic (kinematic) or inelastic (producing a change in the

internal state of an atom). The latter type generally result in relaxation of the atomic state. Processes of this type can be modelled by identifying an interaction Hamiltonian, determining the evolution of the atomic state for a given set of collision parameters, then averaging the effects of many random collisions (i.e. over the space of possible collision parameters) to obtain the average change to the density matrix. Some of the more important effects resulting from atom-atom interactions are summarized below.

Diffusion. As discussed in §6.1.1, collisions limit the movement of atoms and thereby increase the time atoms remain in the beam region.

Velocity Diffusion. Collisions cause atoms to change velocities, resulting in sudden changes to the Doppler shift an atom experiences. Since only resonant atoms are effectively pumped and probed by the fields, velocity-changing collisions limit the average time an atom interacts with the fields. If the time between collisions is shorter than the response time of the atom, an atom will be knocked off resonance before the atom has time to determine whether or not the field is resonant—before the coherence has time to build up. Velocity-changing collisions can measurably increase the effective ground state relaxation rate [98]. Optical coherences are affected far less, since they have much shorter lifetimes than Raman coherences.

Spin relaxation. In §5.4.3 we saw that ground state coherences in alkalis involve nuclear and electron spins. Any process that randomizes the orientation of spin will therefore cause relaxation of hyperfine and Zeeman coherences. Such processes include spin-exchange (in which spins of like atoms interact) and spin-orbit interactions (coupling between the spin of one atom and the field of another atom's orbiting electron). The cross section for spin exchange between sodium atoms is 10^{-14} cm^2 . The cross section for spin-orbit relaxation of sodium ground states in helium is on the order of 10^{-26} cm^2 [95]. These lead to relaxation rates $\sim 6 \times 10^{-11} \text{ Hz cm}^3 \mathcal{N}$ and $\sim 10^{-5} \text{ Hz/torr}$, respectively. For realistic experimental conditions, say $\mathcal{N} = 2 \times 10^{11} \text{ cm}^{-3}$ and 1 torr of helium, these rates are negligible. Collisions with the walls of the container strongly disturb the electronic spin, and in fact it is often the case that the spin is completely randomized by a single collision. However, it is known among vapor physicists that coating the walls with paraffin wax can almost completely eliminate spin relaxation in wall collisions. This approach does not appear to be viable

for sodium since moderately high temperatures (150 °C) are required to produce a sufficient number density for most experiments.

Pressure broadening. The excited states of alkali atoms are less tightly bound than the ground states and are much more strongly affected by the forces which act during a collision. Effects such as disorientation of the electronic and nuclear spins, transitions between states of different J or F , and dephasing of excited states become relevant at pressures on the order of 1 torr. The net result is that the lifetime of optical coherences (coherences between excited states and ground states) is decreased; correspondingly, the spectral line is broadened. A vapor may be self-broadened, but pressure broadening can also occur as a result of interaction with a foreign gas. Whatever the cause, the (half) width of the spectral line typically goes as $\gamma_E = \frac{1}{2}\Gamma_E + \beta P$ where P is the pressure of the broadening gas and β is the broadening coefficient. In most of my experiments, a helium buffer gas was the dominant perturber. At a typical vapor temperature of 150 °C, the broadening coefficient for the FWHM of the sodium $3P_{1/2}$ level is $3.9 \times 10^{-9} \text{ cm}^3 \text{ rad/s}$ [99], which translates to $\beta = 10 \text{ MHz/torr}$.

As pressure broadening is an excited state phenomenon, it does not directly affect ground state coherences. However, an increase in the optical linewidth results in a decrease in the optical pumping rate [cf. eqn. (2.4)], which reduces the steady dark state population. Therefore pressure broadening is a hindrance to coherent population trapping.

Quenching. In a collision between an atom and a molecule of a foreign gas, the atom may transfer energy to the molecule and de-excite without emitting a photon; fluorescence of the atom is *quenched*. Quenching could conceivably help (or hinder) coherent population trapping by causing the atom to de-excite to a superposition of ground states with the right (or wrong) sign; but coherent de-excitation with preferential sign seems unlikely. It is more likely that quenching hinders coherent preparation by decreasing the excited state lifetime, which increases the optical linewidth and reduces the optical pumping rate.

Quenching is common with molecular perturbers; nitrogen (N_2), for example, is known to be very effective in quenching alkali vapors. Inert atoms, on the other hand, have fewer channels for energy transfer and generally have extremely low quenching cross sections. Most of my experiments

were performed with a helium buffer gas, so in principle quenching should not occur. But even in those experiments in which nitrogen buffer gas was used, the effect on coherent preparation was slight. Thus I conclude that quenching was not an important process in any of my experiments.

Radiation Trapping. If the absorption length is smaller than the extent of the vapor, then the resonant fluorescence is likely to be absorbed and re-emitted many times before it leaves the vapor. The fluorescence builds up to form a background of incoherent⁵ radiation which can be seen as a diffuse glow surrounding the illuminated part of the vapor. If the vapor is dense enough, this background can become intense enough that the rate at which it optically pumps population out of a dark state is non-negligible. Thus radiation trapping is capable of hindering coherent population trapping. A recent experiment [100] in rubidium vapor, involving a geometry similar to that of my experiments, indicates that radiation trapping can make a significant contribution to the ground state relaxation rate at number densities $\sim 10^{12} \text{ cm}^{-3}$. Although the number density in my experiments is closer to 10^{11} cm^{-3} , the critical number density depends on enough experimental parameters that radiation trapping cannot be summarily dismissed. An experimental investigation of the effect of radiation trapping in our setup would be a prime candidate for future work.

6.3 Considerations Associated with Propagation

In a nonlinear medium, both the fields and the optical properties of the medium can vary in complicated ways throughout the course of propagation. One could imagine that the fields which prepare the medium in the desired way at the input evolve in such a way that after some distance they no longer produce the desired material state. I now consider some potentially relevant aspects of spatial evolution.

Attenuation of the control fields. In an ideal situation, absorption would be very large in the absence of coherent preparation and negligibly small when the vapor is coherently prepared. In many experiments, including my own, coherent preparation does not lead to complete transparency. Often the control fields are significantly weaker at the exit of the vapor than the input; therefore the

⁵Spontaneously emitted light is often called incoherent, which is true in the sense that the light has no definite phase. However, it should not be forgotten that spontaneous emission is the result of *coherent* evolution of the state of joint system consisting of the atom(s) and electromagnetic continuum.

degree of coherent population trapping varies along the length of the vapor, being largest at the input and smallest at the exit. According to the 3-state model, a coherently prepared medium acts like a simple saturable absorber with a low saturation intensity, allowing one to qualitatively understand the evolution of the fields. The ground state coherence and Raman scattering susceptibility will decrease with distance, to the point that absorption of the probe and signal may dominate over Raman scattering.

Intensity Divergence. Propagation may also cause the control fields to become highly imbalanced. An asymmetry in the input intensities or line strengths will cause one field to be absorbed more than the other. Propagation only exaggerates this difference since the weaker a field becomes, the less it saturates its corresponding transition and the larger its absorption coefficient becomes. Thus the tendency is to end up with one strong field and one weak field. If this occurs under coherent trapping conditions, then the hyperfine coherence will decrease with propagation distance as the hyperfine populations become more and more imbalanced.

The Kerr Effect. The refractive index experienced by either control field will depend on the intensity of both fields. A Gaussian beam can undergo self-focusing or self-defocusing because the intensity-dependent refractive index varies from the center to the edge of the beam. In my experiments, the vapor density and beam power are too low and the beam diameter is too large for self-focusing to be significant. Even so, one might imagine that the different phase shifts experienced by different parts of the beam could lead to problems associated with transverse phase dependence (see the discussion “transverse uniformity” in the next section). However, the Kerr effect should be unimportant for a couple of reasons. Firstly, most of the experiments are performed at line center, where the susceptibility is almost completely imaginary (absorptive rather than dispersive). Secondly, both fields will acquire similar if not the same phase shifts in the case that they have the same intensities. Thus the *relative* phase variation (which is what determines the phase of the dark state) should be quite small.

Wave mixing. A pair of intense fields can undergo wave mixing in many types of nonlinear media. When population trapping enhances the quantum coherence, wave mixing can occur with even greater efficiency. For example, in §7.3 I show data in which four-wave mixing induced by

coherent population trapping causes power transfer from one control field to the other. The larger the ground hyperfine splitting, the further this process is from resonance and the smaller the susceptibility. Hence four-wave mixing of the control fields is almost certainly negligible in atoms such as Rubidium, for which the ground hyperfine splitting is much larger than the Doppler width. But even in sodium, the mixing process is found to be conservative and sufficiently weak that it has little to no impact on coherent population trapping (see §7.3).

Coherent Raman scattering is, of course, also a wave mixing process. The analysis of §3.3 ignores the fact that the probe and signal fields affect the dark state. This interaction does not necessarily prevent coherent population trapping [38]; nevertheless, in my experiments, the probe was kept much weaker than the control fields to the extent that it had little to no observable effect on the degree of electromagnetically induced transparency.

Phase-matching. Wave mixing processes are subject to phase matching criteria: if momentum is not conserved in a multiphoton transition, i.e. if the wavevectors of the fields do not sum to zero, then the sign of the nonlinear process will oscillate with distance, resulting in little net change in the fields. Some processes are automatically phase-matched. EIT is one such process: since the phase of the dark state is determined at each point by the fields themselves, the wavevector of the dark state exactly makes up for the difference in the wavevectors of the fields. (However, the dark state grating is subject to washout, §6.1.2.) Coherent Raman scattering will be phase-matched if the difference in probe and signal wavevectors matches that of the control fields. In my experiments, the control fields are so similar in frequency (as are the probe and signal fields) that the reciprocal of the wavevector mismatch is larger than the length of the cell. Thus for both fundamental and technical reasons, phase-matching is not a concern.

Nonlinear absorption. In a saturable absorber, the light intensity decreases linearly for intensities far above the saturation intensity, and only decays exponentially well below the saturation intensity. This does not present a physical problem, but it does make analysis more difficult. Even for straightforward saturation of the form $(1 + I/I_{\text{sat}})^{-1}$, the evolution of the intensity is mathematically nontrivial (the solution is a transcendental equation). In a medium such as sodium vapor, in which the saturation does not follow a simple form (cf. Fig. 5.7), it is very difficult to solve

the “inverse problem”—i.e., to use the transmittance to obtain an accurate determination of the intensity (or intensity-dependent absorption coefficient) at an arbitrary point within the vapor. One must numerically propagate the beam, adjusting the (possibly many) parameters of the medium in order to obtain a fit to the measured transmittance. A calculation of the transmission spectrum may take from hours to days depending on the sophistication of the physical model. In lieu of lengthy calculations, one must rely on intuition built upon idealized media to close the gap between theory and experiment.

6.4 Technical Considerations

Besides complications arising from fundamental physics, there are complications associated with the practical realities of implementing an experiment.

Polarization control. In my experiments, the control fields are intended to be cross polarized. There are several places in the optical train where the polarization may be corrupted. First, the two control fields are combined at a polarizing beamsplitter and coupled into a polarization-maintaining fiber. The beam splitter ensures that the two components entering the fiber are perpendicular to a very high degree (extinction ratio of several thousand to 1). If the axis of the fiber is not aligned to the fields, the polarizations of the fields will be scrambled. Some residual polarization mixing also occurs in propagation through the fiber. The measured polarization purity of the light exiting the fiber (defined as power in the desired polarization divided by the power in the undesired polarization) was on the order of 2000 and was subject to both thermal drift and mechanical stress (i.e. it depended on the exact way in which the fiber was coiled).

The second potential cause of polarization mixing is the birefringence of the windows on the cell containing the sodium vapor. If the crystal axes of the windows are not aligned to the field polarizations, then polarization mixing will result. When the cell was built, the entrance and exit windows were aligned with a laser to minimize polarization mixing. In the end, the polarization purity of the entire optical train varied in the range 300-1500.

The effect of polarization rotation or scrambling on coherent population trapping may be estimated as follows. In the worst case, the unwanted polarization components act as incoherent pump

fields. Thus they increase the effective relaxation rate by R/P , where P is the polarization purity. This means the Raman saturation parameter is limited to $R/(\gamma_G + R/P) \leq P$. A saturation parameter of $P \sim 500$ is large enough to achieve strong coherent trapping. This analysis is overly conservative, however. As discussed in §5.4.4, even the “wrong” kind of input polarization (parallel polarized fields) produces some degree of coherent preparation. Thus I do not expect small amounts of polarization mixing to have any significant effect on coherent population trapping in a sodium vapor, although this is a point which could be explored further.

Transverse uniformity. If the control fields do not have the same transverse dependence, the phase of the dark state (i.e. the phase of the hyperfine coherences) may vary across the diameter of the beams. Movement of an atom across the beam diameter will cause a decay of the net coherence of the vapor, much like grating washout. By having both fields pass through a spatial filter (such as a single mode fiber), their transverse modes are guaranteed to be identical as they enter the cell. But since one field sees the ordinary refractive index of the window while the other sees the extraordinary index, the relative phase of the two fields depends on the thickness of the window. A wedged or otherwise non-uniform window will result in a variation in relative phase of the fields and of the dark state across the diameter of the beam. By examining interference fringes formed by the Fresnel reflections at each surface, I observed that both input and output windows had slight wedges. The input window was measured to have a wedge of 7 waves per transverse centimeter. Since the ordinary and extraordinary refractive indices of the sapphire differ by only 0.5%, across a 0.4 cm diameter beam the relative phase of the control fields varies by only $0.005 \times 7 \times 0.4 = 0.01$ waves. Thus for all purposes the phase of the dark state is the same across the beam diameter.

Transverse spatial dependence should not be ignored, though, even when it is the same for both fields. Consider the typical situation that the fields have a Gaussian profile. Atoms near the center of the beam see the most intense fields and are most strongly coherently prepared; atoms in the periphery experience weaker fields and are less completely pumped into trap states. Diffusion is expected to smooth out spatial variations in the average atomic state to some extent; nevertheless, both the degree of electromagnetically induced transparency and Raman susceptibility are likely to vary over the beam area. Any measurement that collects the entirety of a beam exiting the vapor

must be regarded as a weighted average of beamlets that experienced different optical properties.

Phase and Frequency Stability of the Control Fields. The relative phase of the control fields is $\phi_R = \phi_2 - \phi_1 + 2\pi(\nu_2 - \nu_1)t$, where $\phi_{1,2}$ is the phase of control field 1,2. If ϕ_R is not constant in time, the phase of the dark state will be continually changing and the coherent population trapping will be less complete than it would otherwise. The impact of temporal phase fluctuation can be estimated using the Bloch vector model. In this model, fluctuation in the relative phase of the control fields appears as fluctuation in the polar angle of the pumping vector \vec{R} . To lowest order in the dark state phase slip $\Phi = \arg(\rho_{21}) - \phi_R + \pi$, the time-averaged coherence and absorption are, for $\delta = 0$,

$$\overline{\rho_{21}} = -\overline{\left(\frac{\vec{R}}{R + \gamma_G}\right)} = -\frac{s}{1+s} \overline{\cos \Phi} \quad (6.18)$$

$$\overline{\text{absorption}} \propto 1 - \frac{\overline{\vec{R} \cdot \vec{\rho}}}{R + \gamma_G} = \frac{1+s(1 - \overline{\cos \Phi})}{1+s}. \quad (6.19)$$

where $\overline{\dots}$ denotes an average over time. For a field phase fluctuation of the form $\phi_R = \phi_{\max} \sin \omega_\phi t$, it can be shown that $\overline{\cos \Phi} \simeq J_0(\Phi_{\max})$ where $\Phi_{\max} = \left(\omega_\phi / \sqrt{\omega_\phi^2 + (R + \gamma_G)^2}\right) \phi_{\max}$. For $\overline{\cos \Phi} = 0.9$, the coherence cannot exceed 90% of the maximal value, and the absorption can never be reduced more than 90%. Clearly, phase fluctuations have an adverse effect.

Control fields with a stable relative phase can be formed using two frequency- and phase-locked lasers, or by deriving both control fields from a single laser and a modulator. Of course, in either case the driving electronics must be stable. In our experimental setup the Raman beat note is obtained by the use of several frequency-shifting modulators. Unfortunately, we discovered that the drivers for some of the modulators possess a 300 kHz phase modulation, causing the phase of one control field to vary sinusoidally with an amplitude of 1.2 rad. This modulation visibly broadened the Raman spectra. The simulation results shown in Fig. 6.3 indicate that the modulation was severe enough to hinder EIT in some experiments. However, I did perform one experiment using a different configuration which was free of the phase modulation, and found in that particular case that EIT was not noticeably improved.

Stray magnetic fields. As discussed in sections 5.3.3, 5.4.3, and 5.5.2, magnetic fields cause

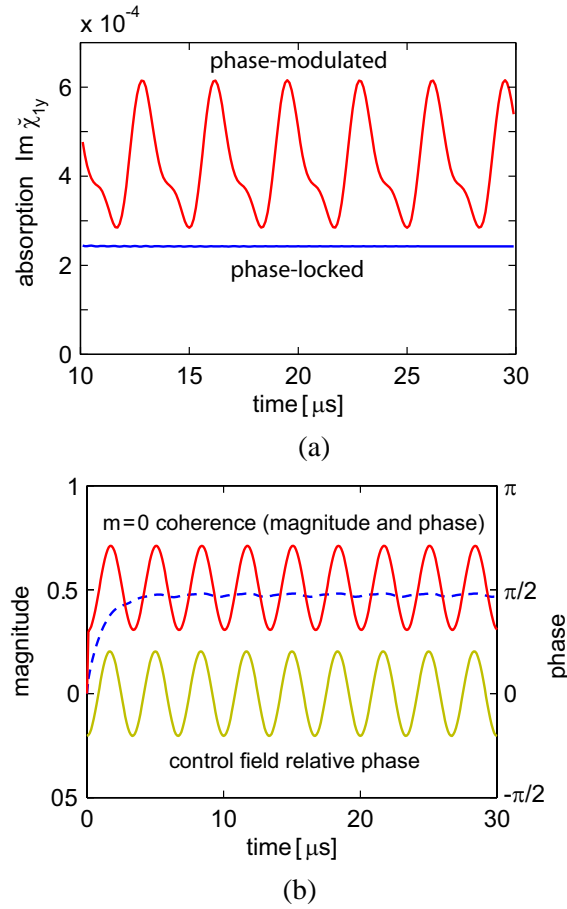


Figure 6.3: The adverse effect of fluctuation (or in this case, modulation) of the relative phase of the control fields on EIT and CRS. (a) In this simulation the average absorption is nearly twice as large with phase modulation than without it. (b) Although the magnitude (dashed line) of the hyperfine coherence is hardly affected, the phase (solid line) varies with that of the control field. This phase variation will be imparted to any field generated by coherent Raman scattering. *Parameters:* $\Omega_{1y} = \Omega_{2x} = 25$ MHz, $\Delta = 189$ MHz, $\delta = 0$, $B_z = 4$ G, helium pressure 3 torr ($\Gamma_g = 0.5$ kHz, $\gamma_G = 3$ kHz, $\gamma_E = 35$ kHz), and phase modulation $\phi_R = 0.64 \sin[2\pi(300 \text{ kHz})t]$.

level shifts and transitions between ground states. While a strong, spatially uniform, longitudinal field can be useful for isolating the $m = 0$ dark state, weak and/or non-uniform fields broaden the dark state resonance (via dark state decay or inhomogeneous level shifts). There is also a type of relaxation associated with motion through a spatially varying field, whose rate is proportional to the gradient of the field and the atom velocity [91]. In any case, spurious magnetic fields hinder coherent population trapping. According to Table B.3, the magnetic field interaction energies for the sodium $3S_{1/2}$ states are on the order of 1 MHz/G. Thus, a vapor with a ground state relaxation rate $\gamma_G = 10$ kHz will be affected by fields as weak as 10 mG. Our magnetometers were not sensitive enough to measure such fields. However, it was found that wrapping a sheet of high permeability metal around the vapor cell noticeably narrowed the dark state resonances. Due to the awkward geometry of the vapor cell apparatus and the lack of sufficiently sensitive magnetometers, the strength of stray magnetic fields in the interior of the vapor cell is largely unknown. However, the effects of stray fields are manifest in the net relaxation rate of the vapor. In §7.2 I will present data which shows that we were able to achieve ground state relaxation rates as small as several hundred Hz, which indicates that stray magnetic fields were not a limiting factor.

Fresnel reflections. Reflections at the back window surface produce counterpropagating fields that interfere with the control fields. At low to modest vapor densities, the refractive index of the vapor is close to unity, meaning that the field reflection coefficient is just $r = (n - 1)/(n + 1)$ where n is the index of the window. For sapphire windows ($n = 1.75$), $r = 0.27$, which is not negligibly small. Since both control fields experience the same reflection coefficient, and both fields have approximately the same wavevector, the relative phase of the reflected fields is the same as that of the incident control fields. Thus although a longitudinal grating is formed, both fields experience the same interference pattern in both phase and amplitude, Hence the optical grating does not lead to a dark state spatial grating. Wave mixing processes are also unlikely to develop because any atomic grating which does form has a very high spatial frequency and is subject to severe grating washout. If there remains any doubt about the influence of reflections, the overlap between incident and reflected fields can be greatly reduced by tilting the beam axis relative to the window normals.

Vapor Impurities. It has been noted that unless great care is taken, a vapor cell typically

contains enough impurities to dramatically alter the vapor's optical and spin relaxation rates [101]. The vacuum system I used is functional, but not ideal or well characterized. The vacuum station itself could reach pressures between 10^{-6} and 10^{-7} torr, but the station was removed from the cell by two meters of tubing. Owing to the restriction of flow this creates, the background pressure in the cell was likely higher. Additionally, the system contained a line to backfill the cell with an inert buffer gas, such as helium. This line was made of copper tubing, whose joints are known not to hold high vacuum. I was also unable to obtain impurity data for the buffer gases I used. In all, vapor purity is the least well characterized aspect of my experiments.

6.5 Simulation of Coherent Preparation of Sodium Vapor

A model which takes into account all the physics just discussed would be intractable as well as unnecessarily complicated, since I have argued that many of the complications can safely be ignored. Complications which certainly need to be included are atom transit, Doppler shifts, and collisional broadening of the excited states. A very complete model would yield the set of equations

$$\frac{d}{dt}\rho(\mathbf{r},v) = -\frac{i}{\hbar}[\mathbf{H}(\mathbf{r}),\rho] - \Gamma(\rho) + D\nabla^2\rho - \gamma_{\text{vcc}} \left[\rho - \int \mathbf{W}_{v'\rightarrow v}\rho(\mathbf{r},v') dv' \right] \quad (6.20)$$

$$\frac{d}{dz}\mathbf{E}(\mathbf{r},\mathbf{z}) = i\frac{\mathcal{N}}{2k\varepsilon_0}\text{Tr}(\boldsymbol{\mu}_E\rho) \quad (6.21)$$

together with appropriate boundary conditions. Here ρ is the density matrix, \mathbf{E} is the electric field, \mathbf{r} is position, v is longitudinal velocity, \mathbf{H} is the Hamiltonian describing interaction between an atom and electric and magnetic fields, Γ is term which accounts for spontaneous emission and other state-randomizing forms of relaxation (see eqn. (C.33) and §D.2), $D\nabla^2$ accounts for diffusion, γ_{vcc} is the rate of velocity-changing collisions, and $\mathbf{W}_{v'\rightarrow v}$ describes the nature of velocity redistribution in a collision. Analytically solving eqn. (6.20) alone, much less together with eqn. (6.21), is all but impossible; even numerical solution is rather imposing. One is therefore motivated to seek reasonable simplifications. The transverse spatial dependence may be eliminated mathematically, as it is experimentally, by performing an intensity-weighted spatial average. In the case that wall collisions and other influences outside the illumination region completely thermalize the atomic

state, one may approximately account for diffusion by causing the spatially averaged density matrix $\bar{\rho}$ to decay and be replaced by the thermal equilibrium state $\bar{\rho}^{\text{eqb}}$ at some rate Γ which is on the order of the transit rate Γ_{trans} . Similarly, one can account for velocity changes by integrating over the velocity probability distribution and adding γ_{vcc} to the appropriate decoherence rate parameters. For greater accuracy, the total effective relaxation rates may be obtained from experiment. By alternately solving eqns. (6.20) and (6.21), one may determine the longitudinal evolution of the fields and the ensemble density matrix. I have developed a set of computer routines to perform this task. Additional details of the model and its numerical implementation are given in Appendix D.

Figs. 6.4 and 6.5 show the results of simulation of coherent population trapping in sodium vapor with 3 torr of helium and a longitudinal magnetic field of 4 G. The control fields were taken to be 10 mW Gaussian beams of radius $r = 1$ mm. The average nominal Rabi frequencies are then $\Omega_{1y} = \Omega_{2x} = 25$ MHz and the relaxation coefficients are $\Gamma_G = 0.5$ kHz, $\gamma_G = 3$ kHz, and $\gamma_E = 35$ MHz (see Fig. 7.6). These are the conditions of some of the experiments discussed in chapter 7. This calculation ignores four-wave mixing of the control fields, laser instabilities, inhomogeneous stray magnetic fields, vapor impurities, and the influence of extraneous optical fields (“wrong” polarization components and resonance fluorescence). Fig. 6.4 shows the two-field absorption spectrum of the D1 line when tuned to the Raman resonance and when tuned away from the Raman resonance. Both fields experience a significant reduction of absorption due to coherent population trapping. At the center of the Doppler-broadened D1 line ($\Delta = 95$ MHz), three absorption dips are visible corresponding to the $m = -1, 0, 1$ dark states discussed in Chapter 5 (Fig. 6.5). The absorption of both fields is reduced by a factor of 7 at the $m = 0$ Raman resonance ($\delta = 0$). The full-width-half-max of this absorption dip is 1 MHz, which can be attributed almost wholly to power broadening⁶. The average coherences between pairs of ground states with $m = -1, 0, 1$ are shown in Fig. 6.5b. The Doppler-averaged $m = 0$ coherence is largest at $0.2i$. Since it is found that the atoms resonant with the fields have maximal coherence ($0.5i$), we may say that about 40% of the atoms are coherently prepared.

⁶Based on the analysis in §3.1, the half-linewidth may be interpreted as effective pumping rate R . Then eqn. (6.9) predicts the resonant absorption reduction to be $(1 + s_0)^{1/2} = (1 + R/\gamma_G)^{1/2} \approx 11$, a value which is not in bad agreement with the result of the full calculation.

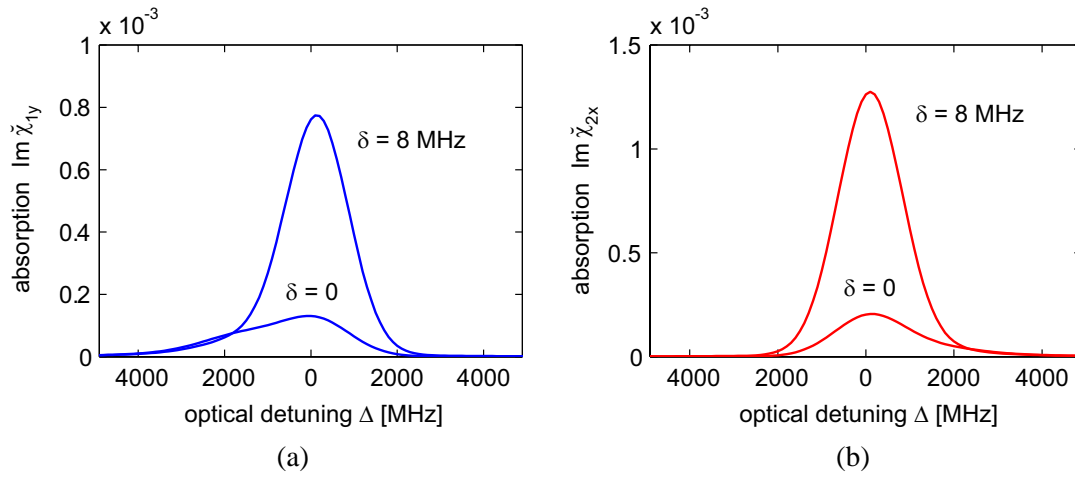


Figure 6.4: Simulation of EIT in a sodium vapor with helium buffer gas. The Doppler-broadened absorption spectra of both fields are significantly reduced at the Raman resonance ($\delta = 0$) as a result of coherent population trapping. *Parameters:* $\Omega_{1y} = \Omega_{2x} = 25$ MHz, beam radius $r = 1$ mm, $B_z = 4$ G, helium pressure $P_{\text{He}} = 3$ torr ($\Gamma_G = 0.5$ kHz, $\gamma_G = 3$ kHz, $\gamma_E = 35$ kHz).

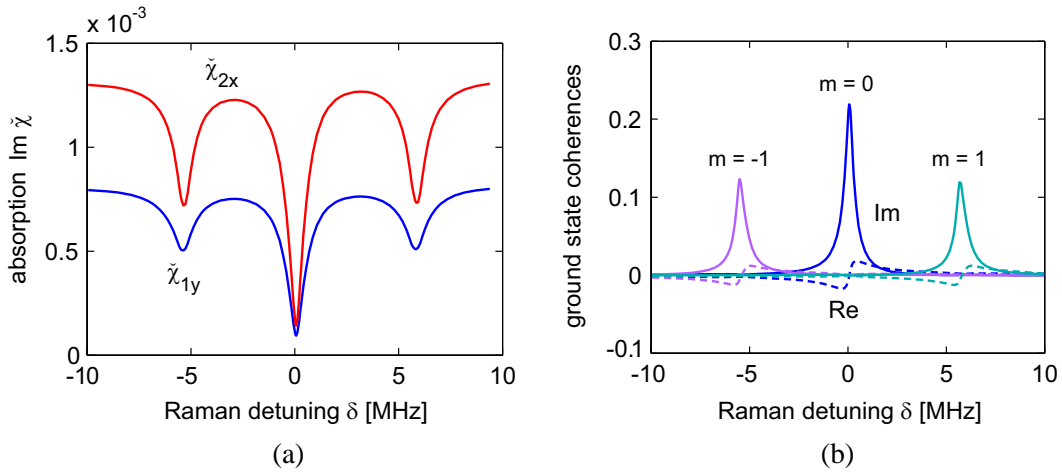


Figure 6.5: EIT and Raman coherence features in the presence of an applied longitudinal magnetic field. (a) The absorption dips. (b) The hyperfine coherences. The parameters of the simulation are the same as that of Fig. 6.4.

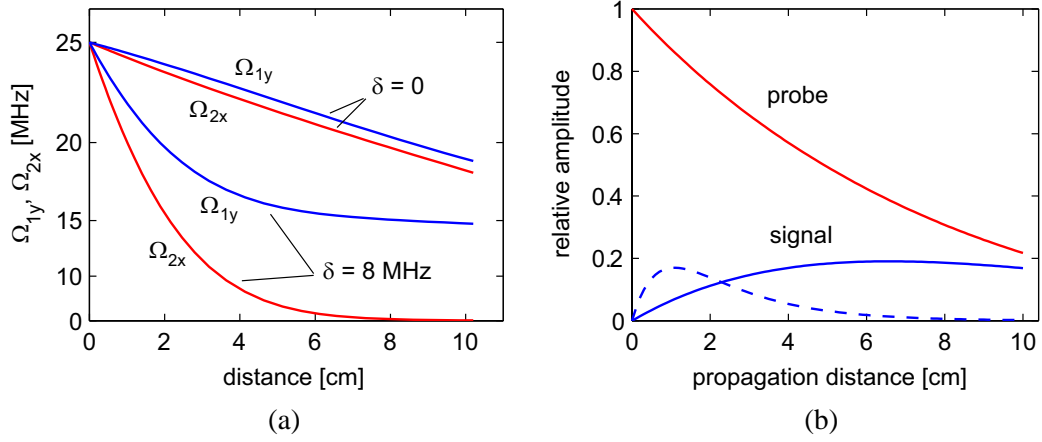


Figure 6.6: Spatial evolution of the control fields (a) and coherent Raman scattering signal (b). The number density is $\mathcal{N} = 2 \times 10^{11} \text{ cm}^{-3}$; the other calculation parameters are the same as those in the previous figures. (a) The attenuation of the control fields is significantly reduced at the Raman resonance ($\delta = 0$). In the off-resonant case, the inequality of line strengths for the $F = 1$ and $F = 2$ hyperfine transitions causes intensity divergence. (b) Generation of a coherent Raman signal via D2 transitions. When all four fields are tuned to the centers of their respective lines, Raman generation is overcome by absorption (dashed line). When the fields are tuned to the red side of the D1 and D2 lines, the Raman signal emerges with a maximum of 4% of the input probe power.

The model predicts that the attenuation of the fields is significantly reduced at the central Raman resonance (Fig. 6.6a). For this calculation the number density was taken to be $\mathcal{N} = 2 \times 10^{11} \text{ cm}^{-3}$. The calculation also shows intensity divergence in the Raman-detuned case; the fact that $F = 2$ states are more strongly coupled than $F = 1$ states causes Ω_{2x} to be attenuated much faster than Ω_{1y} .

At $\delta = 0$, the (non-normalized) Raman scattering susceptibility is $\chi_{12} = (0.4 + 4i) \times 10^{-6}$, while the self- (single-field) susceptibilities are $\chi_{11} = (-0.3 + 9i) \times 10^{-6}$ and $\chi_{22} = (0.1 + 10i) \times 10^{-6}$. These numbers are obtained when, for zero-velocity atoms, the control fields are resonant with the $3P_{1/2}$, $F' = 2$ level and the probe field is resonant with the $3P_{3/2}$, $F'' = 2$ level. The Raman susceptibility is less than half the self susceptibilities, but not because the coherence is not maximal; rather, it is because there are more and/or larger non-vanishing matrix elements for the single-field processes than the Raman process. An 8-cm long vapor is about 8 times the absorption

length for the probe and signal fields. Over this many absorption lengths, the Raman scattering becomes overwhelmed by resonant absorption so that almost no signal field emerges from the vapor. However, by tuning both the control fields and the probe fields about 1 GHz to the red side of the D1 and D2 lines, respectively, the signal power peaks at the end of the vapor⁷, reaching about 4% of the input probe power (Fig. 6.6b). This conversion efficiency is reasonably large compared to many other wave mixing processes, but is much smaller than one might have expected given that the participating atoms have maximal coherence.

6.6 Summary

In this chapter I considered a great variety of physical phenomena which have the potential to affect coherent preparation of a vapor such as sodium. Doppler shifts and transit of atoms through the illumination region are perhaps the two most significant of these phenomena. Doppler shifts broaden the optical resonances, but are found to have a minimal effect on the width of Raman resonances provided that the fields are copropagating and not tightly focused. Raman line widths of 10's of Hz are possible in principle. Nevertheless, the broadening of the optical line reduces the effective rate of optical pumping into the dark state, such that the amount of electromagnetically induced transparency is only the square root of what it would be without Doppler broadening. The effective coherence of the vapor for resonant Raman scattering is not reduced, although the Raman susceptibility is reduced by the same line-broadening factor as the linear susceptibility.

Atom transit may be ballistic or diffusive. In either case, the average atomic density matrix of the illuminated part of the vapor contains contributions from atoms with different histories. The interplay between transport, velocity randomization, and the quantum state evolution makes realistic simulation numerically challenging. Transit effects may be accounted for in an approximate way by adding relaxation terms with appropriate coefficients to the equation of motion of the atomic density matrix.

⁷In calculating the spatial evolution of the probe and signal fields, the influence of the probe and signal fields on the coherent population trapping was neglected. Also, the spatial evolution of the dark state was ignored as it was found to change little over the course of propagation.

Collisions also play a major role in vapor physics, producing velocity changes, level shifts, and relaxation of both optical and Raman (spin) coherences. While collisional relaxation of the ground states is negligible for the alkali and inert gas densities typical of my experiments, collisions strongly affect excited states. The collisional effect most relevant to coherent population trapping is pressure broadening of the optical line, which results in a reduced trapping rate.

The experimentalist must also take care to control the stability and uniformity of the optical and magnetic fields. Fluctuations in the relative phase or frequency of the control fields effectively broaden the Raman line, reducing the maximum coherence that can be produced. Fluctuating or spatially varying magnetic fields can have a similar effect, although a strong longitudinal field can help isolate Raman resonances with different magnetic numbers. It is very important that the control fields have the same spatial profiles, particularly that they have the same transverse phase dependence; otherwise, Raman coherences will rapidly decay in the manner of grating washout.

Wave mixing and saturation complicate attempts at coherent preparation in that the control fields may attenuate at different rates and new frequency components may be generated which directly interact with the dark states and remove or transfer power between the control fields. If the vapor is optically thick, the state in which the vapor is prepared may vary with propagation distance.

Coherent preparation of a vapor under realistic conditions was studied with several calculations. The calculations predict that nearly half the atoms in the illumination region can be prepared with maximum hyperfine coherence using 10-milliwatt, collimated control fields and a few torr of buffer gas. This produces a significant but not overwhelming degree of electromagnetically induced transparency (reduction of the absorption by a factor of 7). While the coherence for Raman scattering through the D2 states is maximal, more states effectively participate in absorption than in Raman scattering, causing Raman scattering to be dominated by absorption when all fields are tuned to line center. In a vapor which is on the order of eight (resonant) absorption lengths, a maximum conversion efficiency of 4% is predicted. Ultimately, the feasibility of coherently preparing a sodium vapor in a useful way seems to be limited more by the structure of sodium itself than complications arising from vapor physics.

Chapter 7

Experimental Studies of Coherence in Sodium Vapor

This chapter details my experimental studies of ground state coherence in sodium vapor. The first section describes the equipment and optical layout used to perform all the experimental studies. Section 7.2 investigates relaxation, which competes with optical pumping and limits the degree of coherence that can be obtained. In §7.3, the effect of coherence on the optical properties of the vapor is examined. Finally, the use of coherence to perform signal frequency conversion is demonstrated in §7.4. Broadly speaking, the experimental studies show that coherent population trapping in sodium vapor results in distinctive and potentially useful coherent optical effects. In particular, hyperfine coherence was used to transfer amplitude and phase signals from one wavelength to another with excellent fidelity. Nevertheless, the signatures of coherence were smaller than expected, indicating that attempts at coherent preparation were only partially successful.

7.1 The Experimental Setup

Fig. 7.1 shows the setup used to create and characterize ground state coherence in sodium vapor. The primary equipment consisted of: two Coherent 699 ring dye lasers, each able to produce several hundred mW of narrow band (~ 10 MHz) radiation; a Burleigh 4500 wavemeter having a precision

of 10^{-4} nm (100 MHz) and an accuracy of 10^{-3} nm (1 GHz); a Brimrose acousto-optic modulator with a computer-tunable frequency between 1.5 and 2.0 GHz; several Isomet acousto-optic modulators with center frequencies of 80 MHz and bandwidths of 15 MHz; a few silicon detectors; a balanced detector with saturation intensity of 2 mW and bandwidth of 600 MHz; a photomultiplier tube (PMT); a 300 MHz digital oscilloscope; a 1.8 GHz spectrum analyzer; and an 8 cm long, stainless-steel sodium cell built by myself (Fig. 7.2). The sodium vapor was produced by heating approximately 1 g of bulk sodium to a temperature between 150 °C and 200 °C depending on the desired number density. The heating was accomplished using several loops of fiberglass heating tape. The temperature was monitored by several type-E thermocouple wires placed in direct contact with the cell at various locations. The entire cell was surrounded with fiberglass insulation. A metal valve connected the cell to a vacuum system which allowed the cell to be evacuated as needed but also to be filled with various buffer gases. The vacuum system regularly reached pressures of 10^{-6} torr. The ends of the cell were fitted with sapphire windows, chosen because of their resistance to corrosion¹. The *c*-axis of the sapphire was in the plane of the window. The windows were carefully oriented such that the crystal axes were aligned with the polarizations of the fields, thereby minimizing birefringent effects. The cell itself was surrounded by a cylinder of high permeability metal to minimize stray magnetic fields and to align any residual fields along the axis of the cell (the *z* axis). A pair of Helmholtz coils placed near the ends of the mu-metal casing were sometimes used to produce a longitudinal magnetic field within the cell.

Dye laser #1 was used to create quantum coherence between the $F = 1$ and $F = 2$ hyperfine levels of the $3S_{1/2}$ level. It supplied two control fields, linearly and orthogonally polarized, nominally tuned to the D1 line ($3S_{1/2} \rightarrow 3P_{1/2}$, 589.8 nm), but differing in frequency by the hyperfine splitting of the $3S_{1/2}$ level (1772 MHz). The light first passed through one of the acousto-optic modulators (MOD1) which allowed the control fields to be intensity modulated. Approximately 1/3 of the light was double-passed² through a second Isomet module (MOD2) whose frequency could

¹Due to the highly reactive nature of sodium, ordinary glass will darken after a few days of exposure to a sodium vapor.

²The reflective double pass geometry allowed the frequency of the beam to be shifted without changing its direction. In the single pass geometry, the dependence of spatial mode on RF frequency resulted in unacceptably large variation in the amount of power coupled into the fiber.

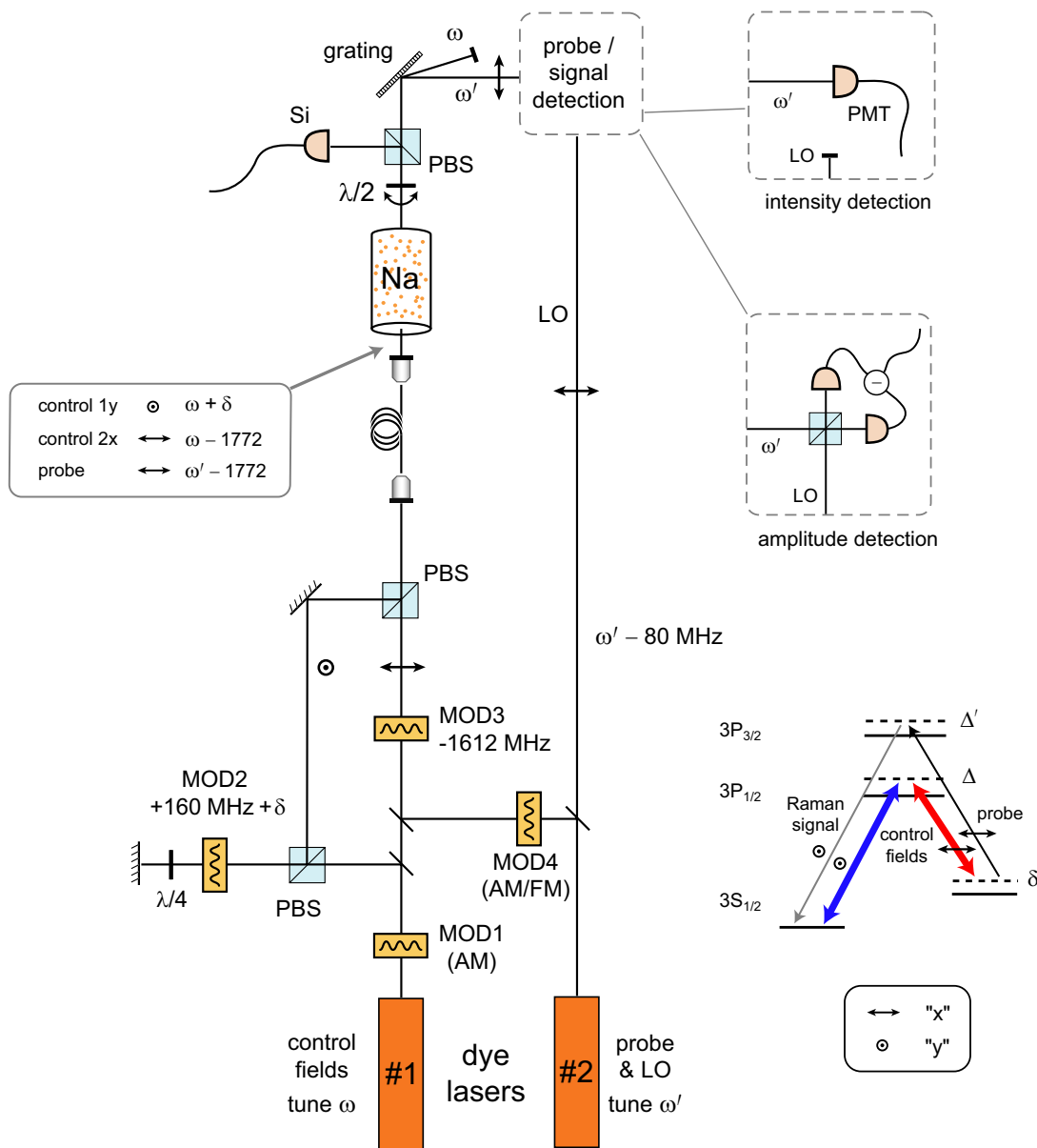


Figure 7.1: A schematic of the experimental setup. For the frequency conversion experiments, the probe and signal field amplitudes were measured using balanced heterodyne detection. For the other experiments, the probe and signal were detected directly. *Notation:* PBS = polarizing beamsplitter; $\lambda/2$ ($\lambda/4$) = half-wave (quarter-wave) plate; Si = silicon detector; PMT = photomultiplier tube; MOD = acoustooptic modulator; AM = amplitude modulation; FM = frequency modulation; LO = local oscillator.

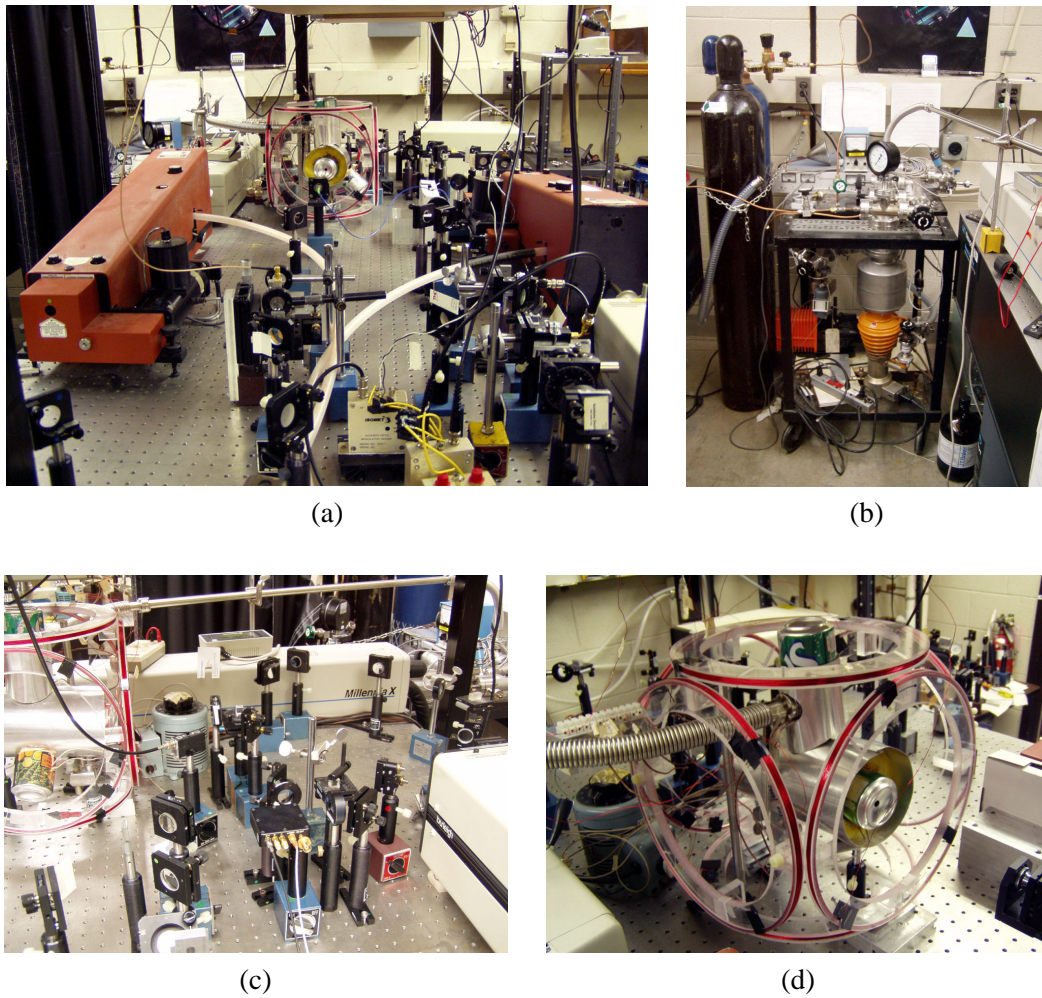


Figure 7.2: The experimental apparatus. (a) Lasers and modulators. (b) The vacuum system. (c) Detection. (d) The sodium cell. (Yes, those are soda cans. Cut in half, they make good non-magnetic, non-flammable end casings.)

be controlled by a voltage from a function generator. MOD2 provided a total shift of $160 + \delta$ MHz, where $|\delta| \lesssim 4$ MHz. The remaining 2/3 of the light passed through the Brimrose modulator (MOD3) which provided a fixed frequency shift of -1612 MHz. These two fields were combined at a polarizing beamsplitter and coupled (with a typical efficiency of 45%) into a single-mode, polarization-maintaining optical fiber. The light exiting the fiber was collimated (at a diameter of 2 mm) by a $5\times$ objective and directed into the sodium cell. The fiber functioned as a spatial filter which not only produced a smooth Gaussian input to the cell, but (more importantly) ensured that the control fields had identical spatial modes.

Dye laser #2 provided both a probe beam to scatter off the hyperfine coherence and a reference for heterodyne detection of the scattered field. The probe component was passed through a fourth modulator (MOD4) which provided either amplitude or frequency modulation of the probe, depending on the experiment. This laser was tuned to the D2 line ($3S_{1/2} \rightarrow 3P_{3/2}$, 589.2 nm) so that the probe interacted with the $3S_{1/2}$ coherence but was spectrally distinguishable from the control fields.

The light exiting the cell was passed through another polarizing beamsplitter, which separated the probe and one control field from the signal and other control field. A $\lambda/2$ plate prior to the beamsplitter allowed one to choose which pair of fields was sent to which detector. The fields transmitted by the beamsplitter were separated by a reflective diffraction grating with a ruling of 2400 mm^{-1} . In the hyperfine relaxation experiments, the D2 light was detected directly with the PMT; in the absorption/transparency experiments, the D1 light was detected directly by silicon detectors; in the signal conversion experiments, the D2 light was heterodyne detected with the balanced mixer.

The output of each dye laser was usually between 200 and 300 mW. The power (measured just prior to the cell input window) of each control field was typically 10 mW, corresponding to an average intensity of 80 mW/cm^2 . Accounting for the 7% reflection loss of the cell window, this intensity corresponds to a nominal Rabi frequency of 24 MHz in the vapor. The power of the probe field was typically 1 mW.

7.2 Coherence Relaxation Studies

As discussed in previous chapters, the rate of decay of the ground state coherence is a critical experimental parameter. The more rapid the decoherence, the less coherence can be generated and the weaker the associated optical effects. To first approximation, the effective decoherence rate for the vapor is just the linewidth of the Raman resonance. However, the relationship between linewidth (a frequency) and decoherence (a rate) is complicated by power broadening, inhomogeneous broadening, and the intrinsic nonlinearity of the system [cf. eqn. (3.19)]. A direct measure of the decoherence rate can be obtained by using a weak probe to monitor, as a function of time, the decay of the coherence after the driving fields are turned off. This free decay signal has very little background, is independent of the control field power, and includes the effects of inhomogeneous broadening (due to Doppler shifts or stray magnetic fields) in the manner relevant to intended uses of the coherence.

Relaxation of both the hyperfine population and hyperfine coherence in sodium vapor was studied as a function of the partial pressure of helium in the cell. To measure the population relaxation, the probe field was tuned to the $3S_{1/2}, F = 2 \leftrightarrow 3P_{3/2}$ transition, the x polarized control field was tuned to the $3S_{1/2}, F = 2 \leftrightarrow 3P_{1/2}$ transition, and the y polarized control field was blocked (Fig. 7.3a). The control field was chopped on and off using MOD1 with a period ~ 40 ms. When the control field was on, the population would be rapidly optically pumped out of the $F = 2$ level into the $F = 1$ level, causing the probe absorption to decrease. When the control field was off, the population would slowly relax back to the $F = 2$ level, causing the absorption to “charge up” to its thermal equilibrium value (Fig. 7.3b). To measure the coherence relaxation, the y polarized field was unblocked. When the control fields were on, the hyperfine coherence would develop and lead to coherent Raman scattering of the probe field (Fig. 7.4a). When the control fields were off, the coherence would decay, leading to a similar decay of the signal (scattered) power (Fig. 7.4b).

In principle, only one trace would be needed per rate constant to be determined. In practice, three traces were taken for most data points. Because of imperfect separation of the probe and control fields at the output, and because the control fields were generally much stronger than the transmitted probe or signal fields, each trace would contain a non-negligible contribution from the

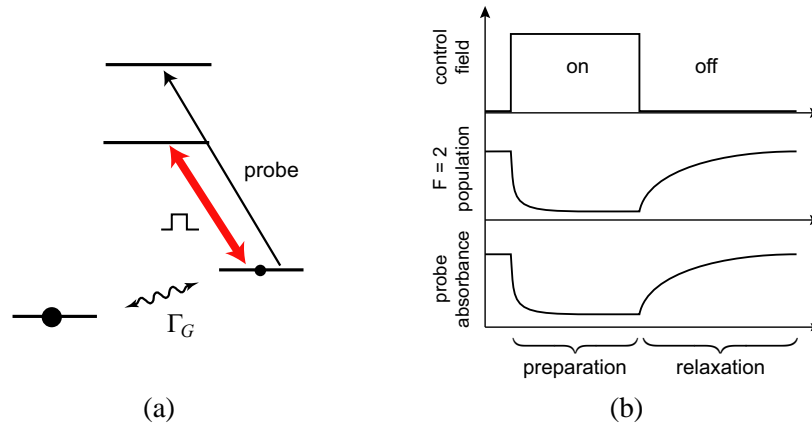


Figure 7.3: The scheme for measuring the ground hyperfine population relaxation rate Γ_G . The transmittance of the probe is monitored after the control field is turned off and the population relaxes back to the $F = 2$ hyperfine level.

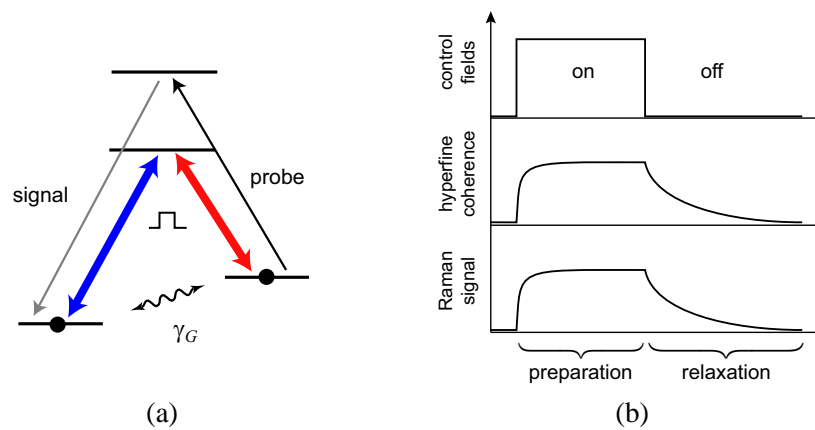


Figure 7.4: The scheme for measuring the ground hyperfine decoherence rate γ_G . The strength of the CRS signal is monitored when the control fields are turned off and the ground hyperfine coherence they created decays away.

chopped control field(s). To determine this contribution, a first trace (a background) was taken with the probe field absent. A second trace was then taken with the probe beam. At helium pressures above about 1 torr, the optical pumping produced by the probe itself made a noticeable contribution to the measured decay constant. In these cases, a third trace was taken with half the probe power so that the zero-power rate could be extrapolated.

It should also be noted that a DC magnetic field in the z direction was applied to the cell for these measurements. As discussed in §5.4, the D1 Λ system possesses a number of dim states which involve coherences between different combinations of ground states. Residual magnetic fields which perturb the Zeeman degeneracy can cause these coherences to have slightly different Raman transition frequencies. In such cases the coherences will dephase as they decay, resulting in a more rapid decay of the net hyperfine coherence and a broadening of the Raman feature. However, if a “strong” magnetic field is applied, the Zeeman degeneracy is lifted, and only the $m = 0$ dark state [eqn. 5.23] has its Raman resonance at $\delta = 0$. The contributions to the net hyperfine coherence from the other dim states become smaller (because they are off-resonant) and spectrally distinguishable from that of the desired dark state. Experimentally, it was found that the Raman feature at $\delta = 0$ narrowed slightly and that the hyperfine coherence decayed a little less quickly when the magnetic field was applied.

The population in the $F = 2$ hyperfine level can be written as $\rho_{22} = \rho_{22}^{\text{eqb}} + \Delta\rho_{22}f_{\text{pop}}(t)$, where $f_{\text{pop}}(t)$ ($0 \leq f_{\text{pop}}(t) \leq 1$) describes the relaxation after the control field is turned off. As the absorption seen by the probe is proportional to ρ_{22} , the transmittance of the probe has the form

$$T_{\text{probe}} = \exp[-A^{\text{eqb}} - \Delta A f_{\text{pop}}(t)]. \quad (7.1)$$

The primary mechanism for population relaxation is believed to be exodus of atoms from the beam region; spin-changing cross sections for the $3S_{1/2}$ states are too small to have a noticeable effect (see §6.2). As discussed in §6.1.1, diffusion leads to relaxation with a characteristic curve $(1 + \Gamma t)^{-1}$. Fig. 7.5a shows a typical population relaxation curve $-\ln T_{\text{probe}}$ together with the best fit to a

function of the form $A^{\text{eqb}} + \Delta A f_{\text{pop}}(t)$, where

$$f_{\text{pop}}(t) = \begin{cases} 1 & t \leq t_0 \\ \frac{1}{1 + \Gamma(t - t_0)} & t \geq t_0 \end{cases}. \quad (7.2)$$

The quantities A^{eqb} , ΔA , t_0 , and Γ are the free parameters of the fit. The fact that the data is fit well with a function of this form confirms that the population relaxation is indeed due to diffusion. As expected, the relaxation rate Γ decreases with increasing density of buffer gas.

The average hyperfine coherence of the vapor ρ_{21} can be written as $\rho_{21} = \rho_{21}^{\text{max}} f_{\text{coh}}(t)$, where $f_{\text{coh}}(t)$ describes the decay of coherence after the control fields are turned off. In the weak scattering regime, the signal field is proportional to $\int_0^L \rho_{21} E_{\text{probe}} dz$. Hence the power P_{signal} of the generated signal field is proportional to $|f_{\text{coh}}(t)|^2$. Fig. 7.5b shows a typical experimental trace of $\sqrt{P_{\text{signal}}}$ together with the best fitting function of the form $\rho_{21}^{\text{max}} f_{\text{coh}}(t)$ where

$$f_{\text{coh}}(t) = \begin{cases} 1 & t \leq t_0 \\ \frac{\exp[-\gamma_{\text{deph}}(t - t_0)]}{1 + \Gamma(t - t_0)} [(1 - X) + X \cos 2\pi\nu_L(t - t_0)] & t \geq t_0 \end{cases}. \quad (7.3)$$

The motivation for (7.3) is as follows: Firstly, the diffusion of coherently prepared atoms out of the beam causes the average coherence to fall off as the fraction of remaining atoms, i.e. as $[1 + \Gamma(t - t_0)]^{-1}$. Secondly, unspecified mechanisms (e.g. collisions) can cause the coherence of any single atom to decay as $\exp[-\gamma_{\text{deph}}(t - t_0)]$. Finally, a fraction X of the total coherence is due to the $m = 1$ and $m = -1$ dark states, whose Raman frequencies differ from that of the $m = 0$ dark state by the Larmor frequency ν_L . The value of ν_L can be obtained by measuring the frequency separation of the Zeeman-split Raman features in the spectral domain. The value of Γ can be obtained from analysis of the population relaxation. This leaves ρ_{21}^{max} , t_0 , and γ_{deph} as the free parameters of the fit.

By differentiating (7.2) and (7.3) we find that $\dot{f}_{\text{pop}}(t_0) = -\Gamma f_{\text{pop}}(t_0)$ and $\dot{f}_{\text{coh}}(t_0) = -(\Gamma + \gamma_{\text{deph}}) f_{\text{coh}}(t_0)$. That is, the effective decay constants for the hyperfine population and coherence are $\Gamma_G = \Gamma$ and $\gamma_G = \Gamma + \gamma_{\text{deph}}$. The dependence of Γ_G and γ_G on helium pressure is shown in Fig. 7.6.

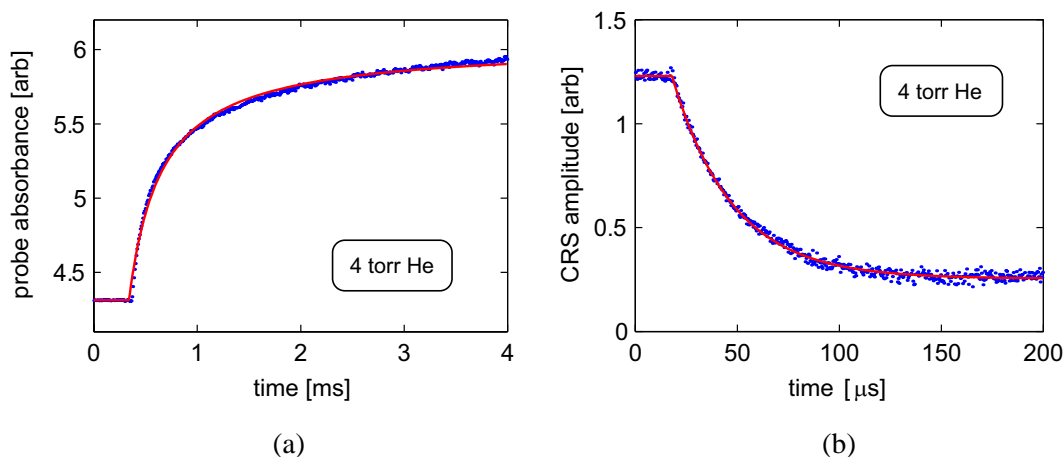


Figure 7.5: Typical data and fits for relaxation of hyperfine population (a) and hyperfine coherence (b).

With no buffer gas (not shown), Γ_G and γ_G are both about 0.1 MHz, corresponding to the ballistic transit time of about 1.6 μ s. As expected, both of the decay rates decrease as the amount of buffer gas increases. At high pressures, decoherence rates as small as several hundred Hz are obtained. Surprisingly, the decoherence rate is consistently 5-10 times larger than the population relaxation rate. Both datasets show a linear trend with a slope of approximately -1 , which is the expected pressure dependence of a process governed by diffusion. At high pressures the slope appears to become slightly smaller. This is most likely a manifestation of pressure broadening of the ground states. But whatever the mechanisms of relaxation are, it is clear that the addition of buffer gas can dramatically reduce the hyperfine decoherence rate and lead to millisecond lifetimes for dark states. Of itself, this should greatly improve the ability to coherently trap population. However, as discussed in §6.2, the decrease in the ground state decoherence rate with pressure is somewhat compensated by an increase in the optical decoherence rate, so that the ability to saturate the Raman transition does not increase as much as one would like. With a collisional broadening coefficient of 10 MHz/torr, the Raman saturation parameter peaks at a few torr (Fig. 7.7). This result suggests that adding buffer gas to increase the amount of hyperfine coherence is of limited usefulness.

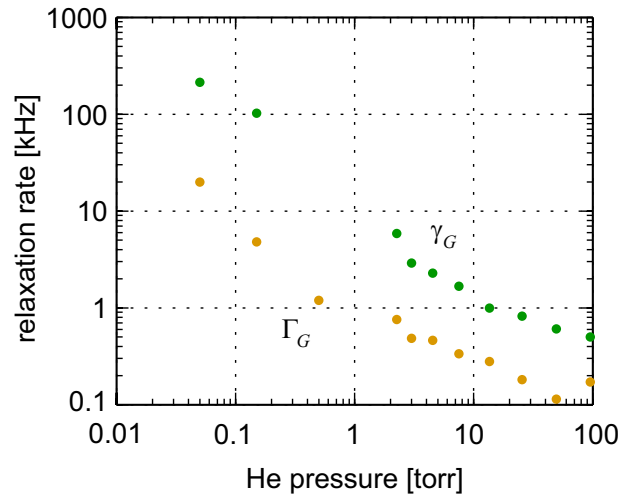


Figure 7.6: A buffer gas can greatly increase the time an atom spends interacting with the control fields, thereby decreasing the ground state relaxation rates.

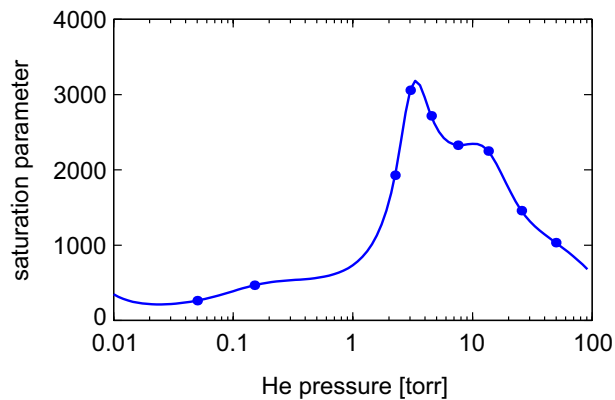


Figure 7.7: A plot showing how the nominal Raman saturation parameter $(\Omega_x^2 + \Omega_y^2)/(4\gamma_G\gamma_E)$, which indicates the ability to trap ground state population, is affected by the simultaneous narrowing of the Raman line and broadening of the optical line in the presence of buffer gas. For our experimental geometry, a pressure of about 3 torr is optimal. Note, the actual degree of saturation in sodium is much less than the nominal saturation parameter (see Fig. 5.7 and the discussion on page 65). The values indicated by dots were computed using the measured values of γ_G and taking $\Omega_x = \Omega_y = 25$ MHz, $\gamma_E = 5$ MHz + $10P_{\text{He}}$. The curve is an interpolation to guide the eye.

7.3 Coherence-Induced Transparency, Absorption, and Raman Scattering

A number of effects resulting from coherent preparation were observed. To provide some context for these results, the single field absorption spectrum of “pure” sodium vapor at different intensity regimes is shown in Fig. 7.8. At very weak intensities, two broad transmission dips (absorption peaks) are discernable, corresponding to the excitation of the $F = 1$ and $F = 2$ hyperfine levels to the $3P_{1/2}$ manifold. The weak field transmittance is accurately given by

$$T = \exp\left(-\frac{2\pi}{\lambda}L \operatorname{Im} \chi\right) \quad (7.4)$$

where

$$\operatorname{Im} \chi = 0.076 \cdot N \lambda^3 \times \left[\frac{1}{48}g(\Delta) + \frac{5}{48}g(\Delta - 189) + \frac{5}{48}g(\Delta + 1772) + \frac{5}{48}g(\Delta + 1772 - 189) \right], \quad (7.5)$$

$$g(\Delta) = \frac{\gamma_E}{\Delta_{\text{rms}}} \sqrt{\frac{\pi}{2}} \exp\left(-\frac{1}{2} \frac{\Delta^2}{\Delta_{\text{rms}}^2}\right) \quad (7.6)$$

and the parameters are: cell length $L = 8$ cm, wavelength $\lambda = 590$ nm, atom density $N = 1.4 \times 10^{11} \text{ cm}^{-3}$, excited state decoherence rate $\gamma_E = 5$ MHz, and Doppler width $\Delta_{\text{rms}} = 662$ MHz. (The number density is in good agreement with the value $1.7 \times 10^{11} \text{ cm}^{-3}$ which is based on a measurement of the cell temperature.) The factors $\frac{1}{48}$ and $\frac{5}{48}$ are the effective strengths of the transitions between the various D1 hyperfine levels (see Table A.1). At higher intensities, the two transmission dips merge into a single dip approximately halfway between the $F = 1$ and $F = 2$ resonances. This effect is a manifestation of (incoherent) optical pumping between the ground hyperfine levels: at either resonance the resonant ground state is strongly depopulated, so that the absorption is not very strong; but between the two resonances, there is no net optical pumping and the absorption is maximum, in spite of the fact that the field is significantly detuned from both resonances.

With two fields, I observed signatures of hyperfine coherence (Fig. 7.9). Each trace is the

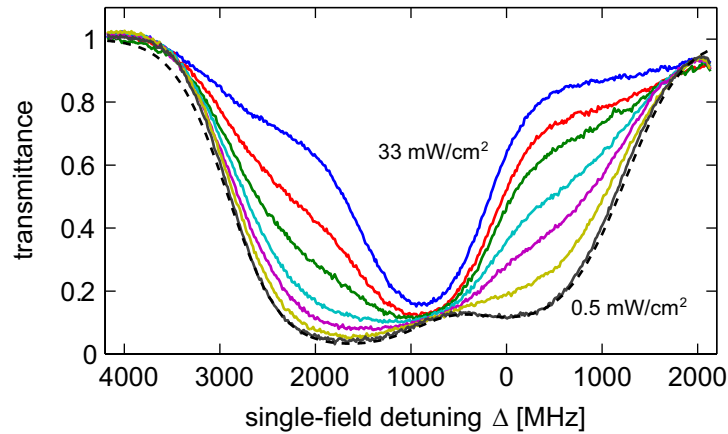


Figure 7.8: The transmittance of a single field of various intensities through an 8 cm-long sodium vapor. In units of mW/cm^2 , the intensities are 0.5, 1.5, 4, 6, 11, 17, and 33. The dashed line shows the theoretical transmittance assuming a number density of $1.4 \times 10^{11} \text{ cm}^{-3}$.

transmittance of one of the control fields. To obtain this data, the frequency of dye laser #1 (which supplied both control fields) was scanned slowly ($\approx 3 \text{ Hz}$) across the Doppler-broadened D1 line (a range of 10 GHz). Simultaneously, the frequency of MOD2 was rapidly³ ($\approx 60 \text{ Hz}$) dithered over a range of about 10 MHz. Hence the beat note of the fields was swept across the Raman resonance many times at different places within the Doppler profile. Each narrow feature in Fig. 7.9 is associated with the creation of coherence between of the $F = 1$ and $F = 2$ hyperfine levels.

Near the center of the D1 line, both fields show increased transmittance (reduction of absorption) at the Raman resonance, which is the signature of coherent population trapping. In the wings, a surprisingly different behavior occurs: one field apparently experiences coherently induced absorption while the other experiences coherently induced transparency and/or gain. (This behavior will be explained at the end of this section.). The data of Fig. 7.9 were taken with a small background pressure ($\sim 0.5 \text{ torr}$) of helium gas. Similar experiments were performed with varying pressures of helium, nitrogen, or argon. It was found that the coherently induced transparency features were not increased significantly by adding any amount of any kind of buffer gas, and that in fact too

³Care must be taken not to scan too rapidly, lest the Raman feature be broadened. As a rule-of-thumb, to measure a spectral feature of bandwidth $\Delta\nu$ Hz, the sweep rate (in Hz/s) should be well below $\Delta\nu^2/2\pi$.

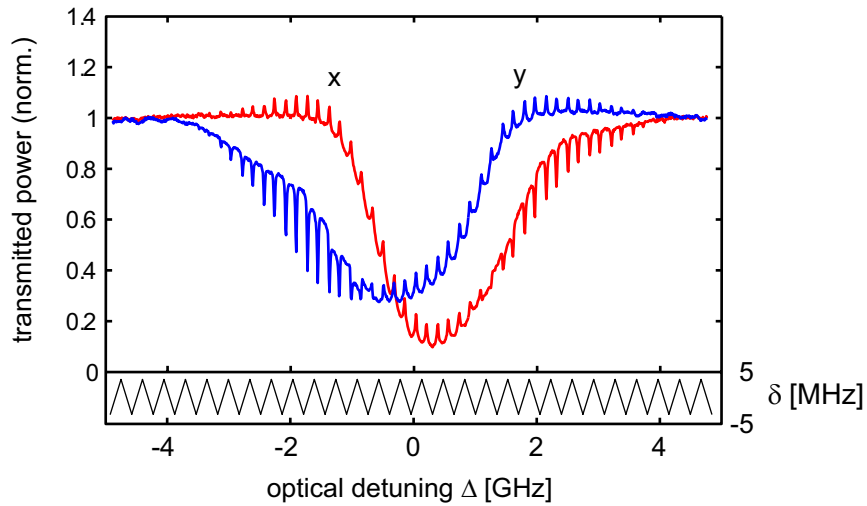


Figure 7.9: The two-field spectrum of the sodium D1 line, separated by polarization component. While the optical detuning Δ is swept slowly, the Raman detuning δ is rapidly dithered. Sweeping Δ reveals the Doppler-broadened structure of the D1 line. Scanning δ reveals the effect of hyperfine coherence each time the beat note of the fields equals the Raman frequency.

much buffer gas diminished coherent effects (Fig. 7.10; similar behavior was observed with Ar and N_2). It is my belief that the increase in the transit time was counteracted by the decrease in the optical pumping rates of the fields due to pressure broadening, so that addition of buffer gas did not significantly increase the ratio of pumping rate to relaxation rate.

The transparency feature and Raman scattering peak shown in Fig. 7.11a,b are typical. In these plots, the control fields were tuned to the center of the D1 line and the probe field was tuned to maximize the scattered signal. No magnetic field was applied. Both features have triangular lineshapes and are of sub-natural linewidth. When a longitudinal magnetic field was applied, the transparency feature was observed to split into three features (Fig. 7.11c; compare to Fig. 6.5). The Raman scattering spectrum also contained three features, appearing very similar to the three transparency features.

In the end, the signatures of coherent preparation (and by inference the amount of hyperfine coherence) were never dramatically large. In light of chapters 5 and 6 this is perhaps not too sur-

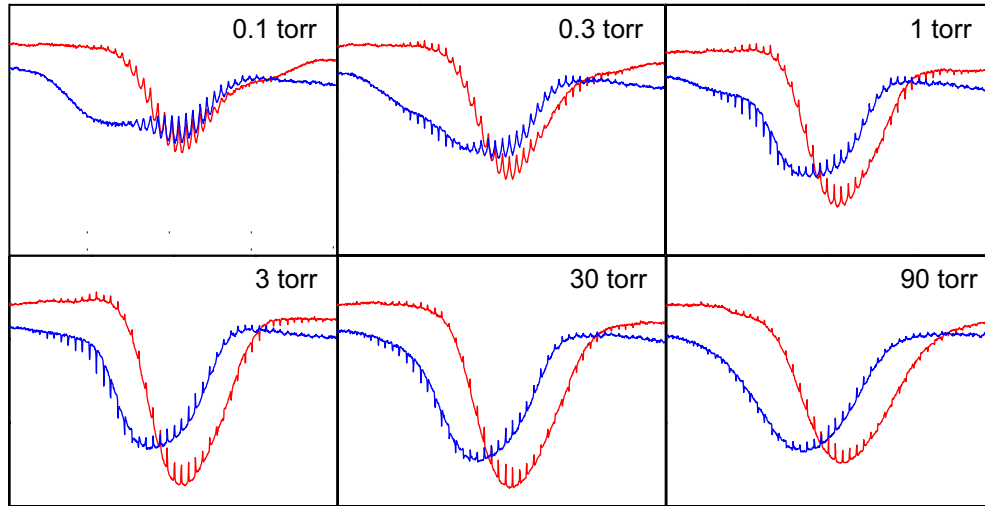


Figure 7.10: Two-field spectra of sodium in the presence of helium at various partial pressures. Although adding buffer gas increases the lifetime of the ground state coherence, the size of the Raman features (and thereby the degree of hyperfine coherence) is evidently not increased.

prising; complications from the multiplicity of states and vapor physics hinder coherent population trapping. Even so, the simulations in Chapter 6 predicted signatures of coherent preparation roughly 3-5 times larger. Radiation trapping is a good candidate for the discrepancy between simulation and experiment, since it would contribute to the ground state relaxation rate during coherent preparation but would not contribute to the measured relaxation rate used for the simulations, which was obtained with the control fields turned off. It is also possible that unidentified factors, for example vapor impurities, were in some part responsible.

Apart from mode matching (which was ensured by the use of the optical fiber), the intensity of the control fields was the controllable parameter which had the most impact on the strength of the coherent effects. Sometimes it was observed that applying a longitudinal magnetic field of several Gauss would slightly heighten and narrow the central ($\delta = 0$) transparency and Raman scattering features, suggesting the slightly deleterious presence of stray magnetic fields. The strongest coherent effects were observed with optical intensities $\gtrsim 80 \text{ mW} / \text{cm}^2$ ($\Omega_x, \Omega_y \gtrsim 25 \text{ MHz}$) and with buffer gas pressures $\lesssim 5 \text{ torr}$. Under such conditions, the absorption coefficient of the vapor would

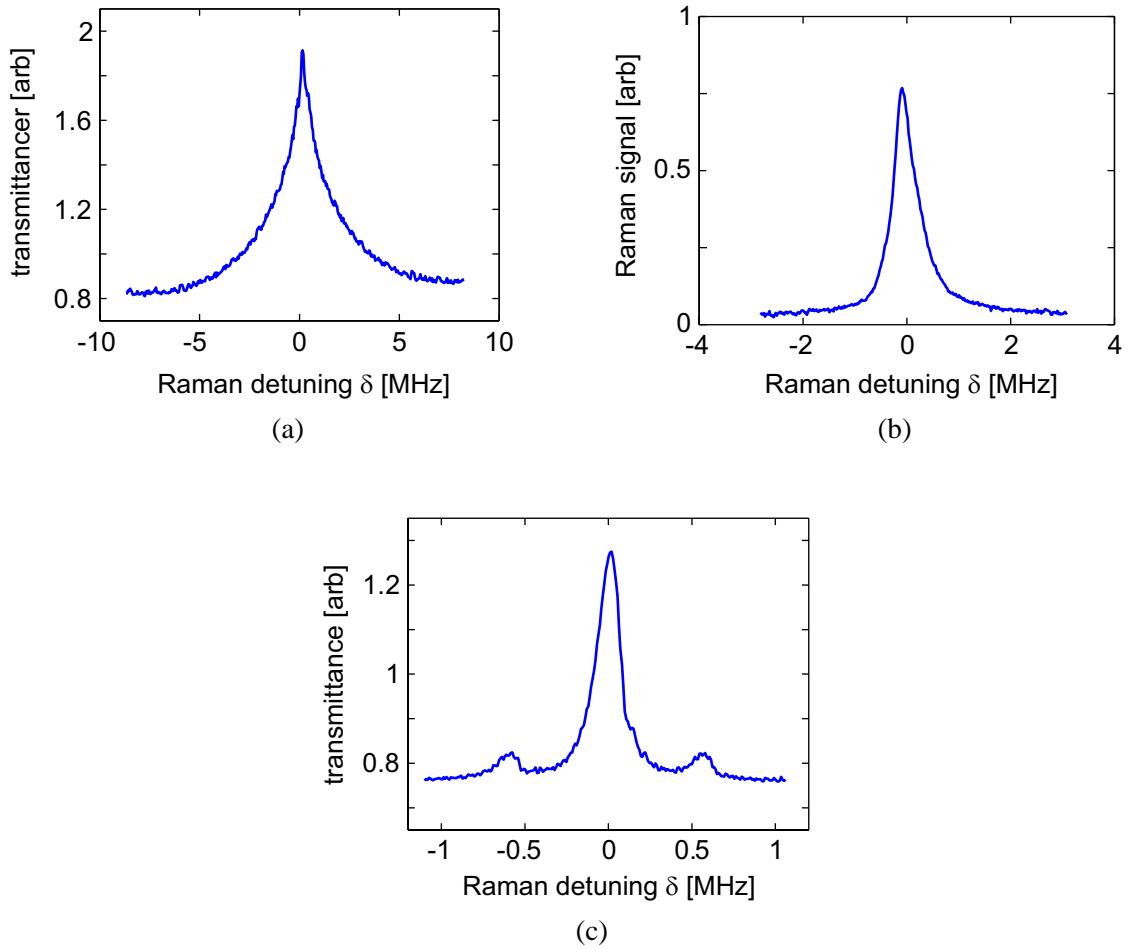


Figure 7.11: Typical data showing optical features which result from ground state coherence. (a) Electromagnetically induced transparency at the Raman resonance. (b) Coherently induced Raman scattering. (c) EIT in the presence of a DC longitudinal magnetic field. The data were taken on different days, under different conditions, but in all three cases the control fields were tuned to the center of the D1 line.

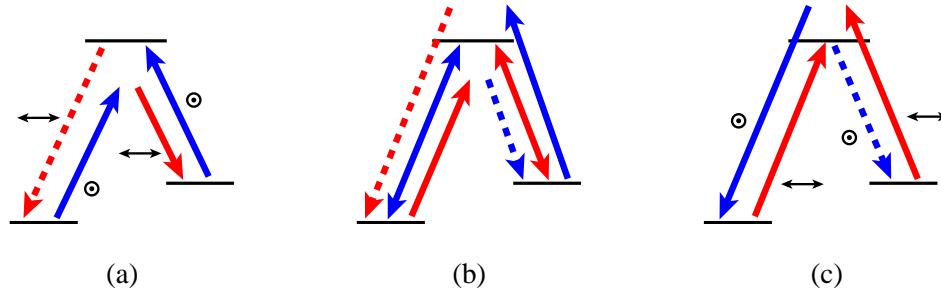


Figure 7.12: Coherently induced wave mixing between the control fields. On the red or blue side of the D1 line (a,c) wave mixing transfers power from one polarization to the other. At the center of the line (b), both processes occur. However, the evolution is conservative, and there is no change in the total power in either polarization component. In all three regions, new frequency components are produced.

be reduced at Raman resonance by an estimated 30-35% (based on a typical change in transmittance from 12% to 27% and the assumption of exponential attenuation), while the Raman scattering efficiency would be roughly 0.5% (resulting in a few μW of scattered signal).

I now return to the subject of the unexpected absorption and gain features in the wings of the D1 line. Upon frequency resolving the transmitted fields, it was found that in each wing, one of the polarization components contained not only the transmitted control field, but a new frequency component $2 \times 1772 \text{ MHz}$ away from the control field. This frequency component was present only when the control fields were tuned to the Raman resonance. This observation indicates the presence of four-wave mixing with the control fields. Indeed, the features in the wings of Fig. 7.9 can be understood by the two FWM processes illustrated in Fig. 7.12a,c. On the red side of the D1 line, the higher frequency control field (Ω_{1y}) becomes resonant with the lower frequency transition ($F = 2$ to $3P_{1/2}$), Fig. 7.12a. At the Raman resonance, coherent population trapping creates a small amount of hyperfine coherence (small because the control fields are far detuned). This coherence induces Stokes scattering of the Ω_{1y} field into the x polarization. Hence, power is transferred from the y polarization to the x polarization. On the blue side of the line, the situation is reversed (Fig. 7.12c): the Ω_{2x} field becomes resonant with the $F = 1$ to $3P_{1/2}$ transition, and coherently induced anti-Stokes scattering transfers power from the x polarization to the y polarization.

One might expect that similar FWM processes also occur near the center of the D1 line (Fig. 7.12b), and that these processes might interfere with EIT. Indeed, frequency-resolved detection revealed that new frequency components are also generated in this region of the D1 line. However, the generated fields are significantly weaker than the control fields. Analysis of this process in a 3-state system indicates that the characteristic length for generation of the new field components is larger than the length for residual absorption of the control fields by the factor $(\nu_2 - \nu_1)/[\gamma_E(1 + s)]$. Numerical studies confirm that under realistic conditions, the generated field components remain very small. Furthermore, it can be shown that the mixing process is conservative; generation of the new fields does not diminish the total power in either polarization. Thus FWM does not affect EIT features such as those found in the spectra of Fig. 7.9.

7.4 Frequency Conversion of an Optical Signal Using Hyperfine Coherence

Although the generation of hyperfine coherence and the optical effects it produces are interesting topics for academic study, the scientist is often asked by friends, relatives, and funding agencies, What is it good for? As mentioned previously, a material coherence can act as an oscillator which mixes with an optical signal, shifting it up or down in frequency. The usefulness of this approach depends on the fidelity, bandwidth, efficiency of the conversion. In principle the fidelity is excellent, since the scattered field is directly proportional to the input field; the efficiency is high, since the typical conversion length can be as short as an absorption length (see §3.3.1); and the bandwidth is large, being (in the case of resonant scattering) the width of the inhomogeneously-broadened line, which is ~ 1 GHz in sodium. Although the frequency shift obtained with sodium is not large, the principle applies just as well to systems with ground (or metastable) states that have much larger frequency separations which cannot be obtained using RF technologies.

To study frequency conversion of a signal in sodium, an amplitude modulated probe beam was scattered off the coherence created by two CW control fields (Fig. 7.1). MOD1 was set to provide constant output (no intensity modulation), and the frequency of MOD2 was adjusted to bring the

control fields into resonance with the Raman transition. The light from dye laser #2 was downshifted by 80 MHz and amplitude modulated with a 4 MHz square wave by MOD4, forming a probe field with a time-varying envelope $E_p(t)$. The probe field passed through MOD3, where it was downshifted by 1612 MHz together with the horizontally polarized control field. Just before the cell, the probe power was 1.3 mW. Inside the cell, the probe field scattered off the hyperfine coherence created by the control fields, generating a vertically polarized “signal” field with envelope $E_s(t)$ at a carrier frequency 1772 MHz above that of the probe. Thus the frequency of the signal field was $-80 - 1612 + 1772 = 80$ MHz higher than dye laser #2. I found that the power of the signal reached a maximum of about $8 \mu\text{W}$ when dye laser #1 and dye laser #2 were tuned to the centers of their Doppler-broadened lines (D1 and D2 respectively). The signal field was angularly separated from the remnant of the vertically polarized control field by reflecting the beam off the grating. Immediately following the grating was a lens of focal length 1000 mm. At the back focal plane of the lens, the control and signal fields were a few hundred microns wide and separated by about 3 mm. A $750 \mu\text{m}$ pinhole passed only the signal field. The signal field was combined with a local oscillator field E_{LO} from dye laser #2; the power of the local oscillator was 1 mW. The intensity of the combined fields,

$$I = \left| E_{\text{LO}} + iE_s(t)e^{-2\pi i(80 \text{ MHz})t} \right|^2 \quad (7.7)$$

$$= |E_{\text{LO}}|^2 + |E_s(t)|^2 + iE_{\text{LO}}^*E_s(t)e^{-2\pi i(80 \text{ MHz})t} + \text{c.c.} \quad (7.8)$$

was measured with the balanced detectors and the beat note was monitored on a digital oscilloscope. Since E_{LO} was constant (to the extent that dye laser #2 was stable), the beat note was proportional to $E_s(t)$. By numerically isolating the positive-frequency portion of the beat note and downshifting it by 80 MHz, the complex amplitude $E_s(t)$ of the scattered field was obtained.

To compare $E_s(t)$ to the input probe field $E_p(t)$, a second measurement was made. For this measurement, the control fields were blocked and the unshifted component of the probe field from MOD3 was coupled into the fiber. Dye laser #2 was tuned well outside the D2 line to ensure that the probe field did not interact with the vapor. The half-wave plate after the vapor cell was rotated

so that the horizontally polarized probe and control fields were passed to the grating. The intensity at the balanced detector was then

$$I = \left| E_{\text{LO}} + iE_p(t)e^{2\pi i(80\text{MHz})t} \right|^2 \quad (7.9)$$

$$= |E_{\text{LO}}|^2 + |E_p(t)|^2 + iE_{\text{LO}}^*E_p(t)e^{2\pi i(80\text{MHz})t} + \text{c.c.} \quad (7.10)$$

To obtain $E_p(t)$, the negative-frequency portion of the beat note was numerically isolated and up-shifted by 80 MHz.

Fig. 7.13a shows a portion of the traces $\text{Re } E_p(t)$ and $\text{Re } E_s(t)$. The traces have been normalized and time-shifted to coincide. Clearly, the signal field envelope $E_s(t)$ is identical to the input field envelope $E_p(t)$. The fidelity of the conversion is $|\mathcal{F}| = 0.99$ where

$$\mathcal{F} = \frac{\int E_p^*(t)E_s(t) dt}{\sqrt{\int |E_p(t)|^2 dt} \sqrt{\int |E_s(t)|^2 dt}}. \quad (7.11)$$

The normalized spectral densities $|E_p(\nu)|$ and $|E_s(\nu)|$ are shown in Fig. 7.13b, where

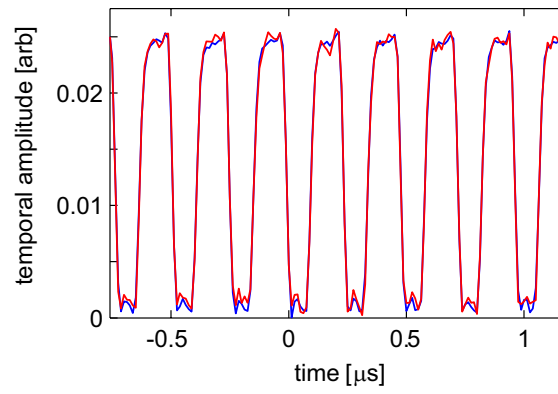
$$E_{\text{s,p}}(\nu) \equiv \frac{1}{\sqrt{2\pi}} \int E_{\text{s,p}}(t) \exp(2\pi i\nu t) dt. \quad (7.12)$$

Again, the faithfulness of the conversion process is evident as the two spectra are nearly identical. A slightly more informative measure of the faithfulness of the scattering process is the complex transfer function

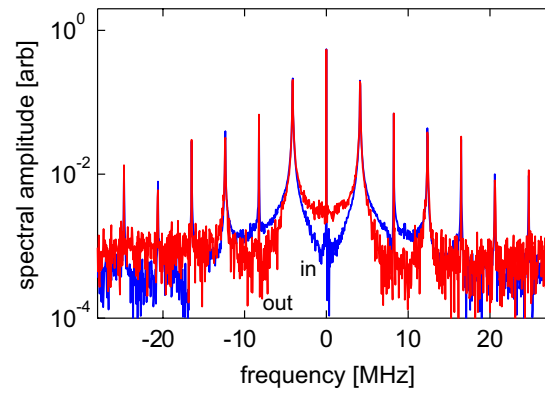
$$T(\nu) \equiv \frac{E_s(\nu)/\sqrt{\int |E_s(t)|^2 dt}}{E_p(\nu)/\sqrt{\int |E_p(t)|^2 dt}}. \quad (7.13)$$

Perfect reproduction of the signal occurs if $T(\nu) = 1$. Fig. 7.13c shows the magnitude and phase of $T(\nu)$. Within experimental error, the transfer function describes a flat, uniform response up to the highest measurable frequency components in the signal. As was predicted in §3.3.2, the bandwidth of the scattering process is not limited to the homogeneous line width (10 MHz).

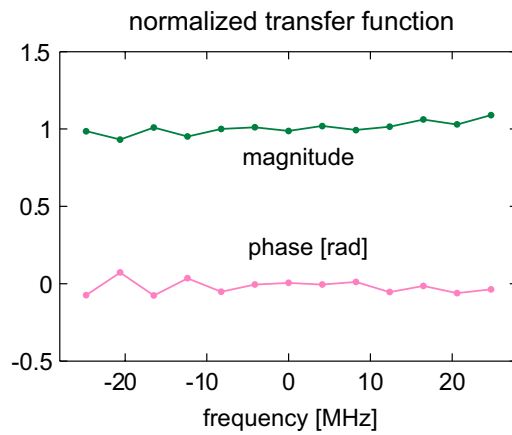
To demonstrate that a phase-encoded signal can also be converted using coherent scattering, MOD4 was changed from an amplitude modulator to a frequency (or phase) modulator with a



(a)



(b)



(c)

Figure 7.13: Frequency conversion of an amplitude-modulated optical signal using coherent Raman scattering. (a) The temporal amplitudes of the input and output fields. (b) The spectral amplitudes of the input and output fields. (c) The magnitude and phase of the normalized transfer function (evaluated at locations of spectral peaks); a value of unity at all frequencies means perfect reproduction of the input field. For this particular signal, the conversion fidelity was 99%.

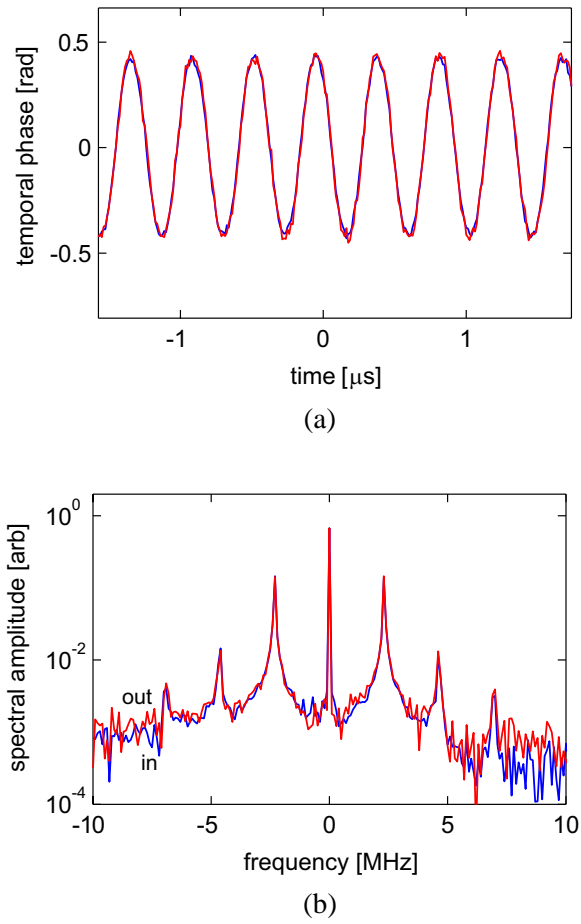


Figure 7.14: Frequency conversion of a phase (frequency) modulated optical signal using coherent Raman scattering. (a) The temporal phases of the input and output fields. (b) The spectral amplitudes of the input and output fields. The conversion fidelity for this signal was 99.9%.

period of about $0.5 \mu\text{s}$. Again, two measurements were performed, one to obtain $E_s(t)$ and one to obtain $E_p(t)$. The temporal phases and spectral densities of the probe and signal field envelopes are shown in Fig. 7.14. Once again, the scattered field is essentially identical to the input field. In this experiment, the fidelity was 0.999.

7.5 Summary

The generation of quantum coherence in a sodium vapor was demonstrated in a variety of experiments. Coherence between the $3S_{1/2}$ hyperfine levels was generated when two cross-linearly polarized control fields tuned to the D1 line were applied to the vapor and the beat note of the fields was within a few hundred kHz of the hyperfine level separation (1772 MHz). As a result of coherent population trapping, the absorption of the control fields was reduced by 30-35% and a probe field tuned to the D1 line was Raman scattered with 0.5% efficiency. It was also found that coherent preparation induces four-wave mixing processes involving the control fields, resulting in electromagnetically induced gain and absorption features in the wings of the D1 line. Arguments suggest that similar FWM processes do not significantly influence the coherent preparation of the vapor at line center.

The effects of introducing an inert buffer gas into the vapor were also investigated. It was found that tens of torr of He, Ar, or N_2 can significantly increase the hyperfine population and coherence lifetimes (milliseconds or more), but nevertheless the degree of coherence does not increase. The decrease in relaxation is compensated by a decrease in the efficacy of the control fields due to pressure broadening of the excited states. Although both ground state relaxation rates show the expected trend for a diffusive process, a satisfactory explanation is lacking as to why the ground state coherence lifetime is consistently 5-10 times smaller than the population lifetime.

Finally, coherent preparation was used to demonstrate wavelength conversion of amplitude and phase information imprinted on a weak probe field. Both AM and FM signals with multi-MHz bandwidths were Raman scattered into new frequency bands with extremely high fidelity (> 99%). The measured transfer function for the conversion was very broad and uniform, indicating a conversion bandwidth of at least tens of MHz.

Chapter 8

Summary and Perspective

8.1 Summary

Coherent preparation is an approach to nonlinear optics in which multiple optical fields put a medium into a superposition of quantum states with large coherence. The quantum coherence leads to interference between optically induced transitions, and thereby mediates strong interactions between light fields. In the process called coherent population trapping, a medium settles into a superposition state that is completely uncoupled from the exciting fields. In this work I have explored coherent population trapping with a view toward its utility in converting optical signals from one frequency band to another. In particular, I have performed a detailed analysis of the physics of coherent population trapping in alkali vapors and have performed numerical and experimental studies of optical processes which result from creating ground state hyperfine coherence in sodium.

Although a two-state system can be made to exhibit phenomena similar to those associated with coherent population trapping, the clearest examples of coherent preparation involve at least three states and two fields. I found that such a system can be modelled rather nicely using a geometrical formalism based upon Bloch's vector. This model brings out the major principles of coherent population trapping, namely: (1) ground state coherence builds up to a large value at the Raman resonance; (2) dramatic reduction of the absorption occurs in conjunction with the build-up of coherence; and (3) the peak coherence and transparency increase with the ratio of the optical excitation

rate to the ground state relaxation rate. One also finds that a weak field can Raman scatter off the ground state coherence, producing a field that carries the amplitude and phase content of the input field, but shifted in frequency by the Raman frequency. This coherent Raman scattering can be as efficient as linear scattering, allowing 100% of the power to be converted to the new frequency in a few resonant absorption lengths. The scattering can also have a very large bandwidth, being equal to the total spectral width of the excited band or inhomogeneously broadened level. Coherent Raman scattering is also predicted to transfer (under ideal conditions) the quantum state of the probe field to the Raman scattered field.

Analysis of coherent population trapping in many-state, few-level systems can sometimes be aided by diagonalizing the photoexcitation operator. The ground states of the diagonalization generalize the bright and dark states which are commonly employed in discussions of 3-state systems. In this basis, coherent population trapping can be understood as a competition between optical pumping—out of strongly coupled (bright) states into weakly coupled (dark) states—and ground-state relaxation. The difficulty of coherent population trapping generally increases with the number of ground states, for several reasons which ultimately reduce to the fact that, the more states there are, the more possibilities nature has to put the system in a state other than the one you want. Analysis of the sodium D1 states reveals that two essentially independent systems exist, one for each of the excited hyperfine levels, and that each of these systems possesses multiple dark states, only some of which possess Raman (hyperfine) coherence. However, application of a longitudinal magnetic field lifts the degeneracy and isolates a single dark state that is a superposition of the $|F = 1, m = 0\rangle$ and $|F = 2, m = 0\rangle$ states. This dark state has maximal coherence and is capable of inducing coherent Raman scattering via the D2 line with relatively high efficiency.

A wide variety of factors which can affect experimental implementations of coherent population trapping in vapors were considered. The most important factors are Doppler shifts, transit of atoms from the illumination region, spin relaxation due to wall collisions, and pressure broadening of the excited states. Some influences, such as ground state relaxation due to collisions between vapor atoms, velocity diffusion, and wave mixing, are also typically present; however, they are too weak to have a significant effect in experiments involving only modest vapor densities. Radiation trapping

may or may not be important, depending on the details of the experiment. In addition, successful coherent preparation requires certain technical criteria to be met, most notably good spatial mode overlap of the control fields, phase and frequency stability of the control fields, and elimination of stray fields. These requirements are not overly stringent, however, and can be satisfied with reasonable experimental effort. Simulations predict that relatively large amounts of hyperfine coherence (involving $\sim 50\%$ of all illuminated atoms, or $\simeq 100\%$ of resonant illuminated atoms, in a maximally coherent state) should be achievable under realistic experimental conditions. Nevertheless, electromagnetically induced transparency and especially coherent Raman scattering are predicted to be surprisingly less pronounced in sodium than in idealized 3-state systems. Under the conditions believed to exist in my experiments, resonant absorption should be reduced by a factor of about 7, while the maximum efficiency of Raman scattering with a several-cm thick vapor is limited to a few percent. The reason for this latter situation is that more D2 hyperfine states can participate in absorption of the probe and scattered fields than in Raman scattering.

Besides analytical studies, a number of experiments were conducted. The critical ground state relaxation rate was measured directly as a function of the density of an inert buffer gas (helium). Reduction of the population and coherence relaxation rates to $\lesssim 1$ kHz was possible with several tens of torr of buffer gas. However, the accompanying pressure broadening of the excited state was found to compensate for the advantage gained by increasing the ground state lifetime, such that a density of about 3 torr was optimal for our experimental geometry. Both electromagnetically induced transparency and coherent Raman scattering were clearly demonstrated, although to a lesser degree than simulations predicted. The reduction in absorption at Raman resonance was inferred to be 35% (transparency factor of 1.5) on a typical day, while the Raman scattering efficiency was typically 0.5 to 1%. Argon and nitrogen were also tried as buffers with little difference in the results.

Finally, and most significantly, frequency conversion of optical signals using coherent Raman scattering was demonstrated. Both amplitude- and frequency-(phase-) modulated signals with bandwidths well in excess of 10 MHz were transferred from an input probe beam to a Raman scattered beam with excellent ($> 99\%$) fidelity, demonstrating the potential of this technique.

Several issues remain unresolved. The first is the fact that the ground state decoherence rate is

5-10 times larger than the population relaxation rate over several orders of magnitude of buffer gas pressure. No mechanism which can explain this feature has come to mind. The second unresolved issue is the discrepancy between the relatively pronounced coherent effects predicted by simulation and the underwhelming effects seen in the laboratory. Roughly speaking, simulations predicted coherent effects 4-5 times stronger than what was observed. The most obvious explanation for this discrepancy is a ground state relaxation mechanism not included in the model. While this argument might seem to be irrelevant in light of the fact that experimentally measured relaxation rates were used for the simulations, one could argue that the measured rates are not entirely appropriate for the simulations. For example, the ground state relaxation rates were measured “in the dark” and would not include relaxation caused by radiation trapping, which would only occur during actual coherent preparation. Excited state relaxation was modelled using rates reported in the literature, which were assumed (but not verified) to be appropriate for our own vapor. It is possible that impurities significantly altered the (single-field) optical properties of the vapor when buffer gas was added to the system, as the vacuum system I used is now understood to be not of high quality. One could also argue that relaxation was modelled in too simple a manner—that a few exponential decay parameters do not suffice to characterize the complex spatio-temporal aspects of diffusion and collisional relaxation. Although this is a fair point, I doubt it could explain a factor of 4-5 discrepancy. I would be more inclined to believe that the relative phase modulation of the control fields (which was inadvertently imposed by the frequency shifting modulators) was a factor limiting EIT and CRS in my experiments; although it could not have been the only factor, since the EIT and CRS signals did not improve significantly on the one day in which the modulation was eliminated by a reconfiguration of the apparatus. While none of these unresolved issues is critical, they are worthy topics of future efforts in both experimental and theoretical domains.

8.2 Perspective

The goal of this research was to study and demonstrate the feasibility of using coherent preparation to perform frequency conversion of light while preserving the spectral and temporal structure of the field. By this criteria the research was a clear success: a deep understanding of coherent population

trapping was gained and high-quality frequency conversion of optical signals was demonstrated. But it is fair to say that sodium, and perhaps even alkali vapors in general, are less than ideal for implementing coherently-induced nonlinear optical processes. Certainly they are capable of providing clear demonstrations of the desired physics. But at least sodium seems to have limited usefulness as a functional coherent medium. While the bandwidth and fidelity of frequency conversion were very satisfactory, the efficiency was less than one would hope, especially since electromagnetically induced processes are supposed to have an advantage of efficiency compared to traditional nonlinear processes.

Much of the problem lies in the structure of sodium itself. The ground hyperfine splitting is barely larger than the Doppler width, meaning that a non-negligible fraction of atoms are nearer to the “wrong” transition. The multiplicity of ground states makes trapping harder than in simpler systems (such as atoms with smaller nuclear spin). The fact that sodium has a higher vapor temperature than other alkalis means that ground state relaxation must be controlled by the use of a buffer gas, which limits diffusion but also broadens the optical transitions. The critical hindrance to efficient coherent Raman scattering through the D2 levels arises from the similarity of their energies combined with the differences in their selection rules. If the excited levels were separated by more than a Doppler width, it would be possible to perform coherent Raman scattering through one level without the resonant absorption associated with the adjacent levels.

In retrospect I would choose a medium other than sodium and use different experimental technologies. ^{87}Rb , for example, has the same D1 structure as sodium (and therefore has the same dark state(s)), but the hyperfine levels are better separated. The transitions can be excited using diode lasers, which are more reliable and easier to work with than ring dye lasers. Because sufficient vapor densities can be achieved without requiring high temperatures, wall coatings may be used to increase ground state lifetimes without producing the detrimental excited state broadening that occurs with the use of buffer gases. In this case a professionally-made closed glass cell could be used instead of an assembled steel cell, eliminating the need to build a high-quality vacuum system. I would better shield the cell from stray magnetic fields and use a solenoid rather than Helmholtz coils to produce a more uniform longitudinal magnetic field. Together, these changes should result

in improved experimental results. And as I indicate below, there may be vapors even better than rubidium.

Given the time, I would also like to refine the model which was the basis for all my simulations. A more accurate model of collisional relaxation, which allows for different relaxation modes, would not increase the computational costs of simulation. Furthermore, I would like to incorporate diffusion and velocity changing collisions explicitly (i.e. to solve eqn. (6.20)) without increasing the computational cost by two orders of magnitude. It may be possible to do this by treating velocity diffusion perturbatively and utilizing the symmetry of the cell to isolate a small number of dominant diffusion modes.

With more coherence, stronger transparency, and more efficient Raman scattering, one could imagine a number of interesting experiments. To start, there are the many proposed uses of EIT and ground state coherence mentioned in chapter 1. In §3.3 it was predicted that CRS preserves the quantum properties of the converted light. It would be interesting to prepare a pair of polarization-entangled beams, shift one to a different frequency using CRS, and then verify that Bell's inequalities can be violated using the shifted beam. Far from being an academic issue, the ability to preserve quantum entanglement in shifting from one wavelength to another could be a significant enabling technology for distributed quantum cryptographic systems [102–105] and the “quantum internet” [106]. A more ambitious experiment, which would require extremely large transparency, would be to frequency convert a squeezed state [107] and show that the squeezing is preserved.

Of course, frequency conversion of even classical state information has scientific and telecommunication applications. While my studies in sodium clearly show the potential for coherent population trapping to perform this task, it will not be considered seriously as a practical technique until more convenient media with much better performance are found. Lead vapor has been used to demonstrate EIT with much greater success than sodium [14]. I would consider using vapors for further fundamental studies of coherent preparation; but they are still too inconvenient for widespread use. A number of groups have begun studying coherent population trapping and EIT in solids [72, 108–110], including both doped crystals [111–113] and semiconductors [70, 79, 114–119]. The challenge of using solids is that strong interactions between electrons

and neighboring atoms usually leads to rapid relaxation of quantum coherences. Clearly, there is much opportunity for progress.

In conclusion, there are some technical challenges which remain before coherent preparation leaves the laboratory. But it is a real phenomenon based on readily accessible physics. It is reasonable to hope that continuing developments in material science and/or nanofabrication technologies in the next few years will lead to media that can be easily and conveniently prepared in maximally coherent states. And in turn, these media will form the heart of devices that perform a variety of useful tasks, including frequency conversion of optical signals.

References

- [1] G. Alzetta, A. Gozzini, L. Moi, and G. Orriols. “An experimental method for the observation of r.f. transitions and laser beam transitions in oriented Na vapors.” *Nuovo Cimento B* **36**, 5 (1976).
- [2] H. R. Gray, R. M. Whitley, and C. R. Stroud, Jr. “Coherent trapping of atomic populations.” *Optics Letters* **3**, 218–220 (1978).
- [3] U. Fano. “Effects of configuration interaction on intensities and phase shifts.” *Physical Review* **124**, 1866 (1961).
- [4] W. Chow, M. Scully, and J. Stoner, Jr. “Quantum-beat phenomena described by quantum electrodynamics and neoclassical theory.” *Physical Review A* **11**(4), 1380–8 (1975).
- [5] J. Mlynek and W. Lange. “A simple method of observing coherent ground state transients.” *Optics Communications* **30**, 337–340 (1979).
- [6] D. A. Cardimona, M. G. Raymer, and C. R. Stroud, Jr. “Steady-state quantum interference in resonance fluorescence.” *Journal of Physics B* **15**, 55–64 (1982).
- [7] M. S. Malcuit, D. J. Gauthier, and R. W. Boyd. “Suppression of amplified spontaneous emission by the four-wave mixing process.” *Physical Review Letters* **55**, 1086–1089 (1985).
- [8] S. E. Harris, J. E. Field, and A. Imamoglu. “Nonlinear optical processes using electromagnetically induced transparency.” *Physical Review Letters* **64**, 1101–1110 (1990).

- [9] J. Gea-banacloche, Y. Q. Li, S. Z. Jin, and M. Xiao. “Electromagnetically induced transparency in ladder-type inhomogeneously broadened media - theory and experiment.” *Physical Review A* **51**(1), 576–584 (1995).
- [10] D. J. Fulton, S. Shepherd, R. R. Moseley, B. D. Sinclair, and M. H. Dunn. “Continuous-wave electromagnetically induced transparency - a comparison of V-system, Lambda-system, and cascade systems.” *Physical Review A* **52**(3), 2302–2311 (1995).
- [11] S. Wielandy and A. L. Gaeta. “Investigation of electromagnetically induced transparency in the strong probe regime.” *Physical Review A* **58**(3), 2500–2505 (1998).
- [12] D. A. Shapiro. “Field splitting of a nonabsorbing state.” *Journal of Experimental and Theoretical Physics* **88**(6), 1072–1078 (1999).
- [13] M. Lukin, S. Yelin, M. Fleischhauer, and M. Scully. “Quantum interference effects induced by interacting dark resonances.” *Physical Review A* **60**(4), 3225–8 (1999).
- [14] A. Kasapi, M. Jain, G. Y. Yin, and S. E. Harris. “Electromagnetically induced transparency: Propagation dynamics.” *Physical Review Letters* **74**, 2447–2450 (1995).
- [15] M. Yan, E. G. Rickey, and Y. F. Zhu. “Electromagnetically induced transparency in cold rubidium atoms.” *Journal of the Optical Society of America B* **18**(8), 1057–1062 (2001).
- [16] C. Y. Ye, Y. V. Rostovtsev, A. S. Zibrov, and Y. M. Golubev. “Quantum interference in atomic vapor controlled by a magnetic field.” *Optics Communications* **207**, 227–31 (2002).
- [17] K. Motomura and M. Mitsunaga. “High-resolution spectroscopy of hyperfine Zeeman components of the sodium D-1 line by coherent population trapping.” *Journal of the Optical Society of America B* **19**(10), 2456–2460 (2002).
- [18] A. Lezama, S. Barreiro, A. Lipsich, and A. M. Akulshin. “Coherent two-field spectroscopy of degenerate two-level systems.” *Physical Review A* **61**, 013801 (1999).
- [19] J. Kim, K. Kim, H. Moon, M. Kwon, and H. Park. “Enhancement of electromagnetically induced absorption in Cs atoms.” *Journal of the Korean Physical Society* **39**, 859 (2001).

- [20] C. Andreeva, S. Cartaleva, Y. Dancheva, V. Biancalana, A. Burchianti, C. Marinelli, E. Mariotti, L. Moi, and K. Nasyrov. “Coherent spectroscopy of degenerate two-level systems in Cs.” *Physical Review A* **66**, 012502/1–12 (2002).
- [21] C. Goren, A. D. Wilson-Gordon, M. Rosenbluh, and H. Friedmann. “Electromagnetically induced absorption due to transfer of coherence and to transfer of population.” *Physical Review A* **67**, 33807–1–8 (2003).
- [22] A. Taichenachev, A. Tumaikin, and V. Yudin. “Electromagnetically induced absorption in a four-state system.” *Physical Review A* **61**, 011802/1 (2000).
- [23] H. Y. Ling and S. Barbay. “Large index of refraction with vanishing absorption in the 2-level atomic system driven by a strong-field.” *Optics Communications* **111**(3-4), 350–359 (1994).
- [24] Z. Ficek and T. Rudolph. “Quantum interference in a driven two-level atom.” *Physical Review A* **60**(6), R4245–R4248 (1999).
- [25] E. Fiordilino, F. Morales, and R. Daniele. “Phase control of the harmonic yield in a two color laser driven two level atom.” *Laser Physics* **10**(1), 111–115 (2000).
- [26] R. S. Bennink, R. W. Boyd, C. R. Stroud, and V. Wong. “Enhanced self-action effects by electromagnetically induced transparency in the two-level atom.” *Physical Review A* **63**(3), 033804 (2001).
- [27] Z. Ficek, J. Seke, A. V. Soldatov, G. Adam, and N. N. Bogolubov. “Multilevel coherence effects in a two-level atom driven by a trichromatic field.” *Optics Communications* **217**(1-6), 299–309 (2003).
- [28] Y.-Q. Li and M. Xiao. “Transient properties of an electromagnetically induced transparency in three-level atoms.” *Optics Letters* **20**, 1489–1491 (1995).
- [29] E. A. Korsunsky, W. Maichen, and L. Windholz. “Dynamics of coherent optical pumping in a sodium atomic beam.” *Physical Review A* **56**(5), 3908–3915 (1997).

- [30] A. D. Greentree, T. B. Smith, S. R. de Echaniz, A. V. Durrant, J. P. Marangos, D. M. Segal, and J. A. Vaccaro. “Resonant and off-resonant transients in electromagnetically induced transparency: Turn-on and turn-off dynamics.” *quant-ph* **0109090** (2001).
- [31] P. Valente, H. Failache, and A. Lezama. “Comparative study of the transient evolution of Hanle electromagnetically induced transparency and absorption resonances.” *Physical Review A* **65**, 023814/1 (2002).
- [32] J. Oreg, F. T. Hioe, and J. H. Eberly. “Adiabatic following in multilevel systems.” *Physical Review A* **29**, 690 (1984).
- [33] R. N. Shakhmuratov, J. Odeurs, R. Coussement, P. Megret, G. Kozyreff, and P. Mandel. “Electromagnetically induced transparency via adiabatic following of the nonabsorbing state.” *Physical Review Letters* **87**(15), 153601 (2001).
- [34] S. Harris. “Normal modes for electromagnetically induced transparency.” *Physical Review Letters* **72**(1), 52–5 (1994).
- [35] M. Fleischhauer and T. Richter. “Pulse matching and correlation of phase fluctuations in Lambda systems.” *Physical Review A* **51**, 2430–2442 (1995).
- [36] M. Fleischhauer, U. Rathe, and M. O. Scully. “Phase-noise squeezing in electromagnetically induced transparency.” *Physical Review A* **46**, 5856–5859 (1992).
- [37] L. V. Hau, S. E. Harris, Z. Dutton, and C. H. Behroozi. “Light speed reduction to 17 metres per second in an ultracold atomic gas.” *Nature* **394**, 594 (1999).
- [38] E. A. Korsunsky and D. V. Kosachiov. “Phase-dependent nonlinear optics with double-Lambda atoms.” *Physical Review A* **60**, 4996–5009 (1999).
- [39] M. Lukin, P. Hemmer, M. Löffler, and M. Scully. “Resonant enhancement of parametric processes via radiative interference and induced coherence.” *Physical Review Letters* **81**(13), 2675–8 (1998).

- [40] A. Zibrov, M. Lukin, and M. Scully. “Nondegenerate parametric self-oscillation via multi-wave mixing in coherent atomic media.” *Physical Review Letters* **83**(20), 4049–52 (1999).
- [41] M. D. Lukin, A. B. Matsko, M. Fleischhauer, and M. O. Scully. “Quantum noise and correlations in resonantly enhanced wave mixing based on atomic coherence.” *Physical Review Letters* **82**, 1847–1850 (1999).
- [42] J. P. Marangos. “Electromagnetically induced transparency.” *Journal of Modern Optics* **45**, 471–503 (1998).
- [43] L. Windholz. “Coherent population trapping in open and closed systems.” *Acta Physica Polonica A* **97**, 259–74 (2000).
- [44] M. Kitano and T. Nakanishi. “Unconventional forms of light.” *Oyo Buturi* **72**, 681–90 (2003).
- [45] R. W. Boyd and M. O. Scully. “Efficient infrared imaging upconversion via quantum coherence.” *Applied Physics Letters* **77**(22), 3559–3561 (2000).
- [46] A. Merriam, S. Sharpe, M. Shverdin, D. Manuszak, G. Yin, and S. Harris. “Efficient nonlinear frequency conversion in an all-resonant double-lambda system.” *Physical Review Letters* **84**(23), 5308–11 (2000).
- [47] P. R. Hemmer, D. P. Katz, J. Donoghue, M. Cronin-Golomb, M. S. Shariar, and P. Kumar. “Efficient low-intensity optical phase conjugation based on coherent population trapping in sodium.” *Optics Letters* **20**, 982–984 (1995).
- [48] Y. Q. Li and M. Xiao. “Enhancement of nondegenerate four-wave mixing based on electromagnetically induced transparency in rubidium atoms.” *Optics Letters* **21**(14), 1064–1066 (1996).
- [49] B. L. Lu, W. H. Burkett, and M. Xiao. “Nondegenerate four-wave mixing in a double-lambda system under the influence of coherent population trapping.” *Optics Letters* **23**(10), 804–806 (1998).

- [50] V. G. Arkhipkin, D. V. Manushkin, S. A. Myslivets, and A. K. Popov. “Raman frequency mixing under coherent population trapping conditions.” *Quantum Electronics* **28**(7), 637–642 (1998).
- [51] S. Wang, D. G. Ducreay, R. Pina, M. Yan, and Y. F. Zhu. “Coherent population trapping and four-wave mixing via dark states in a doppler-broadened open Rb system.” *Physical Review A* **6103**(3), 033805 (2000).
- [52] A. F. Huss, N. Peer, R. Lammegger, E. A. Korsunsky, and L. Windholz. “Efficient Raman sideband generation in a coherent atomic medium.” *Physical Review A* **6301**(1), 013802 (2001).
- [53] S. P. Tewari and G. S. Agarwal. “Control of phase matching and nonlinear generation in dense media by resonant fields.” *Physical Review Letters* **56**, 1811–1814 (1986).
- [54] H. Schmidt and A. Imamoglu. “Giant Kerr nonlinearities obtained by electromagnetically induced transparency.” *Optics Letters* **21**, 1936–1938 (1996).
- [55] H. Wang, D. Goorsky, and M. Xiao. “Enhanced kerr nonlinearity via atomic coherence in a three-level atomic system.” *Physical Review Letters* **87**, 073601 (2001).
- [56] S. E. Harris and L. V. Hau. “Nonlinear optics at low light levels.” *Physical Review Letters* **82**, 4611–4614 (1999).
- [57] D. F. V. James and P. G. Kwiat. “Atomic-vapor-based high efficiency optical detectors with photon number resolution.” *Physical Review Letters* **89**(18), 183601 (2002).
- [58] A. Imamoglu. “High efficiency photon counting using stored light.” *Physical Review Letters* **89**(16), 163602 (2002).
- [59] O. A. Kocharovskaya and Y. I. Khanin. “Coherent amplification of an ultrashort pulse in a 3-level medium without a population-inversion.” *JETP Letters* **48**(11), 630–634 (1988).
- [60] M. O. Scully, S. Y. Zhu, and A. Gavrielides. “Degenerate quantum-beat laser - lasing without inversion and inversion without lasing.” *Physical Review Letters* **62**(24), 2813–2816 (1989).

- [61] S. E. Harris. “Lasers without inversion - interference of lifetime-broadened resonances.” *Physical Review Letters* **62**(9), 1033–1036 (1989).
- [62] J. Mompart and R. Corbalan. “Lasing without inversion.” *Journal of Optics B* **2**, R7 (2000).
- [63] R. Wynands and A. Nagel. “Precision spectroscopy with coherent dark states.” *Applied Physics B* **68**(1), 1–25 (1999).
- [64] S. Knappe, R. Wynands, J. Kitching, H. G. Robinson, and L. Hollberg. “Characterization of coherent population-trapping resonances as atomic frequency references.” *Journal of the Optical Society of America B* **18**(11), 1545–1553 (2001).
- [65] M. Fleischhauer and M. O. Scully. “Quantum sensitivity limits of an optical magnetometer based on atomic phase coherence.” *Physical Review A* **49**(3), 1973–1986 (1994).
- [66] A. Nagel, L. Graf, A. Naumov, E. Mariotti, V. Biancalana, D. Meschede, and R. Wynands. “Experimental realization of coherent dark-state magnetometers.” *Europhysics Letters* **44**(1), 31–36 (1998).
- [67] I. Novikova and G. R. Welch. “Magnetometry in dense coherent media.” *Journal of Modern Optics* **49**(3-4), 349–358 (2002).
- [68] D. Budker, W. Gawlik, D. F. Kimball, S. M. Rochester, V. V. Yashchuk, and A. Weis. “Resonant nonlinear magneto-optical effects in atoms.” *Reviews of Modern Physics* **74**(4), 1153–1201 (2002).
- [69] M. Kash, V. Sautenkov, A. Zibrov, L. Hollberg, G. Welch, M. Lukin, Y. Rostovtsev, E. Fry, and M. Scully. “Ultraslow group velocity and enhanced nonlinear optical effects in a coherently driven hot atomic gas.” *Physical Review Letters* **82**(26), 5229–32 (1999).
- [70] C. J. Chang-Hasnain, K. Pei-cheng, K. Jungho, and C. Shun-lien. “Variable optical buffer using slow light in semiconductor nanostructures.” *Proceedings of the IEEE* **91**(11), 1884–97 (2003).

- [71] N. W. Carlson, W. R. Babbitt, Y. S. Bai, and T. W. Mossberg. “Spectrally ordered Zeeman coherences and optical pulse-shape storage.” *Journal of the Optical Society of America B* **2**(6), 908–914 (1985).
- [72] B. S. Ham, M. S. Shahriar, M. K. Kim, and P. R. Hemmer. “Frequency-selective time-domain optical data storage by electromagnetically induced transparency in a rare-earth-doped solid.” *Optics Letters* **22**, 1849–1851 (1997).
- [73] D. Phillips, A. Fleischhauer, A. Mair, R. Walsworth, and M. Lukin. “Storage of light in atomic vapor.” *Physical Review Letters* **86**(5), 783–6 (2001).
- [74] A. S. Zibrov, A. B. Matsko, O. Kocharovskaya, Y. V. Rostovtsev, G. R. Welch, and M. O. Scully. “Transporting and time reversing light via atomic coherence.” *Physical Review Letters* **88**(10), 103601 (2002).
- [75] J. M. Taylor, C. M. Marcus, and M. D. Lukin. “Long-lived memory for mesoscopic quantum bits.” *Physical Review Letters* **90**(20), 206803 (2003).
- [76] H. Schmidt and R. J. Ram. “All-optical wavelength converter and switch based on electromagnetically induced transparency.” *Applied Physics Letters* **76**, 3173–3175 (2000).
- [77] J. Clarke, H. Chen, and W. A. V. Wijngaarden. “Electromagnetically induced transparency and optical switching in a rubidium cascade system.” *Applied Optics* **40**, 2047–2051 (2001).
- [78] M. Yan, E. G. Rickey, and Y. F. Zhu. “Observation of absorptive photon switching by quantum interference.” *Physical Review A* **64**04(4), 041801 (2001).
- [79] M. Takeoka, D. Fujishima, and F. Kannari. “Coherent control of the polarization of ultrashort optical pulses using electromagnetically induced transparency.” *Japanese Journal of Applied Physics, Part I* **40**(1), 137–41 (2001).
- [80] B. S. Ham. “Dark resonance based optical switching.” *Journal Of Modern Optics* **49**(14-15), 2477–2484 (2002).

- [81] F. Vaudelle, J. Gazengel, and G. Rivoire. “Image transfer from an exciting laser beam to a stimulated Raman beam: The role of the scattered wave phase in a Fourier optical setup.” *Journal of the Optical Society of America B* **14**(9), 2260–2267 (1997).
- [82] M. Katsuragawa, J. Q. Liang, F. L. Kien, and K. Hakuta. “Efficient frequency conversion of incoherent fluorescent light.” *Physical Review A* **65**(2), 025801 (2002).
- [83] C. Iaconis and I. A. Walmsley. “Spectral phase interferometry for direct electric-field reconstruction of ultrashort optical pulses.” *Optics Letters* **23**, 792–794 (1998).
- [84] R. Brewer and E. Hahn. “Coherent two-photon processes: Transient and steady-state cases.” *Physical Review A* **11**, 1641 (1975).
- [85] C. C. Gerry. “Bloch vector for a Raman coupled system with Stokes and anti-Stokes fields: Quantum interference effects.” *Optics Communications* **88**, 353–356 (1992).
- [86] J. Kim, J. Lee, A. Choe, and Y. Rhee. “Geometrical representation of coherent-excitation methods using delayed and detuned lasers.” *Physical Review A* **55**, 3819 (1997).
- [87] V. V. Kozlov, O. Kocharovskaya, and M. O. Scully. “Effective two-level Maxwell-Bloch formalism and coherent pulse propagation in a driven three-level medium.” *Physical Review A* **59**(5), 3986–3997 (1999).
- [88] Z. Ficek and H. S. Freedhoff. “Spectroscopy in polychromatic fields.” *Progress In Optics* **40**, 389–441 (2000).
- [89] H. L. Anderson, editor. *A Physicist’s Desk Reference: The Physics Vade Mecum*. 2nd edn. (American Institute of Physics, New York, 1989).
- [90] R. Holler, F. Renzoni, L. Windholz, and J. H. Xu. “Coherent population trapping on the sodium D-1 line in high magnetic fields.” *Journal of the Optical Society of America B* **14**(9), 2221–2226 (1997).
- [91] W. Happer. “Optical pumping.” *Reviews of Modern Physics* **44**(2), 169–250 (1972).

- [92] M. A. Bouchiat and J. Brossel. "Relaxation of optically pumped rb atoms on paraffin-coated walls." *Physical Review* **147**, 41–54 (1966).
- [93] D. R. Lide, editor. *CRC Handbook of Chemistry and Physics*. 72nd edn. (CRC Press, 1992).
- [94] T. Mossberg, A. Flusberg, R. Kachru, and S. R. Hartmann. "Study of the velocity-changing collisions between Na atoms and either He or Co." *Bulletin of the American Physical Society* **24**(1), 25–25 (1979).
- [95] A. T. Ramsey and L. W. Anderson. "Spin relaxation in an optically oriented sodium vapor." *Il Nuovo Cimento* **32**(5), 1151–1157 (1964).
- [96] A. Javan, O. Kocharovskaya, H. Lee, and M. O. Scully. "Narrowing of electromagnetically induced transparency resonance in a Doppler-broadened medium." *Physical Review A* **66**(1), 013805 (2002).
- [97] S. Brandt, A. Nagel, R. Wynands, and D. Meschede. "Buffer-gas-induced linewidth reduction of coherent dark resonances to below 50 Hz." *Physical Review A* **56**(2), R1063–R1066 (1997).
- [98] C. Tamm, E. Buhr, and J. Mlynek. "Raman heterodyne studies of velocity diffusion effects in radio-frequency-laser double-resonance." *Physical Review A* **34**(3), 1977–1994 (1986).
- [99] R. Walkup, A. Spielfiedel, D. Ely, W. D. Phillips, and D. E. Pritchard. "Pressure-broadening rates from the near-wing amplitude." *Journal of Physics B* **14**(12), 1953–1961 (1981).
- [100] A. B. Matsko, I. Novikova, M. O. Scully, and G. R. Welch. "Radiation trapping in coherent media." *Physical Review Letters* **87**(13), 133601 (2001).
- [101] F. A. Franz. "Rubidium spin relaxation in the rare gases under ultraclean conditions." *Physical Review* **139**(3A), A603–A611 (1965).
- [102] C. Bennett, F. Bessette, G. Brassard, L. Salvail, and J. Smolin. "Experimental quantum cryptography." *Journal of Cryptology* **5**, 3 (1992).

- [103] C. Bennett, G. Brassard, C. Crepeau, R. Jozsa, A. Peres, and W. Wootters. “Teleporting an unknown quantum state via dual classical and einstein-podolsky-rosen channels.” *Physical Review Letters* **70**, 1895 (1993).
- [104] D. Bouwmeester, K. Mattle, J. Pan, H. Weinfurter, A. Zeilinger, and M. Zukowski. “Experimental quantum teleportation of arbitrary quantum states.” *Applied Physics B* **67**, 749 (1998).
- [105] K. Mattle, H. Weinfurter, P. Kwiat, and A. Zeilinger. “Dense coding in experimental quantum communication.” *Physical Review Letters* **76**, 4656 (1996).
- [106] D. J. Jackson, J. D. Franson, G. Gilbert, and G. Milburn. “Introduction to the issue on quantum internet technologies.” *IEEE Journal Of Selected Topics In Quantum Electronics* **9**(6), 1453–1454 (2003).
- [107] R. Loudon and P. L. Knight. “Squeezed light.” *Journal of Modern Optics* **34**, 709–759 (1987).
- [108] K. Ichimura, K. Yamamoto, and N. Gemma. “Evidence for electromagnetically induced transparency in a solid medium.” *Physical Review A* **58**(5), 4116–20 (1998).
- [109] B. S. Ham, P. R. Hemmer, M. K. Rim, and S. M. Shahriar. “Quantum interference and its potential applications in a spectral hole-burning solid.” *Laser Physics* **9**, 788–96 (1999).
- [110] H. Schmidt, D. E. Nikonov, K. L. Campman, K. D. Maranowski, A. C. Gossard, and A. Imamoglu. “Quantum interference in semiconductor quantum wells.” *Laser Physics* **9**, 797–812 (1999).
- [111] K. Yamamoto, K. Ichimura, and N. Gemma. “Enhanced and reduced absorptions via quantum interference: Solid system driven by a RF field.” *Physical Review A* **58**(3), 2460–6 (1998).
- [112] B. S. Ham, M. S. Shahriar, and P. R. Hemmer. “Electromagnetically induced transparency over spectral hole-burning temperature in a rare-earth-doped solid.” *Journal of the Optical Society of America B* **16**(5), 801–4 (1999).

- [113] E. Kuznetsova, O. Kocharovskaya, P. Hemmer, and M. O. Scully. “Atomic interference phenomena in solids with a long-lived spin coherence.” *Physical Review A* **66**(6), 63802–1–13 (2002).
- [114] A. Imamoglu. “Electromagnetically induced transparency with two dimensional electron spins.” *Optics Communications* **179**(1-6), 179–82 (2000).
- [115] L. Silvestri, F. Bassani, G. Czajkowski, and B. Davoudi. “Electromagnetically induced transparency in asymmetric double quantum wells.” *European Physical Journal B* **27**(1), 89–102 (2002).
- [116] M. Phillips and W. Hailin. “Spin coherence and electromagnetically induced transparency via exciton correlations.” *Physical Review Letters* **89**(18), 186401/1–4 (2002).
- [117] S. Chesi, M. Artoni, G. C. La Rocca, F. Bassani, and A. Mysyrowicz. “Polaritonic stop-band transparency via exciton-biexciton coupling in cucl.” *Physical Review Letters* **91**(5), 057402/1–4 (2003).
- [118] M. C. Phillips, W. Hailin, I. Romyantsev, N. H. Kwong, R. Takayama, and R. Binder. “Electromagnetically induced transparency in semiconductors via biexciton coherence.” *Physical Review Letters* **91**(18), 183602/1–4 (2003).
- [119] W. W. Chow, H. C. Schneider, and M. C. Phillips. “Theory of quantum-coherence phenomena in semiconductor quantum dots.” *Physical Review A* **68**(5), 053802/1–10 (2003).

Appendix A

Effective Matrix Elements for Multiplets

In the absence of strong electric or magnetic fields, the states of an atom fall into groups of states having the same (or approximately the same) energy but different values of angular momentum. The multiplicity of states at the same level of energy is called *Zeeman structure*. In many experiments the Zeeman structure is neither evident nor of interest. In modelling such experiments one would like to be able to ignore the Zeeman structure and talk about optical fields coupling pairs of levels rather than pairs of states. In this chapter I show how the matrix elements of the Zeeman states may be used to derive effective matrix elements for spontaneous and stimulated transitions between levels. As we will see, the effective matrix elements for these two processes are not necessarily the same.

- **The effective matrix element for spontaneous emission.** Consider a pair of levels E and G . From a study of the interaction of a two-state system with the electromagnetic continuum (§C.2.3), one finds that the rate of spontaneous emission from a state e to a lower-energy state g is

$$C |\boldsymbol{\mu}_{eg}|^2 \rho_{ee}. \quad (\text{A.1})$$

where C is a constant of proportionality. The rate of decay out of e into G is $\sum_{g \in G} C |\boldsymbol{\mu}_{eg}|^2 \rho_{ee}$.

Hence the total rate at which population moves from level E to level G is

$$\dot{\rho}_{EE} = \sum_{e \in E} \dot{\rho}_{ee} = - \sum_{\substack{e \in E \\ g \in G}} C |\boldsymbol{\mu}_{eg}|^2 \rho_{ee} = - \sum_{g \in G} C |\boldsymbol{\mu}_{eg}|^2 \rho_{EE} \quad (\text{any } e). \quad (\text{A.2})$$

In the last step I have used the well-known fact that $\sum_{g \in G} |\boldsymbol{\mu}_{eg}|^2$ is the same for all Zeeman states e within an atomic level. (This fact can be derived from the principle of isotropy.) From this equation, we see that the effective matrix element for spontaneous emission from level E to level G is

$$\mu_{EG,\text{spont}}^2 \equiv \sum_{g \in G} |\boldsymbol{\mu}_{eg}|^2 \quad (\text{any } e). \quad (\text{A.3})$$

The quantity

$$b_{EG} = \frac{\sum_{g \in G} |\boldsymbol{\mu}_{eg}|^2}{\sum_{\text{all } g} |\boldsymbol{\mu}_{eg}|^2} = \frac{\mu_{EG,\text{spont}}^2}{\mu^2} \quad (\text{A.4})$$

is called the *branching ratio*.

- **The effective matrix element for absorption.** According to Fermi's Golden Rule, the rate of population transfer from a state g to an unpopulated state e is

$$C' |\hat{\boldsymbol{\epsilon}} \cdot \boldsymbol{\mu}_{eg}|^2 \rho_{gg} \quad (\text{A.5})$$

where $\hat{\boldsymbol{\epsilon}}$ is the direction of the field and C' is another constant of proportionality. The total rate of population loss out of g into E is $\sum_{e \in E} C' |\hat{\boldsymbol{\epsilon}} \cdot \boldsymbol{\mu}_{eg}|^2 \rho_{gg}$. Now, let us suppose that all the states in G are equally and incoherently populated. This is not unreasonable, as excited state decay and interaction with a thermal reservoir will both tend to distribute population more or less evenly and incoherently among the ground states. In particular, this condition holds under conditions of weak illumination such that excitation rate is much smaller than the

rate of thermalization. The total rate at which population is removed from G is then

$$\dot{\rho}_{GG} = \sum_{g \in G} \dot{\rho}_{gg} = \sum_{\substack{e \in E \\ g \in G}} C' |\hat{\mathbf{e}} \cdot \boldsymbol{\mu}_{eg}|^2 \rho_{gg} = \frac{\rho_{GG}}{N_g} \sum_{\substack{e \in E \\ g \in G}} C' |\hat{\mathbf{e}} \cdot \boldsymbol{\mu}_{eg}|^2 \quad (\text{A.6})$$

where N_G is the number of states in level G . Hence, the effective matrix element for excitation from G to E is

$$\mu_{G \rightarrow E}^2 = \frac{1}{N_G} \sum_{\substack{e \in E \\ g \in G}} |\hat{\mathbf{e}} \cdot \boldsymbol{\mu}_{eg}|^2. \quad (\text{A.7})$$

- **The effective matrix element for stimulated emission.** The analysis above did not make any assumptions about whether level E or G was higher. Hence, one might expect that the matrix element for stimulated emission could be obtained simply by changing e for g and E for G . However, the result would only be relevant if the excited states were equally and incoherently populated, which is generally not the case. Rather, excitation from a ground state produces a superposition of excited states which is coupled back to the ground state by the same coefficient. (We know the coefficient is the same because the interaction Hamiltonian must be Hermitian). Hence the effective coefficient for stimulated emission is the *same* as that for absorption:

$$\mu_{E \rightarrow G}^2 = \mu_{G \rightarrow E}^2. \quad (\text{A.8})$$

Tables A.1 and A.2 show the effective matrix elements for the sodium D1 and D2 hyperfine levels, which may be calculated from the matrix elements given in Tables B.1 and B.1. The sum of the transition strengths is 16/48 for D1 and 32/48 for D2, which is why it is sometimes said that the strengths of the D1 and D2 lines (relative to a two-state transition) are 1/3 and 2/3, respectively.

Before concluding this appendix, a disclaimer is in order. While the effective matrix elements derived here are useful in some situations, one should keep in mind that it is generally impossible to summarize the interactions between all the states in a many-state, few-level system with just a few parameters. Apart from a few specialized situations, there are no shortcuts to obtaining quantitatively accurate results.

	branching ratio	coupling strength	population	line strength
F', F	$b_{F'F}$	$\check{\mu}_{F'F}^2$	ρ_{FF}	$\check{\mu}_{F'F}^2 \rho_{FF}$
1,1	$\frac{1}{6}$	$\frac{1}{18}$	$\frac{3}{8}$	$\frac{1}{48}$
2,1	$\frac{1}{2}$	$\frac{5}{18}$	$\frac{3}{8}$	$\frac{5}{48}$
1,2	$\frac{5}{6}$	$\frac{1}{6}$	$\frac{5}{8}$	$\frac{5}{48}$
2,2	$\frac{1}{2}$	$\frac{1}{6}$	$\frac{5}{8}$	$\frac{5}{48}$

Table A.1: The effective parameters for sodium D1 hyperfine transitions. (F denotes the ground level, F' denotes the excited level.)

	branching ratio	coupling strength	population	line strength
F'', F	$b_{F''F}$	$\check{\mu}_{F''F}^2$	ρ_{FF}	$\check{\mu}_{F''F}^2 \rho_{FF}$
0,1	1	$\frac{1}{9}$	$\frac{3}{8}$	$\frac{2}{48}$
1,1	$\frac{5}{6}$	$\frac{5}{18}$	$\frac{3}{8}$	$\frac{5}{48}$
2,1	$\frac{1}{2}$	$\frac{5}{18}$	$\frac{3}{8}$	$\frac{5}{48}$
1,2	$\frac{1}{6}$	$\frac{1}{30}$	$\frac{5}{8}$	$\frac{1}{48}$
2,2	$\frac{1}{2}$	$\frac{1}{6}$	$\frac{5}{8}$	$\frac{5}{48}$
3,2	1	$\frac{7}{15}$	$\frac{5}{8}$	$\frac{14}{48}$

Table A.2: The effective parameters for sodium D2 hyperfine transitions. (F denotes the ground level, F'' denotes the excited level.)

Appendix B

Matrix Elements of the Electric and Magnetic Dipole Operators

In this appendix I evaluate the matrix elements of the electric dipole operator $\hat{\mu}_E$ and the magnetic dipole operator $\hat{\mu}_B$. I choose as a basis the eigenstates of the total angular momentum, which in this context includes orbital angular momentum, electronic spin, and nuclear spin. Formulas for the matrix elements are derived in the orbital state basis, followed by a discussion of how they are combined to yield the matrix elements for hyperfine states (eigenstates of the total angular momentum). Finally, the matrix elements are evaluated for states of the sodium D1 and D2 lines and listed in several tables.

B.1 Derivation of the Matrix Elements

B.1.1 The Eigenstates of Angular Momentum

If the Hamiltonian for a spinless particle is rotationally symmetric, the eigenstates of the Hamiltonian are also eigenstates of orbital angular momentum \mathbf{L} . These eigenstates may be written

$$|n, l, m_l\rangle = R_{nl}(r)|l, m_l\rangle, \quad (\text{B.1})$$

$$|l, m_l\rangle = F_l^{m_l}(\theta) e^{im_l\phi} \quad (\text{B.2})$$

where n is the principle quantum number, l is the quantum number for \mathbf{L}^2 and m_l is the quantum number for L_z . $R_{nl}(r)$ is a radial function that depends on the form of the potential. $F_l^{m_l}(\theta) = N_l^{m_l} P_l^{m_l}(\cos \theta)$ where $P_l^m(\mu)$ is the (l, m) associated Legendre polynomial and $N_l^m = [(2l + 1)(l - m)!/4\pi(l + m)!]^{1/2}$ is a normalization constant. The F functions have the property

$$\int_0^\pi F_{l'}^m(\theta) F_l^m(\theta) \sin \theta d\theta = \frac{1}{2\pi} \delta_{ll'} \quad (\text{B.3})$$

such that $\langle l', m_l' | l, m_l \rangle = \delta_{ll'} \delta_{m_l m_l'}$.

For a particle with spin, one may form a set of basis states from outer products of the orbital angular momentum states $|n, l, m_l\rangle$ and spin states $|s, m_s\rangle$. For an atomic electron, the nuclear spin state $|i, m_i\rangle$ is also relevant in which case the basis states have the form $|n, l, m_l\rangle |s, m_s\rangle |i, m_i\rangle$.

B.1.2 Evaluation of $\hat{\mu}_E$ for Orbital Angular Momentum States

The electric dipole operator is $\hat{\mu}_E = -e\mathbf{r}$ where \mathbf{r} is the position. Since \mathbf{r} does not act on spin states, we need only to calculate the dipole matrix elements $\langle n', l', m_l' | \mathbf{r} | n, l, m_l \rangle$. For readability, I will abbreviate m_l as m . In spherical coordinates,

$$x = r \sin \theta \cos \phi \quad (\text{B.4})$$

$$y = r \sin \theta \sin \phi \quad (\text{B.5})$$

$$z = r \cos \theta. \quad (\text{B.6})$$

Then

$$\begin{aligned} \langle n', l', m_l' | z | n, l, m \rangle &= \int_0^\infty R_{n'l'}^*(r) R_{nl}(r) r^3 dr \\ &\quad \times \int_0^\pi F_{l'}^{m_l'}(\theta) F_l^m(\theta) \cos \theta \sin \theta d\theta \int_0^{2\pi} e^{i(m - m_l')\phi} d\phi \end{aligned} \quad (\text{B.7})$$

$$= 2\pi R_{n'l'}^* \delta_{mm'} \int_0^\pi F_{l'}^m(\theta) F_l^m(\theta) \cos \theta \sin \theta d\theta \quad (\text{B.8})$$

where $R_{nl}^{n'l'}$ denotes the radial component of the matrix element. The integral can be evaluated by making use of the orthogonality and recursion relations of the Legendre polynomials. After several lines of algebra, one obtains

$$\langle n', l', m' | z | n, l, m \rangle = R_{nl}^{n'l'} \delta_{mm'} \left(\delta_{l', l-1} \sqrt{\frac{(l'+m)(l'-m)}{(2l+1)(2l'+1)}} + \delta_{l', l+1} \sqrt{\frac{(l+m)(l-m)}{(2l+1)(2l'+1)}} \right). \quad (\text{B.9})$$

For the transverse components it is convenient to write $x = (\sigma_+ + \sigma_-)/\sqrt{2}$ and $y = (\sigma_+ - \sigma_-)/\sqrt{2}i$ where

$$\sigma_+ \equiv \frac{1}{\sqrt{2}} r \sin \theta e^{i\phi} \quad (\text{B.10})$$

$$\sigma_- \equiv \frac{1}{\sqrt{2}} r \sin \theta e^{-i\phi}. \quad (\text{B.11})$$

We have

$$\langle n, l', m' | \sigma_+ | n, l, m \rangle = 2\pi R_{nl}^{n'l'} \delta_{m', m+1} \int_0^\pi F_{l'}^{m+1}(\theta) F_l^m(\theta) \sin \theta \sin \theta d\theta. \quad (\text{B.12})$$

A little algebra yields

$$\langle n', l', m' | \sigma_+ | n, l, m \rangle = R_{nl}^{n'l'} \times \delta_{m', m+1} \left(\delta_{l', l-1} \sqrt{\frac{(l-m)(l'-m)}{2(2l+1)(2l'+1)}} - \delta_{l', l+1} \sqrt{\frac{(l'+m')(l+m')}{2(2l+1)(2l'+1)}} \right). \quad (\text{B.13})$$

Now,

$$\langle n' l' m' | \sigma_- | n l m \rangle = \langle n l m | \sigma_-^\dagger | n' l' m' \rangle^* = \langle n l m | \sigma_+ | n' l' m' \rangle^*. \quad (\text{B.14})$$

Thus, we can obtain the matrix elements for σ_+ from those of σ_- simply by making the switches $l \leftrightarrow l'$ and $m \leftrightarrow m'$ and conjugating the result. To express the final answer, I note that the position vector can be written as $\mathbf{r} = \sigma_+ \hat{\sigma}_- + \sigma_- \hat{\sigma}_+ + z \hat{\mathbf{z}}$ where $\hat{\sigma}_\pm = (\hat{\mathbf{x}} \pm i \hat{\mathbf{y}})/\sqrt{2}$ are the circular unit

vectors. The final result is therefore

$$\begin{aligned}
\langle n', l', m' | \hat{\boldsymbol{\mu}}_E | n, l, m \rangle = & -eR_{nl}^{n'l'} \times \\
& \left[\delta_{mm'} \left(\delta_{l',l+1} \sqrt{\frac{(l'+m)(l'-m)}{(2l+1)(2l'+1)}} + \delta_{l',l-1} \sqrt{\frac{(l+m)(l-m)}{(2l+1)(2l'+1)}} \right) \hat{\mathbf{z}} \right. \\
& + \delta_{m',m-1} \left(\delta_{l',l+1} \sqrt{\frac{(l'-m')(l-m')}{2(2l+1)(2l'+1)}} - \delta_{l',l-1} \sqrt{\frac{(l+m)(l'+m)}{2(2l+1)(2l'+1)}} \right) \hat{\boldsymbol{\sigma}}_+ \\
& \left. + \delta_{m',m+1} \left(\delta_{l',l-1} \sqrt{\frac{(l-m)(l'-m)}{2(2l+1)(2l'+1)}} - \delta_{l',l+1} \sqrt{\frac{(l'+m')(l+m')}{2(2l+1)(2l'+1)}} \right) \hat{\boldsymbol{\sigma}}_- \right]. \quad (\text{B.15})
\end{aligned}$$

This expression is physically valid for $|m| < l$ and $|m'| < l'$. As a computational expression, it should be taken to vanish when these inequalities are not satisfied.

B.1.3 Evaluation of $\hat{\boldsymbol{\mu}}_B$ for Orbital States and Spin States

The magnetic dipole operator has both orbital and spin contributions:

$$\hat{\boldsymbol{\mu}}_B = -\frac{e}{2m_e} \hat{\mathbf{L}} + \frac{e}{2m_e} g_e \hat{\mathbf{S}} + \frac{e}{2m_n} g_n \hat{\mathbf{I}} \quad (\text{B.16})$$

where m_e , m_n are the electron and nucleon masses and g_e , g_n are the electron and nucleon Lande factors (approximately -2 and 2 , respectively). If the spin and orbital components do not vanish, the contribution from the nuclear spin is negligible since $m_n \gg m_e$. Thus

$$\hat{\boldsymbol{\mu}}_B = -\frac{e}{2m_e} (\hat{\mathbf{L}} + 2\hat{\mathbf{S}}). \quad (\text{B.17})$$

The expressions for the matrix elements have the same form for both $\hat{\mathbf{L}}$ and $\hat{\mathbf{S}}$ operators, so it is convenient to perform the derivation using the generic angular momentum operator $\hat{\mathbf{J}}$. In terms of the circular unit vectors, $\hat{\mathbf{J}} = \left(\hat{J}_+/\sqrt{2} \right) \hat{\boldsymbol{\sigma}}_- + \left(\hat{J}_-/\sqrt{2} \right) \hat{\boldsymbol{\sigma}}_+ + \hat{J}_z \hat{\mathbf{z}}$ where $\hat{J}_\pm = \hat{J}_x \pm i\hat{J}_y$ is the

raising (lowering) operator. Using the fundamental properties of these operators, we have

$$\begin{aligned} \langle j', m' | \hat{\mathbf{J}} | j, m \rangle = \hbar \delta_{j', j} \left[\sqrt{\frac{j(j+1) - mm'}{2}} \delta_{m', m+1} \hat{\sigma}_- \right. \\ \left. + \sqrt{\frac{j(j+1) - mm'}{2}} \delta_{m', m-1} \hat{\sigma}_+ + m \delta_{m', m} \hat{\mathbf{z}} \right] \end{aligned} \quad (\text{B.18})$$

and thus

$$\begin{aligned} \langle l', m'_l, s', m'_s | \hat{\boldsymbol{\mu}}_B | l, m_l, s, m_s \rangle = \\ - \frac{e}{2m_e} \delta_{l, l'} \delta_{s, s'} \left[\delta_{m'_s, m_s} \langle l', m'_l | \hat{\mathbf{L}} | l, m_l \rangle + 2 \delta_{m'_l, m_l} \langle s', m'_s | \hat{\mathbf{S}} | s, m_s \rangle \right]. \end{aligned} \quad (\text{B.19})$$

B.1.4 Obtaining $\hat{\boldsymbol{\mu}}_E$ and $\hat{\boldsymbol{\mu}}_B$ for Hyperfine States

When the particle of interest is an electron bound to a nucleus, the Hamiltonian includes the electron spin (\mathbf{S}) and nuclear spin (\mathbf{I}). The uncoupled basis for the angular momentum consists of states of the form $|l, m_l\rangle |s, m_s\rangle |i, m_i\rangle$. (I'll ignore the quantum number n in this section.) In many cases the physically relevant basis is the coupled basis whose states are of the form $|f, m_f, l, s, i, j\rangle$. These states may be called ‘‘hyperfine’’ states since they are relevant when one resolves the hyperfine structure of an atom. Here j is the quantum number for $\mathbf{J}^2 = (\mathbf{L} + \mathbf{S})^2$, f is the quantum number for the total angular momentum \mathbf{F} ($\mathbf{F}^2 = (\mathbf{L} + \mathbf{S} + \mathbf{I})^2$), and m_f is the quantum number for the z projection of \mathbf{F} . The matrix elements between these states can be determined by expanding them in terms of the orbital angular momentum eigenstates and summing up the relevant matrix elements.

To relate the hyperfine states to the orbital angular momentum states, I first write states of ‘‘good’’ \mathbf{J} in terms of the \mathbf{L} and \mathbf{S} states:

$$|j, m_j, l, s\rangle = \sum_{m_l, m_s} C_{j, m_j, m_l, m_s}^{l, s} |l, m_l\rangle |s, m_s\rangle. \quad (\text{B.20})$$

Here $C_{j, m_j, m_l, m_s}^{l, s}$ is the Clebsch-Gordon coefficient¹. Then, these \mathbf{J} states may be combined with

¹I implement the Clebsch-Gordon coefficients as six-index tensor which vanishes for $m_j \neq m_l + m_s$.

the **I** states to yield the **F** states:

$$|f, m_f, l, s, i, j\rangle = \sum_{m_i, m_j} C_{f, m_f, m_j, m_i}^{j, i} |j, m_j, l, s\rangle \quad (\text{B.21})$$

$$= \sum_{m_i, m_j} \sum_{m_l, m_s} C_{f, m_f, m_j, m_i}^{j, i} C_{j, m_j, m_l, m_s}^{l, s} |l, m_l\rangle |s, m_s\rangle |i, m_i\rangle \quad (\text{B.22})$$

$$\equiv \sum_{m_l, m_s, m_i} Q_{f, m_f, m_l, m_s, m_i}^{l, s, i, j} |l, m_l\rangle |s, m_s\rangle |i, m_i\rangle \quad (\text{B.23})$$

where $Q_{f, m_f, m_l, m_s, m_i}^{l, s, i, j} \equiv \sum_{m_j} C_{f, m_f, m_j, m_i}^{j, i} C_{j, m_j, m_l, m_s}^{l, s}$. The matrix element between different *F* states is then

$$\begin{aligned} \langle f', m'_f, l', s', i', j' | \hat{\boldsymbol{\mu}} | f, m_f, l, s, i, j \rangle &= \sum_{m'_l, m'_s, m'_i} \sum_{m_l, m_s, m_i} \left(Q_{f', m'_f, m'_l, m'_s, m'_i}^{l', s', i', j'} \right)^* Q_{f, m_f, m_l, m_s, m_i}^{l, s, i, j} \\ &\times \langle l', m'_l, s', m'_s, i', m'_i | \hat{\boldsymbol{\mu}} | l, m_l, s, m_s, i, m_i \rangle. \end{aligned} \quad (\text{B.24})$$

For the electric dipole operator one has

$$\begin{aligned} \langle f', m'_f, l', s', i', j' | \hat{\boldsymbol{\mu}}_E | f, m_f, l, s, i, j \rangle &= \\ \delta_{ss'} \delta_{ii'} \sum_{m'_l, m_l} \left[\sum_{m_i, m_s} \left(Q_{f', m'_f, m'_l, m'_s, m_i}^{l', s', i', j'} \right)^* Q_{f, m_f, m_l, m_s, m_i}^{l, s, i, j} \right] &\langle l', m'_l | \hat{\boldsymbol{\mu}}_E | l, m_l \rangle \end{aligned} \quad (\text{B.25})$$

and for the magnetic dipole operator one has

$$\begin{aligned} \langle f', m'_f, l', s', i', j' | \hat{\boldsymbol{\mu}}_B | f, m_f, l, s, i, j \rangle &= \delta_{ll'} \delta_{ss'} \delta_{ii'} \sum_{m'_l, m_l} \sum_{m'_s, m_s} \\ \left[\sum_{m_i} \left(Q_{f', m'_f, m'_l, m'_s, m_i}^{l', s', i', j'} \right)^* Q_{f, m_f, m_l, m_s, m_i}^{l, s, i, j} \right] &\langle l, m'_l, s, m'_s | \hat{\boldsymbol{\mu}}_B | l, m_l, s, m_s \rangle. \end{aligned} \quad (\text{B.26})$$

B.2 Computed Matrix Elements

B.2.1 Matrix Elements of the Electric Dipole Operator

The tables in this section list the relative values of the electric dipole operator μ_E , that is, the elements of the normalized operator $\check{\mu}_E = \mu_E/\mu$. Tables B.1 and B.2 include electronic and nuclear spin-orbit coupling and are relevant to the $3S \rightarrow 3P$ transitions of sodium (as well as to the $5S \rightarrow 5P$ transitions of ^{87}Rb). Due to space limitations, the vector nature of the matrix elements has been suppressed. However, this is no real loss as the vector component follows a simple pattern: Within each quadrant, elements along the diagonal ($m = m'$) have \hat{z} polarization, elements above the diagonal ($m = m' + 1$) have $\hat{\sigma}_+$ polarization, and elements below the diagonal ($m = m' - 1$) have $\hat{\sigma}_-$ polarization.

The elements listed in Table B.1 satisfy

$$\sum_{F', m'} |\langle F', m', 1, \frac{1}{2}, \frac{3}{2}, \frac{1}{2} | \check{\mu}_E | F, m, 0, \frac{1}{2}, \frac{3}{2}, \frac{1}{2} \rangle|^2 = 1 \quad (\text{B.27})$$

$$\sum_{F, m} |\langle F', m', 1, \frac{1}{2}, \frac{3}{2}, \frac{1}{2} | \check{\mu}_F | F, m, 0, \frac{1}{2}, \frac{3}{2}, \frac{1}{2} \rangle|^2 = 1. \quad (\text{B.28})$$

The branching ratios $b_{F'F}$ for spontaneous emission and the effective matrix elements $\check{\mu}_{F'F}$ for are given by the partial sums

$$b_{F'F} = \sum_{m, m'} |\langle F', m' | \check{\mu}_E | F, m \rangle|^2 \quad (\text{B.29})$$

$$\check{\mu}_{F'F}^2 = \sum_{m, m'} |\langle F', m' | \check{\mu}_E \cdot \hat{\epsilon} | F, m \rangle|^2 \quad (\text{B.30})$$

where $\hat{\epsilon}$ is any unit vector. The values of $b_{F'F}$ and $\check{\mu}_{F'F}$ for the D1 hyperfine levels are given in Appendix A.

Electric Dipole Matrix Elements for the Sodium D1 Line

	$ 1, -1\rangle$	$ 1, 0\rangle$	$ 1, 1\rangle$	$ 2, -2\rangle$	$ 2, -1\rangle$	$ 2, 0\rangle$	$ 2, 1\rangle$	$ 2, 2\rangle$
$\langle 1, -1 $	$\sqrt{\frac{1}{12}}$	$-\sqrt{\frac{1}{12}}$		$\sqrt{\frac{1}{2}}$	$\sqrt{\frac{1}{4}}$	$-\sqrt{\frac{1}{12}}$		
$\langle 1, 0 $	$-\sqrt{\frac{1}{12}}$	0	$-\sqrt{\frac{1}{12}}$		$\sqrt{\frac{1}{4}}$	$\sqrt{\frac{1}{3}}$	$-\sqrt{\frac{1}{4}}$	
$\langle 1, 1 $		$-\sqrt{\frac{1}{12}}$	$-\sqrt{\frac{1}{12}}$			$\sqrt{\frac{1}{12}}$	$\sqrt{\frac{1}{4}}$	$-\sqrt{\frac{1}{2}}$
$\langle 2, -2 $	$\sqrt{\frac{1}{2}}$			$-\sqrt{\frac{1}{3}}$	$\sqrt{\frac{1}{6}}$			
$\langle 2, -1 $	$\sqrt{\frac{1}{4}}$	$\sqrt{\frac{1}{4}}$		$\sqrt{\frac{1}{6}}$	$-\sqrt{\frac{1}{12}}$	$\sqrt{\frac{1}{4}}$		
$\langle 2, 0 $	$-\sqrt{\frac{1}{12}}$	$\sqrt{\frac{1}{3}}$	$\sqrt{\frac{1}{12}}$		$\sqrt{\frac{1}{4}}$	0	$\sqrt{\frac{1}{4}}$	
$\langle 2, 1 $		$-\sqrt{\frac{1}{4}}$	$\sqrt{\frac{1}{4}}$			$\sqrt{\frac{1}{4}}$	$\sqrt{\frac{1}{12}}$	$\sqrt{\frac{1}{6}}$
$\langle 2, 2 $			$-\sqrt{\frac{1}{2}}$				$\sqrt{\frac{1}{6}}$	$\sqrt{\frac{1}{3}}$

Table B.1: The matrix elements of the normalized electric dipole operator $\tilde{\mu}_E$, evaluated for states in the sodium $3S_{1/2}$ and $3P_{1/2}$ levels. In this table, $|F, m\rangle$ is shorthand for $|F, m, l, s, i, j\rangle = |F, m, 0, \frac{1}{2}, \frac{3}{2}, \frac{1}{2}\rangle$ and $\langle F', m'|$ is short for $\langle F', m', l', s', i', j'| = \langle F', m', 1, \frac{1}{2}, \frac{3}{2}, \frac{1}{2}|$.

Electric Dipole Matrix Elements for the Sodium D2 Line

	$ 1, -1\rangle$	$ 1, 0\rangle$	$ 1, 1\rangle$	$ 2, -2\rangle$	$ 2, -1\rangle$	$ 2, 0\rangle$	$ 2, 1\rangle$	$ 2, 2\rangle$
$\langle 0, 0 $	$-\sqrt{\frac{1}{3}}$	$-\sqrt{\frac{1}{3}}$	$\sqrt{\frac{1}{3}}$					
$\langle 1, -1 $	$\sqrt{\frac{5}{12}}$	$-\sqrt{\frac{5}{12}}$		$-\sqrt{\frac{1}{10}}$	$-\sqrt{\frac{1}{20}}$	$\sqrt{\frac{1}{60}}$		
$\langle 1, 0 $	$-\sqrt{\frac{5}{12}}$	0	$-\sqrt{\frac{5}{12}}$		$-\sqrt{\frac{1}{20}}$	$-\sqrt{\frac{1}{15}}$	$\sqrt{\frac{1}{20}}$	
$\langle 1, 1 $		$-\sqrt{\frac{5}{12}}$	$-\sqrt{\frac{5}{12}}$			$-\sqrt{\frac{1}{60}}$	$-\sqrt{\frac{1}{20}}$	$\sqrt{\frac{1}{10}}$
$\langle 2, -2 $	$\sqrt{\frac{1}{2}}$			$\sqrt{\frac{1}{3}}$	$-\sqrt{\frac{1}{6}}$			
$\langle 2, -1 $	$\sqrt{\frac{1}{4}}$	$\sqrt{\frac{1}{4}}$		$-\sqrt{\frac{1}{6}}$	$\sqrt{\frac{1}{12}}$	$-\sqrt{\frac{1}{4}}$		
$\langle 2, 0 $	$-\sqrt{\frac{1}{12}}$	$\sqrt{\frac{1}{3}}$	$\sqrt{\frac{1}{12}}$		$-\sqrt{\frac{1}{4}}$	0	$-\sqrt{\frac{1}{4}}$	
$\langle 2, 1 $		$-\sqrt{\frac{1}{4}}$	$\sqrt{\frac{1}{4}}$			$-\sqrt{\frac{1}{4}}$	$-\sqrt{\frac{1}{12}}$	$-\sqrt{\frac{1}{6}}$
$\langle 2, 2 $			$-\sqrt{\frac{1}{2}}$				$-\sqrt{\frac{1}{6}}$	$-\sqrt{\frac{1}{3}}$
$\langle 3, -3 $				1				
$\langle 3, -2 $				$\sqrt{\frac{1}{3}}$	$\sqrt{\frac{2}{3}}$			
$\langle 3, -1 $				$-\sqrt{\frac{1}{15}}$	$\sqrt{\frac{8}{15}}$	$\sqrt{\frac{2}{5}}$		
$\langle 3, 0 $					$-\sqrt{\frac{1}{5}}$	$\sqrt{\frac{3}{5}}$	$\sqrt{\frac{1}{5}}$	
$\langle 3, 1 $						$-\sqrt{\frac{2}{5}}$	$\sqrt{\frac{8}{15}}$	$\sqrt{\frac{1}{15}}$
$\langle 3, 2 $							$-\sqrt{\frac{2}{3}}$	$\sqrt{\frac{1}{3}}$
$\langle 3, 3 $								-1

Table B.2: The matrix elements of the normalized electric dipole operator $\check{\mu}_E$, evaluated for states in the sodium $3S_{1/2}$ and $3P_{1/2}$ levels. In this table, $|F, m\rangle$ is shorthand for $|F, m, l, s, i, j\rangle = |F, m, 0, \frac{1}{2}, \frac{3}{2}, \frac{1}{2}\rangle$ and $\langle F', m'|$ is short for $\langle F', m', l', s', i', j'| = \langle F', m', 1, \frac{3}{2}, \frac{3}{2}, \frac{1}{2}|$.

The elements listed in Table B.2 satisfy

$$\sum_{F',m'} |\langle F', m', 1, \frac{1}{2}, \frac{3}{2}, \frac{1}{2} | \check{\mu}_E | F, m, 0, \frac{1}{2}, \frac{3}{2}, \frac{3}{2} \rangle|^2 = 2 \quad (\text{B.31})$$

$$\sum_{F,m} |\langle F', m', 1, \frac{1}{2}, \frac{3}{2}, \frac{1}{2} | \check{\mu}_E | F, m, 0, \frac{1}{2}, \frac{3}{2}, \frac{3}{2} \rangle|^2 = 1. \quad (\text{B.32})$$

The values of $b_{F'F}$ and $\check{\mu}_{F'F}$ for the D2 hyperfine levels are given in Appendix A.

B.2.2 Matrix Elements of the Magnetic Dipole Operator

Tables B.3 and B.4 list some of the matrix elements for the magnetic dipole operator μ_B . More specifically, they give the matrix elements of $(2m_e/e\hbar)\mu_B = -(\hat{\mathbf{L}} + 2\hat{\mathbf{S}})/\hbar$ for the Zeeman states of the sodium $S_{1/2}$ and $P_{1/2}$ levels. Note that the diagonal elements in these tables go as $-g_F m$, where g_F is the Lande factor.

Magnetic Dipole Matrix Elements for the Sodium $3S_{1/2}$ States

	$ 1, -1\rangle$	$ 1, 0\rangle$	$ 1, 1\rangle$	$ 2, -2\rangle$	$ 2, -1\rangle$	$ 2, 0\rangle$	$ 2, 1\rangle$	$ 2, 2\rangle$
$\langle 1, -1 $	$-\frac{1}{2}$	$\frac{1}{2}$		see adjoints				
$\langle 1, 0 $	$\frac{1}{2}$	0	$\frac{1}{2}$					
$\langle 1, 1 $		$\frac{1}{2}$	$\frac{1}{2}$					
$\langle 2, -2 $	$-\sqrt{\frac{3}{2}}$			1	$-\sqrt{\frac{1}{2}}$			
$\langle 2, -1 $	$-\sqrt{\frac{3}{4}}$	$-\sqrt{\frac{3}{4}}$	0	$-\sqrt{\frac{1}{2}}$	$\frac{1}{2}$	$-\sqrt{\frac{3}{4}}$		
$\langle 2, 0 $	$\sqrt{\frac{1}{4}}$	-1	$-\sqrt{\frac{1}{4}}$		$-\sqrt{\frac{3}{4}}$		$-\sqrt{\frac{3}{4}}$	
$\langle 2, 1 $		$\sqrt{\frac{3}{4}}$	$-\sqrt{\frac{3}{4}}$			$-\sqrt{\frac{3}{4}}$	$-\frac{1}{2}$	$-\sqrt{\frac{1}{2}}$
$\langle 2, 2 $			$\sqrt{\frac{3}{2}}$				$-\sqrt{\frac{1}{2}}$	-1

Table B.3: The matrix elements of the operator $(2m_e/e\hbar)\boldsymbol{\mu}_B$, evaluated for the states in the sodium $3S_{1/2}$ levels. In this table, $|F, m\rangle$ is shorthand for $|F, m, l, s, i, j\rangle = |F, m, 0, \frac{1}{2}, \frac{3}{2}, \frac{1}{2}\rangle$ and $\langle F, m|$ is shorthand for the adjoint state. Interaction energies can be obtained by multiplying these elements by $-e/2m_e = -1.4 \text{ MHz / Gauss}$.

Magnetic Dipole Matrix Elements for the Sodium $P_{1/2}$ States

	$ 1, -1\rangle$	$ 1, 0\rangle$	$ 1, 1\rangle$	$ 2, -2\rangle$	$ 2, -1\rangle$	$ 2, 0\rangle$	$ 2, 1\rangle$	$ 2, 2\rangle$
$\langle 1, -1 $	$-\frac{1}{6}$	$\frac{1}{6}$		see adjoints				
$\langle 1, 0 $	$\frac{1}{6}$	0	$\frac{1}{6}$					
$\langle 1, 1 $		$\frac{1}{6}$	$\frac{1}{6}$					
$\langle 2, -2 $	$-\sqrt{\frac{1}{6}}$			$\frac{1}{6}$	$-\sqrt{\frac{1}{18}}$			
$\langle 2, -1 $	$-\sqrt{\frac{1}{12}}$	$-\sqrt{\frac{1}{12}}$		$-\sqrt{\frac{1}{18}}$	$\frac{1}{3}$	$-\sqrt{\frac{1}{12}}$		
$\langle 2, 0 $	$\sqrt{\frac{1}{36}}$	$-\sqrt{\frac{1}{9}}$	$-\sqrt{\frac{1}{36}}$		$-\sqrt{\frac{1}{12}}$	0	$-\sqrt{\frac{1}{12}}$	
$\langle 2, 1 $		$\sqrt{\frac{1}{12}}$	$-\sqrt{\frac{1}{12}}$			$-\sqrt{\frac{1}{12}}$	$-\frac{1}{6}$	$-\sqrt{\frac{1}{18}}$
$\langle 2, 2 $			$\sqrt{\frac{1}{6}}$				$-\sqrt{\frac{1}{18}}$	$-\frac{1}{3}$

Table B.4: The matrix elements of the operator $(2m_e/e\hbar)\boldsymbol{\mu}_B$, evaluated for the states in the sodium $^2P_{1/2}$ levels. In this table, $|F, m\rangle$ is shorthand for $|F, m, l, s, i, j\rangle = |F, m, 1, \frac{1}{2}, \frac{3}{2}, \frac{1}{2}\rangle$ and $\langle F, m|$ is shorthand for the adjoint state. Interaction energies can be obtained by multiplying these elements by $-e/2m_e = -1.4 \text{ MHz/Gauss}$.

Appendix C

Relaxation in Quantum Systems

A quantum system which interacts with its environment typically evolves irreversibly and experiences a dissipation of energy. This phenomenon is known variously as *relaxation*, *decay*, or *damping*. A familiar example of relaxation is the spontaneous decay of an atom from an excited state to a lower state by emission of a photon. For many calculations it is sufficient to treat relaxation phenomenologically, i.e. to “fix up” the density matrix equations by adding relaxation terms with coefficients chosen to match observed relaxation rates. However, interaction with the environment can also produce effects other than relaxation. Such effects include frequency shifts of transitions, spontaneous transfer of coherence from excited states to ground states [22] and the coupling of dipole oscillations associated with different transitions [6]. In order to make sure that all the relevant phenomena are represented, and to predict the values of the relaxation coefficients, one must explicitly treat the environment and its interaction with the system of interest. In this appendix I give my own abbreviated derivation of the Bloch-Redfield theory of relaxation, which considers a generic system coupled to a generic environment. By formally solving the dynamical equations and eliminating the environment variables, an equation of motion for the reduced density matrix of the system is obtained. To illustrate the use of the theory, I conclude with a few examples involving atoms and the electromagnetic continuum.

C.1 Derivation of the Relaxation Terms

Suppose we have a system S coupled to a reservoir R . If the reservoir's modes of excitation span a wide range of frequencies, then energy will flow essentially one-way, from the system to the reservoir. The reason for this is that once energy from the system is distributed across the many modes of the reservoir, the modes never come back into phase with the system all at the same time to return the energy. This is the mechanism responsible for decay of a quantum system.

Let us write the total Hamiltonian as

$$\hat{H} = \hat{H}_S + \hat{H}_R + \hat{H}_I \quad (\text{C.1})$$

where \hat{H}_S is the Hamiltonian for our system alone, \hat{H}_R is the Hamiltonian for the reservoir alone, and \hat{H}_I is the interaction energy which accounts for the coupling between S and R . To describe the state of S at a given time we will use the transition/population operators $\hat{S}_{jk}(t)$, where

$$\hat{S}_{jk}(0) \equiv |j\rangle\langle k| \quad (\text{C.2})$$

and $|j\rangle$ is the j th eigenstate of S . [Recall that these Heisenberg operators are simply related to the density matrix elements in the Schrodinger picture: $\langle \hat{S}_{jk}(t) \rangle = \rho_{kj}(t)$]. We will model the reservoir as a collection of independent harmonic oscillators¹. The coordinate of the μ th harmonic oscillator or “mode” is $\hat{a}_\mu + \hat{a}_\mu^\dagger$ where $[\hat{a}_\mu, \hat{a}_{\mu'}^\dagger] = \delta_{\mu\mu'}$. Then

$$\hat{H}_S = \left[\sum_j \hbar\omega_j \hat{S}_{jj} \right] \hat{I}_R \quad (\text{C.3})$$

$$\hat{H}_R = \left[\sum_\mu \hbar\Omega_\mu \hat{a}_\mu^\dagger \hat{a}_\mu \right] \hat{I}_S \quad (\text{C.4})$$

where ω_j is the natural frequency of system eigenstate j , Ω_μ is the natural frequency of mode μ , and \hat{I} stands for the identity operator. Lowest-order coupling between S and R yields an interaction

¹This model is more applicable than it would first seem. The fact is, *any* system will act like a harmonic oscillator (or set of harmonic oscillators) near its equilibrium point.

Hamiltonian of the form

$$\hat{H}_I = \hbar \sum_{j>k} \sum_{\mu} \left(g_{jk,\mu} \hat{S}_{jk} + g_{jk,\mu}^* \hat{S}_{kj} \right) \left(\hat{a}_{\mu} + \hat{a}_{\mu}^{\dagger} \right). \quad (\text{C.5})$$

Here $g_{jk,\mu}$ is the coupling coefficient between the $k \rightarrow j$ transition and mode μ . The normally ordered form² of this Hamiltonian is

$$\hat{H}_I = \hbar \sum_{j,k} \sum_{\mu} g_{jk,\mu} \hat{S}_{jk} \hat{a}_{\mu} + g_{jk,\mu}^* \hat{a}_{\mu}^{\dagger} \hat{S}_{kj}. \quad (\text{C.6})$$

The sum above includes energy-conserving terms as well as non-conserving terms. The non-conserving terms lead to counter-rotating components in the dynamical equations which contribute little over timescales comparable to the evolution time of the system. Such terms can be effectively removed by setting $g_{jk,\mu}$ to zero for $\omega_j < \omega_k$. (If they are to be retained, then one should set $g_{kj,\mu} = g_{jk,\mu}^*$.) The aim now is to eliminate the reservoir variables and obtain dynamical equations for the \hat{S}_{jk} 's alone. We will find that the presence of the interaction Hamiltonian leads to additional terms in these equations which describe decay and frequency shifts in the states of S .

The Heisenberg equations of motion for the system operators are

$$\frac{d}{dt} \hat{S}_{jk} = \frac{i}{\hbar} \left[\hat{H}, \hat{S}_{jk} \right] \quad (\text{C.7})$$

$$= \frac{i}{\hbar} \left[\hat{H}_S, \hat{S}_{jk} \right] + \frac{i}{\hbar} \left[\hat{H}_R, \hat{S}_{jk} \right] + \frac{i}{\hbar} \left[\hat{H}_I, \hat{S}_{jk} \right]. \quad (\text{C.8})$$

Now

$$\left[\hat{H}_S, \hat{S}_{jk} \right] = \hbar(\omega_j - \omega_k) \hat{S}_{jk} \equiv \hbar\omega_{jk} \hat{S}_{jk}, \quad (\text{C.9})$$

$$\left[\hat{H}_R, \hat{S}_{jk} \right] = 0, \quad (\text{C.10})$$

$$\left[\hat{H}_I, \hat{S}_{jk} \right] = \hbar \sum_l \sum_{\mu} \left(g_{lj,\mu} \hat{S}_{lk} - g_{kl,\mu} \hat{S}_{jl} \right) \hat{a}_{\mu} + \hat{a}_{\mu}^{\dagger} \left(g_{jl,\mu}^* \hat{S}_{lk} - g_{lk,\mu}^* \hat{S}_{jl} \right). \quad (\text{C.11})$$

²As the system and reservoir variables are independent, they will always commute. We are therefore free to impose whichever ordering suits us at the start of the problem.

Therefore

$$\frac{d}{dt}\hat{S}_{jk} = -i\omega_{kj}\hat{S}_{jk} + i\sum_l\sum_\mu\left[\left(g_{lj,\mu}\hat{S}_{lk} - g_{kl,\mu}\hat{S}_{jl}\right)\hat{a}_\mu + \hat{a}_\mu^\dagger\left(g_{jl,\mu}^*\hat{S}_{lk} - g_{lk,\mu}^*\hat{S}_{jl}\right)\right]. \quad (\text{C.12})$$

Similarly, we have for the reservoir operators

$$\left[\hat{H}_S, \hat{a}_\mu\right] = 0, \quad (\text{C.13})$$

$$\left[\hat{H}_R, \hat{a}_\mu\right] = -\hbar\Omega_\mu\hat{a}_\mu, \quad (\text{C.14})$$

$$\left[\hat{H}_I, \hat{a}_\mu\right] = -\hbar\sum_{j',k'}g_{j'k',\mu}^*\hat{S}_{k'j'} \quad (\text{C.15})$$

which gives

$$\frac{d}{dt}\hat{a}_\mu = -i\Omega_\mu\hat{a}_\mu - i\sum_{j',k'}g_{j'k',\mu}^*\hat{S}_{k'j'}. \quad (\text{C.16})$$

This differential equation is linear in the unknowns and may be integrated formally:

$$\hat{a}_\mu(t) = \hat{a}_\mu(t_0)e^{-i\Omega_\mu(t-t_0)} - i\sum_{j',k'}g_{j'k',\mu}^*\int_{t_0}^te^{-i\Omega_\mu(t-t')}\hat{S}_{k'j'}(t')dt' \quad (\text{C.17})$$

The term $\hat{a}_\mu(t_0)\exp[-i\Omega_\mu(t-t_0)] \equiv \hat{a}_{\mu,\text{hom}}(t)$ describes the free evolution of the reservoir from its “initial state” which may be taken to be in the infinite past. Substituting eqn. (C.17) into eqn. (C.12) with $t_0 \rightarrow -\infty$ gives

$$\begin{aligned} \frac{d}{dt}\hat{S}_{jk} = & -i\omega_{kj}\hat{S}_{jk} + i\sum_l\sum_\mu\left[\left(g_{lj,\mu}\hat{S}_{lk} - g_{kl,\mu}\hat{S}_{jl}\right)\hat{a}_{\mu,\text{hom}}(t) + \hat{a}_{\mu,\text{hom}}^\dagger(t)\left(g_{jl,\mu}^*\hat{S}_{lk} - g_{lk,\mu}^*\hat{S}_{jl}\right)\right] \\ & + \sum_\mu\sum_{l,j',k'}\left[\left(g_{lj,\mu}\hat{S}_{lk} - g_{kl,\mu}\hat{S}_{jl}\right)g_{j'k',\mu}^*\int_{-\infty}^te^{-i\Omega_\mu(t-t')}\hat{S}_{k'j'}(t')dt' \right. \\ & \quad \left. - \int_{-\infty}^te^{i\Omega_\mu(t-t')}\hat{S}_{j'k'}(t')dt'g_{j'k',\mu}\left(g_{jl,\mu}^*\hat{S}_{lk} - g_{lk,\mu}^*\hat{S}_{jl}\right)\right] \end{aligned} \quad (\text{C.18})$$

The homogeneous terms are not of interest here; in the common situation that the reservoir is initially in its ground state, the normally ordered expectation values vanish and do not affect the density

matrix. We are left to evaluate terms of the form

$$\text{damping term} = \hat{S}_{wx}(t) \sum_{\mu} g_{ab,\mu} g_{cd,\mu}^* \int_{-\infty}^t e^{\mp i\Omega_{\mu}(t-t')} \hat{S}_{yz}(t') dt'. \quad (\text{C.19})$$

To accomplish this task we invoke the premise that the reservoir is “large”. Specifically, a reservoir is expected to be spectrally dense, broad, and smooth. “Dense” means that the mode frequency spacing is much smaller than the reciprocal of the longest timescale of interest. “Broad” means that the bandwidth of the modal distribution is much larger than the bandwidth of any dynamical variable of interest. Finally, “smooth” means that the coupling coefficients are essentially constant over the bandwidth of any \hat{S}_{jk} .

Under the assumption of denseness, the discrete sum over modes may be replaced by an integral. From here on, instead of using the index μ to number the reservoir modes, let us identify each mode according to its frequency Ω and a parameter χ which includes all remaining degrees of freedom. Then $g_{ab,\mu}$ is rewritten as $g_{ab}(\Omega, \chi)$ and the sum over μ is replaced by $\int \int_0^{\infty} D(\Omega, \chi) d\Omega d\chi$ where $D(\Omega, \chi)$ is the density of modes. With these replacements, eqn. (C.19) becomes

$$\hat{S}_{wx}(t) \int \int_0^{\infty} \int_{-\infty}^t g_{ab}(\Omega, \chi) g_{cd}^*(\Omega, \chi) D(\Omega, \chi) \hat{S}_{yz}(t') e^{\mp i\Omega(t-t')} dt' d\Omega d\chi. \quad (\text{C.20})$$

Now,

$$\begin{aligned} \int_{-\infty}^t \hat{S}_{yz}(t') e^{\mp i\Omega(t-t')} dt' &= e^{\mp i\Omega t} \int_{-\infty}^t \left[\int_{-\infty}^{\infty} \hat{S}_{yz}(\omega) e^{-i\omega t'} d\omega \right] e^{\pm i\Omega t'} dt' \\ &= e^{\mp i\Omega t} \int_{-\infty}^{\infty} \hat{S}_{yz}(\omega) \left[\int_{-\infty}^t e^{-i(\omega \mp \Omega)t'} dt' \right] d\omega. \end{aligned}$$

Making use of the Fourier identity

$$\int_{-\infty}^0 e^{i\omega t} dt = \pi\delta(\omega) + \frac{i}{\omega} \quad (\text{C.21})$$

we have

$$\int_{-\infty}^t e^{-i(\omega \mp \Omega)t'} dt' = \left[\pi\delta(\omega \mp \Omega) - \frac{i}{\omega \mp \Omega} \right] e^{-i(\omega \mp \Omega)t}. \quad (\text{C.22})$$

Putting these results into eqn. (C.20) gives

$$\text{damping term} = \hat{S}_{wx}(t) \int \int_{-\infty}^{\infty} \hat{S}_{yz}(\omega) G_{abcd}^{\pm}(\omega, \chi) e^{-i\omega t} d\omega d\chi \quad (\text{C.23})$$

where

$$G_{abcd}^{\pm}(\omega, \chi) \equiv \int_0^{\infty} g_{ab}(\Omega, \chi) g_{cd}^*(\Omega, \chi) D(\Omega, \chi) \left[\pi \delta(\omega \mp \Omega) - \frac{i}{\omega \mp \Omega} \right] d\Omega. \quad (\text{C.24})$$

Now, under the assumptions of broadness and smoothness of the reservoir, $G_{abcd}^{\pm}(\omega, \chi)$ is a slowly varying function of frequency compared to $\hat{S}_{yz}(\omega)$. Thus it is a good approximation to simply evaluate $G_{abcd}^{\pm}(\omega, \chi)$ at ω_{yz} , the natural frequency of $\hat{S}_{yz}(\omega)$. Thus

$$\text{damping term} \approx \hat{S}_{wx}(t) \hat{S}_{yz}(t) \int \tilde{G}_{abcd}^{\pm}(\omega_{yz}, \chi) d\chi \quad (\text{C.25})$$

Since operators such as $\hat{S}_{wx}(t) \hat{S}_{yz}(t)$ reduce to $\hat{S}_{wz}(t)$, the equation of motion for the system operators is finally reduced to an ordinary differential equation:

$$\begin{aligned} \frac{d}{dt} \hat{S}_{jk} &= -i\omega_{kj} \hat{S}_{jk} + \text{homogeneous terms} \\ &+ \sum_{l,m} \int \left[G_{l_j m k}^+(\omega_{mk}, \chi) \hat{S}_{lm} - G_{kl ml}^+(\omega_{ml}, \chi) \hat{S}_{jm} \right. \\ &\quad \left. - G_{ml jl}^-(\omega_{lm}, \chi) \hat{S}_{mk} + G_{m_j lk}^-(\omega_{jm}, \chi) \hat{S}_{ml} \right] d\chi \end{aligned} \quad (\text{C.26})$$

Eqn. (C.26) is the general solution for the situation of “weak” coupling to a broad, smooth, dense reservoir. It can be cast in a simpler form if we make one additional assumption. Let us suppose that each term such as $\int G_{abcd}^{\pm}(\omega, \chi) d\chi$ is factorable such that it can be written in the form

$$\int G_{abcd}^{\pm}(\omega, \chi) d\chi = g_{ab} g_{cd}^* \eta(\pm\omega). \quad (\text{C.27})$$

This occurs, for example, if we can factor g_{ab} : $g_{ab}(\Omega, \chi) = \mu_{ab} C(\Omega, \chi)$. Now, I note that any given term in eqn. (C.26) will not have a significant long-term effect unless its frequency is close to that

of \hat{S}_{jk} . For example, the term $\tilde{G}_{l_j m_k}^+(\omega_{mk}, \chi) \hat{S}_{lm}$ is important only for $\omega_{ml} \approx \omega_{kj}$, or equivalently $\omega_{mk} \approx \omega_{lj}$. Thus there is no harm in replacing $\eta(\omega_{mk})$ with $\sqrt{\eta(\omega_{mk})\eta(\omega_{lj})}$. This factorization allows us to write

$$\sum_{l,m} \int G_{l_j m_k}^+(\omega_{mk}, \chi) \hat{S}_{lm} d\chi \approx [\mathbf{g}^\dagger \hat{\mathbf{S}} \mathbf{g} + i \mathbf{d}^\dagger \hat{\mathbf{S}} \mathbf{d}]_{kj}$$

where $\hat{\mathbf{S}}$ is the matrix whose j, k element is the operator \hat{S}_{kj} and \mathbf{g} and \mathbf{d} are matrices whose elements are

$$[\mathbf{g}]_{ab} = \mu_{ab} \sqrt{\pi \int C^2(\omega_{ab}, \chi) D(\omega_{ab}, \chi) d\chi} \quad (\text{C.28})$$

$$[\mathbf{d}]_{ab} = \mu_{ab} \sqrt{\int \int_0^\infty \frac{C^2(\Omega, \chi)}{\omega_{ab} - \Omega} D(\Omega, \chi) d\Omega d\chi}. \quad (\text{C.29})$$

Upon performing a similar decomposition of the remaining terms, we find that eqn. (C.26) can be expressed more concisely as the matrix equation

$$\frac{d}{dt} \hat{\mathbf{S}} = \frac{i}{\hbar} [\hat{H}_S, \hat{\mathbf{S}}] + \text{homogeneous terms} \quad (\text{C.30})$$

$$+ (2\mathbf{g}^\dagger \hat{\mathbf{S}} \mathbf{g} - \mathbf{g} \mathbf{g}^\dagger \hat{\mathbf{S}} - \hat{\mathbf{S}} \mathbf{g} \mathbf{g}^\dagger) - i (\mathbf{d} \mathbf{d}^\dagger \hat{\mathbf{S}} - \hat{\mathbf{S}} \mathbf{d} \mathbf{d}^\dagger). \quad (\text{C.31})$$

To obtain the equation of motion for ρ , the (reduced) density matrix of the system, I note that $\rho = \langle \hat{\mathbf{S}} \rangle$. As indicated previously, the expectation value of the homogeneous terms vanishes for the case that the reservoir is initially in its ground state. At last we arrive at the main result of this appendix:

$$\frac{d}{dt} \rho = -\frac{i}{\hbar} [\mathbf{H}_s, \rho] + \mathbf{\Gamma} - i \mathbf{\Delta} \quad (\text{C.32})$$

where

$$\mathbf{\Gamma} \equiv 2\mathbf{g}^\dagger \rho \mathbf{g} - \mathbf{g} \mathbf{g}^\dagger \rho - \rho \mathbf{g} \mathbf{g}^\dagger, \quad (\text{C.33})$$

$$\mathbf{\Delta} \equiv \mathbf{d} \mathbf{d}^\dagger \rho - \rho \mathbf{d} \mathbf{d}^\dagger. \quad (\text{C.34})$$

The first term in eqn. (C.32) describes the evolution of the system in the absence of coupling to the

reservoir. Γ describes population relaxation and decoherence while Δ describes frequency shifts. I note that if there is more than one reservoir, each adds a separate matrix. That is, $\Gamma \rightarrow \Gamma_1 + \Gamma_2 + \dots$ and $\Delta \rightarrow \Delta_1 + \Delta_2 + \dots$.

C.2 Examples

C.2.1 Decay and Frequency shift in a two-level system

With two levels ($\omega_2 > \omega_1$), and under the rotating wave approximation, the only non-zero elements of \mathbf{g} and \mathbf{d} are the (2,1) elements. We may write these matrices as

$$\mathbf{g} = \begin{pmatrix} 0 & 0 \\ \sqrt{\gamma} & 0 \end{pmatrix} \quad (\text{C.35})$$

$$\mathbf{d} = \begin{pmatrix} 0 & 0 \\ \sqrt{\delta} & 0 \end{pmatrix}. \quad (\text{C.36})$$

where the values of γ and δ are determined by the intrinsic coupling constant g_{21} and the integrals over the mode parameters ω, χ . Then

$$\mathbf{\Gamma} = \begin{pmatrix} 2\gamma\rho_{22} & -\gamma\rho_{12} \\ -\gamma\rho_{21} & -2\gamma\rho_{22} \end{pmatrix}, \quad \mathbf{\Delta} = \begin{pmatrix} 0 & -\delta\rho_{12} \\ \delta\rho_{21} & 0 \end{pmatrix} \quad (\text{C.37})$$

and we obtain the density matrix equation

$$\frac{d}{dt} \begin{pmatrix} \rho_{11} & \rho_{12} \\ \rho_{21} & \rho_{22} \end{pmatrix} = \begin{pmatrix} 2\gamma\rho_{22} & [-i(\omega_{12} - \delta) - \gamma]\rho_{12} \\ [-i(\omega_{21} + \delta) - \gamma]\rho_{21} & -2\gamma\rho_{22} \end{pmatrix}. \quad (\text{C.38})$$

C.2.2 Decoherence in a two-level system

Consider coupling of the upper state in a two-level system to itself via a reservoir mode of zero frequency. In this case the interaction can be expressed in terms of matrices:

$$\mathbf{g} = \begin{pmatrix} 0 & 0 \\ 0 & \sqrt{\gamma} \end{pmatrix}, \quad \mathbf{d} = \begin{pmatrix} 0 & 0 \\ 0 & \sqrt{\delta} \end{pmatrix}. \quad (\text{C.39})$$

for appropriate values of γ and δ . Then

$$\mathbf{\Gamma} = \begin{pmatrix} 0 & -\gamma\rho_{12} \\ -\gamma\rho_{21} & 0 \end{pmatrix}, \quad \mathbf{\Delta} = \begin{pmatrix} 0 & -\delta\rho_{12} \\ \delta\rho_{21} & 0 \end{pmatrix}. \quad (\text{C.40})$$

This kind of coupling leads to decoherence and frequency shifts without changing the population relaxation rate. Pressure broadening is an example of this effect.

C.2.3 The Spontaneous Emission Rate and Lamb Shift

Suppose that the reservoir is the electromagnetic field. The quantized electromagnetic field is described by the operator

$$\hat{\mathbf{E}}(\mathbf{r}, t) = \sum_p \int_0^\infty \sqrt{\frac{\hbar\omega}{16\pi^3\epsilon_0}} \left[\boldsymbol{\epsilon}_{\mathbf{k},p} \hat{a}_{\mathbf{k},p}(\mathbf{r}, t) + \boldsymbol{\epsilon}_{\mathbf{k},p} \hat{a}_{\mathbf{k},p}^\dagger(\mathbf{r}, t) \right] d^3k$$

where \mathbf{k} is the wavevector, $\omega = |\mathbf{k}|c$ is the mode frequency, $p = 1, 2$ indexes the polarization, and $\boldsymbol{\epsilon}_p$ is a unit vector definition the direction of polarization. Instead of the wavevector it will be convenient to use the frequency and spherical angles of \mathbf{k} to label each mode. Now, consider that the system is located at the origin and is small compared to the wavelength of any field it might emit. In this case the interaction Hamiltonian may be approximated as $\hat{H}_I = -\boldsymbol{\mu} \cdot \hat{\mathbf{E}}(\mathbf{0}, 0)$, which yields the coupling constants

$$g_{ab}(\omega, \chi) \equiv g_{ab}(\omega, \theta, \phi, p) = \sqrt{\frac{\omega}{16\pi^3 c^3 \epsilon_0 \hbar}} (\boldsymbol{\epsilon}_p \cdot \boldsymbol{\mu}_{ab}). \quad (\text{C.41})$$

The number of modes of a given polarization in a differential volume element is $\omega^2 \sin \theta$. Thus

$$\int g_{ab}(\omega, \chi) g_{cd}^*(\omega, \chi) D(\omega, \chi) d\chi = \frac{\omega}{16\pi^3 c^3 \varepsilon_0 \hbar} \sum_p \int_0^\pi \int_0^{2\pi} (\boldsymbol{\epsilon}_p \cdot \boldsymbol{\mu}_{ab}) (\boldsymbol{\epsilon}_p \cdot \boldsymbol{\mu}_{cd})^* \omega^2 \sin \theta d\theta d\phi. \quad (\text{C.42})$$

Without loss of generality, let us first assume that $\boldsymbol{\mu}_{ab}$ and $\boldsymbol{\mu}_{cd}$ are parallel. If we call this direction the “north pole” of a spherical coordinate system, then it is convenient to choose $\hat{\boldsymbol{\theta}}$ and $\hat{\boldsymbol{\phi}}$ as the two polarization unit vectors perpendicular to the wavevector. Then

$$\sum_p (\boldsymbol{\epsilon}_p \cdot \boldsymbol{\mu}_{ab}) (\boldsymbol{\epsilon}_p \cdot \boldsymbol{\mu}_{cd})^* = \mu_{ab} \mu_{cd}^* \left[(\hat{\boldsymbol{\theta}} \cdot \hat{\boldsymbol{z}})^2 + (\hat{\boldsymbol{\phi}} \cdot \hat{\boldsymbol{z}})^2 \right] \quad (\text{C.43})$$

$$= \mu_{ab} \mu_{cd}^* \sin^2 \theta. \quad (\text{C.44})$$

Then

$$\sum_p \int_0^\pi \int_0^{2\pi} (\boldsymbol{\epsilon}_p \cdot \boldsymbol{\mu}_{ab}) (\boldsymbol{\epsilon}_p \cdot \boldsymbol{\mu}_{cd})^* \sin \theta d\theta d\phi = \mu_{ab} \mu_{cd}^* \int_0^\pi \int_0^{2\pi} \sin^3 \theta d\theta d\phi \quad (\text{C.45})$$

$$= \frac{8\pi}{3} \mu_{ab} \mu_{cd}^*. \quad (\text{C.46})$$

On the other hand, if $\hat{\boldsymbol{\mu}}_{ab}$ and $\hat{\boldsymbol{\mu}}_{cd}$ are perpendicular, say in the z and x directions, then

$$\sum_p (\boldsymbol{\epsilon}_p \cdot \boldsymbol{\mu}_{ab}) (\boldsymbol{\epsilon}_p \cdot \boldsymbol{\mu}_{cd})^* = \mu_{ab} \mu_{cd}^* \left[(\hat{\boldsymbol{\theta}} \cdot \hat{\boldsymbol{z}}) (\hat{\boldsymbol{\theta}} \cdot \hat{\boldsymbol{x}}) + (\hat{\boldsymbol{\phi}} \cdot \hat{\boldsymbol{z}}) (\hat{\boldsymbol{\phi}} \cdot \hat{\boldsymbol{x}}) \right] \quad (\text{C.47})$$

$$= \mu_{ab} \mu_{cd}^* \sin \theta \cos \theta \cos \phi \quad (\text{C.48})$$

which leads to

$$\sum_p \int_0^\pi \int_0^{2\pi} (\boldsymbol{\epsilon}_p \cdot \boldsymbol{\mu}_{ab}) (\boldsymbol{\epsilon}_p \cdot \boldsymbol{\mu}_{cd})^* \sin \theta d\theta d\phi = 0. \quad (\text{C.49})$$

Thus, for arbitrary $\hat{\boldsymbol{\mu}}_{ab}$ and $\hat{\boldsymbol{\mu}}_{cd}$,

$$\int g_{ab}(\omega, \chi) g_{cd}^*(\omega, \chi) D(\omega, \chi) d\chi = \frac{\omega^3}{6\pi c^3 \varepsilon_0 \hbar} \boldsymbol{\mu}_{ab} \cdot \boldsymbol{\mu}_{cd}^*. \quad (\text{C.50})$$

According to eqns. (C.28) and (C.29), the elements of the \mathbf{g} and \mathbf{d} matrices are then

$$[\mathbf{g}]_{ab} = \sqrt{\frac{\omega_{ab}^3}{6\pi\hbar\varepsilon_0 c^3}} \boldsymbol{\mu}_{ab} \quad (\text{C.51})$$

$$\equiv \sqrt{\gamma_{ab}} \hat{\boldsymbol{\mu}}_{ab} \quad (\text{C.52})$$

$$[\mathbf{d}]_{ab} = \sqrt{\frac{1}{6\pi^2\hbar\varepsilon_0 c^3}} \int_0^\infty \frac{\Omega^3}{\omega - \Omega^3} d\Omega \boldsymbol{\mu}_{ab}. \quad (\text{C.53})$$

$$\equiv \sqrt{\delta_{ab}} \hat{\boldsymbol{\mu}}_{ab}. \quad (\text{C.54})$$

where $\hat{\boldsymbol{\mu}}_{ab} = \boldsymbol{\mu}_{ab}/|\boldsymbol{\mu}_{ab}|$. Unfortunately, the integral determining δ_{ab} diverges. However, the upper frequency limit of ∞ is unreasonable, since the electric dipole approximation becomes invalid at short wavelengths (high frequencies). Hence it is customary to cut off the frequency integration at some maximum frequency ω_{\max} . For a two-level system, we obtain the spontaneous emission rate 2γ and an estimate³ of the Lamb shift:

$$2\gamma = \frac{\omega_{21}^3 |\mu_{21}|^2}{3\pi\hbar\varepsilon_0 c^3} \quad (\text{C.55})$$

$$\delta = \frac{|\mu_{21}|^2}{6\pi^2\hbar\varepsilon_0 c^3} \int_0^{\omega_{\max}} \frac{\Omega^3}{\omega - \Omega} d\Omega. \quad (\text{C.56})$$

³Some derivations of the Lamb shift lead to an integral over $\omega^2\Omega/(\omega - \Omega)$ instead of $\Omega^3/(\omega - \Omega)$. The origin of this discrepancy can be traced to the use of $\mathbf{p} \cdot \mathbf{A}$ for the interaction Hamiltonian instead of $-\boldsymbol{\mu} \cdot \mathbf{E}$. As the two Hamiltonians are related by a gauge transformation, they must lead to the same result in an exact calculation. Which is better to use in the case of approximations has been the subject of many complicated discussions; unfortunately, there is no general answer. The present approach indicates the source of the Lamb shift but is too simple to really predict its value. (I thank Prof. Eberly for a brief but helpful discussion on this point.)

Appendix D

Theory for Numerical Solution of a Two-Manifold System

My research has been greatly assisted by the ability to model the spectral and temporal response of both physical and idealized atomic systems. This modelling was performed with a set of computer routines and user interface (Fig. D.1) that I wrote in MATLAB. The set of routines is extremely flexible as the density matrix equations are constructed at run-time in accordance with user input, rather than being hard-coded. In this appendix I present the mathematical theory behind the computer routines. §D.1 presents a physical model for the class of systems under study. §D.2 derives the master equation, and §D.3 discusses the numerical methods used to obtain its solutions. Finally, §D.4 explains how polarizations and susceptibilities are obtained from a solution to the master equation.

D.1 The Physical Model

The purpose of this model is to allow one to determine the optical response of an alkali vapor illuminated by a several classical fields. To this end, I consider a system whose states can be grouped into two sets or manifolds: a set of “ground” states, and a set of “excited” states. The ground manifold and excited manifold are assumed to be separated by an optical frequency, while within each manifold there may be hyperfine levels separated by radio frequencies. Each hyperfine

Two-Manifold Atom Modeller Ryan Bennink, 2004

System Sodium D1

Ground level
 # Hyperfine levels 2
 Multiplicities 3 5
 Hyperfine intervals 1772 MHz

Excited level
 # Hyperfine levels 2
 Multiplicities 3 5
 Hyperfine intervals 189 MHz

Spontaneous emission rate 10 MHz
 Ground level dephasing rate 0 MHz
 Excited level dephasing rate 0 MHz
 Ensemble relaxation rate 0 MHz
 Magnetic field [Bx By Bz] [0 0 0] Gauss

Control field
 Nominal Rabi frequency 25 MHz
 Detuning 0 MHz
 Polarization [0 1 0]
 [XYZ ...]

Probe field
 Nominal Rabi frequency 25 MHz
 Detuning -1772 MHz
 Polarization [1 0 0]
 [XYZ ...]

Idler field
 Nominal Rabi frequency 0 MHz
 Detuning 1772 MHz
 Polarization [0 0 1]
 [XYZ ...]

Calculation Frequency scan + Spatial propagation
 Include Floquet orders up to ± 1

Frequencies -10:0.1:10 MHz
 Add to:
 Control field frequency Ground h.f. intervals
 Probe field frequency Excited h.f. intervals
 Doppler broaden the result 700 MHz rms
 Frequencies -4000:1:4000 MHz

Times 0:0.01:5 μ s
 Start with a thermal distribution
 the remembered final state

Distance 100 [mm] # Density 0.04 [$N\lambda^3$]

Intensity scale 40 steps
 Apply scaling to:
 Control field Probe field Idler field

Plot
 X: Frequency scan variable
 Y: abs value of
 Rabi frequency Probe
 Dipole moment Control
 Density matrix element 1.1
 Floquet order 1
 divided by the Rabi frequency
 component Control order 0

Calculate
 Plot as new Plot as additional
 Save Results Remember final Load

Figure D.1: The user interface for the computer routines used to model “two-manifold” atomic systems.

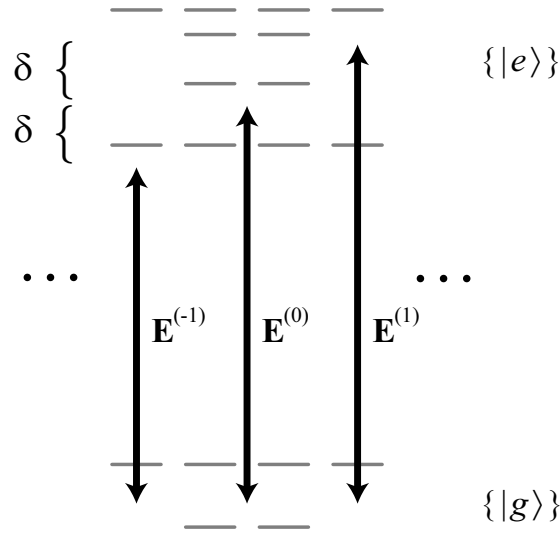


Figure D.2: The type of system under study, consisting of a set of ground states $|g\rangle$ coupled to a set of excited states $|e\rangle$ by optical fields $\mathbf{E}^{(m)}$ with frequency spacing δ . The influences of ensemble relaxation and a DC magnetic field are also included in the model.

level may further consist of multiple Zeeman states. This system interacts with a polychromatic field which consists of several frequency components spaced at regular intervals. I also allow for the presence of a DC magnetic field which causes level shifts and transitions between Zeeman states.

The system is specified by

- the energy or frequency of each hyperfine level
- the degeneracy of each hyperfine level
- the vector matrix elements of the electric and magnetic dipole operators
- the frequencies and complex amplitudes of all the fields, and
- the value of the DC magnetic field.

The state energies are relative to an arbitrary origin. When providing the input parameters for a calculation it is convenient to specify the energies relative to the lowest-lying states of each manifold and to specify the center field frequency relative to these states. The density matrix equations are

easiest to solve, though, when as much time dependence as possible has been eliminated. This is done by moving to a frame which rotates with the central field component. In this frame, the frequency of the m th spectral component is $m\delta$.

Regarding the matrix elements, values for real atoms can be obtained as described in Appendix B; however arbitrary values may also be used to define idealized systems. Whether the system is real or fictitious, only the relative values of the electric dipole matrix elements are needed. As discussed in §5.1, the relevant atomic quantities can be expressed conveniently in terms of the relative values, with the spontaneous emission rate providing the absolute scale where needed. The spontaneous emission rate also determines the nominal matrix element, which allows the electric field amplitudes to be specified in terms of nominal Rabi frequencies instead of in laboratory units.

D.2 Derivation of the Master Equation

D.2.1 Equation of Motion for a Single Atom

Ignoring damping processes for the moment, the equation describing the evolution of the density matrix for a single atom is

$$\frac{d}{dt}\hat{\rho} = -\frac{i}{\hbar}[\hat{H}, \hat{\rho}] \quad (\text{D.1})$$

where, in the electric and magnetic dipole approximations,

$$\hat{H} = \left(\sum_a \hbar\omega_a |a\rangle\langle a| \right) - \hat{\boldsymbol{\mu}}_E \cdot \mathbf{E} - \hat{\boldsymbol{\mu}}_B \cdot \mathbf{B} \quad (\text{D.2})$$

for the electric field $\mathbf{E}(t) = \tilde{\mathbf{E}}(t) + \tilde{\mathbf{E}}^*(t)$, the magnetic field \mathbf{B} , the bare-atom eigenstate energies $\hbar\omega_a$, and the electric and magnetic dipole operators $\hat{\boldsymbol{\mu}}_E, \hat{\boldsymbol{\mu}}_B$. Evaluating $[\hat{H}, \hat{\rho}]$ yields

$$\dot{\rho}_{ab} = -i(\omega_a - \omega_b)\rho_{ab} + \frac{i}{\hbar} \sum_x (\boldsymbol{\mu}_{ax,B}\rho_{xb} - \rho_{ax}\boldsymbol{\mu}_{xb,B}) \cdot \mathbf{B} \quad (\text{D.3})$$

$$+ \frac{i}{\hbar} \sum_x (\boldsymbol{\mu}_{ax,E}\rho_{xb} - \rho_{ax}\boldsymbol{\mu}_{xb,E}) \cdot \tilde{\mathbf{E}}(t) + \frac{i}{\hbar} \sum_x (\boldsymbol{\mu}_{xa,E}^*\rho_{xb} - \rho_{ax}\boldsymbol{\mu}_{bx,E}^*) \cdot \tilde{\mathbf{E}}^*(t). \quad (\text{D.4})$$

All terms involving $\boldsymbol{\mu}_{jk,E}$ or $\boldsymbol{\mu}_{jk,E}^*$ with $\omega_j < \omega_k$ correspond to off-resonant or counter-rotating terms, which I drop in accordance with the rotating-wave approximation. The strength of the coupling between a pair of states (e for excited, g for ground) and the m th sideband of the optical field may be expressed as the Rabi frequency

$$\Omega_{eg}^{(m)} = \frac{2\boldsymbol{\mu}_{eg,E} \cdot \mathbf{E}^{(m)}}{\hbar}. \quad (\text{D.5})$$

where $\tilde{\mathbf{E}}(t) = \sum_m \mathbf{E}^{(m)} e^{-im\delta t} e^{-i\omega_c t}$. In similar fashion the strength of interaction with the magnetic field is conveniently expressed in terms of the magnetic Rabi frequency

$$L_{gg'} = \frac{2\boldsymbol{\mu}_{gg',B} \cdot \mathbf{B}}{\hbar} \quad (\text{D.6})$$

for each pair of ground states g, g' (or excited states e, e'). Let the states be organized so that all the ground states are indexed first, followed by all the excited states. Then it is convenient to define Rabi frequency matrices

$$\mathbf{R}^{(m)} = \begin{pmatrix} \mathbf{0} & \mathbf{0} \\ [\Omega_{eg}^{(m)}] & \mathbf{0} \end{pmatrix}, \quad \mathbf{L} = \begin{pmatrix} [L_{gg'}] & \mathbf{0} \\ \mathbf{0} & [L_{ee'}] \end{pmatrix} \quad (\text{D.7})$$

where $[Z_{ab}]$ denotes the matrix whose elements are Z_{ab} .

I now move into the frame that rotates with the central field component. In this frame the slowly-varying density matrix $\boldsymbol{\rho}$ obeys

$$\begin{aligned} \dot{\rho}_{ab} &= i(\Delta_b - \Delta_a)\rho_{ab} + \frac{i}{2} \sum_x L_{ax} \rho_{xb} - \frac{i}{2} \sum_y \rho_{ay} L_{yb} \\ &+ \frac{i}{2} \sum_x \sum_m R_{ax}^{(m)} e^{-im\delta t} \rho_{xb} - \frac{i}{2} \sum_y \sum_m \rho_{ay} R_{yb}^{(m)} e^{-im\delta t} \\ &+ \frac{i}{2} \sum_x \sum_m R_{xa}^{(m)*} e^{+im\delta t} \rho_{xb} - \frac{i}{2} \sum_y \sum_m \rho_{ay} R_{by}^{(m)*} e^{+im\delta t}. \end{aligned} \quad (\text{D.8})$$

This may be written in tensor notation as

$$\frac{d}{dt}\boldsymbol{\rho} = \mathbf{M}\boldsymbol{\rho} \quad (\text{D.9})$$

where $\mathbf{M} = \sum_m \mathbf{M}^{(m)} e^{-im\delta t}$ and

$$M_{abxy}^{(0)} \Big|_{\text{no damping}} = i(\Delta_b - \Delta_a)\delta_{ax}\delta_{by} + \frac{i}{2} \left[(L_{ax} + R_{ax}^{(0)} + R_{xa}^{(0)*})\delta_{by} - \delta_{ax}(L_{yb} + R_{yb}^{(0)} + R_{by}^{(0)*}) \right] \quad (\text{D.10})$$

$$M_{abxy}^{(m)} = \frac{i}{2} \left[(R_{ax}^{(m)} + R_{xa}^{(-m)*})\delta_{by} - (R_{yb}^{(m)} + R_{by}^{(-m)*})\delta_{ax} \right]. \quad (\text{D.11})$$

As discussed in Appendix C, coupling to the electromagnetic continuum adds the terms

$$2\mathbf{G}^\dagger \boldsymbol{\rho} \mathbf{G} - \mathbf{G} \mathbf{G}^\dagger \boldsymbol{\rho} - \boldsymbol{\rho} \mathbf{G} \mathbf{G}^\dagger \quad (\text{D.12})$$

to the expression for $\dot{\boldsymbol{\rho}}$, where

$$\mathbf{G}_{ab} = \begin{cases} \sqrt{\gamma_{ab}} \hat{\boldsymbol{\mu}}_{ab} & a \in \{e\}, b \in \{g\} \\ 0 & \text{else} \end{cases}, \quad (\text{D.13})$$

$$\gamma_{ab} = \frac{\omega_0^3 |\mu_{ab}|^2}{6\pi \hbar \varepsilon_0 c^3}. \quad (\text{D.14})$$

We have

$$\begin{aligned} \left[2\mathbf{G}^\dagger \boldsymbol{\rho} \mathbf{G} - \mathbf{G} \mathbf{G}^\dagger \boldsymbol{\rho} - \boldsymbol{\rho} \mathbf{G} \mathbf{G}^\dagger \right]_{ab} &= 2 \sum_{xy} (\mathbf{G}^\dagger)_{ax} \cdot \mathbf{G}_{yb} \rho_{xy} - \sum_{n,x} \mathbf{G}_{an} \cdot (\mathbf{G}^\dagger)_{nx} \rho_{xb} \\ &\quad - \sum_{n,y} \rho_{ay} \mathbf{G}_{yn} \cdot (\mathbf{G}^\dagger)_{nb}. \end{aligned} \quad (\text{D.15})$$

This gives

$$M_{abxy}^0 = M_{abxy}^0 \Big|_{\text{no damping}} + 2(\mathbf{G}^\dagger)_{ax} \cdot \mathbf{G}_{yb} - \sum_n \mathbf{G}_{an} \cdot (\mathbf{G}^\dagger)_{nx} \delta_{by} - \sum_n \delta_{ax} \mathbf{G}_{yn} \cdot (\mathbf{G}^\dagger)_{nb}. \quad (\text{D.16})$$

A similar set of terms may be added to incorporate dephasing. For simplicity, I assume that each state dephases via a separate interaction channel. The additional terms then have the form $\delta_{ax}\delta_{by}[(\gamma_{\text{deph},x} + \gamma_{\text{deph},y})\delta_{xy} - \gamma_{\text{deph},x} - \gamma_{\text{deph},y}]$ where $\gamma_{\text{deph},x}$ is the dephasing rate of state x .

D.2.2 Equation of Motion for the Atomic Ensemble

Eqn. (D.9) is the equation of motion for a single atom. In the case of an atomic vapor, atomic motion produces a continuous turnover of the atoms in the illumination region, with optically prepared atoms being replaced by atoms from a reservoir in some state ρ^{rsv} . The ensemble density matrix may be written as

$$\bar{\rho} = \frac{1}{N} \sum_{j=1}^N \rho_j. \quad (\text{D.17})$$

where N is the number of atoms in the illumination region and ρ_j is the density matrix of the j th atom. Let $p(\tau) d\tau$ be probability that an atom remains in the illumination region between τ and $\tau + d\tau$ seconds. Then $(dp(\tau)/d\tau) p^{-1} d\tau$ is probability that an atom which has remained for a time τ will leave in the interval $d\tau$. The equation of motion for $\bar{\rho}$ is then

$$\frac{d}{dt} \bar{\rho}(t) = \frac{1}{N} \sum_{j=1}^N \frac{d}{dt} \rho_j + \frac{1}{N} \sum_{j=1}^N \frac{1}{p(t-t_j)} \frac{dp(t-t_j)}{dt} (\rho_j - \rho^{\text{rsv}}). \quad (\text{D.18})$$

Now, the first term is given by eqn. (D.9). Assuming that all atoms experience the same illumination,

$$\frac{1}{N} \sum_{j=1}^N \frac{d}{dt} \rho_j = \frac{1}{N} \sum_{j=1}^N \mathbf{M} \rho_j = \mathbf{M} \bar{\rho}. \quad (\text{D.19})$$

To evaluate the second term, I pick a particular form for p :

$$p(\tau) = \Gamma e^{-\Gamma\tau} \quad (\text{D.20})$$

which implies that all atoms inside the illumination region have an equal chance of leaving it in a given (short) time interval. This is not the most realistic model (for instance, in §6.1.1 we found that $f(\tau) = \int_0^\tau p(t) dt = (1 + \Gamma\tau)^{-1}$ for diffusive motion), but it makes the resulting equations much

simpler. With $p^{-1}dp(t - t_j)/dt = \Gamma$ we obtain

$$\frac{d}{dt}\bar{\rho}(t) = \mathbf{M}\bar{\rho} - \Gamma(\bar{\rho} - \rho^{\text{rsv}}). \quad (\text{D.21})$$

The density matrix will contain frequency components at all multiples of δ :

$$\bar{\rho} = \sum_{m=-\infty}^{\infty} \bar{\rho}^{(m)} e^{-im\delta t}. \quad (\text{D.22})$$

Here $\bar{\rho}^{(m)}$ denotes the component of the ensemble density matrix at frequency $m\delta$, which is accurate to all orders in the field strengths¹. Then (D.21) becomes

$$\frac{d}{dt} \sum_{m=-\infty}^{\infty} \bar{\rho}^{(m)} e^{-im\delta t} = \sum_{m''} \mathbf{M}^{(m'')} e^{-im''\delta t} \sum_{m'} \bar{\rho}^{(m')} e^{-im'\delta t} - \Gamma \sum_{m=-\infty}^{\infty} \bar{\rho}^{(m)} e^{-im\delta t} + \Gamma \rho^{\text{rsv}}. \quad (\text{D.23})$$

This yields the Floquet relation

$$\frac{d}{dt} \bar{\rho}^{(m)} = \sum_n \mathbf{M}^{(n)} \bar{\rho}^{(m-n)} + (im\delta - \Gamma) \bar{\rho}^{(m)} + \delta_{m,0} \Gamma \rho^{\text{rsv}} \quad (\text{D.24})$$

This equation may either be solved directly in the steady-state case or numerically integrated to obtain temporal behavior of the system.

D.3 Solving the Master Equation in the Steady-State

The steady-state solution of (D.24) is appropriate for modelling the interaction between time-independent field components and an atom of constant velocity. In this case we have

$$\sum_n \mathbf{M}^{(n)} \bar{\rho}^{(m-n)} + (im\delta - \Gamma) \bar{\rho}^{(m)} = -\delta_{m,0} \Gamma \rho^{\text{rsv}}. \quad (\text{D.25})$$

¹For small or vanishing values of δ the various orders of the Floquet series should probably be summed to get a physically meaningful result, as there is little distinction between them.

This equation describes a linear system of equations which may be expressed symbolically in matrix form as

$$\mathbf{B}\mathbf{s} = -\mathbf{z}, \quad (\text{D.26})$$

where

$$\mathbf{s} = \begin{pmatrix} \vdots \\ \bar{\rho}^{(-1)} \\ \bar{\rho}^{(0)} \\ \bar{\rho}^{(1)} \\ \vdots \end{pmatrix}, \quad \mathbf{z} = \Gamma \begin{pmatrix} \vdots \\ 0 \\ \boldsymbol{\rho}^{\text{rsv}} \\ 0 \\ \vdots \end{pmatrix}, \quad (\text{D.27})$$

and

$$\mathbf{B} = \begin{pmatrix} \ddots & & \vdots & & & \\ & \mathbf{M}^0 + (-i\delta - \Gamma)\mathbf{I} & \mathbf{M}^{(-1)} & \mathbf{M}^{(-2)} & & \\ \dots & \mathbf{M}^{(+1)} & \mathbf{M}^0 - \Gamma\mathbf{I} & \mathbf{M}^{(-1)} & \dots & \\ & \mathbf{M}^{(+2)} & \mathbf{M}^{(+1)} & \mathbf{M}^0 + (i\delta - \Gamma)\mathbf{I} & & \\ & & \vdots & & \ddots & \end{pmatrix}. \quad (\text{D.28})$$

In implementing (D.26) on a computer, the matrices $\bar{\rho}^{(m)}$ and $\boldsymbol{\rho}^{\text{rsv}}$ are reshaped into column vectors and the rank-4 tensors $\mathbf{M}^{(m)}$ are reshaped into matrices. If the number of states is N and the Floquet series is truncated at F terms, then \mathbf{s} is of length FN^2 and \mathbf{B} is of size $FN^2 \times FN^2$. Clearly, the computational demands grow rapidly with the number of states. On a personal computer with an 850 MHz Intel processor and 256 MB RAM, a 3-order solution of the sodium D1 system ($F = 3$, $N = 16$) requires approximately 1/3 second.

Now a confession must be made: $\mathbf{M}^{(0)}$ is singular, which means that \mathbf{B} as given above cannot be inverted. This singularity is artificial, however; it occurs because conservation of population makes one of the equations redundant. To eliminate this artificial singularity and normalize the solution, I replace one of the population rate equations in (D.26) with an equation expressing conservation of population:

$$\sum_{aa} \bar{\rho}_{aa}^{(m)} = \delta_{m,0}. \quad (\text{D.29})$$

D.4 Calculating Optical Properties

D.4.1 Calculating Dipole Moments and Susceptibilities

Once the ensemble density matrix components $\bar{\rho}^{(m)}$ have been obtained, the induced atomic dipole moment can be calculated. The complex amplitude of the atomic dipole moment at frequency $\omega_c + m\delta$ is

$$\mathbf{p}(\omega_c + m\delta) = \sum_{eg} \boldsymbol{\mu}_{eg}^* \bar{\rho}_{eg}^{(m)}. \quad (\text{D.30})$$

The polarization and susceptibility are related to atomic dipole moment by $\mathbf{P} = \mathcal{N}\mathbf{p}$ and $\chi = \mathbf{P}/(\varepsilon_0\mathbf{E})$ where \mathcal{N} is the atomic number density and \mathbf{E} is the appropriate input field. Terms with $m = 0$ correspond to pump susceptibilities, terms with $m = 1$ correspond to probe susceptibilities, and terms with $m = -1$ correspond to idler susceptibilities. Terms with $|m| > 1$ correspond to higher-order processes. The polarization is not broken down into contributions from particular nonlinear orders, but if desired they can be obtained by a polynomial fit to solutions calculated over some range of Rabi frequencies.

To determine, for example, the dressed linear susceptibility of a right-hand circularly polarized probe beam, the relevant quantity is $\mathbf{p}(\omega_c + \delta) \cdot (\hat{\mathbf{x}} + i\hat{\mathbf{y}})^* / \sqrt{2}$ as calculated with a small value for the probe Rabi frequency.

D.4.2 Spatial Propagation

Under steady-state conditions, the m th order of the electric field obeys

$$\left(\frac{\partial^2}{\partial z^2} + k_m^2 \right) \mathbf{E}^{(m)} = -\frac{k_m^2}{\varepsilon_0} \mathbf{P}^{(m)} \quad (\text{D.31})$$

where $k_m = \omega_m/c = (\omega_0 + m\delta)/c$ is the free-space wavevector. (I assume all fields are co-propagating.) The solution for each field will consist of a rapidly oscillating factor $\exp(ik_m z)$, which is of little interest, and a slowly varying amplitude $\mathbf{A}^{(m)}$ whose evolution is affected by $\mathbf{P}^{(m)}$. The common dependence $\exp(ik_0 z)$ may be factored out. Then, under the typical condition

$\left| \partial^2 \mathbf{A}^{(m)} / \partial z^2 \right| \ll \left| k \partial \mathbf{A}^{(m)} / \partial z \right|$, we have

$$\frac{\partial \mathbf{A}^{(m)}}{\partial z} = \frac{i}{2} k_m \mathbf{P}^{(m)} \exp(-im\delta z/c). \quad (\text{D.32})$$

Here $\mathbf{P}^{(m)}$ is obtained by solving the master equation (D.9) with the field components $\mathbf{E}^{(m)} = \mathbf{A}^{(m)} \exp(-im\delta z/c)$.